ANALYSIS OF WEAK INTERACTIONS IN P450 SYSTEMS

A thesis submitted to the University of Manchester for the degree of Doctor of Philosophy in the Faculty of Engineering and Physical Sciences

2013

IDORENYIN SUNDAY EKANEM

SCHOOL OF CHEMICAL ENGINEERING AND ANALYTICAL SCIENCE

LIST OF CONTENTS

LIST OF FIGURES

LIST OF TABLES

LIST OF EQUATIONS

LIST OF ABBREVIATIONS

4-PI:	4-phenyl imidazole
ARHD:	Aromatic ring hydroxylating dioxygenases
AUC:	Analytical ultracentrifugation
BH_4:	Tetrahydrobiopterin
BM3:	Flavocytochrome P450 BM3 from *Bacillus megaterium*
BMP:	The heme domain of BM3
BMR:	The reductase domain of BM3
BS^3:	Bis (sulfosuccinimidyl) suberate
BSA:	Bovine serum albumin
CaM:	Calmodulin
CG-MALLS:	Composite gradient multi-angle laser light scattering
CO:	Carbon monoxide
CPR:	Cytochrome P450 reductase domain
CPO:	Chloroperoxidase
CSV:	Comma separated values
CYP:	Cytochrome P450
DEAE:	Diethylaminoethyl cellulose
DEER:	Double electron-electron resonance
DFDNB:	1,5-Difluoro-2,4-dinitrobenzene
DMP:	Dimethyl pimelimidate dihydrochlride
DNA:	Deoxyribonucleic acid
DTT:	DL-Dithiothreitol
EDC:	1-Ethyl-3-[3-dimethylaminopropyl]Carbodiimide Hydrochloride
EDTA:	Ethylenediaminetetraacetic acid
ELDOR:	Electron-electron double resonance
EPR:	Electron paramagnetic resonance
e.t.:	Electron transfer
FAD:	Flavin adenine dinucleotide
FDX:	Ferredoxins
FLD:	Flavodoxins
FMN:	Flavin mononucleotide
FRET:	Fluorescence resonance energy transfer
HA:	Hydroxyapatite

H(F)PLC:	High (fast) performance liquid chromatography
IPTG:	Isopropyl-beta-D-thiogalactopyranoside
ITC:	Isothermal titration calorimetry
k_{cat}:	Normalised rate constant
KCl:	Potassium chloride
K_d:	Dissociation constant
k_{obs}:	Observed rate constant
k_{off}:	Apparent de-binding rate constant
k_{on}:	Second order ligand binding rate constant
KPi:	Inorganic potassium phosphate
LB:	Luria Bertani (medium)
MCD:	Magnetic circular dichroism
MSR:	Methionine synthase reductase
NADH (NAD^+):	Reduced (oxidized) nicotinamide adenine dinucleotide
NADPH: ($NADP^+$):	Reduced (oxidized) nicotinamide adenine dinucleotide phosphate
NMR:	Nuclear magnetic resonance
NOS:	Nitric oxide synthase
NPG:	N-palmitoylglycine
NSD:	Normalised spatial discrepancy
OD:	Optical density
PDA:	photodiode array
PPI:	Protein-protein interaction
QELS:	Quasi-elastic light scattering
Q-seph:	Quaternary amino Sepharose
R_g:	Radius of gyration
r_H:	Hydrodynamic radius
Rz:	Reinheitszahl
RR:	Resonance Raman spectroscopy
SANS:	Small angle neutron scattering
SAXS:	Small angle X-ray scattering
SDS-PAGE:	Sodium Dodecyl Sulfate Polyacrylamide Gel Electrophoresis
SEC-MALLS:	Size exclusion chromatography-multi-angle laser light scattering
SERRS:	Surface enhanced Resonance Raman spectroscopy

SINS: Self-interaction nanoparticle spectroscopy

SiR: Sulphite reductase

SLS: Static light scattering

SOC: Super optimal broth with catabolite repression

SVC: Second osmotic virial coefficient

TB: Terrific broth (media)

TEMED: Tetramethylethylenediamine

UV: Ultraviolet

ABSTRACT

The University Of Manchester

Idorenyin Sunday Ekanem

Doctor of Philosophy

Analysis of Weak Interactions in P450 Systems

May 2013

Many methods are used for screening/characterisation of strong protein-protein interactions (PPIs), but there has been slow progress in understanding weak PPIs due to technical difficulties. In this thesis, combined biophysical and structural approaches were used to study weak PPIs in a model cytochrome P450 (P450) system. P450s are biotechnologically important heme-binding oxidase enzymes involved in lipid, steroid and drug metabolism. *Bacillus megaterium* P450 BM3 (BM3) was used as a model. BM3 is a high activity P450 with its redox partner (an FAD- and FMN-binding reductase) linked to the P450 in a single polypeptide. Genetic dissection enabled generation of individual P450 (BMP) and P450 reductase (BMR) domains, as well as separate FAD- and FMN-binding domains.

Preliminary work on BM3, BMP and BMR used equilibrium optical binding and showed blue (type I) heme Soret band shifts with substrates (N-palmitoylglycine, lauric acid), and red (type II) shifts with inhibitors (imidazole, 4-phenyl imidazole), consistent with typical P450 behaviour. Steady-state kinetic catalytic efficiency of BM3 in reducing cytochrome *c* was higher than for BMR, suggesting that BMP promotes interactions between BMR/cytochrome *c*. Interactions between BMP/BMR domains were studied by examining NADPH-dependent electron transfer (e.t.) rate between these domains using stopped-flow absorption spectroscopy, and across a range of ionic strengths. The inter-domain e.t. rate in the reconstituted system was ~1000-fold less than in intact BM3. Elevated ionic strength decreased the e.t. rate in both systems, and particularly for the reconstituted domains. Slow BMP reduction by NADPH in absence of BMR was also observed over longer time scales.

Biophysical methods were used in quaternary structural characterization of BM3 and its domains. BM3 reversibly dimerizes (mostly stabilized by electrostatic interactions) with a dissociation constant (K_d) of 0.29 µM. Reversible dimerization was also seen for BMR, but with a weaker K_d than BM3. The FAD domain is near-fully dimerized most likely due to intermolecular disulphide bonds, while FMN and heme domains are monomers. Results indicate that BMR domain interactions regulate BM3 dimerization. The BM3 shape is compact and globular, BMR is compact and ellipsoidal, and the FAD domain is globular with extended ends. Differences between FAD domain crystal and solution structures suggest conformational differences possibly due to disulphide bonds stabilizing solution dimer. 6 different BMR conformations were obtained by rigid body modelling, all showing that BMR exists in an "open" conformation with respect to orientation of its FAD and FMN domains.

DECLARATION

I declare that no portion of the work in this thesis have been submitted in support of an application for any degree, or other qualification, at this or any other university or other institute of learning.

COPYRIGHT STATEMENT

ACKNOWLEDGEMENTS

DEDICATION

I dedicate this thesis to my son, Joshua Etiene-abasi Usoh. Your arrival brought so much joy into my heart and inspiration to complete this training. Thank you dear son, I love you.

CHAPTER 1

Introduction and Literature Review

CHAPTER ONE: INTRODUCTION AND LITERATURE REVIEW

1.0 INTRODUCTION

The cytochrome P450 family is a highly diversified set of *b*-type heme-containing proteins with an unusual characteristic absorbance of light at wavelengths near 450 nm when reduced and complexed with carbon monoxide. Cytochrome P450s (CYPs) are a multi-gene superfamily of heme-containing enzymes that carry out extremely diverse reactions including the metabolism of steroids and fatty acids as well as the detoxification (via biotransformation) of many drugs and xenobiotics (chemical substances that are foreign to the body). They are present in vertebrates, invertebrates, plants, fungi, yeast and bacteria, to mention but a few, and catalyse these reactions by inserting an atom of oxygen into their substrates, generally utilizing electrons provided from a redox partner. Thus effective interactions of cytochromes P450 with their redox partners are indispensable and an understanding of their mechanism of interaction is crucial. Complexes formed between cytochromes P450 and their redox partners, as well as most other electron transfer proteins, are known to be weak and transient (*1*).

Studies on human cytochrome P450 has been on-going for over half a century now. However, its membrane-bound nature and insolubility has posed great limitations to advancements in this area, emphasizing the need for a model. Cytochrome P450cam (CYP101A1), a camphor hydroxylase isolated from *Pseudomonas putida*, has served as the model system for cytochromes P450 for around thirty years (*2*). A few years after the discovery of cytochrome P450cam (*3*), a fusion enzyme whose P450 and redox partner are contained within one polypeptide chain emerged and accelerated the understanding of P450 mechanisms by also serving as a model (*4*). This is the flavocytochrome P450 BM3 isolated from *Bacillus megaterium* (BM3, CYP102A1).

BM3 is a self-sufficient fatty acid monooxygenase discovered by Armand Fulco and his group over two decades ago. The interaction between this cytochrome P450 enzyme and its linked reductase domain is strong due to the covalent linkage and electron transfer is efficient, leading to the highest fatty acid hydroxylase activity (17000 min^{-1}) ever observed in cytochromes P450 (*5*). However, questions remain with regards to the

enzyme mechanism mainly because crystallization of full length BM3 has remained elusive and no high resolution structure exists. With the rapid advancements in recombinant DNA technology, it has been possible to truncate this enzyme into its two separate domains: the P450 and reductase domains (*6*), one of which (the P450 domain) has been crystallized . However, the reconstituted system has a thousand-fold reduction in both the fatty acid hydroxylase activity of the enzyme (*7*) and electron transfer between the two domains (as shown in this work). Given the ease of expression, purification, and characterization with added stability of these domains when individually expressed, it might be possible to reconstruct the structure of the intact BM3 enzyme from the structures of their individual domains.

Reconstructing the BM3 enzyme requires understanding of the origin of the weak protein-protein interactions (PPIs) between the domains and the weak dimerization in the intact BM3 system, which is believed to be the catalytically active form in NADPH-dependent fatty acid hydroxylation (*8, 9*). It is important to note that while a large number of methods have been developed to screen and characterize strong protein-protein interactions, the technical difficulties involved in trapping weak complexes in solution has made the process of understanding weak PPIs considerably slower (*10, 11*). In this study, weak interactions are defined as those with dissociation constants in the micromolar range and above according to the classification of PPIs by Nooren and Thornton (*12*). The various types of non-covalent interactions that govern weak PPIs are detailed in section 1.3.2 of this thesis.

 In this work, we aim to use a combination of different techniques to analyse weak interactions that occur in cytochromes P450, using flavocytochrome P450 BM3 and its domains as a model. From a broader perspective, weak PPIs are important in a wide range of physiological processes and aberrant PPIs may be responsible for several human diseases, such as Alzheimer's, sickle cell anemia, and rheumatoid arthritis (*13*). In this respect, methods exploited in this thesis for studies of PPIs in the P450 BM3 system should find applications for defining weak PPIs in biomedically relevant systems and disease states.

1.0.1 Objectives of the Study

The main objectives of this research include

- ❖ Optimize expression and purification of the full length as well as the different domains of the BM3 enzyme

- ❖ Characterize binding of substrates and inhibitors to the full length enzyme and the P450 domain using steady state kinetics and optical titration methods

- ❖ Investigate the reduction of various electron acceptors by the full length enzyme and the reductase domain using steady state kinetics

- ❖ Conduct preliminary studies on the characterization of weak interactions between the BM3 domains across different solution conditions using stopped flow techniques

- ❖ Examine the oligomeric state of BM3 and its respective domains in solution

- ❖ Conduct an in-depth characterization of the protein shape, size, and hydrodynamic properties; and of the weak protein-protein interactions for BM3 and the individual domains using static and dynamic light scattering, small-angle X-ray scattering (SAXS), and analytical ultracentrifugation (AUC).

- ❖ Use modelling methods to match SAXS and hydrodynamic data, and possibly resolve the structure of BM3 and its reductase domains as there are no available crystal structures.

- ❖ Relate the obtained structural information to BM3 activities and functions and evaluate the mechanisms of redox partner recognition.

1.0.2 Layout of the Thesis

The layout of this report is as follows.

- ➢ Chapter 1 contains the introduction and literature survey, which is further divided into three sections. The first section introduces the cytochrome P450 superfamily as part of the heme-thiolate protein group. Further, the classification and the general catalytic mechanism of cytochromes P450 are explained with a schematic representation of the catalytic cycle. This section also offers a brief introduction of the diflavin reductase class of enzymes, a family to which the flavocytochrome P450 BM3 enzyme belongs. The second section presents a comprehensive review on BM3. The overall structure-function relationship is

highlighted including the effects of substrate binding, roles of residues revealed via mutational studies, and details of the electron transfer mechanism. The final section is a review of biologically relevant weak protein-protein interactions, which includes the methods that have been used so far to study these interactions and the factors that govern these interactions in solution.

➢ Chapter 2 details the experimental procedures used in this work

➢ Chapter 3 is the first results chapter, which covers preparation of plasmid DNA and purification of BM3 and the various domains and equilibrium optical titration analysis of ligand binding and steady-state kinetics of BM3. In addition, stopped-flow techniques have been used to characterize the interactions (in terms of kinetic activity) within the full length BM3 enzyme and between the P450 (BMP) and reductase (BMR) domains of both the intact and reconstituted enzymes.

➢ Chapter 4 covers results of hydrodynamic studies and structural analysis of BM3 and the individual domains. First, the oligomerization states of BM3 and the various domains (BMP, BMR, FAD, and FMN) were determined and characterized using a combination of SEC-MALLS and AUC techniques. CG-MALLS and cross-linking methods were employed in further characterization of the BM3 dimer. This chapter also provides results of crystallization trials for the BMR mutant- C773A.

➢ Chapter 5 is the final results chapter. Here the results from SAXS analysis on BM3 and its domains are shown. Also, we propose models for the structure of full length BM3 and the reductase domains, which are consistent with the SAXS and hydrodynamic data discussed in the previous chapter.

➢ The results are all discussed and conclusions are drawn in chapter 6. This chapter also details recommendations for further studies.

1.1 THE CYTOCHROME P450 SUPERFAMILY

Cytochromes are coloured proteins that contain one or several heme groups (hemoproteins) with distinctive UV-visible-light absorption spectra, and which act as electron acceptors/donors in electron transfer processes. These hemoproteins can be classified based on the heme prosthetic group type or how the heme atom coordinates to the protein. Of particular interest to this study are the *b*-type cytochromes (containing heme b as the prosthetic group) which are the most common class of cytochromes.

Heme *b* differs from some of the other cytochrome groups in that the heme iron is non-covalently attached to an amino acid side chain on the neighbouring apoprotein. Heme *b* is the most frequently found heme cofactor, with other hemes arising from chemical modifications of, or covalent linkages to, the basic heme *b* scaffold. The structure of heme *b* consists of a large porphyrin ring system with two propionate side chains and an iron atom in the centre bonded to four nitrogen atoms of the porphyrin ring, forming a planar structure (Figure 1.1). Examples of heme *b* containing hemoproteins are oxygen transport proteins such as haemoglobin and myoglobin, the cytochrome P450 enzymes, cytochrome b_{562}, nitric oxide synthase, selected peroxidases, and cyclooxygenases (*14*). Further, these *b*-type cytochromes can be characterized based on the ligand to which the porphyrin iron is bound. While haemoglobin, myoglobin and most peroxidases have a histidine ligand, others such as prostacyclin synthase, chloroperoxidase, nitric-oxide synthase, and cytochromes P450 have an evolutionary conserved cysteine ligand (*15*). The former group are usually termed the heme-imidazole proteins while the latter group of enzymes are termed heme-thiolate proteins.
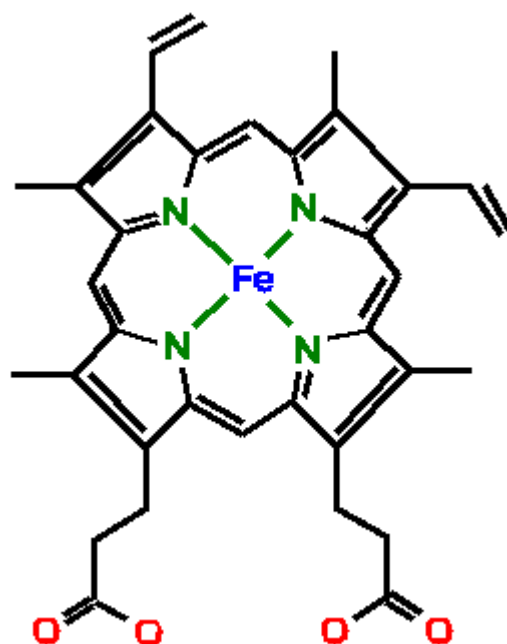
Figure 1.1: Structure of heme b. *The heme contains iron protoporphyrin IX which has two propionate, two vinyl and 4 methyl side chains with molecular formula* $C_{34}H_{32}O_4N_4Fe$

1.1.1 Heme-Thiolate Proteins

Cytochromes P450 (CYP) were the first hemoproteins observed to have a thiolate group (from a conserved cysteine) as the axial ligand of the heme iron, hence the CYPs are also known as heme-thiolate proteins. CYP is also the most studied of the group closely followed by nitric oxide synthase (NOS). Heme-thiolate proteins catalyse monooxygenase (CYP and NOS) and haloperoxidase (such as chloroperoxidase) reactions (*16*). Monooxygenases and haloperoxidases mediate oxidation of their substrates by the incorporation of a single molecule of oxygen using dioxygen (O_2) and hydrogen peroxide (H_2O_2) respectively as oxygen donors (*17*). Heme-thiolate proteins exhibit an unusual characteristic absorbance of light at wavelengths near 450 nm when reduced and complexed with carbon monoxide.

1.1.1.1 Heme-Thiolate Haloperoxidases

Chloroperoxidase (CPO) was the first heme-thiolate haloperoxidase to be discovered about 6 decades ago by Hager and co-workers in *Caldariomyces fumago*, an ascomycetous fungus (*18, 19*). CPO catalyses a broad range of reactions including bromination, chlorination, iodination, epoxidation, sulfoxidation, benzylic hydroxylation, N-dealkylation and classic peroxidation (*20, 21*).

Two other heme-thiolate haloperoxidases, *Agrocybe aegerita* peroxidase (AaP) and *Coprinus radians* peroxidase (CrP), were discovered by the Hofrichter group in the last decade from agaric and coprophilous mushrooms respectively (*22*). AaP and CrP catalyse similar reactions to the CPO but, in contrast to the CPO, also extracellularly catalyse hydroxylation of aromatic compounds. They are thus classed as aromatic peroxygenases and, unlike other heme peroxidases, their physiological relevance is yet to be understood.

1.1.1.2 Nitric oxide synthase

Nitric oxide synthases (NOSs) belong to the enzyme class EC 1.14.13.39 and are metalloproteins solely responsible for the production of nitric oxide (NO, also called nitrogen monoxide) from L-arginine in the mammalian system. NO is a free radical and a highly reactive diatomic gas that acts as an intercellular messenger with important physiological roles in cardiovascular, nervous and immune systems (*23-26*). The majority of the published work on NOS enzymes is focussed on mammalian NOS.

However, NOS has also been characterized in bacteria and some other organisms, but only recently in plants (*24, 27-30*).

Three isoforms of NOS have been discovered and studied extensively, two of which are constitutively expressed: neuronal NOS (nNOS) in nerve cells, skeletal and heart muscles and endothelial NOS (eNOS) in vascular endothelial cells. The third isoform is the inducible NOS (iNOS) which is only expressed when triggered in response to cytokines (*23, 31, 32*). These isoforms have 50-60% amino acid sequence identity (*27*) but play distinctive physiological roles; hence NOSs are highly versatile enzymes. Some of these roles include regulation of vascular tone and blood pressure, inhibition of blood clotting, nerve signalling, sphincter relaxation, penile erection and angiogenesis (*24, 25, 32, 33*).

Mammalian NOS is active as a homodimer, with each monomer comprising of an N-terminal oxygenase domain linked to a C-terminal reductase domain in a single polypeptide chain. The linker region is about 30 amino acids in length and contains a binding site for calmodulin (CaM), one of the five co-factors required for NOS activity. The other co-factors are iron-protoporphyrin IX (heme *b*) and tetrahydrobiopterin (BH_4) with binding sites in the oxygenase domains; and flavin adenine dinucleotide (FAD) and flavin mononucleotide (FMN) bound to the reductase domain (*24, 32*). BH_4 has been suggested to play roles in the NOS redox process and in dimer assembly and stabilization (*23*). The oxygenase and reductase domains also bind the substrates L-arginine and nicotinamide adenine dinucleotide phosphate [NADP(H)] respectively. Full length NOS and its various domains resemble cytochrome P450 and its P450 reductase (CPR) in sequence and structure, although the reductase domains have higher similarity than the oxygenase domains. A greater level of similarity (in terms of domain construction and mechanisms) is seen between NOS and the flavocytochrome P450 BM3 from *Bacillus megaterium*, the enzyme of study in this work.

Catalytically, NOS converts L-arginine to L-citrulline and nitric oxide (NO) via two distinct oxygenation reactions requiring the consumption of three exogenous electrons, provided by NADPH, and two molecules of oxygen (*23, 32*). A stable intermediate, N-ω-hydroxy-L-arginine (NOHA) is formed in the process after the first oxygenation step. NO is then produced by the further oxidation of the guanidine nitrogen of L-arginine.

1.1.2 Cytochromes P450

Cytochromes P450 (CYPs) are a multi-gene superfamily of heme-containing enzymes, the vast majority of which utilize redox partners to transfer electrons from reducing substrates (nicotinamide coenzymes – NADH or NADPH) to the P450 heme center, from which the electrons are moved to molecular oxygen and then to organic substrates. CYPs are found in all biological kingdoms and unlike NOSs with only three major isoforms, 2009 statistics show 120 animal, 126 plant, 459 fungal, and 196 bacterial CYP families (*34*).

CYPs were first discovered by Garfinkel and Klingenberg and christened by Omura and Sato due to their characteristic (signature) Soret absorption maximum at 450 nm in the UV-visible spectrum (Figure 1.2) when complexed with carbon monoxide (*35-37*). All CYPs therefore have very similar spectroscopic properties and share a common protein fold (*38, 39*). Another common structural feature of CYPs is that they all contain binding sites for heme, oxygen (to the heme iron), redox partners and substrates.
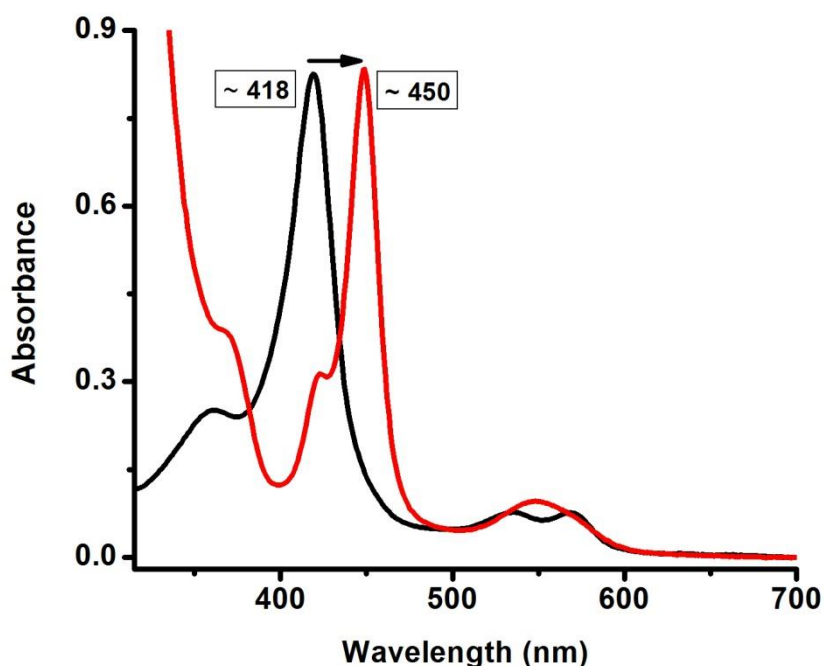
Figure 1.2: Absorption spectrum of cytochrome P450-CO complex formation with flavocytochrome P450 BM3. BM3 in its oxidized form (black) has a characteristic Soret peak at approximately 418 nm. BM3 is first reduced and then complexed with carbon monoxide with a resulting peak at approximately 450 nm (red, see figure 1.5 for steps involved).

Interest in cytochrome P450 was borne out of the desire to understand the metabolism of drugs, carcinogens, and steroids, which remain major focal points. Statistics have shown that about 75% of human drug metabolism is modulated by CYPs (*40*) and six CYP alleles (CYP1A2, CYP2C9, CYP2C19, CYP2D6, CYP2E1 and CYP3A4) have been associated with the majority of human systemic clearance of drugs and xenobiotics (*41*). CYPs carry out metabolism (of steroids and fatty acids) and detoxification (of drugs and xenobiotics) via extremely diverse and complex reactions including heteroatom dealkylation and oxygenations, sulphoxidations, epoxidations, deaminations, C-hydroxylations, desulphurations, dehalogenations, peroxidations, and N-oxide reductions (*42, 43*).

Further, CYPs have caught the attention of pharmaceutical and fine chemical industries as potential biocatalysts based on their versatility and the broad range of substrates on which they are known to catalyse oxidation reactions. As a result, much of the research on CYPs has been focused on engineering them into dynamic biocatalysts for biotechnology (food and agriculture), medicine (drug synthesis and metabolites) and bioremediation using approaches such as conserved sequence motif analysis, directed evolution, rational mutagenesis, and site-directed mutagenesis (*44-46*).

Catalytically, CYPs insert one atom of molecular oxygen into organic substrates while the other oxygen is reduced to water as shown in Figure 1.3.

$$\text{Reduced P450} \qquad \text{Oxidized P450}$$

$$RH + O_2 \longrightarrow R\text{-}OH + H_2O$$
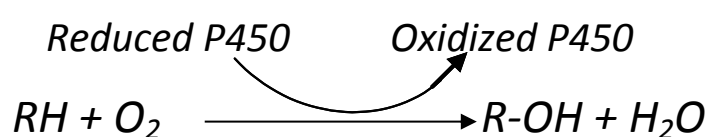
Figure 1.3: Mono-oxygenation reaction catalysed by P450s. Reduced CYPs insert one atom of molecular dioxygen into a wide variety of organic substrates. Electrons are usually derived from redox partners via NAD(P)H, protons are ultimately delivered to reactive P450 oxo species from water molecules via amino acid side chains.

As seen in the figure above, P450 can only catalyse these reactions when it is reduced. Two electrons are donated to P450s by the redox partner, i.e. from the diflavin reductase (CPR) enzyme itself or from accessory proteins (*e.g* ferredoxin or flavodoxin) that transfer electrons to the P450 from a flavoprotein reductase.

1.1.2.1 Classification of Cytochromes P450

Classification of CYPs into families and subfamilies is done by their extent of similarity in amino acid sequence. However, classification can also be based on the nature of the redox partner required. Two major classes of the P450 enzymes are known. Class I represents the prokaryotic system (obtained from bacteria and mitochondria) which consists of the P450 protein itself, a NAD(P)H flavodoxin/ferredoxin reductase, and a ferredoxin. The most highly characterized enzyme of this class is cytochrome P450cam (CYP101A1) from *Pseudomonas putida*. All the proteins in this system in bacteria are soluble. Class II represents the eukaryotic microsomal-type system comprising the P450 and its redox partner - a NADPH-dependent reductase. However, this partner (cytochrome P450 reductase or CPR) has distinct FAD-containing and FMN-containing domains and both P450 and CPR are membrane bound proteins. Classification became more complicated in the 1980s when Fulco's lab discovered the flavocytochrome P450 BM3 enzyme. This enzyme has a P450 domain and a diflavin reductase domain, just like the class II systems. However, these domains are fused into a 119 kDa polypeptide and it is a soluble (not membranous) bacterial enzyme (*47*). P450 BM3 (CYP102A1) is sometimes grouped as a class III enzyme (Class VIII in the figure below). In recent years, the discovery of other enzymes that interact with diverse types of reductases or are fused to other types of proteins has added further complexity to the issue of P450 redox system classification resulting in up to ten different classes (Figure 1.4; (*42*)). A notable example is the soluble eukaryotic P450nor (also known as CYP55A1; Class IX) that does not require any other electron transfer protein but directly accepts electrons from NADH. Another example is the CYP74 family of enzymes (Class X) which requires neither and electron source nor oxygen for its synthase/lyase reactions (*48*).

| CLASS I: (e.g CYP101A1) | NAD(P)H | → | Ferredoxin Reductase (FAD/FMN) | → | Ferredoxin (Fe-S) | → | P450 |
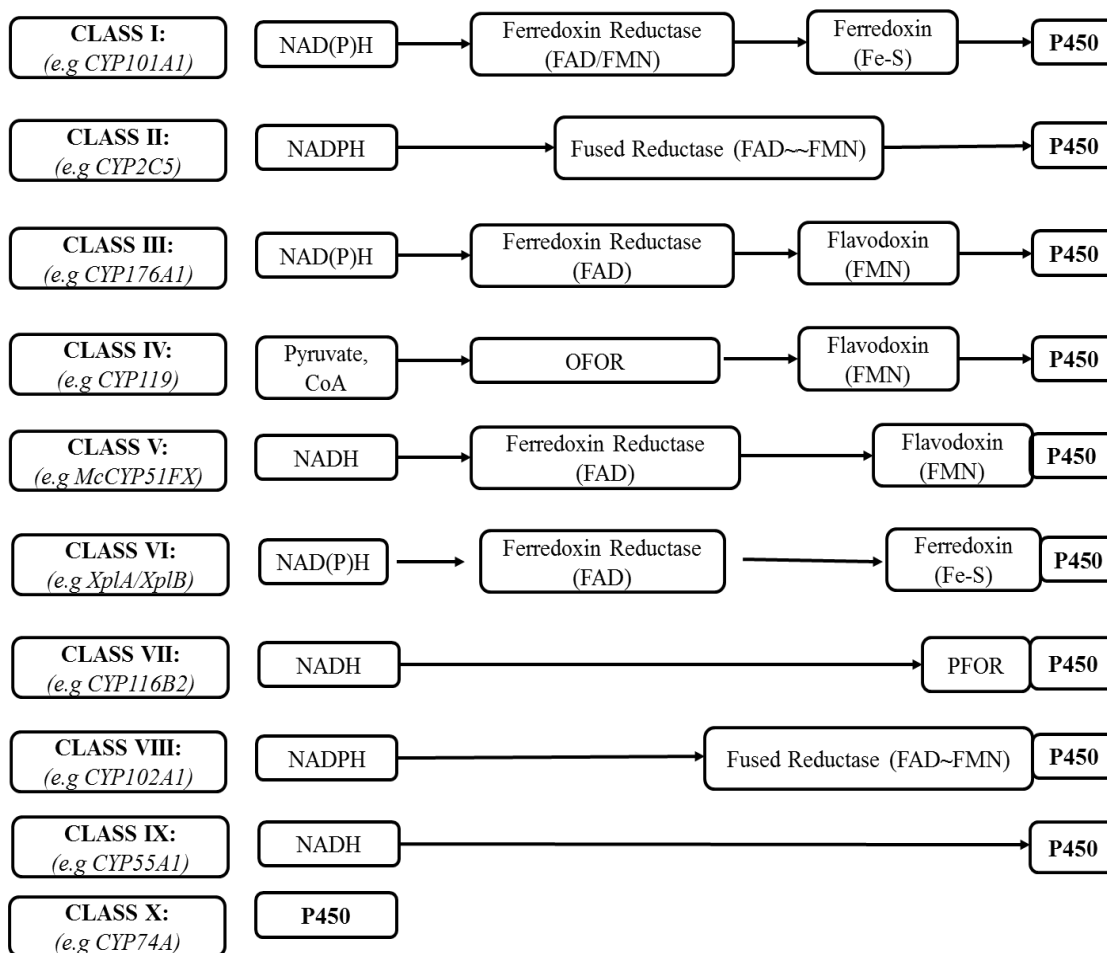
Figure 1.4: Classes of Cytochrome P450 redox systems. *Image modified from (42). NADPH (reduced nicotinamide adenine dinucleotide phosphate); FAD (flavin adenine dinucleotide); FMN (flavin mononucleotide); Fe-S (iron-sulfur clusters); P450 (Cytochrome P450); CoA (Coenzyme A); OFOR (2-oxoacid:ferredoxin oxidoreductase); NADH (reduced nicotinamide adenine dinucleotide); PFOR (phthalate-family oxygenase reductase).*

1.1.2.2 The Catalytic Cycle of Cytochrome P450 Enzymes

Substrate hydroxylation by cytochromes P450 is described by the catalytic cycle shown in Figure 1.5. Firstly, the substrate binds to the heme iron displacing a weakly coordinated distal water molecule and causing a change in spin state from the six-coordinate to the five-coordinate form. The first electron transfer results in the reduction of heme iron, facilitating oxygen binding to the ferrous heme iron. The oxygen binding step follows and this can be inhibited by carbon monoxide (step 9), as a stable ferrous-CO adduct is formed. Binding of oxygen facilitates the second one-electron transfer to the heme iron and subsequent protonations which result in the homolytic scission of the O-O bond to form a highly active oxyferryl species (steps 4-6). The high valent iron

species resulting from step 6 (known as P450 compound 1; P450-I) is considered to be the key active oxygen intermediate of the reaction cycle (*49*) but could not be characterized for many years due to its instability and transient nature. On the other hand, chloroperoxidase compound 1 (CPO-I) is highly stable and can be prepared in high yields (*50*), thus making it a biological model for P450-I. In a review of simple and complex reactions catalysed by cytochromes P450 (*43*), this key active oxygen intermediate is described as a $Fe^{III}O$ instead of a $Fe^{IV}O$ as presented here in the catalytic cycle. Very recently, P450-I was confirmed to be an oxyferryl species when a high yield of P450-I (~75%) was trapped and characterized from a reaction between ferric CYP119 and *m*-chloroperbenzoic acid (*51*). This oxyferryl intermediate is considered to abstract a hydrogen atom from the substrate, and then to "rebound" the hydroxyl group to facilitate substrate oxidation. The dissociation of the hydroxylated product and the return of a water molecule as the 6th ligand to the heme iron mark the completion of the cycle, resulting in a fully oxidized P450 ready for the next cycle. In general, protons are transported to the active site from water molecules and via certain active site amino acid side chains, while the electrons are donated by NAD(P)H and delivered via cofactors bound to the redox partners.
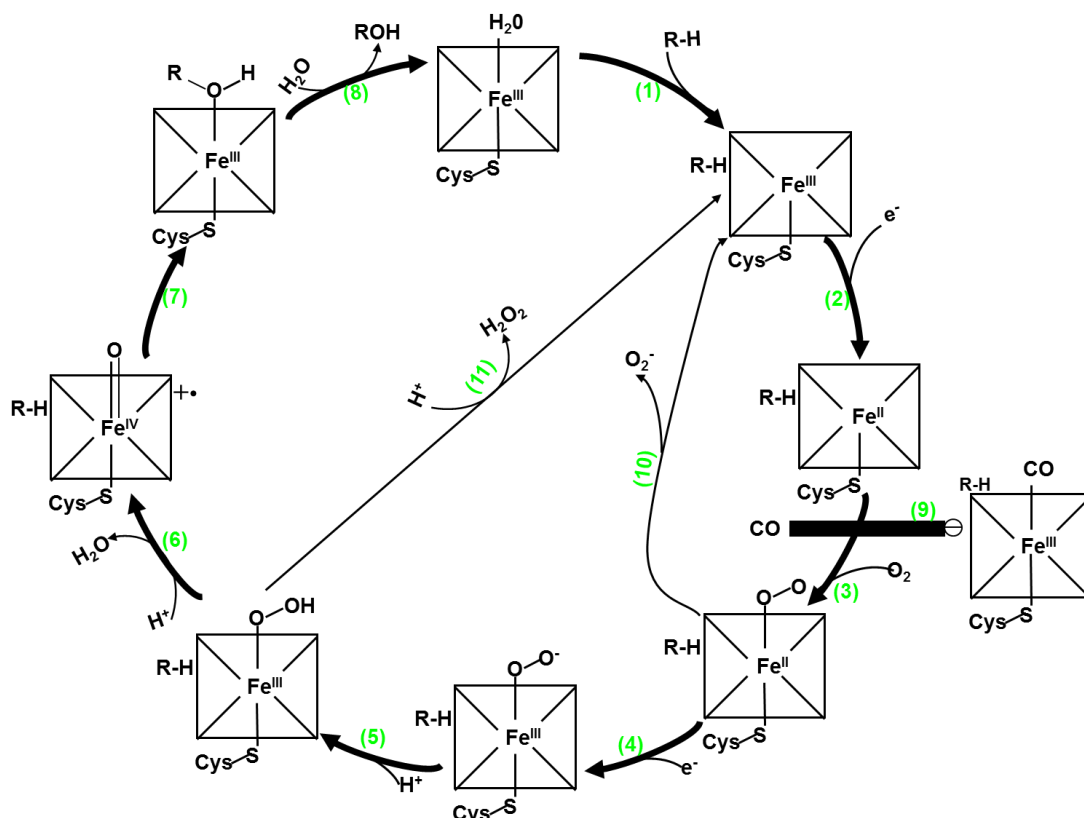
***Figure 1.5: The catalytic cycle of cytochromes P450.** Intermediates are discussed in the preceding text. Pathways of collapse of the ferrous-oxy (ferric-superoxo) and ferric hydroperoxo intermediates are shown, generating superoxide and peroxide, respectively (steps 10 and 11). These actions result in the return of the heme iron to the resting (ferric) state and can occur if electron/proton delivery is inefficient or if substrate is inappropriately postioned in the active site.*

1.1.3 Cytochrome P450 Reductase: Diflavin Reductases

As seen in section *1.1.2.2*, the functioning of almost all cytochromes P450 (Class I to VIII) essentially requires interactions with their redox partner, the reductase and/or flavodoxin/ferredoxin. In microsomal P450s, the redox partner required is cytochrome P450 reductase (CPR) which is a diflavin reductase. CPR is a membrane-bound, 75-80 kDa (*52*) protein whose solved crystal structure (for a soluble fragment devoid of a membrane anchor region) revealed that it has four structural domains: FMN-binding, connecting, FAD-binding, and NADPH-binding domains (*53*). It can also be said that CPR has hydrophobic and hydrophilic binding domains. While the hydrophobic domain is involved in anchoring of the protein to the membrane, the hydrophilic domain contains binding sites for all the co-factors and electron acceptors including the P450 partner protein (*54*). Nitric oxide synthase (NOS) is another mammalian heme thiolate

protein containing a diflavin reductase (see section *1.1.1.2*). Crystal structures of eNOS and iNOS heme domains have been solved [See reviews (*55, 56*)], as have the heme (*57*) and reductase domains of rat nNOS (*58*).

Other diflavin reductases include human methionine synthase reductase (MSR), human dual flavin novel reductase 1 (NR1) and sulphite reductase (SiR). Human MSR is a 78 kDa protein which catalyses transmethylation of homocysteine to methionine and forms an air stable semiquinone when reduced by NADPH (*59*). NR1 is a 67 kDa protein with cytochrome *c* and ferricyanide reductase activities, whose role is not fully known. It is, however, thought to play a role in carcinogenesis (*60*). SiR catalyzes the reduction of sulphite to sulphide. Crystal structures indicate that it is made up of an α- and a β-subunit (*61*). The 66 kDa α-subunit can be cleaved into a 23 kDa FMN-binding and a 43 kDa FAD-binding domain.

The interactions between cytochrome P450 and its redox partners in microsomal P450s have been well studied in the past 50 years, but understanding the mechanisms involved has been impeded due to the complexities in the structure of the various forms of P450s purified from *e.g* pig, rabbit, or rat liver (*52*). However, the ability to successfully express, purify and genetically dissect cytochrome P450 BM3 from *Bacillus megaterium* (BM3), which has about 33 % amino acid identity with certain mammalian P450 enzymes (*62*), has brought new insights into the various interaction mechanisms between the redox partners. Unlike in microsomal P450s, where the reductase (CPR) is separate from the P450, both domains are tethered together in BM3. A lot of similarities have been observed between these microsomal and microbial types of P450 redox enzyme systems, and CPR is 31.5% structurally identical to BM3 reductase (*63*). They are both members of the diflavin reductase family in the sense that their reductases contain equimolar concentrations of FAD and FMN co-factors in a single chain and that these are contained within structurally homologous protein scaffolds. Detailed information about BM3 and structural analysis of the domains of BM3 is given in the following section.

1.2 FLAVOCYTOCHROME P450 BM3

Flavocytochrome P450 BM3 (BM3) is a self-sufficient enzyme that has attracted the interest of many researchers. This section begins with an introduction into self-sufficient CYPs, the majority of which are natural fusion proteins, which have been isolated to date. In the following section, the story that led to the uniqueness of the BM3 enzyme is told; which then leads us to a general understanding of BM3's structure and function. The different observations that led to the proposition of the generally agreed electron transfer mechanism are also presented. The concluding parts of this section describe recent advances in the field of BM3, including its role as a potential industrial biocatalyst as well as the question of its oligomerization.

1.2.1 Self-Sufficient P450s: What's the Catch?

The study of Cytochromes P450 (CYPs) has been on-going for over 50 years. While most of these studies concentrate on deciphering the physiological roles of CYPs in relation to drug metabolism, a large percentage of P450 research has been focussed on tackling three known setbacks of CYPs which include limited stability, need for redox partners and low levels of activity (*64*). Enzymes that solely catalyse reactions without requiring the assistance of additional proteins are termed self-sufficient. With the exception of cytochrome P450nor, all the self-sufficient enzymes characterised to date have their redox partners fused to the cytochrome P450 domain on the same polypeptide chain.

These self-sufficient fusion proteins have been observed to exhibit high rates of catalytic activity thereby overcoming two of the three setbacks of CYPs. A typical example is our enzyme of choice, flavocytochrome P450 BM3 (BM3) which has been shown to have the highest known rate of fatty acid metabolism [17,000 min^{-1} with arachidonic acid (*5*)]. While the physiological functions of most of these self-sufficient fusion proteins are unknown, a great deal of protein engineering resources have been channelled towards generating artificial fusion proteins using the self-sufficient fusion P450s as models to enable *e.g* improved protein purification and enhanced drug metabolism of known substrates (*65*). A major aim is in designing novel P450s with new properties, desired substrate specificities and high catalytic efficiencies. As observed in a recent review, the catalytic efficiencies of genetically engineered chimeras of cytochromes P450 and reductases to date are no match to that of BM3 (*65*).

For over a decade, BM3 remained the only self-sufficient P450 enzyme identified until advances in genome sequencing led to the discovery of further self-sufficient cytochrome P450 enzymes fused to CPRs or to different redox partners. Characterization of a few of these self-sufficient P450s has been accomplished but most remain uncharacterised. This section describes some of these enzymes that have been isolated and characterised, but first it is pertinent to highlight some components of the usual redox partners associated with cytochromes P450.

Ferredoxins (FDX) are low molecular weight iron-sulphur proteins that mediate electron transfer in wide range of metabolic reactions. They are mostly found in plant and bacterial systems and are grouped based on the nature of their iron-sulphur clusters. Catalysing the transfer of electrons between NAD(P)H and oxidized ferredoxin are ferredoxin reductases which consists of the binding domains for the prosthetic group FAD, the partner fdx, and the co-enzyme NAD(P)H [see class 1 in Fig 1.4 (*66*)]. Alternatively, ferredoxin/flavodoxin reductases can reduce flavodoxins (FLD), which are electron transfer proteins commonly found in bacteria and algae that contain a single molecule of FMN as prosthetic group. FMN and FAD are co-factors derived from riboflavin and which serve as prosthetic groups for many oxidoreductases.

Two major groups of self-sufficient P450s characterised to date are the cytochrome P450-CPR fusion and P450-dioxygenase reductase-like fusion enzymes (see classes II and VII in Fig 1.4).

1.2.1.1 P450-CPR Fusion Enzymes

This group of enzymes consists mainly of the CYP102A and the CYP505 families. CYP102A1 (also known as BM3) is the first and most characterised member of the CYP102A family. The cytochrome P450 domain of the enzyme is covalently linked at the N-terminal to a reductase domain binding FAD and FMN as prosthetic groups (Figure 1.5).
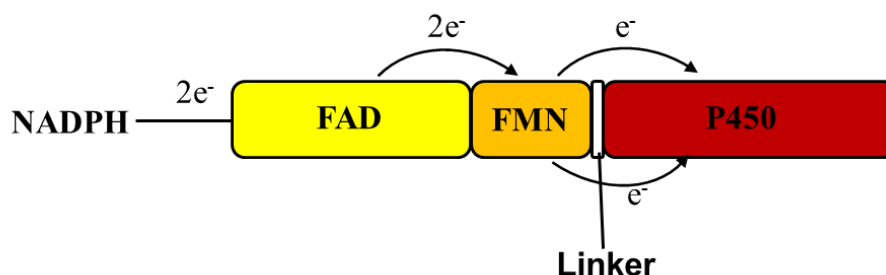
Figure 1.6: Electron transfer through the different domains of flavocytochrome P450 BM3. *The various domains are coloured in solution as shown in the figure. The oxidised FAD and FMN domains are in yellow/orange while the heme-binding P450 domain is in red.*

CYP102A1 is a soluble fatty acid hydroxylase isolated from *Bacillus megaterium* although its reductase domain bears close resemblance to eukaryotic cytochrome P450 reductase (CPR). Detailed characterisation of CYP102A1 is discussed in section 1.2.2. Genome databases reveal over 50 homologues of CYP102A1 (*67*), but only a few have been expressed and partially characterised to date. Examples include CYP102A2 and CYP102A3 from *Bacillus subtilis*; CYP102A5 from *Bacillus cereus* and CYP102A7 from *Bacillus licheniformis*. These isoforms have been reviewed recently (*67*).

The complete genome sequencing of the gram-positive *Bacillus subtilis* (*68*) revealed that out of the eight genes that encode CYPs, CYP102A2 with 59% identity and CYP102A3 with 77% identity (*69, 70*) to BM3 were identified as P450-CPR fusion proteins. The physiological roles of these enzymes are currently unknown but CYP102A1 is proposed to be involved in fatty acid detoxification while CYP102A2 and A3 might play significant roles in regulation of membrane fluidity (*71*).

The primary structural arrangements for all four enzymes are exactly as seen in BM3, with the C-terminal (CPR) domain comprising the binding sites for FMN, FAD and NADPH. They are also similar (as far as is known) in terms of their mechanism of substrate binding and electron transfer but can be distinguished based on their substrate preferences and product spectrum. CYP102A2 and A3 show high preference for long-chain unsaturated and branched-chain fatty acids while CYP102A1 and A5 metabolizes both saturated and unsaturated fatty acids (preferred) as well as N-acyl amino acids (*71-74*). CYP102A7 on the other hand is active towards medium chain fatty acids, but exhibits high preference for saturated fatty acids (*75*). Also, CYP102A1, A2, A3 and A7

are observed to hydroxylate fatty acids at ω-1, 2 and 3 positions while no ω-3 hydroxylation is observed for CYP102A5.

The first eukaryotic counterpart of BM3 to be isolated and characterised was CYP505A1 (also known as P450foxy) from the fungus *Fusarium oxysporum* (*76*). It is quite similar to BM3 in terms of self-sufficiency, primary structural arrangement, molecular mass and high catalytic turnover (*77*). It is a membrane-bound enzyme which hydroxylates a wide range of fatty acids. The k_{cat} values are similar for fatty acids of varying chain length, but catalytic efficiency (k_{cat}/K_m) is superior for longer chain (C12-C16) fatty acids (*78*). Another eukaryotic counterpart of BM3 with 33% identity to BM3 and 41% identity to P450foxy is CYP505B1 from *Fusarium verticilloides (79)*.

1.2.1.2 P450-Dioxygenase Reductase-Like Fusion Enzymes

Aromatic ring hydroxylating dioxygenases (ARHDs) are non-heme iron containing dioxygenases that catalyse substrate dihydroxylation via incorporation of two atoms of dioxygen into their substrates (*80*). A typical example of class I ARHDs is the phthalate dioxygenase system where electrons are transferred from NADH through a FMN and [2Fe-2S] containing reductase to the oxygenase system comprising of an iron binding site and a Rieske-type iron-sulphur cluster (a 2Fe-2S centre with iron atoms coordinated by two cysteine and two histidine residues). A similar system has been observed within the P450 fusion enzymes where electrons are transferred to the heme iron centres of the CYP116B P450s from reductases resembling the phthalate family of oxygenases [PFOR (*81*)].

The CYP116A family whose first member, CYP116A1 from *Rhodococcus erythropolis* strain N186/21 was identified in the mid-1990s is a typical 3-component class I P450 redox partner system (*82*). CYP116A1 was shown to be involved in the oxidative degradation of thiocarbamate herbicides and atrazine (*83*). The P450 domain (ThcB) is reduced by a [2Fe2S] ferredoxin (ThcC) and a NAD(P)H-dependent ferredoxin reductase (ThcD).

CYP116B2 (P450 RhF) from *Rhodococcus* sp. strain NCIMB 9784 was the first P450-PFOR fusion enzyme to be characterised (*84*). The C-terminal domain of P450 RhF was found to be fused to a reductase partner comprising of FMN- and NADH-binding domains and a [2Fe-2S] centre. Expression in *E. coli* yielded soluble forms of the

protein which was shown to catalyse the NADH-dependent O-dealkylation of 7-ethoxycoumarin (*85*) and of substituted aromatic alkyl ethers (*86*) without the aid of any other protein. The monomeric intact P450 RhF enzyme has been successfully genetically dissected into the iron sulphur, FMN and heme binding domains, similar to domain dissection done in BM3 (*87*).
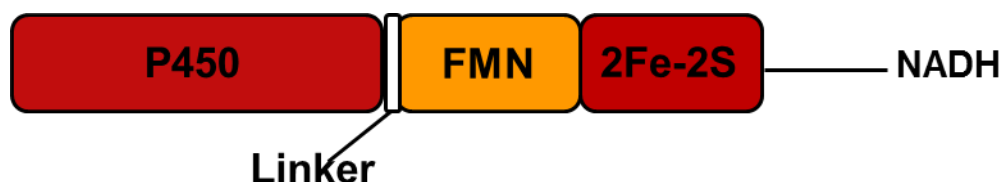
Figure 1.7: The different domains of Cytochrome P450 RhF (CYP116B2). The CYP116B family currently consists of three characterised members (CYP116B1-3), which share the above domain organisation. Related enzymes are evident from other genome sequences.

The primary structural organization of CYP116B1 from *Cupriavidus metallidurans* (formerly known as *Ralstonia metallidurans)* is the same as that for CYP116B2 (*88*). However, CYP116B1 is proposed to be involved in oxidative degradation of thiocarbamate herbicides, as seen for CYP116A1. Further P450-PFOR fusion genes were found in four β-proteobacterial species following a Blast search (*81, 82*). Although the self-sufficiency of the enzymes from *Burkholderia cepacia, Burkholderia mallei* and *Burkholderia pseudomallei* is yet to be confirmed, they exhibit 52-56% identity to P450 ThcB (CYP116A1) in the heme domain and 63-66% identity to P450 RhF (CYP116B2).

Another non-characterised P450 fusion protein exhibiting 93% identity to P450 RhF and 55% identity to P450 ThcB was isolated from *Rhodococcus ruber* (*89*). The fusion system comprising of ferredoxin, flavin-containing reductase and P450 domain was shown to catalyse hydroxylation of polycyclic aromatic hydrocarbons. Other redox partner fusion P450s include MCCYP51FX from *Methylococcus capsulatus*, SYK181 from a soil metagenome library and XplA from *Rhodococcus rhodochrous*. MCCYP51FX is a sterol 14α-demethylase with strong identity to CYP51B1 from *Mycobacterium tuberculosis* and comprised of a P450 domain linked to a C-terminal ferredoxin (3Fe-4S type) via an alanine rich linker (*90*). XplA on the other hand has its P450 domain linked to a flavodoxin-like protein at the N-terminal (*91*). It catalyses the

degradation of the Royal Demolition eXplosive (RDX) hexahydro-1,3,5-trinitro-1,3,5-triazine. SYK181 is a fatty acid hydroxylase with 46% sequence identity to P450 BM3 and having CPR fusion characteristics (*92*).

Another fusion cytochrome P450 protein has been recently identified. CYP6001A1 from *Aspergillus nidulans* is a bifunctional P450 fusion protein between a fatty acid heme dioxygenase/peroxidase at the N-terminal and a P450 heme thiolate protein at the C-terminal (*93*). This enzyme is also catalytically self-sufficient, with the peroxidase domain catalysing oxidation of linoleic, and the P450 domain isomerising the product into 5,8-dihydroxyoctadecadienoic acid, a fungal hormone. P450nor (CYP55A1) from *Fusarium oxysporum* was the next self-sufficient protein to be isolated after BM3, although it is not a fusion protein (*94*). It is not a monooxygenase, but instead accepts electrons directly from NADH and solely catalyses nitric oxide reduction (forming N_2O), bypassing the requirement of a protein redox partner (*95-97*).

A number of artificial P450 fusion proteins have been generated in attempts to maximize catalytic efficiency. In a recent review of natural and artificial P450 enzymes (*65*), a table comparing the kinetic parameters of some fusion proteins was constructed. It was observed that the "metabolic potencies" (i.e the k_{cat}/K_m ratio) of the engineered systems were still a lot lower than our model enzyme, CYP102A1. In a similar table (Table 1.1) for some natural fusion CYPs, it can be seen that CYP102A1 (P450 BM3) still has the highest catalytic efficiency in comparison to other natural self-sufficient fusion P450s characterized to date.

Table 1.1: Comparison of kinetic parameters of some self-sufficient CYPs

Fusion P450	Substrate oxidised [(reference)]	K_M (µM)	k_{cat} (min⁻¹)	k_{cat}/K_M (min⁻¹µM⁻¹)
CYP102A1	Arachidonic acid [(5)]	4.70 ± 0.25	17100 ± 190	3640 ± 245
CYP102A1	Lauric acid [(5)]	288 ± 15	5140 ± 90	17.8 ± 1.4
CYP102A2	15-methylpalmitic acid [(73)]	56.8 ± 11.1	6105 ± 500	107.5
CYP102A3	15-methylpalmitic acid [(73)]	68.3 ± 15.9	3845 ± 415	56.3
CYP102A5	Linoleic acid [(72)]	31.6 ± 0.4	6730 ± 50	213
CYP102A7	13-methyl-tetradecanoic acid [(75)]	16.5 ± 2.2	1264 ± 58.9	76.6
P450 RhF	7-methoxycoumarin O-dealkylation [(86)]	620	1.6	0.003
P450 RhF	7-ethoxycoumarin O-dealkylation [(85)]	0.22 ± 0.01	4.9 ± 0.1	22.27
P450foxy	Pentadecanoic acid [(78)]	8	1300	163
	Hexadecanoic acid [(78)]	10	1800	180

Despite the increase in the number of these enzymes characerised, there is no known structure of any full length self-sufficient CYP to date. This could be as a result of the complex multi-domain nature of the enzymes, resulting in difficulties in their crystallization (*88*). As the physiological roles of these CYPs are yet to be defined it is therefore imperative to ascertain their structures. Understanding the intriguing structural features of the fused enzymes responsible for their very fast metabolic rates and high catalytic efficiencies (using BM3 in this case) will serve as a model not only to understand CYPs as a whole, but should also enable us to correctly tailor the engineering of artificial chimeras with potentially important physiological and industrial roles. CYP102A1 (BM3) remains the self-sufficient CYP with the highest catalytic efficiency. The following sections give detailed characteristic information on this unusual enzyme.

1.2.2 The BM3 Story: Putting the Pieces Together

The Fulco laboratory in 1974 discovered a "cell-free hydroxylation system" from *Bacillus megaterium* that could hydroxylate saturated and monounsaturated fatty acids at the ω-1, ω-2, and ω-3 positions (*98*). The major products were obtained at the ω-2 position and the highest activity was observed with a C_{15} substrate, which increased with higher lipid concentration. The hydroxylase activity was also found to increase with higher protein concentration, consistent with an enzymatic activity (*99*). The preference for the ω-2 position with no observed ω-hydroxylations (when compared with most related mammalian P450 systems) drew attention to the uniqueness of this system. Moreover, a search for co-factors involved in the hydroxylase activity of this enzyme revealed only two co-factors, NADPH and O_2 (*98*).

Subsequent analysis revealed that this system was also capable of the hydroxylation of fatty amides (*100*) and D-hydroxystearate (*101*), as well as in the hydroxylation and epoxidation of palmitoleic acid (*102*). Based on these results it was proposed that the enzyme-substrate complex is governed by hydrophobic interactions (*100, 102*). However, there was a non-hydrophobic binding region on the enzyme surface (*101*). This model was later modified to indicate that the terminal methyl group of the fatty acid is sequestered by the enzyme via strong hydrophobic interactions and specifically with an active site phenylalanine residue (Phe87) while the carboxyl-terminal end is bound to the enzyme via polar interactions near the mouth of the substrate entry cavity (*102*).

Additionally, in a quest to detect inhibitors of the hydroxylase activity, it was noted that carbon monoxide (CO) inhibits about 50 % of the activity, with no recorded inhibition by catalase and superoxide dismutase (*103*). The inhibition was reversed by ferredoxin, cysteine or glutathione. This gave the first clue of an involvement of cytochrome P450-like reductase-type components. By investigating the CO binding spectrum of this enzyme, the cytochrome P450 component was identified (i.e. an unusual heme optical signal from the main [Soret] feature at 450 nm) (*99*).

Isolation of the crude cytochrome P450, free from other cytochromes (*47*), made it easy to characterize a self-sufficient 119 kDa cytochrome P450 mono-oxygenase (*4*). This enzyme was named BM3 to distinguish it from previously isolated and partially characterized class I BM1 and BM2 proteins from *Bacillus megaterium* by the same

research group. The BM3 enzyme had one mole of FMN and FAD each per mole of heme and has a cytochrome *c* reductase activity in the presence of NADPH (through its reductase domain). Moreover in the presence of long chain fatty acids, the enzyme, which is typically isolated and purified in a low spin ferric heme iron electronic configuration, was converted to high spin (Figure 1.8). The ferric P450s can exist in either a low spin (S= $^1/_2$) or high spin (S=$^5/_2$) state, and these states are in equilibrium. The binding of substrates often (as with BM3) results in the displacement of the 6th (water) ligand to the heme iron, and the conversion of low spin heme to high spin. The high spin ferric form has a more positive reduction potential, and this enables efficient electron transfer from the reductase when substrate is bound such that fatty acid oxidation occurs and uncoupling of electron transfer is minimised (*104*).
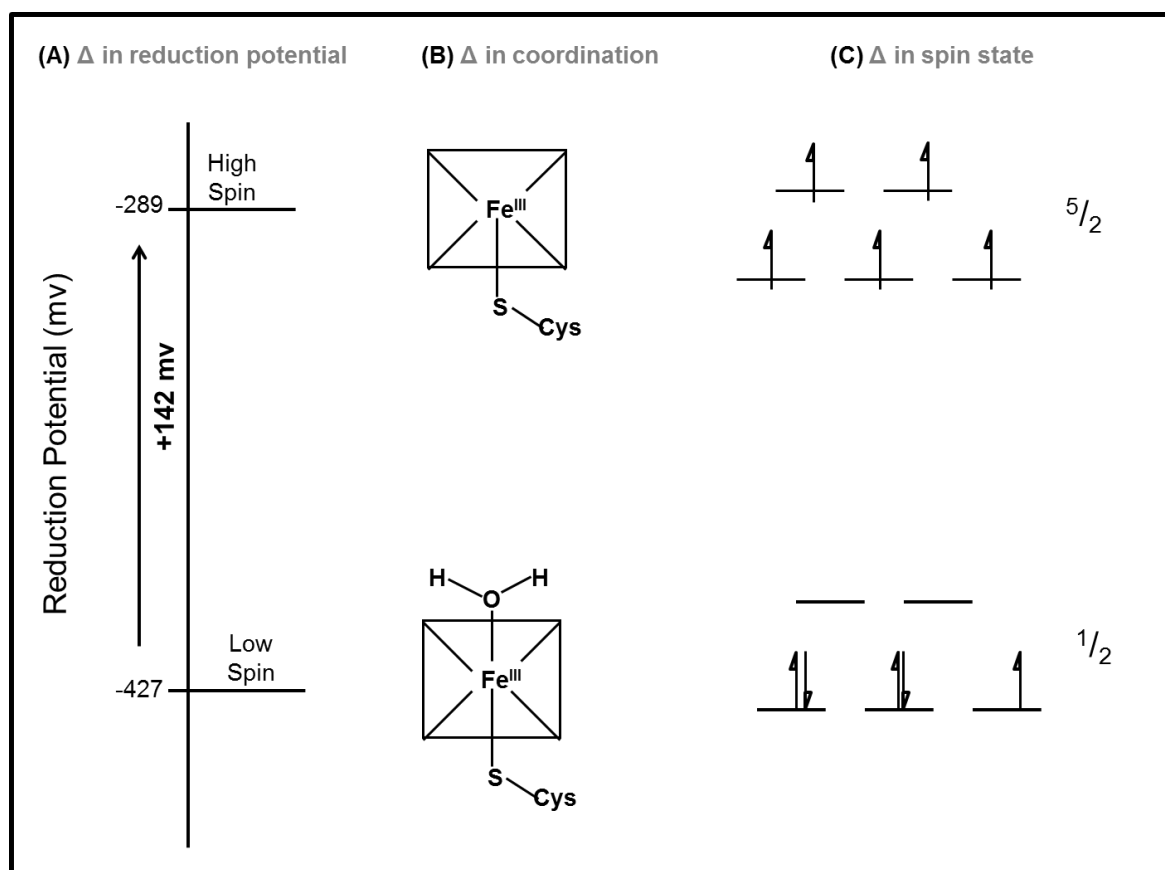
Figure 1.8: Reduction potential and spin state changes in flavocytochrome P450 BM3. *Binding of substrates to BM3 usually results in reorganisation within the d-orbitals of the heme iron as the 5 electrons occupying the orbitals become unpaired (C). Further, the water molecule at the sixth position of the heme iron is displaced, changing the co-ordination state of the heme iron from a 6-coordinated to a 5-coordinated state (B). This also results in an increase (by ~142 mV) in the reduction potential of the heme iron[A, (105)].*

In further studies, the enzyme was genetically dissected into two functional domains: a 55 kDa heme-containing domain at its N-terminal portion (which binds fatty acids) and a 66 kDa FAD- and FMN-containing domain derived from the C-terminal portion and with a cytochrome *c* reductase activity (*6*). The latter domain was found to possess great similarities to the mammalian microsomal P450 reductases (CPRs). Amino acid sequence analysis indicates that the heme domain has about 25 % identity with the fatty acid ω-hydroxylases of the cytochrome P450 family IV, while the reductase domain exhibits 33 % identity with the mammalian hepatic NADPH:P450 reductases (*62*), In general, the conserved domains exhibit up to 50 % amino acid sequence similarity with the eukaryotic cytochromes P450. Reconstitution of the fatty acid hydroxylase activity of the domains resulted in the formation of similar regio-isomeric products as the full length enzyme, signifying that the activity is retained, although product formation is substantially decreased when domains are separated (*106*).

Approximately two decades afterwards, this well characterized flavocytochrome P450 BM3 enzyme is not only known to have the highest oxidase activities observed among all cytochromes P450, but now serves as a model to understand the activities of all cytochromes P450. Moreover, genetic engineering has revealed that BM3 has great prospects in oxychemical production in various industries, revealing its biotechnological potential.

1.2.3 Flavocytochrome P450 BM3: Structure and Function

One of the prerequisites for understanding the mechanism of action of an enzyme is an in-depth examination of the structure-function relationship of that enzyme. This section begins with a full description of the structure of the BM3 enzyme, giving a short introduction on the fatty acid hydroxylase activity of BM3. The interactions of the different domains of BM3 with substrates, inhibitors, and other compounds are discussed. The effects of these interactions on enzyme structure, the catalytic rates and binding affinities, and the roles played by different residues of this enzyme on its various molecular interactions are highlighted here.

1.2.3.1 The BM3 Structure

As seen in section 1.1, cytochromes P450 are monooxygenases that must accept electrons from their redox partner to perform their activities. The majority of the human P450 systems (with exception of mitochondrial forms) are microsomal and consist of separate P450 and reductase components. On the other hand, flavocytochrome P450 BM3 has both domains on a single polypeptide chain of 119 kDa and has a total of 1048 residues (*62*). This single polypeptide chain contains the P450 domain (residues ~1-455), the reductase domain (FAD- and FMN- binding domains; residues ~471-1048) and a linker peptide region (residues ~456-470) connecting the P450 and reductase domain (Figure 1.9). The exact length of the linker is not known but it is believed to contain between 10-15 residues, including prolines (*54*). Based on reconstitution experiments and site-directed mutagenesis, the role of the linker region is to correctly position the reductase domain relative to the heme for efficient electron transfer, with linker length (as opposed to its amino acid composition) being the most important factor (*107, 108*).
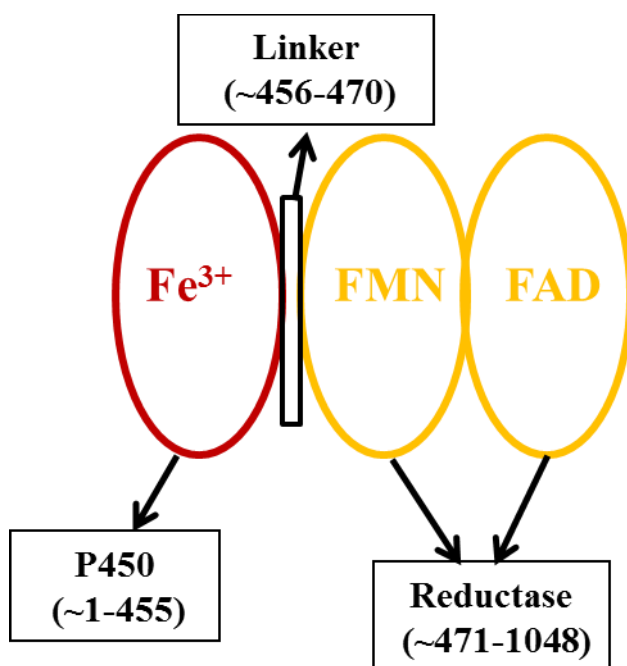
Figure 1.9: The different domains of flavocytochrome P450 BM3 showing the approximate amino acid numbers per domain.

Employing recombinant DNA techniques, genetic dissection of the BM3 enzyme into two catalytically functional domains was made possible (*6*). Also, the FAD (FAD/NADPH binding) and FMN domains of the reductase were separately cloned and

expressed (*109, 110*). Expression, purification and characterization of these three distinct domains (Heme, FAD, and FMN) were achieved, allowing for an improved understanding of the BM3 structure (that is, enabling structural and other studies on the isolated domains).

The most sophisticated method for obtaining structural information about proteins and macromolecules is by analyzing their crystal structures. Despite the large number of resources invested in attempts to crystallize the full length BM3 enzyme, it has still not been possible to achieve this goal. However, crystal structures of the substrate-free (*111*) and substrate- bound forms of the P450 domain (*112, 113*), and the P450-FMN domain (*114*) are available. The crystal structure for the last piece of the puzzle, the FAD/NADPH binding domain, has been solved recently by the Munro's group (*115*). Comparative analyses of these structures have provided great insights into the structure of flavocytochrome P450 BM3.

The crystal structure of the substrate-free heme domain was solved by Ravichandran *et al*. (*111*) using X-ray diffraction (Figure 1.10A). This structure is comprised of about 70% α-domain and 22% β-domain (i.e. two subdomains with substantial representation of the indicated secondary structure components) separated by the heme and an extended loop of 28 residues. The heme is located between the *I* and *L* helices of the α-domain, with the heme iron (in the low-spin spate) hexa-coordinated by four pyrrole nitrogens, a cysteine (proximal) axial ligand (Cys400) and a molecule of water as the 6th (distal) axial ligand. The *I* helix, which runs across the face of the heme, houses several amino acid residues that play important catalytic roles in BM3. The substrate binding site is a long hydrophobic funnel-shaped channel with an extensive β-structure embedded in between sheet 1 and some residues of the β-domain, *B'*, and *F* helices and the sheet 4 of the α-domain. Several non-aromatic hydrophobic residues (Figure 1.10B) involved in substrate binding and recognition, oxygen activation *etc* (Section 1.2.3.4) line the active site channel. Some of these residues include:

- ❖ Ala264 whose carbonyl group forms a hydrogen bond with the distal axial water molecule on the heme
- ❖ Arg47 whose side chain extends into the open end of the substrate binding pocket and is likely involved in interactions with substrate carboxylate

❖ Phe87 which lies perpendicular to the heme and forms close van der Waals interactions with the heme, on the distal face of the protein heme. Phe87 interacts with substrate ω-methyl to prevent its oxidation.

While the substrate binding site is known to be on the distal face of the heme (orientation with respect to the heme ligands, that is, on the same side as the axial water ligand), the redox partner docking site is located on the proximal face of the heme. This proposed docking site for the reductase domain is a rectangular depression with an exposed hydrophobic floor, which consists primarily of a cluster of positively charged residues on the outer edge and several non-polar residues on the inner portion (*111*).

Comparing the crystal structures of the substrate-free and substrate-bound forms, conformational differences apparently arising from the interactions of the substrates with the protein have been delineated, and these structural changes are discussed in section 1.2.3.3.
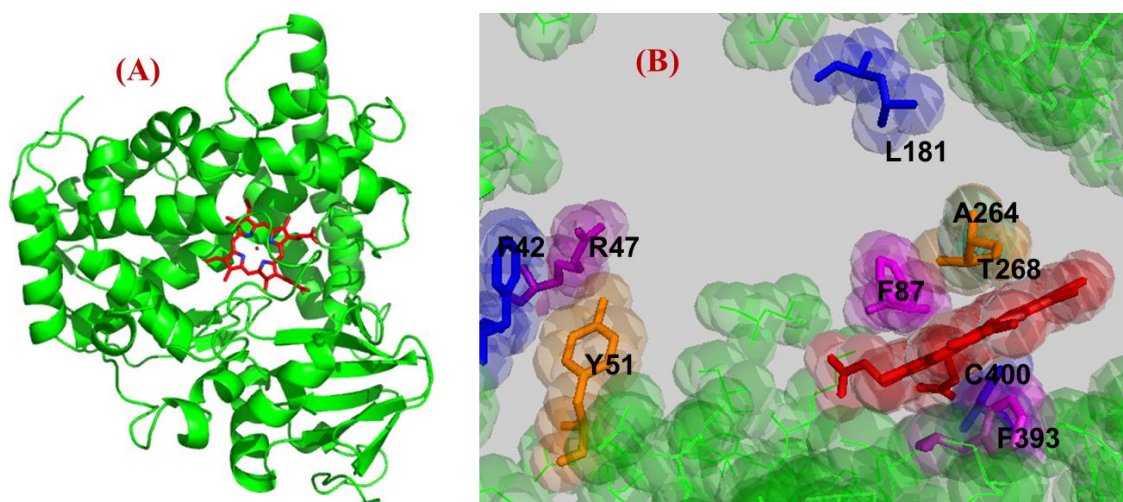
Figure 1.10: Crystal structure of substrate-free BM3 P450 domain. PDB ID: 2HPD. (A) The heme-containing P450 domain showing the porphyrin ring (red) with the central iron shown as a dot (magenta) and the pyrrole nitrogen atoms in blue. (B) The substrate binding pocket showing the various residues lining the channel leading to the heme. The roles of the residues flanking the active site as shown are discussed in details in section 1.2.3.3.

To date, no known crystal structure of the intact BM3 reductase domain (BMR) is available. However, the structure of rat liver cytochrome P450 reductase (CPR) was determined a few years ago by X-ray crystallography (*53*) and is often used to describe the BM3 reductase structure, and the structures of other members of the diflavin reductase family (Figure 1.11). This structure comprises the FMN-binding, FAD-

binding, and NADPH-binding domains, and a connector domain linking the FMN- and FAD-binding domains. The FMN-binding domain has a structure similar to the microbial flavodoxins, while the FAD-binding domain is similar to the ferredoxin reductases. The core of the FMN-binding domain is made up of parallel β-sheets, while those of the FAD-binding domain are anti-parallel. The binding pockets of the FMN and FAD isoalloxazine rings are mainly hydrophobic (*52*). With the availability of the crystal structure of the BM3 FAD-domain, various modeling techniques can be applied to generate models of BMR which can be compared to CPR as will be discussed in Chapter 5 of this thesis.

Stability studies on BM3 domains have shown that the heme domain is thermodynamically more stable than the reductase domain (*116*). Also, the presence of the flavin domain is believed to alter the structure of the heme domain to allow more water accessibility to the distal pocket of the full length enzyme (*117*).
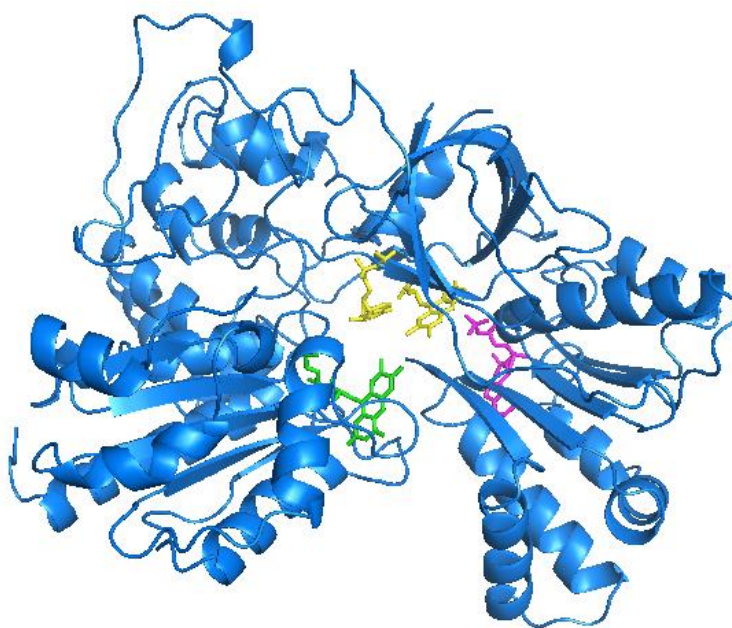
Figure 1.11: Crystal structure of rat liver cytochrome P450 reductase. *PDB ID: 1AMO. The structure shows the flavins FAD- yellow, FMN- green) and its electron donor, NADP(H) (magenta) (53).*

1.2.3.2 Fatty Acid Hydroxylation by BM3

Wild type BM3 hydroxylates a wide range of substrates into an even broader spectrum of products ranging from primary to secondary and even tertiary oxidised molecules (*118*). The substrate preference is for long chain saturated (*e.g.* lauric, myristic, and palmitic acids) and unsaturated fatty acids (*e.g.* palmitoleic and arachidonic acids). However, via mutation of residues within the active site, the substrate selectivity has been extended to short chain (*119*) and branched chain fatty acids (*71*), albeit with rates much lower than those observed for long chain fatty acids. Studies have also shown that BM3 exhibits very strong affinity for fatty amide derivatives of amino acids such as N-palmitoyl glycine and N-fatty acylated amino acids such as N-palmitoyl-L-methionine (*113, 120*). Other substrates for wild type BM3 include short-chain alkylbenzenes and long-chain alkylbenzoic acids (*121*).

Product distribution generally consists of ω-1, 2, and 3 hydroxylated fatty acids. With palmitic acid, hydroxylation is mostly at the ω-2 position, with substantial contributions from the ω-1 and 3 positions; while with arachidonic acid, 99 % of the hydroxylation is at the ω-2 position (*122*). It has been reported that hydroxylation of fatty acids at the ω-position has also been made possible via mutation of the active site residue, Phe87 (*123*). However, other groups have reported that the position of hydroxylation actually migrates away from the ω-end of the molecule in Phe87 mutants (*124*). A hyperbolic dependence of fatty acid hydroxylation rate on substrate concentration is observed. Moreover, reconstitution of the fatty acid hydroxylase activity of BM3 does occur with the genetically dissected heme and diflavin domains. However, this results in only about a thousandth of the activity of the intact enzyme (*7*). Hydroxylation of lauric acid at δ-,γ- and β-positions was achieved recently by mutation of amino acids (V8, S72, F87, and I263) around the substrate binding pocket (*125*).

Besides fatty acids, BM3 has been engineered to metabolize a wide range of substrates, ranging from alkanes to indole, and often with structures exhibiting little or no resemblance to the fatty acid substrates of the native enzyme (*126, 127*). This is an indication that BM3 is an "all-rounder" and also demonstrates its "pliability", in that its active site can be engineered to accommodate a wide range of different molecules. Further, genetic engineering and directed evolution mutagenesis around the active site and other parts of the substrate-binding pocket of BM3 have revealed several novel BM3 substrates and reactions (discussed in section 1.2.5).

1.2.3.3 Substrate Binding: Conformational Changes

Understanding the conformational changes that occur upon substrate binding is central to understanding the structure-function relationship of BM3. In this section, I discuss all observed structural changes that result on binding of the various substrates to the heme domain, as well as to the P450 BM3 holoenzyme.

Electron Paramagnetic resonance (EPR) and Resonance Raman (RR) spectroscopic studies on the heme domain and holoenzyme of flavocytochrome P450 BM3 have shown that the heme iron of the substrate free enzyme exists in the low-spin ferric (Fe^{3+}) state in the absence of substrate (*7*). Titration with palmitic acid shows a type I spectral shift (with the major Soret band of the heme iron shifting from ~419 nm to ~397 nm), which when compared with results obtained from RR studies is indicative of a heme iron conversion from a hexa-coordinated low spin form to a penta-coordinated high spin form (*7*). The change in spin state is as a result of an electronic reorganization in the heme iron d-orbitals. In recent studies, temperature jump spectroscopy was used to analyse the rate of spin-state relaxation in substrate-free and NPG-bound forms of wild type (WT) and F87G heme domains. Accurately measurable rates of relaxation were observed only for the substrate-bound proteins (800 s^{-1} for WT, 2500 s^{-1} for F87G), and it was concluded that spin-state transition kinetics were "conformationally gated by a (substrate) transition from the distal binding site of the fatty acid to a position proximal to the heme iron" (*128*). The likely role of Phe87 side chain in the reaction step rate limiting this spin state conversion was thus apparent.

Subsequent studies confirming the change in spin state using NMR observed, in addition, a remarkable increase in the distance between the heme iron and the co-ordinated water protons from 2.6 to 5.2 Å on binding of lauric acid (*129*). This indicates an expulsion of a water molecule from the sixth co-ordinated position of the iron. Moreover, the NPG-bound heme domain crystal structure (*113*) revealed that, on substrate binding, most of the solvent molecules that line the active site channels are expelled, leaving three water molecules, two (WAT500 and WAT501) of which are rearranged. WAT501, originally held in place by the carbonyl oxygens and amide backbones of Ile263-Glu267 and Ala264-Thr268, appears to relocate to a different position where it is stabilized by the carbonyl oxygen of Ala264 and the amide backbone of Thr269. In the same way, WAT500, stabilized by weak ligation to the heme and hydrogen bonding to Ala264, is rearranged to sit in a nearby site where

stabilization is offered by hydrogen bonds of Ala264 and Thr268. Apparently, expulsion of the water molecule which forms the distal axial ligand to the heme results in the change in spin state from low spin to high spin as the hexa-coordinated species converts to the penta-coordinated form.

Vital steps in the P450 catalytic cycle (Figure 1.5) are the protonations of the ferric peroxy and ferric hydroperoxy species that form following the second electron transfer to the heme iron. The source of the protons required for these steps is not certain, but models have been proposed. Interestingly, one of the models proposes a cascade where the acidic residue Glu267 protonates the water molecule in the groove of the I-helix (in this case, WAT501) which in turn transfers the protons to Thr268 and finally to the iron-bound oxygen (*111*). However, from the crystal structure, Haines group deduced that the repositioning of WAT500 to a location still close to the heme might imply that it plays a role in the charge stabilization (*113*). While there is no concrete experimental evidence as to the source of the proton (s), the involvement of Thr268 is almost certain, as replacement of this residue results in loss of coupling of electron transfer to substrate oxidation (*130*).

Another obvious change induced by substrate binding to the P450 is the increase in redox potential of the ferric heme iron by over 100 mV, facilitating its reduction (section 1.2.4) by electron transfer from the FMN cofactor in the reductase domain (*131*). In essence, binding of substrates to the heme causes expulsion of the water molecule that forms the sixth coordination site of the ferric heme, leading to a change in the heme iron ligation and its spin state from hexa-coordinated low spin (S=1/2) to penta-coordinated high spin (S=5/2), and subsequent increase in heme iron reduction potential.

1.2.3.4 Substrate Binding: Rearrangement and Roles of Residues

As revealed by the crystal structure, the substrate binding site is made of a long funnel-shaped channel lined with hydrophobic residues (Figure 1.12). When substrates bind to the heme domain, a great deal of structural rearrangements of these residues occur, leading even to formation of salt bridges, hydrogen bonding and van der Waals interaction with the substrate. Using mutational analysis, many of these residues have been identified, and their roles elucidated.

The crystallization of substrate free (SF), substrate bound (SB) and inhibitor bound forms of the heme domain has made it possible to understand some protein structural changes that are associated with substrate binding. Comparing the palmitoleic acid-bound and SF forms, it was noticed that the greatest conformational differences occur in the F and G helices and the loop connecting them, as well as within the I-helix (*112*). Further observations include closure of the substrate access channel and the possibility that substrates could adopt multiple conformations within the binding pockets. The involvement of different residues in substrate binding (Arg47, Tyr51, Thr268, Phe87) and the movement of Ala264 away from the heme iron were highlighted, as will be discussed later. Moreover, the crystal structure of NPG-bound heme domain was generated at a higher resolution than that with palmitoleic acid (*113*). Although observations are comparatively in agreement with the palmitoleic acid-bound form, additional information with regards to the role of water molecules (discussed above) and Thr268 and Arg47 residues were obtained.
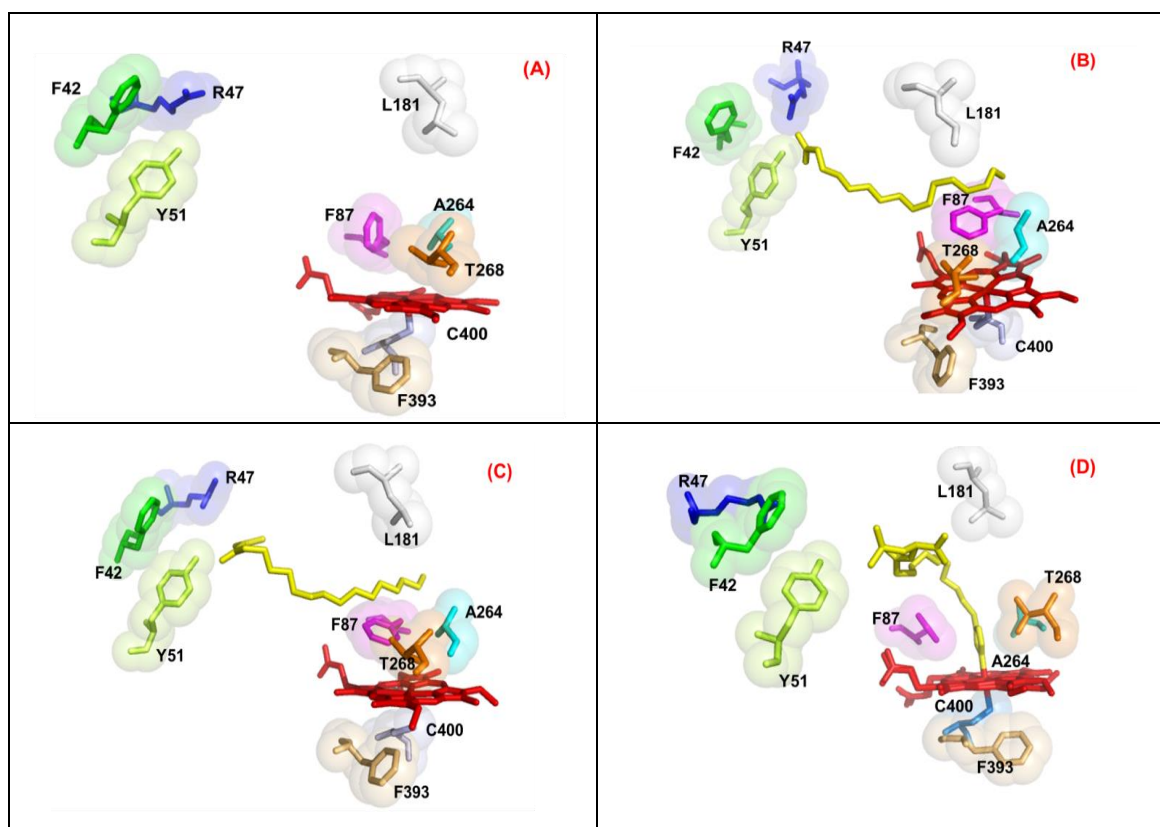
Figure 1.12: Comparison of active site structures of substrate-free (A), substrate-bound (B/C) and inhibitor-bound (D) heme domains of Cytochrome P450 BM3. PDB IDs: 2HPD, 1JPZ, 1FAG, and 3BEN respectively. The substrates [(N-Palmitoylglycine; B) and (Palmitoleic acid; C)] and inhibitor [N-(12-imidazolyl-dodecanoyl)-L –leucine] are coloured yellow while the heme iron centre is coloured red. Figures show major residues flanking the active site of cytochrome P450 BM3, playing various roles. Residues F42, R47 and Y51 are implicated in substrate entry and fatty acid carboxylate binding; L181 contacts the fatty acid alkyl chain; A264 and T268 are placed in the I helix and are involved in substrate interactions, with T268 being involved in protonation of iron-oxo intermediates; F87 is important for regioselectivity of substrate oxidation; C400 is the proximal thiolate ligand to the heme iron; F393 interacts with the heme thiolate ligand and influences reduction potential of the heme iron.

The bond between Thr268 and Ala264 is essential in stabilizing water molecules around the active site of the protein. Thr268, a conserved residue on the C-terminal end of the I-helix, has been proposed to play an important role in oxygen binding and activation. Turnover of a BM3 T268A mutant with lauric acid substrate resulted in uncoupling with much greater production of hydrogen peroxide than was observed for wild-type BM3 under similar conditions (*132*). Further studies with arachidonic and palmitic acids confirmed uncoupling. However, production of a catalase-like activity is thought not to

be a consequence of mutation of Thr268. Moreover, with this mutant it was observed that about 40 % of the enzyme remained in a low spin state (*130*). One possible explanation could be that, with loss of the Thr268 residue, the hydrogen bonding that stabilizes WAT500 in the high spin state is lost, which in turn implies that the equilibrium will tend to shift to the low spin form (*113*). In general, all studies indicate that T268 plays a role in substrate recognition and maintaining catalytic efficiency by proper positioning of the fatty acids and water molecules required for productive hydroxylation (*133, 134*). Thr268 is now considered to hydrogen bond with the ferric-peroxo intermediate to enable its protonation and catalytic cycle progression.

As described earlier, when substrates bind to the BM3 enzyme, there is a displacement of the sixth axial water molecule, which results in a change in spin state from the hexa-coordinated low spin to the penta-coordinated high spin form. The displacement of the water molecule also results in the movement of Ala264 (about 1 Å) away from the heme (Figure 1.12), where it forms a hydrogen bond with Thr268, presumably creating opportunities for oxygen to bind (*112*). The importance of this residue is highlighted when it is mutated from a neutral non-polar alanine to an acidic polar glutamate (*135, 136*). A catalytically active (albeit much lower than wild-type) enzyme results, in which the sixth axial water molecule to the ferric iron is displaced by the Glu264 side chain, forming a new heme iron ligand set in the low spin form for a proportion of molecules in the A264E mutant (the rest have Glu264 interacting with Phe87 and with a water remaining on the heme iron). Substrate binding to this mutant induces a type II spectral shift as seen in inhibitor binding (section 1.2.3.6) with the protein remaining in a low spin form. This occurs since substrate interacts with Phe87 and displaces Glu264 from this position to enable near-complete coordination of the heme iron. Subsequent Ala264 mutations to histidine and lysine resulted in a further set of ligands with the same type of distal coordination (by His264 and Lys264) and type II spectral shift (*137*). An important point from analysis of the A264E mutant was that X-ray crystallography showed it to occupy the SB conformational form, regardless of presence of substrate. Moreover, optical titrations showed it had higher affinity for fatty acid substrates than did wild-type BM3. It was concluded that the SF to SB conformational transition might not reflect substrate binding *per se*, but instead a natural conformational equilibrium for the substrate-free enzyme. In this model, the SB conformation has higher affinity for fatty acids, and thus this form is stabilized by binding of substrate. In subsequent studies, further mutants (A264M, A264Q and A264C) were created (*138*). Resulting

crystal structures indicate that these mutants adopted substrate-bound conformations in the absence of substrates, emphasizing that mutations at A264 is sufficient to alter the conformation of the BM3 heme domain.

Tyr51, Arg47 and Phe87 are three active site residues whose role in substrate binding has been widely investigated. It has been established that fatty acid binding is partly modulated by charge interactions (*102, 120, 139*). Tyr51 and Arg47 are the only two charged/polar residues around the active site channel surface and, as such, are proposed to be involved in anchoring the fatty acids via their carboxylic acid moiety. While Tyr51 is observed to be directly hydrogen bonded to the carboxylic group of the substrates, direct contact for Arg47 is less obvious (*112*). Moreover, binding studies on a R47E mutant suggests that the anchorage role played by Arg47 is not entirely a dominant one (*140*). In a related study, the guanidinium group of Arg47 was found to be ~5 Å away from the carboxyl group of the fatty acid, a distance deemed too far for efficient electrostatic interactions (*113*). Based on these findings, it was proposed that while Tyr51 may be involved in substrate-induced change in spin state, Arg47 seems to play a role in stabilizing the interaction with the fatty acid carboxylate group, as well as influencing the association kinetics (*5, 113*). In essence, although the specific roles of Tyr51 and Arg47 have not been pinpointed, it is a certainty that they are important in substrate binding, as a significant decrease in activity was observed with R47/Y51-altered mutants (*119*). Moreover, the roles played by these residues have been found to be dependent on the chain length of the fatty acid (*141*).

Phe87 flanks the heme end of the active site channel and was shown to have close van der Waals interaction with the heme [Figure 1.12; (*111*)]. The phenyl ring of Phe87 is believed to provide an anchor to the ω-end of fatty acids without being involved in hydroxylation reactions at this end. The ω-hydroxylation of lauric and p-nitrophenoxycarboxylic acids, as well as regio- and stereo-selective hydroxylation of arachidonic acid were apparently achieved by a single mutation at F87V (*123, 139, 141, 142*). Using a combination of crystallographic, kinetic isotope effects and stopped-flow analyses, the role of Phe87 in heme accessibility has been discovered. It controls substrate entry into the active site by 'blocking' the ω-terminal methyl group of substrates, hence impeding binding of large aromatic substrates (*112, 143, 144*). Like the R47/Y51 motif, this control is proposed to be chain length dependent (*141*). Molecular modeling suggested that   Phe87 stabilizes the substrate (-)-alpha-pinene

binding in   different binding modes predicted near the heme (*145*). Hence, Phe87 is central to substrate regio-selectivity and heme accessibility.

The loop containing a cysteine residue that coordinates the heme domain is highly conserved among P450s. The role of a phenylalanine residue (position 393) within this loop was examined and results indicated that Phe393 is not involved in heme incorporation, but is highly linked to the modulation of the thermodynamic properties of the heme (*105*). Using a combination of MCD, EPR and crystallography, it was surprising, but interesting, to observe that this control is accompanied by slight but intimately linked structural changes (*146*). Furthermore, structural examinations indicate that the observed control could be a function of steric interactions between F393 and the vinyl groups of the heme (*147*).

Using SERRS (surface enhanced RR spectroscopy), the positions of the heme vinyl groups were studied on substrate binding, and the effects compared between substrates, the heme domain and holoenzyme, and among different P450s (*148, 149*). In general, subtle differences in vinyl orientation and splitting patterns were observed. It was deduced for P450 BM3 that both lauric and palmitic acids have different binding characteristics of their hydrophobic tails within the pockets. Moreover, it was proposed that the vinyl groups might be important in regulating the different activities of the various isoforms of P450s, perhaps through thermodynamic regulation of the heme.

One unusual property of the P450 BM3 enzyme is that it binds (or appears to bind) substrates at a distance (7.5-7.8 Å) deemed too far for effective hydroxylation. It was proposed that the observed binding effect is a function of structural changes transmitted through the protein structure (*129*). However, reduction of the enzyme-substrate complex was reported to result in a 6 Å movement of the substrate towards the heme iron, probably positioning it for proper hydroxylation (*49*). Moreover, in an attempt to examine the effect of temperature on the enzyme-substrate binding modes, more productive binding modes were observed at high temperatures (*150*). This led to the proposition that while the substrates bind close to the enzyme at near-physiological temperatures, lowering the temperature results in 'sliding' of the substrate to a more distant position.

1.2.3.5 Substrate Binding: Affinity and Turnover

Values obtained for the dissociation (K_d or K_m) and catalytic rate (k_{cat}) constants are usually good indications of the affinity an enzyme has for a substrate, and the catalytic efficiency of the enzyme with that substrate, respectively. Unfortunately, it is very difficult to successfully compare these values for any given substrate with BM3, because of its high sensitivity to differences in experimental conditions.

The rate of NADPH consumption gives a good measure of substrate hydroxylation, and there is, in general, a good correlation between the affinity (K_d, K_m) and the activity of the enzyme with a given substrate. Furthermore, the fatty acid amide derivatives of amino acids appear to bind more tightly to BM3 than any other fatty acids studied to date (*120*). It can also be inferred (from both K_d determinations by optical titration and steady-state turnover analysis) that BM3 has great affinity for long chain fatty acids. Attempts to alter BM3's selectivity towards short chain fatty acids have been somewhat successful, with the alteration of the central portions of the substrate binding cavity (*e.g.* Leu181 and Leu437) having some positive impact on short chain substrate binding (*119*).

In an attempt to understand what influences binding affinities of the enzyme, L-amino acid derivatives of palmitic acid (N-palmitoyl-L-leucine and N-palmitoyl-L-methionine) were synthesized and binding of these substrates to BM3 heme domain was examined (*120*). Marked differences in binding affinities was observed and this was attributed to the desolvation of the amino acid side chains, as there is a seemingly good correlation between the side chain desolvation energies and the binding free energies (derived from binding constants).

1.2.3.6 Inhibitor Binding

Relatively little work has been done in understanding the effects of inhibitor binding on the enzyme structure and function. Initial studies indicate that while binding of substrate converted the spin state to a high spin form, titration with an inhibitor (metapyrone) induced a reversal to a low spin form (*151*). Subsequent studies with ω-imidazolyl carboxylic acids indicate that these are better inhibitors of BM3 enzyme (*152*). It was observed that all inhibitors of this type ligate the ferric heme iron forming low-spin complexes with a type II spectral shift (419-to-424 nm). Cooperativity was observed for

their binding with lauric acid, while with arachidonic acid, a competitive type of inhibition was predominant. There is, however, no denaturation as a consequence of binding of these inhibitors (*153*).

In recent developments, the crystal structure of an inhibitor-bound P450 domain was solved (*154*). The inhibitor was made more potent by attaching amino acids to the ω-imidazolyl fatty acid, creating N-(ω-imidazolyl fatty acyl)-L-amino acid inhibitors. The inhibitor-bound and substrate-bound crystal structures were compared and a great deal of distortion was observed in the I-helix of the inhibitor bound structure. This distortion is attributed to steric conflicts between the imidazole ring and the side chains of Ala264 and Phe87. Additionally, binding of the inhibitor brought about an open conformation of the active site channel, presumably to accommodate the new imidazole ligand.

1.2.3.7 The Reductase Domain

In contrast to the heme domain, there has been a more limited set of genetic engineering studies on the reductase domain of the BM3 (BMR), which is partly due to the unavailability of the crystal structure of this domain. FMN-deficient mutants G570D and W574D (*155*) were constructed for use in analyzing the flavin binding sites of P450 BM3 (*156*), as well as for evaluating electron transfer in flavocytochrome P450 BM3 (*9, 116*). Further mutagenesis work on the reductase domain has been directed at altering co-enzyme (NADH versus NADPH) specificity.

In a later section, the potential of BM3 as an industrial biocatalyst, *e.g.* in the pharmaceutical industries and the energy sector, will be discussed (Section 1.2.5). A single mutation of a tryptophan residue at position 1046 generated results that the researchers described as "promising in terms of generating NADH-specific variants of P450 BM3 for biotechnological exploitation"(*157*). The side chain of W1046 is known to shield the FAD isoalloxazine ring. Mutants W1046A and W1046H were able to induce a significant switch in coenzyme specificity from NADPH to NADH, a less expensive co-enzyme. The role of W1046 is further implicated in the determination of the electron transfer route within the BM3 monomer (Section 1.2.7). Moreover, mutations in the FAD domain of BM3 (S965A, R966A and K972A) in addition to the FAD-shielding W1046A mutation also tilted the coenzyme preference towards NADH (*158*). Cys999, one of the residues that make up the conserved catalytic triad of many diflavin reductases was shown to be involved in co-enzyme binding and in enhancing

hydride transfer from NADPH to the FAD cofactor (*63*). Finally, crystals of BM3 FAD domain were obtained using the mutant C773A/C99A (*115*) and attempts to obtain crystals of the reductase domain using the C773A mutant are discussed in this work.

Still on the subject of phylogenetically conserved residues, comparative sequence analysis of the BMR with related reductases shows that a large section of BMR is missing in ferredoxin reductases. This section was identified as residues 711-821 in BM3 (*107*). Deletion of this fragment results in a mutant with a low cytochrome *c* reductase activity, albeit with a higher activity compared to the FAD domain in isolation. The deleted segment resulted in removal of FMN-binding residues and loss of the cofactor. Since efficient cytochrome *c* reduction requires electron transfer from the FMN, the activity loss was not surprising for this deletion mutant.

1.2.3.8 Interactions of BM3 with Molecular Oxygen (O$_2$), Nitric Oxide (NO) and Carbon Monoxide (CO)

Employing a combination of CD, magnetic (MCD), RR and SERRS techniques to study the spectroscopic characteristics of NO adducts, it was observed that interaction of BM3 with nitric oxide (NO) results in the formation of ferric and ferrous NO adducts (*159*). While the ferric adduct is quite stable and effectively inhibits hydroxylase activity, the ferrous adduct is unstable and reacts readily with oxygen. It was also observed that NO treatment of BM3 heme domain resulted in nitration of one or more tyrosine amino acids, and Tyr51 of the substrate carboxylate binding region was one target residue identified.

Binding of carbon monoxide (CO) to ferrous cytochrome P450 enzymes results in the formation of a ferrous CO complex (Fe^{2+}-CO). This inhibits binding of oxygen to the reduced heme iron and subsequent mono-oxygenation activities of the enzyme (Figure 1.5). Laser flash photolysis was used to observe the interactions of carbon monoxide (CO) with BM3 (*160*). Results show that the kinetics of CO binding to BM3 is second order. However, while a biphasic behaviour (that is, biphasic reaction transients describing CO binding) was observed in the substrate-free form, a monophasic behaviour was observed in the substrate-bound form. In the substrate-free form, the observed biphasic behaviour could be taken as evidence for the existence of multiple protein conformations (such as the open and closed forms). The faster phase is attributed to the open conformation, allowing full diffusion access for CO. The

geometry of the linear ferrous CO and ferric NO bonds is observed to be distorted (*117*). This distortion is attributed to the steric hindrance imposed by the side chain of Phe87 (see section 1.2.3.4).

The study of interaction between the reduced heme iron with molecular oxygen has proven difficult as the resulting oxyferrous complex is transient. Employing low-temperature spectroscopic and high pressure stopped-flow (*161, 162*) techniques to stabilize the complex, the oxygen-binding characteristics of P450 BM3 and NOS have been analysed. The spectral properties of oxyferrous complexes of BM3 were different from those obtained for NOS, but similar to those obtained for microsomal P450s as deduced from the difference spectra. Furthermore, the oxygen- and CO-binding properties (rate and activation volume) of BM3 were similar to one another, while those for NOS differed. From these comparative studies, it was deduced that, in P450 BM3, CO-binding can be used as a model for oxygen binding (*162*).

1.2.4 Electron Transfer in Flavocytochrome P450 BM3

In cytochromes P450, electron flow involves hydride transfer from NADPH to the reductase domain and subsequent electron transfer from the diflavin reductase domain to the heme as shown in Figure 1.6. In flavocytochrome P450 BM3, the interactions at each stage have been well characterized and the role of the NADPH deduced. Furthermore, the electron transfer properties observed for P450 BM3 exhibit similarities to, and marked differences from, other P450s, especially the microsomal P450s.

1.2.4.1 NADPH Reduction of Full Length and Flavoprotein Domain of BM3

A combination of steady state/stopped flow analysis,EPR spectroscopy, and redox potentiometry has been employed to fully understand the mechanism of electron transfer in flavocytochrome P450 BM3. A great challenge is posed in the ability to effectively interpret spectral data obtained on reduction of either the full length enzyme (BM3) or the reductase domain (BMR) using NADPH. Based on previous studies on other cytochrome P450 systems, the wavelengths used for measuring the activities at different stages of the reduction process are shown in Table 1.2.

Table 1.2: Wavelengths specific for analysis of BM3 reduction and electron transfer reactions. *The indicated wavelengths or wavelength regions have been used to examine redox reactions in BM3 involving NADPH-to-FAD, FAD-to-FMN and FMN-to-heme electron transfer.*

WAVELENGTH (nm)	ACTIVITY
450	Formation of a CO adduct
750	Formation of a FAD(H)-NADP(H) charge-transfer complex
350-400	Formation of anionic, red semiquinone
400-500	Indication of a fully reduced flavin
550-650	Formation of a blue, neutral semiquinone

An active reduced BMR domain of BM3 is observed to be in a 2-electron reduced form (*131, 163*) containing a double semiquinone (sq), one neutral and the other anionic (deprotonated). Interestingly, all studies agreed the presence of an anionic sq (on the FMN), which in most cases, is observed to be short-lived. Moreover, the rapid disappearance of the sq species (as seen in EPR studies) on re-oxidation indicates that electron transfer to the heme is from a flavin sq (*116*) which is in a low-potential anionic form (*164*). The Sevrioukova group hypothesised that, based on their results, the FMN was the anionic sq source, as would be expected since it is known that the FMN is the cofactor that donates electrons to the P450 in other systems (*164*). Comparing the difference spectra obtained for inactivated (i.e. "over-reduced" enzyme pre-incubated with NADPH) and re-activated (reoxidized) forms of BM3, the flavin in the anionic sq form was suggested to be most likely the FAD (*163*). But, with studies using FMN-deficient mutants, no peak indicative of a sq was observed, thus indicating it is likely the FMN(*116*). Further proof that the electron source for heme reduction is FMN was derived from stability studies on the sq and hq (hydroquinone) forms of both FAD and FMN. There is a consensus that the FMN sq is thermodynamically less stable compared to the hq form (*131, 164, 165*). The thermodynamically unfavourable anionic FMN sq disproportionates quickly, thus acting as a viable electron donor to the heme (*165*). On the contrary, the hq form of FAD is thermodynamically less stable than the sq form but becomes more stable when NADP(H) is bound (*163*). The inactivated form of the enzyme formed by pre-reduction with NADPH is one in which the FMN is reduced fully to its hq form. Thus, it was concluded that while the FMN sq form transfers

electron to the heme, its hq form is catalytically inactive (or at least much less active) in this function. In another study, the insertion of a glycine residue (betweenTyr536 and Asn537) at a position corresponding to the residue Gly141 in CPR and Gly 57 in *C. beijerinckii* flavodoxin favoured the formation of a more stable neutral form of FMN sq (rather than the anionic sq usually observed in the wild type enzyme) (*166*). However, the purified mutant BMR protein tended to lose the FMN cofactor with one-third and less than one percent activities recorded with ferricyanide and cytochrome *c* respectively.
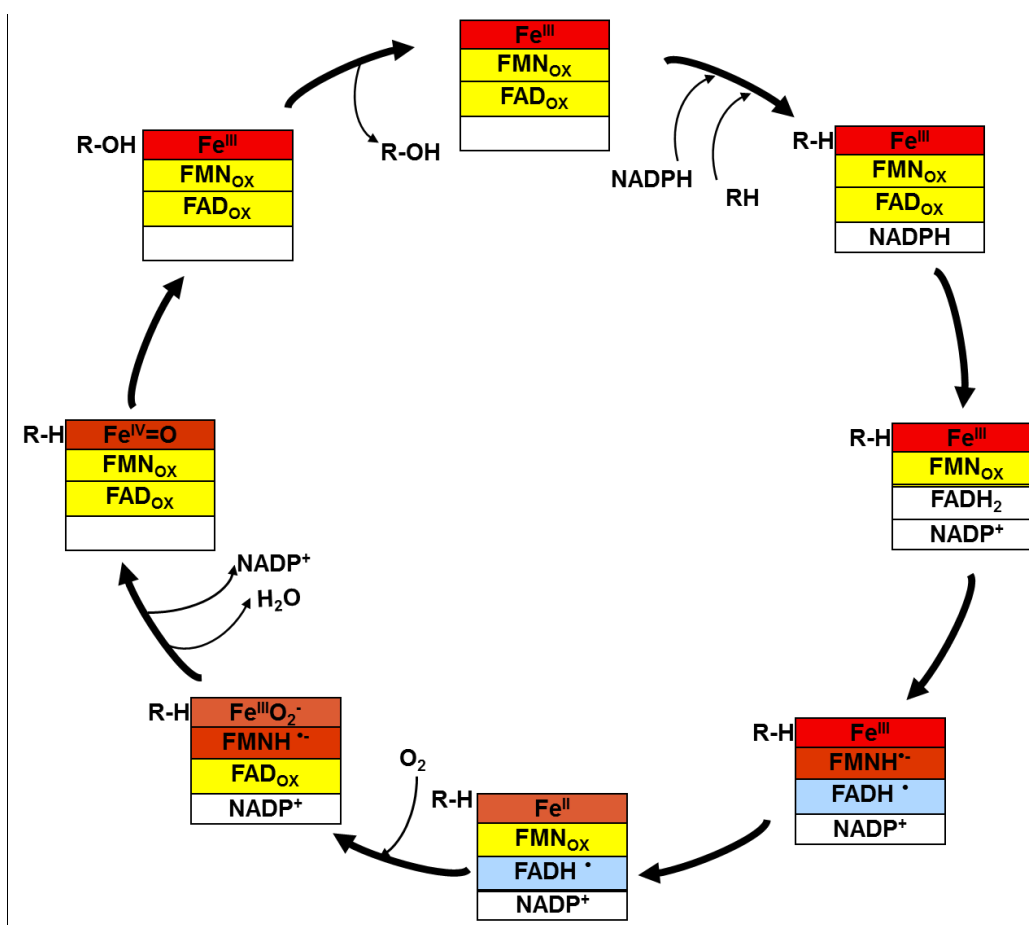
Figure 1.13: Proposed mechanism for electron transfer in flavocytochrome P450 BM3*. The cofactor colour in the respective redox states in solution is as indicated.(Image modified from (163)).*

Thus reduction of BM3 involves a transfer of two electrons from NADPH to FAD forming FAD hydroquinone which in turn serves as a one-electron donor to the FMN forming the FMN semiquinone. The proposed mechanism for the transfer of electron in full length P450 BM3 is as shown in Figure 1.13. From the scheme it is obvious that the hydride and inter-flavin transfer steps are readily reversible.

1.2.4.2 Significance of NADPH Binding

A charge-transfer complex was observed on reduction of BMR with NADPH (*164*). It has been proposed that, besides supplying electron equivalents, NADPH plays a role in stabilizing this complex formed between FAD semiquinone and NADP$^+$ via ionic interactions (*163*). In addition, the bound NADPH facilitates catalysis by modulating the redox potential of the flavin co-factors (*131, 167*). This could be by direct contact with the flavin co-factors (stability) or by inducing conformational changes that alter the environment of the isoalloxazine rings of both flavins (*167*). Furthermore, pre-incubation of BM3 with NADPH in the absence of substrates slowly converts the active enzyme to an inactive three-electron reduced (fully reduced flavin [FMN] and a flavin sq [FAD]) form that is highly inefficient in fatty acid hydroxylation and NADPH oxidation (*4, 163, 168, 169*). However electron transfer to artificial electron acceptors is still possible, and the reoxidation of the flavin(s) that occurs in these processes actually restores the fatty acid oxidase activities. No gross structural alterations appear to accompany this inactivation, but the electrons could be transferred to molecular oxygen to form superoxide ions in the absence of substrate and electron acceptors (*168*). The inhibition of hydroxylase activity by the inactivated enzyme is likely at the level of electron transfer to the heme domain, given that the inactivated enzyme effectively reduces cytochrome *c* (*167*). This is supported by the assumption that the fully reduced flavin observed in the 3-electron reduced enzyme is FMNH$_2$, already established to be incapable of reducing the heme.

It is important to note that NADPH can only bind productively to fully oxidized BM3 (i.e. with oxidized FAD cofactor) (*167*). The binding strength may increase on hydride transfer to the FAD, consistent with the proposed stabilizing role in catalysis, and this may be important in preventing the binding of another NADPH molecule, leading to the generation of an inactive 3-electron reduced form. Moreover, NADPH binding to the FAD domain was observed to decrease as the ionic strength of the buffer increased (*110*). A double occupancy model was proposed for NADPH binding to BM3 based on the observation that the rate constant for flavin reduction shows some apparent inverse dependence on the concentration of NADPH (*63*). This proposal was disputed by Daff (*170*), who re-analyzed the observed data and in comparison with other diflavin reductases came to a conclusion that there is no structural, spectroscopic, or analytical evidence to suggest a second NADPH binding site in NOS, CPR and BM3.

The role of NADPH in the activity studies of the highly catalytically efficient BM3 cannot be overemphasised. However, this co-factor is considered to be expensive and hence alternative means have been sought for driving BM3 catalysis. In section 1.2.3.7, it was shown that mutation of W1046, along with other mutations in the reductase domain, resulted in switching the preference of cofactor for BM3 from NADPH to NADH. Further, the use of cheap Zn dust as electron donor and Cobalt III sepulchrate as the mediator to transfer electrons to multiple BM3 mutants at position Phe87 was also investigated as a cost-effective alternative to NADPH (*171, 172*). Subsequent non-mutational studies examined alternatives for transferring electrons directly to BM3 via electrochemical (*173*), light-driven (*174*), and enzyme-based recycling ((*175*); *i.e* using glycerol dehydrogenase and a soluble transhydrogenase to recycle NADH and NADPH) routes.

1.2.4.3 Factors that Influence Electron Transfer in BM3

While NADPH binding to BM3 is observed to induce conformational changes in the protein (*167*), substrate binding also induces conformational changes in the heme domain which ultimately lead to changes in the electron transfer properties of the FMN domain (*169*). The FMN domain is observed to be highly charged and its polarity increases with increasing ionic strength (*176*). Fluorometric studies also show that the FAD and FMN domains are not in close proximity. These factors, coupled with the observed increase in electron transfer as ionic strength increases, suggest that the interaction between the FAD and FMN domains is modulated by electrostatic forces (*176, 177*). Moreover, this electrostatic interaction between the FAD and FMN domain is also observed to facilitate electron transfer between the FMN and heme domains, avoiding formation of the inactive 2-electron reduced FMN. It was also observed that interactions between the FMN and the heme domain are governed by a mixture of hydrophobic and electrostatic forces, with none dominating.

1.2.4.4 The Rate-Limiting Step

Identifying the rate-limiting step in the electron transfer and overall catalytic process for flavocytochrome P450 BM3 also posed a great challenge. Rate constants for electron transfer across the various complexes were obtained and these constants were dependent on NADPH concentration (*164*). The FMN-to-heme electron transfer rate constants were found to be a thousand-fold less in the reconstituted P450 and reductase domains

(compared to the intact enzyme), indicating the important role of the linker in tethering the domains in close proximity (*178*). For the first electron transfer to the heme iron, there was an apparent dependence of the observed rate constant on the heme reduction potential (*133*). However, a greater percentage of this dependence was thought to be contributed by the spin state shift, with a minor involvement of the shift in reduction potential (*179*).

Results indicate that the rates at which electrons are transferred in the steps preceding FMN reduction are too fast to be the rate-limiting steps. Having eliminated these steps, the rate-limiting steps could either be (i) electron transfer from FMN-to-heme (given that this happens twice in the cycle) or (ii) product release as inferred from the accumulation of high-spin ferric species in the difference spectra obtained during enzyme turnover(*116*). Munro *et al*. (*178*) proposed that, based on their results, the rate limiting step could be the first heme reduction. Redox potentiometric studies supports this hypothesis based on the observation that thermodynamic regulation of electron flow through the cycle is exerted at the substrate binding level(*131*). In the oxidised and substrate-free form, the heme has a very negative redox potential of about -370 mV, making transfer of electron from NADPH (redox potential of -320 mV), thermodynamically disfavoured (Figure 1.14).
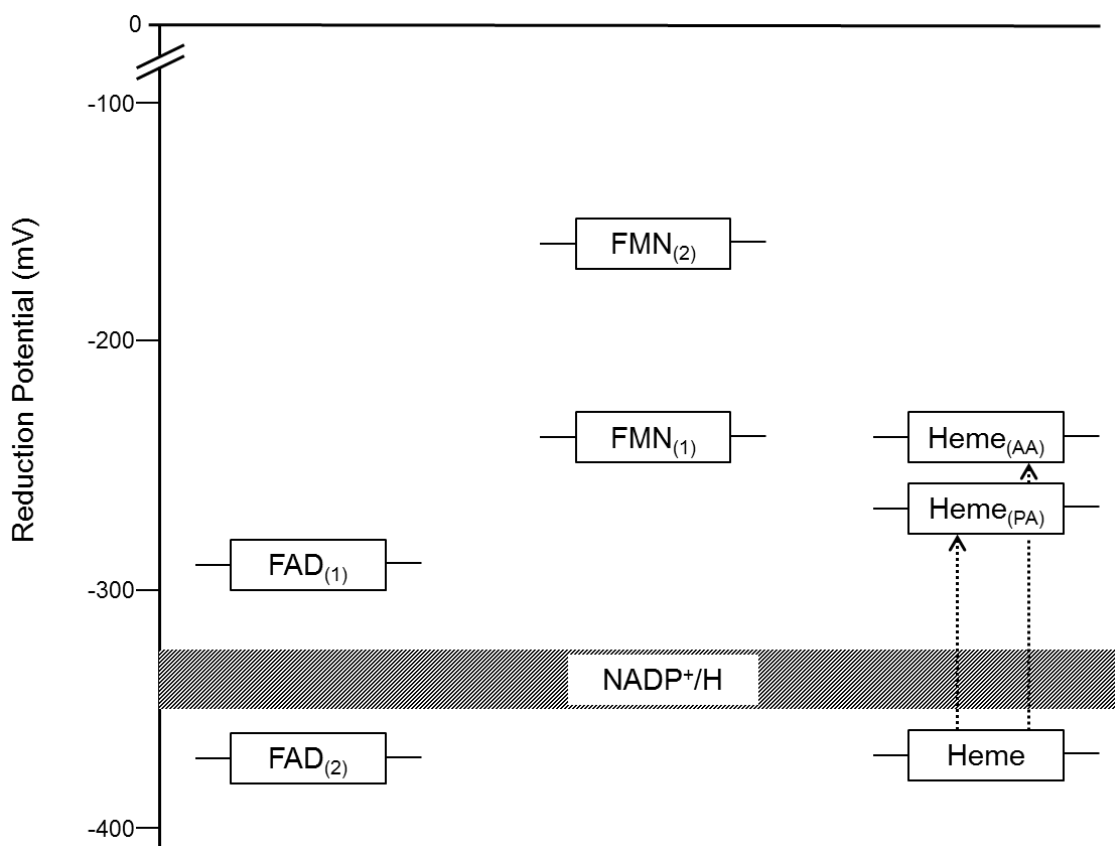
Figure 1.14: Redox potentials of the flavins and heme cofactors determined in domains of BM3. *Image modified from (131)* and updated with FMN measurement values from *(165)*. *The potential shown is relative to the standard hydrogen electrode (SHE) and the elevation of heme potential on binding arachidonic acid (AA) and palmitic acid (PA) is shown. The subscripted numbers indicate the number of electrons on the relevant flavin cofactor. More recent studies by Hanley et al (165) suggest a wider separation between the 1- and 2- electron redox couple of the FMN, bringing the FMN semiquinone potential closer to that of the substrate-bound P450 heme iron to facilitate electron transfer to heme.*

However, substrate binding results in an increase in redox potential (about +130 mV), thus facilitating electron transfer from the NADPH through to the heme (i.e. making thermodynamically favourable the FMN-to-heme electron transfer, and thus electron transfer through the whole enzyme). The thermodynamic control ensures that pointless electron shuttling, as well as production of toxic oxygen radicals, is avoided in the absence of substrate.

1.2.4.5 Electron Transfer to Other Acceptors

Besides the P450 domain of BM3, other non-physiological electron acceptors for the reductase domain have been recognized. Ferricyanide accepts electrons from the FAD cofactor (and also from the FMN, probably to a lesser extent), while cytochrome *c* accepts electrons from both the semiquinone and hydroquinone forms of FMN. Cytochrome *c* reductase activity in the full length enzyme is observed to be higher than in the reductase domain. This could be because the heme domain fixes the orientation of the FMN and avoids unsuccessful collisions with the cytochrome *c* (*176*). Moreover, cytochrome *c* reductase activity of BM3 is enhanced in the presence of bound fatty acid substrates, as well as by inhibition of the enzyme by CO-binding to the P450 heme, implying that structural effects on the heme domain and disruption of electron transport to the heme domain can positively influence the rate of electron transfer to cytochrome *c*, and possibly its mode of docking to the enzyme (*169, 180*).

1.2.4.6 Electron Transfer Properties in BM3 and Microsomal Cytochrome P450s

The BM3 electron transfer properties discussed below exhibit marked differences from the mammalian P450s. Some of these differences include:

❖ In BM3, NADPH binding to oxidized BMR is quite weak although the affinity increases on hydride transfer. In contrast, the binding affinity of house fly P450 reductase to NADPH is much stronger with no significant effects on affinity observed on hydride transfer to the FAD (*167*).

❖ Using a truncated version of BM3 missing the FAD domain, it was observed that the second order rate constant for FMN reduction is greater than that for FAD reduction in Microsomal P450 reductases (*181*). However, this conclusion was drawn from experiments where the reduction of FMN was catalyzed by 5-deazariboflavin generated using laser flash photolysis.

❖ In CPR, electron transfer from the flavin to the heme is via the FMN hydroquinone and/or semiquinone, while in BM3 the FMN semiquinone is the only active form by which electrons are shuttled to the heme (*54*).

Thus there are some significant differences between the redox properties of "general" eukaryotic CPR enzymes and the BM3 reductase (BMR). Electron transfer (including NADPH-dependent FAD reduction and FAD-to-FMN electron transfer) are much faster

in BMR (compared to human CPR, for example) and the BMR undergoes a different electron loading cycle to the eukaryotic CPRs. The eukaryotic CPRs have a stable FMN semiquinone, an on reduction by NADP go through a 1-3-2-1 cycle, where the number indicates the total number of electron on the FAD/FMN cofactors (the "1" indicates the stable 1-electron reduced FMN) and where the FMN hydroquinone is the electron donor to the P450 partner. In contrast, BM3 starts from a fully oxidized form and goes through a 0-2-1-0 cycle, with the FMN (anionic) semiquinone as the heme reductant. In fact, reduction of the BMR FMN to its hydroquinone is associated with activity loss in fatty acid oxidation (*52*)

1.2.5 Flavocytochrome P450 BM3- A Potential Biocatalyst: Directed Evolution

In recent years, most chemical industries have channeled a greater percentage of resources to developing biocatalysts that are faster, cheaper, utilize less energy, and produce less waste than conventional chemical catalysts. Three very important characteristics of a good biocatalyst are stability, versatility and high turnover. Genetic engineering studies have shown that flavocytochrome P450 BM3 possesses, to a greater degree, these characteristics. Hence researchers are capitalizing on these features to uncover the potential of BM3 as a biocatalyst for industrial and pharmaceutical purposes, using both rational and random mutagenesis to alter its substrate recognition properties.

Cytochromes P450 are well known for their role in metabolism of drugs, and other xenobiotics. The interest in flavocytochrome P450 BM3 was directed towards making the enzyme a model for understanding the structure and function of mammalian P450s. However, the ability of a triple mutant (R47L/F87V/L188Q) of P450 BM3 to successively metabolize several drugs and drug-like molecules, albeit at a slower rate than for its typical fatty acid substrate, makes it ideal not only for use as a model system, but also as a potential industrial biocatalyst (*182*). The catalytic activity of this triple mutant for certain drugs (dextromethorphan and 3,4-methylenedioxymethylamphetamine) was about 200-fold greater when compared to the human CYP 2D6 which is known to metabolize these drugs *in vivo* (*183*). Characterization of these mutants suggests an ion pair interaction between a heme carboxylate group of the mutants and the nitrogen groups of the drugs (*184*). In a related

development, these mutants have been found useful in toxicological characterization of new drugs with reference to adverse drug reactions (*185*). Interestingly, wild type BM3 was also observed to metabolize xenobiotics that are typical substrates of human CYP2E1 and CYP3A4 at rates higher than the human enzymes (*186*). Further studies have revealed that wild type and mutant BM3 can hydroxylate other drugs and substrates (such as: 7-ethoxycoumarin, *trans*-resveratrol, lovastatin and methoxyresorufin) that are typically catalyzed by human CYPs (*187-190*).

The energy sector has lately been faced with a lot of challenges as to the best option for the source of renewable energy. One of these options includes developing a biological system to selectively oxidize natural gas sources, such as alkanes. Interestingly, flavocytochrome P450 BM3 has been examined (amongst other enzymes) in this regard. Via directed evolution, it has been possible to engineer BM3 into a mutant that effectively and regio-selectively hydroxylates alkanes at the terminal carbon (*191, 192*). On the other hand, dummy substrates have also been used to trick BM3 into hydroxylation of gaseous alkanes by helping to maintain the alkanes in a position close to the heme iron (*193*). Mutational studies on BM3 have also introduced the enzyme to other sectors, including agriculture (*194*).

Recent studies on BM3 have been channeled towards directed evolution (and other mutagenic methods) to improve activity of BM3; expand the BM3 substrate range and product profiles; and alter regio- and stereo-selectivity of the enzyme. Examples of resulting BM3 reactions include propane mono-oxygenation (*195, 196*); hydroxylation of cyclic and acyclic alkanes (*197*); styrene epoxidation (*198*); desaturation (novel BM3 reaction) and O-dealkylation of alkylbenzenes (*199*); and conversion of indole to indirubin (*200-203*).

1.2.6 Flavocytochrome P450 BM3 and Chimeragenesis

BM3 has also been engineered to produce catalytically functional chimeras with good activity, regio-selectivity and substrate specificity. Domain-swap hybrids of CYP102A1 and CYP102A3 enzymes were produced by replacing the reductase domains of one for the other (*204*). Activity towards 1,2-*para*-nitrophenol (1,2-PNP) was tested and the chimera showed 88% and 38% of CYP102A3 and CYP102A1 activities, respectively. Furthermore, one of the four chimeras of BM3 and neuronal Nitric Oxide Synthase (NOS), the only one containing the reductase domain of BM3, exhibited a high NOS

activity (*205*). This indicates that the BM3 reductase (BMR) domain effectively reduces the heme domain of NOS, although this chimera was structurally unstable. Further, a chimera between BMR and CYP3A4 was created and examined in a bid to further understand the uncoupling in human CYP3A4 which can be as high as 85-95%. Results show that the uncoupling occurs at the heme iron active site and the activity (with regards to product formation) is not significantly affected by the chimeragenesis (*206*).

Fusion of genes coding for rat P450 2C11 with BM3 reductase domain (BMR) or NADPH-P450 reductases (CPR) resulted in chimeras with both cytochrome *c* reductase and arachidonic acid epoxygenase activities (*207*). In the same way, substituting residues 73-84 from insect CYP4C7 into BM3 produced a chimera that shifted regio-specificity of oxidation of terpenoids towards the centre of farnesol and palmitate substrate molecules(*208*). Further chimeragenesis with CYP4C7 involved replacing F87 in the BM3/CYP4C7 chimera with its homologous counterpart from CYP4C7 (leucine) (*209*). This chimera was able to oxidise farnesol to 10,11-epoxy farnesol but not to the original CYP4C7 product:12-hydroxyfarnesol. However, this was achieved by subsequent chimeragenesis in the SRS-5 (327-332) and SRS-1 (78-82) regions (that is, introducing CYP4C7 residues into the BM3 backbone) and by adding the F87L mutation (*210*). The SRS (substrate recognition sequence) regions are conserved parts of P450 structure important to substrate binding. There are approximately 6 such regions across a P450, with most located in the P450 active site (*211*).

Although creation of chimeras poses a lot of challenges, the results obtained clearly show that BM3 can be manipulated to metabolise alternative substrates typical of a wide variety of exogenous P450s, and to yield the same products as those produced by these other P450s. Thus engineered BM3 efficiently interacts with substrate of many other P450s, emphasising its versatility and diversity, and the pliability of its active site.

1.2.7 Dimerization of Flavocytochrome P450 BM3

Black and Martin (*109*) first reported that monomers, dimers and higher oligomers appeared to exist in native BM3, and that there was rapid conversion to a predominantly dimeric form (with molecular weight equal to 230 kDa) that resulted on reduction of the enzyme with DTT as deduced from the sedimentation equilibrium. Further analysis with HPLC size exclusion chromatography revealed that, on reduction of the enzyme with DTT, peaks representative of monomers result, along with substantial peaks for dimers,

trimers and tetramers. This dimerization effect, which is linked to the reductase domain, is independent of DTT concentration and could not have been a result of disulfide linkages. In a later study by Govindaraj and Poulos (*107*), FPLC and SDS-page electrophoresis revealed that, while the full length enzyme dimerizes via interactions other than disulfide linkages, these bonds are the major factors in the observed reductase and FAD dimers. Further analysis provides more evidence that the native enzyme dimerizes in solution and a dimerization mechanism was proposed (*9, 212*). Dimerization equilibrium was observed to be sensitive to ionic strength and the presence/absence of substrates. The evidence includes:

❖ An observed decrease in specific lauric acid hydroxylase activity at low enzyme concentrations, suggestive of dissociation of a dimer into monomers (*9*).

❖ Cytochrome *c* and ferricyanide reductase activities were maintained at low enzyme concentrations, implying that inter-flavin electron transfer is unaffected and that FMN loss is not a major factor explaining diminished laurate hydroxylase specific activity at low BM3 concentration (*9*).

❖ Electron transfer in BM3 using combinations of various mutants, specifically involved in cofactor binding and coordination, indicated electron transfer between the monomers in a BM3 dimer. These mutants included A264H (heme domain inactivation mutant resulting in a non-displaceable 6th ligand to the heme iron), G570D (FMN-depleted mutant), F87Y (regulates heme accessibility), and W1046A (exposes FAD cofactor and promotes binding of NADH). A mixture of A264H and G570D mutants (both inactive in fatty acid oxidation) results in the restoration of fatty acid hydroxylase activity (*9*). Furthermore, in a different study, out of other possible combinations, only two (F87Y and W1046A; F87Y:G570D and W1046A) had high activity towards the substrate (*212*). Based on these results, two distinctive models were proposed for domain interactions within the dimers (Figure 1.15)
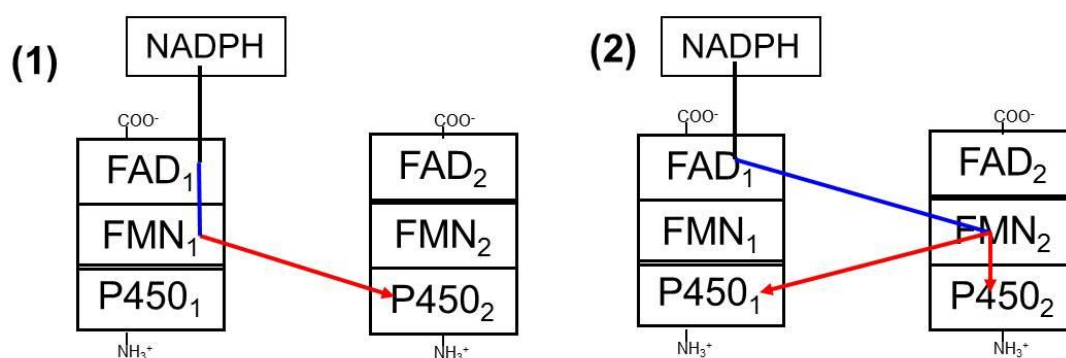
***Figure 1.15: Schematic representation of proposed mechanisms for domain interactions and electron transfer in P450 BM3 dimers** by (1) Neeli et al (9) and (2) Kitazume et al (212). It should be noted that electron transfer in eukaryotic nitric oxide synthase (NOS) enzymes follows the same pathway as shown in scheme 1 (213).*

As seen in the figure above, the first model proposes electron transfer (e.t) from NADPH to FAD to FMN in one monomer, then to the heme of the second monomer. The second model however proposes intermolecular one-electron transfer of electron from the FAD of one monomer to the FMN of the second monomer and subsequent intra-molecular e.t from FMN to the P450 of the same monomer or of the first monomer. Although the possibility of intra-molecular e.t from the FAD to FMN of the same monomer is not completely ruled out by the second model, it is important to note that the conclusions for this model were drawn on the assumption that the W1046A mutant is inactive on its own as a fatty acid hydroxylase. This assumption is however untrue, as Neeli *et al (157)* showed initially that the electron transfer properties of the BM3 enzyme were maintained in this mutant, and that NADH-dependent electron transfer from the mutant to cytochrome *c* (i.e via the FMN cofactor) was efficient. Recent studies have also shown that this mutant (W1046A), constructed in the full length enzyme, is fully active in lauric acid hydroxylation and is catalytically competent with both NADH and NADPH (*8*).

1.2.8 Brief Summary on Flavocytochrome P450 BM3

Flavocytochrome P450 BM3 (BM3) from *Bacillus megaterium* is an efficient P450 system with its redox partner (a diflavin P450 reductase) linked to the heme-containing P450 in a single polypeptide. Genetic dissection has enabled generation of individual P450 (BMP) and P450 reductase (BMR) domains which exhibit weak affinity for one another. This factor, coupled with the ease of expression/purification of the domains and their coloured cofactors with diagnostic absorption characteristics, makes BM3 a

model for cytochromes P450 in every respect including a tool for protein engineering. Since its discovery in the mid 1970's, BM3 has been intensively characterized. Firstly, crystal structures of the P450, FMN and FAD domains have been resolved, simplifying the overall understanding of the fatty acid hydroxylation activities of BM3. Secondly, genetic engineering has enabled demonstration of the "pliability" of BM3 in that its active site can be engineered to accommodate a wide range of different molecules. Thirdly, the electron flow pathway in BM3 has been elucidated and the rate limiting step is proposed to be the first heme reduction. Fourthly, it has been demonstrated (in the last decade) that the functional form of BM3 is a dimer.

Although these results are interesting as it brings us closer to understanding the intriguing factors behind the unusual qualities of BM3, a lot more questions are raised such as:

❖ Is there any other evidence confirming that BM3 is in fact, predominantly dimeric in nature?
❖ How are the monomers arranged within the dimer for efficient electron transfer?
❖ What is the nature of interaction within and between these dimers with relation to BM3's diverse functions?
❖ What is the shape of the dimer?
❖ Are the domains also dimerized?
❖ Is electrostatics fully or partially responsible for redox partner recognition in BM3?

In attempt to answer these questions, it is pertinent to characterize the weak interactions in the BM3 system. In the next section, we review weak protein-protein interactions in cytochrome P450 systems.

1.3 WEAK INTERACTIONS IN CYTOCHROME P450 SYSTEMS

Protein-protein interactions (PPIs) are fundamental to the understanding of various biological processes such as protein folding, signal transduction and electron transfer, and in various biotechnological applications, some of which include drug discovery and therapeutic protein formulation and processing (*214-218*). Moreover, aberrant protein interactions can result in several diseases such as Alzheimer's, sickle cell anemia, familial amyloidotic polyneuropathy, the spongiform encephalopathies, familial

Mediterranean fever, and some forms of rheumatoid arthritis (*13*). Thus, there is a basic need for high-throughput technologies to reveal and measure PPIs and their networks.

Based on the nature of complexes formed, PPIs can be grouped into homo/hetero-oligomeric, obligate/non-obligate and transient/permanent complexes (*12*). Transient complexes could be further classified into strong and weak complexes with the dissociation constants (K_d) of the former in the nanomolar (nM) range and the latter, in the micromolar (µM) range. This study is focussed on characterising the weak interactions (µM range) in cytochromes P450 systems using flavocytochrome P450 BM3 as a model. Characterization of weak PPIs has lagged behind those of strong PPIs for one main reason: lack of structural information for the complexes (due to the high dissociation constant) because complexes are not readily crystallized and, as a consequence, high-resolution models from X-ray diffraction studies do not exist.

This section briefly reviews methods that have been used to elucidate weak PPIs and summarizes the factors that govern these interactions, and the effects of ionic strength on protein interactions. There are already excellent reviews on transient (*10, 219*) and ultra-weak (*220*) PPIs (transient PPIs could have dissociation constants in the µM or nM range while ultra-weak PPIs have dissociation constants in the mM range), which discuss the pros and cons of the various techniques employed in detecting these interactions. Further, the proteomic tools used in measuring transient interactions in metalloproteins (a class of proteins to which CYPs belong) have been reviewed (*221*). Some of the techniques used for detecting weak PPIs are summarized in the following section.

1.3.1 Available Methods for Studying Weak PPIs

In the last decade, the interest in characterizing weak PPIs has grown, especially for those with biological significance. Consequently, some of the methods developed for studying weak interactions are modifications of available techniques for studying strong PPIs. Some of these are discussed in the next sections.

1.3.1.1 Nuclear Magnetic Resonance (NMR)-based approaches

Here, nuclei of the target protein are isotopically labeled and after applying a magnetic field, the nuclei resonate at a particular frequency. The electrons shield the nucleus from these applied forces and, as a result, a larger magnetic field is required. Environmental

changes such as salt, pH and temperature change this shielding effect and induce a chemical shift. These shifts are reflected as cross peaks from which the dissociation constants are deduced. Excellent reviews on this technique detail the various approaches employed (*1, 222-224*).

Recently, combining the basic NMR technique with residual dipolar couplings (RDCs) or measurement of ^{15}N spin relaxation rates from the bound form of both interacting proteins (*225, 226*) has been shown to significantly improve the results. One set-back of using NMR *in vivo* to characterize weak PPIs is the issue of crowding as weak interactions of proteins with cytoplasmic components can affect their NMR detectability (*227*).

1.3.1.2 *Electron Paramagnetic Resonance (EPR)-based and other spectroscopic approaches*

Here, the principle is quite similar to NMR, the basic difference being that the electron spin rather than the nuclear spin is examined when a magnetic field is applied. The common types of EPR used in studying weak PPIs include double electron-electron resonance (DEER) used to measure the distance between labelled paramagnetic centres. The term ELDOR (electron-electron double resonance) is another acronym for the same method, which is often used to measure distances between spin-labelled biological molecules.

The technique of fluorescence resonance energy transfer (FRET, also known as Förster resonance energy transfer) can also be used to explore weak protein-protein interactions. This method is used to measure the energy transfer or distance between fluorophores, which may be non-covalently bound to the proteins, or intrinsic fluorophores such as tryptophan residues. FRET is ideal for monitoring transient interactions using suitable encodable fluorescent proteins (*228*). Further, single molecule FRET (smFRET) is an effective method for studying strong PPIs, but cannot be applied to the study of weak interactions because of the requirement for low detection volumes. At detection volumes of $\sim 10^{-16}$ –to- 10^{-15} L, the lowest concentration range that is guaranteed to contain no more than one fluorophore on average is the nanomolar range. Strong PPIs can be formed at nanomolar concentrations but for weak complexes to be formed, one requires higher concentrations (micromolar range) which will invariably require larger detection volumes. Recent advances have shown that with the use of nanovesicle

trapping, the effective detection volume can be reduced significantly to ~10^{-19} –to- 10^{-21} L, allowing the study of high concentration samples using smFRET (*229*). Some major setbacks of FRET include large noise signals and high sensitivity to the distance between the labelled centres (*230, 231*).

Another spectroscopic technique introduced recently is the self-interaction nanoparticle spectroscopy (SINS). Here, the samples are adsorbed on the surface of gold nanoparticles forming protein-gold conjugates (PGCs). Since the optical properties of these gold nanoparticles are sensitive to inter-particle separation distance, it is possible to monitor the spectroscopic properties of these PGCs to determine the association strength. The observed variation in optical properties of the PGC is characterized as plasmon shift which was demonstrated to correlate with non-specific PPIs for bovine serum albumin (BSA) and ovalbumin (*232*). One of the limitations of the SINS technique is that the affinity of the proteins for the nanoparticles is sensitive to the sequence and structure of the protein. This limitation can be overcome by coating the nanoparticles with avidin (*233*).

1.3.1.3 Small Angle Neutron/X-ray Scattering (SANS/SAXS) and Static Light Scattering (SLS)

In these techniques, incident light radiation is elastically scattered by particles in solution, and the resulting scattering pattern is analysed for the required information. The major difference between SANS, SAXS and SLS is in the type of radiation employed. In each case, the second osmotic virial coefficient (SVC) can be derived from various scattering equations. Measurement of SVC from SANS and SAXS have been reviewed (*234, 235*) and only measurement of SVC from SLS will be discussed in this section.

In the past, SLS has been predominantly used for measuring weak non-specific protein-protein attraction as quantified in terms of the osmotic second virial coefficient. However, in some instances, weak non-specific association can be of a similar magnitude or only slightly weaker than weak specific protein-protein association. As a consequence, recent developments in this SLS technology have focused on measuring protein dissociation constants (as described below). The technology is now proven to be accurate for characterizing interactions with affinities ranging from nanomolar to micromolar.

SVC has proven to be a very powerful experimental tool for characterizing non-specific protein-protein interactions, which control the thermodynamic deviation of an aqueous protein solution from ideality. The SVC more exactly is an average of the protein pair potential of mean force (pmf), which is a solvent-mediated protein-protein interaction averaged over the relative separation and orientation of a pair of proteins. The pmf is given by a sum of all the non-covalent forces that govern weak protein-protein interaction. The SVC can be calculated from light scattering data using the equations below. The intensity of light scattered by the solution is used to calculate the excess Rayleigh ratio from which the SVC is derived. It is important to note that this equation only describes non-specific interactions. Other light scattering equations relating to specific PPIs are discussed in Section 2.4.4. For a solution containing only one protein component denoted by subscript A, the light scattering equation is given by

$$\frac{K^{\circ}c_T}{\bar{R}_{\theta}} = \frac{1}{M_w} + 2B_{AA}c \tag{1.1}$$

Equation 1.1: Light scattering equation for a solution containing one protein component, A.

And for a mixture of proteins A and B, the equation is given by

$$\frac{K^{\circ}c_T}{\bar{R}_{\theta}} = \frac{1}{M_w} + \frac{(2M_A^2 w_A^2 B_{AA} + 4M_A M_B w_A w_B B_{AB} + 2M_B^2 w_B^2 B_{BB})}{M_w^2}c_T \tag{1.2}$$

Equation 1.2: Light scattering equation for a solution containing a mixture of proteins A and B. *where M_w is the weight average molecular weight of all proteins in the solution, B_{AB} is the second virial coefficient between a protein of type A and type B; $\overline{R_{\theta}}$ is the excess Rayleigh ratio ($R_{\theta,sample} - R_{\theta,solvent}$); K° is an optical constant; c_T is total protein concentration; w_A is mass fraction of protein A; w_B is mass fraction of protein B; and M_A, M_B are molecular weights of proteins A and B respectively.*

Attri and Minton (*236*) developed a method to automate dilutions to generate a series of samples with varying protein concentrations to be used in the light scattering detector. This technique is an improvement over traditional light scattering techniques as a considerable amount of proteins and time is saved. An advancement of this technique is the composite gradient multi-angle laser light scattering (CG-MALS). This technique is suitable for measuring specific hetero- and self-association constants for proteins and can be used for analysis such as SVC, as well as kinetic studies (*237*). This is one of the

techniques used to characterize BM3 in this study; further details are given in the Materials and Methods section.

1.3.1.4 Self Interaction Chromatography (SIC)

Here, the protein of interest is immobilized on particles packed in a column and the retention time of the same protein injected on the column is measured (*238*). In this case, the retention time of the protein in the mobile phase is determined from the averaged interaction with the stationary phase. These interactions can be quantified in terms of the second osmotic virial coefficient, which is derived from the retention factor, the amount of protein immobilized per unit area and the phase ratio. The downside of this method is that immobilizing the protein can lead to partial unfolding or denaturation, which will indirectly alter the protein-protein interaction. In addition, a protein in the mobile phase can interact with multiple immobilized proteins at the same time so that the measurement is not strictly related to a two-body interaction.

1.3.1.5 Size Exclusion Chromatography (SEC)

Size exclusion chromatography can also be used for quantifying protein-protein interactions. In this case, weak protein-protein interactions lead to a larger effective size of the protein and a shorter elution time. In this approach, the second osmotic virial coefficient is estimated from analysis of the concentration dependence of the chromatographic partition coefficient (*239, 240*). SEC is, however, prone to error due to the inter-detector delay volume and inter-detector band broadening within the two detectors (*241*).

Other methods for quantifying weak PPIs include analytical ultracentrifugation (AUC) which is a method of choice for characterizing weak specific PPIs or for measuring K_d values (*242*) , paramagnetic relaxation enhancement (PRE) which involves labelling (*243, 244*), bimolecular fluorescence complementation (BiFC) involving the use of yellow fluorescent proteins (YFP, (*245*)), and various cross-linking techniques (*11, 246, 247*).

A closer look at the techniques presented above indicates that each method is expensive in terms of time and protein. The most efficient approach is SIC which is rather complicated because the second osmotic virial coefficient depends weakly on the injected protein concentration, injection volume, and the protein partition coefficient.

Thus this method cannot be used to absolutely quantify the osmotic virial coefficient, and only trends in this parameter can be accurately determined.

1.3.2 Forces that Govern Weak PPIs

Interfaces of 315 protein data bank (PDB) entries of proteins demonstrated to be homodimeric both in solution and crystal were studied recently (*248*). Interfaces of 42 "weak" homodimers (dimers in equilibrium with the monomers, according to literature search) were studied in comparison to those of other homodimers, all determined from X-ray structures. Result showed that the interfaces of these "weak" homodimers are smaller (by a factor of 2.4 on the average), highly conserved, and loosely packed in comparison to the rest of the homodimers. Here, we highlight forces that influence protein interactions in solution, as follows:

1.3.2.1 Electrostatic interactions

These are interactions between charged groups and/or polar residues which can be repulsive when occurring between similarly charged groups or attractive between oppositely charged groups. Interactions between patches of opposite charge have been implicated as a factor in accelerating the rate of complex formation and defining the lifetime of complexes (*249*). Electrostatic interactions are almost always weakened when increasing ionic strength due to decreasing the screening length.

1.3.2.2 Hydrophobic interactions

Attractive forces, commonly referred to as hydrophobic interactions, occur between non-polar regions of amino acids when dissolved in water. The driving force for the attraction is to reduce the exposed non-polar surface exposed to water (*250*). Hydrophobic interactions are highly selective (*251*) and their role in biological processes, as well as their importance as a process engineering tool, cannot be underestimated.

1.3.2.3 Hydrogen bonding

These are highly directional bonds whose classification (covalent or non-covalent) depends on the interacting molecules. In this context, hydrogen bonds can be considered as non-covalent, directional interactions with higher bond energies than most other non-

covalent interactions. Moreover, hydrogen bonds between protein molecules are more favourable than those made between protein polar groups and water. The number of hydrogen bonds is proportional to the subunit interfacial area (*249*).

1.3.2.4 Steric and Van der Waals forces

Steric forces are excluded volume interactions that are repulsive and prevent molecular surfaces overlapping with each other as a consequence of the Pauli exclusion principle. These are balanced by attractive Van der Waals forces that result from attraction between transient dipoles usually induced by rapid movements of electrons (*252*). These interactions fall off rapidly with separation distance r ($V \sim 1/r^6$) where V is the interaction potential. As a result the interacting distances are usually short (between 3 and 4 Å). Although the resulting interactions are significantly weak, they are more numerous than any other interaction and hence contribute significantly to the binding energy of the association.

The above-mentioned forces are non-covalent interactions that are continuously forming and dissociating during weak interactions between proteins. The energetics are inferred from equilibrium binding and kinetic measurements (*253*) and the forces exert influence on both specific (mostly electrostatic) and non-specific (mostly hydrophobic and Van der Waals) interactions (*254*). Hydrophobic interactions are the major forces that drive PPIs, while the other forces confer interfacial specificity. Moreover, these forces can be used as a basis for classifying PPIs. For instance, it has been observed that obligate complexes tend to be more hydrophobic than non-obligate complexes (*255*), and that they have high steric complementarity (*249*).

1.3.3 Effects of Ionic Strength on Weak PPIs

Association rates and binding affinities of proteins are greatly influenced by solution conditions such as temperature, pH, and salt concentrations. Thus, a general understanding of the basic effects of these parameters on protein interactions as inferred from a combination of modelling and biophysical techniques is quite necessary. In addition, determining how the behaviour depends on salt concentration or pH can give insight into the origin of the interactions especially with regards to repulsive and electrostatic forces described above as pH controls the charge distribution on the protein and ionic strength determines the range; increasing ionic strength screens Coulombic

forces. In this study, we have examined the effects of salt concentration to probe electrostatic interactions in the BM3 system.

Studies on protein solubility reveal that the effects of salt could be classified according to two distinct effects on non-specific PPIs, salting-out and salting-in (*256*). Salting-out occurs at high salt concentrations due to unfavourable interactions between the salt ions and the protein residues. One possible reason given for this behaviour is that the salt ions, when at a high concentration, sequester all the water molecules available for hydrogen bonding, thus preventing proteins from forming favourable hydrogen bonding patterns with the water molecules. This results in an effective intramolecular attraction between the protein molecules, which is greatest for non-polar groups. As a consequence, salting-out can be considered as an enhanced hydrophobic interaction. In contrast, the salting-in region has been attributed to favourable interactions between the salt ions and the charged groups on the protein surface. These favourable interactions are linked to an effective repulsion between protein molecules, which is enhanced with increasing the net charge on the protein. Increasing the ionic strength weakens this effect by reducing the range of the interaction. Alternatively, attractive electrostatic interactions between proteins have been observed in solutions with pH near to the pI of the protein, which is linked to isoelectric precipitation. The attraction originates from patches of opposite charge on protein surfaces.

With regards to specific PPIs, increasing the ionic strength has been observed to increase the attraction (*238, 257-259*). On the other hand, similar increases in salt concentration resulted in the reduction of the association rate and free energy of charging protein molecules [34], as well as a reduction in the number of ionization state changes that accompany complex formation during protein interactions (*260*). Detailed analyses of the effects of ionic strength on interactions in cytochrome P450 enzymes have been conducted (*261-263*). Results show that, in some cases, increase in ionic strength results in attractive interactions and enhanced activity; while in other cases salt-induced repulsive interactions were observed. The various mechanisms by which these proteins interact can thus be elucidated by the ionic strength dependence of the interactions. Depending on the type of protein the effect of salt could be explained by one of the following ways

❖ Hydrophobic residues do not like salt. For proteins whose mechanism of interaction is mediated by hydrophobic contacts, the protein molecules could

react to high salt concentrations by changing the conformation to hide their hydrophobic residues, resulting in less favourable interactions between those proteins. Alternatively, if the proteins are unable to bury their hydrophobic groups, increasing salt concentration could enhance the hydrophobic attraction between proteins. These effects are more significant and detectable at salt concentrations greater than 0.5 M.

❖ For proteins whose interactions are predominantly of electrostatic (long range) origin, the overall effect of increasing salt concentration is to make the interactions less attractive. In other words these proteins usually recognize each other through the patches of opposite charge. Increasing ionic strength reduces the range of the interaction by screening effects.

❖ For proteins that are natively fused together, the effect of salts differs when these proteins are taken apart. This is because distances within the fusion protein are sometimes short, meaning the interaction is short ranged. As a result, there is a possibility that the two domains taken apart have the same charge and do not depend on electrostatics for their interactions. If, however, these domains have similar charges, then the net electrostatic interaction is expected to be unfavourable, and the repulsion will be reduced by adding salt.

1.3.4 Weak PPIs in Cytochromes P450

The interaction of cytochromes P450 with their redox partners is essential for their function. As discussed in section 1.1, some CYPs form heterodimers with their reductases to be functional. As a result, an understanding of self-association in CYPs and hetero-association between cytochromes P450 and their redox partners is imperative. With the exception of the fusion CYPs, electron transfer between CYPs and their redox partners requires forming attractive non-covalent interaction which can originate from various factors, although the general consensus seems to indicate a significant role of electrostatics (*264*).

By necessity, the interactions in CYP systems must be weak to allow for efficient electron transfer. Characterizing interactions in CYPs has not gained much attention most likely due to the lack of optimized methods for studying weak PPIs. A literature search has shown that most of the techniques highlighted above have been applied to the study of protein-ligand interactions, but rarely to measure dissociation constants of

weak protein interactions. Very recently, a review of interactions in CYPs leading to oligomerization and highlighting the techniques used and the functional relevance of the oligomers has been published (*265*).

In the last decade, an amount of research has recently developed new methods for measuring PPIs in cytochromes P450 as summarized below:

❖ The most applied techniques to the study of weak PPIs in cytochrome P450 systems are NMR and cross-linking/mass spectrometry.

❖ The relevance of solid-state NMR in structural and interaction studies of full length enzymes that have proven difficult to crystallize, has been discussed using P450, cytochrome b_5 and their reductases as models (*266*).

❖ NMR studies indicate BM3 heme domain-flavodoxin interactions as transient, relatively strong and mediated by a mixture of electrostatic and hydrophobic interactions (*267*).

❖ NMR and SAXS were used to determine that domain motion within CPR is essential for electron transfer. Studies identified a few residues on the FMN domain that must interact with the rest of the protein (*268*).

❖ The interaction sites of CYP2B4 and CYP2B6 formed with their redox partner NADPH:CPR have been identified using a combination of cross-linking and mass spectrometry (*269, 270*).

❖ Further, cross-linking experiments confirmed dimerization of native CYP2C8 in natural membranes, and the residues involved in the dimerization interface were identified (*271*).

❖ A combination of cross-linking, isotope labelling and mass spectrometry was used to identify the interaction surfaces formed between CYP2E1 and the redox partner, cytochrome b_5 (*264*).

❖ FRET and BiFC (bimolecular fluorescence complementation) were used to demonstrate that CYP2C2 self-interacts to form oligomers *in vivo*. Further, weak interactions between CYP2C2 and CYP2E1 were examined as were the interactions between these CYPs and their redox partner, CPR (*272, 273*).

❖ Similarly, FRET was used to investigate the oligomerization of CYP17 and CYP19, both individually and with CPR *in vivo*. Results show that both steroidogenic CYPs homodimerize and also that each CYP heterodimerizes with CPR (*274*).

❖ Using a combination of CD and NMR spectroscopy, a new interaction region between CYP11A1 and its redox partner, adrenodoxin reductase was identified (*275*).

So far, studies on weak PPIs in cytochrome P450 systems have focused on identification of oligomeric states, or of interacting surfaces between separate partners or within an artificial fusion/chimeric protein. There is no report in the literature discussing weak interactions involved in natural fusion proteins. In this work, some of the techniques mentioned in section 1.3.1 are applied to the study of weak interactions in cytochrome P450 systems using the naturally fused flavocytochrome P450 BM3 as the model enzyme. This is the first report examining weak interactions in the cytochrome P450 superfamily. A major aim of the project will be the use of the aforementioned techniques, along with other spectroscopic and hydrodynamic methods, to probe the overall structure of the P450 BM3 dimer and in attempts to provide an accurate molecular model that satisfies the constraints that relate to requirement for inter-monomer electron transfer. Measurements will not only be used for probing the ionic strength dependence of the weak dimerization between monomers of the intact enzyme, but will also be used to study the behaviour of individual domains in order to further identify what surfaces are responsible for the dimerization.

Analysis of Weak Interactions in P450 systems

CHAPTER 2

Materials and Methods

CHAPTER TWO: MATERIALS AND METHODS

2.0 INTRODUCTION

This chapter is divided into four sections. The first section gives general information on materials used in these studies including composition of buffers, columns and gels used. The second section details the procedures used in the preparation of all enzymes used in this study, while the third section gives the various methods employed in substrate binding and activity studies of the enzyme. In the fourth section, the various biophysical techniques used in the characterization of weak protein-protein interactions in flavocytochrome P450 BM3 are discussed.

2.1 GENERAL MATERIALS

2.1.1 Growth and Expression Media

Luria Bertani (LB) and Terrific Broth (TB) media were purchased from ForMedium^{TM} (Norfolk, UK). The solid and liquid media were prepared as described below and sterilized by autoclaving at 121 ℃ before use. The recipes given here are for 1 L solutions. However, this was scaled up or down to the required volume at the given time.

LB agar plates: 40 g of premixed LB agar powder (10 g tryptone, 5 g yeast extract, 10 g NaCl and 15 g agar) were dissolved in 1 L de-ionized distilled water and sterilized by autoclaving. The solution was allowed to cool down slightly (while slowly stirring) and 2 mL of 50 mg/mL carbenicillin (working concentration - 100 µg/mL) stock was added to the solution under sterile conditions and thoroughly mixed. Approximately 15 mL of the mixture was then poured into agar plates, allowed to cool and stored in a refrigerator at 4 ℃ until use.

LB medium: This was prepared by weighing 25 g of premixed powder (containing 10 g tryptone, 5 g yeast extract and 10 g NaCl) and dissolving in 1 L de-ionized distilled water. The solution was sterilized before autoclaving and 1 mL of 50 mg/mL carbenicillin (working concentration - 50 µg/mL) was added to the medium just before inoculation of culture.

TB medium: 36 g of premixed TB powder (containing 12 g tryptone and 26 g yeast extract) and 4 mL glycerol (0.4% v/v) was dissolved in 900 mL de-ionized water and sterilized by autoclaving. The volume was adjusted to 1 L by the addition of 100 mL of filter-sterilized potassium phosphate solution (containing 0.17 M KH_2PO_4 and 0.72 M K_2HPO_4). 1 mL of 50 mg/mL ampicillin (working concentration - 50 µg/mL) was added to the mixture just before culture inoculation.

SOC medium: Super optimal broth with catabolite repression (SOC) medium is a very rich medium used for growing transformed competent/supercompetent cells. It contains 0.5% yeast extract, 2% tryptone, 10 mM NaCl, 2.5 mM KCl, 10 mM $MgCl_2$, 10 mM $MgSO_4$ and 20 mM glucose at pH 7.0.

2.1.2 Culture Reagents

Reagents used in the entire process of cell culture are listed in Table 2.1. These reagents were filter sterilized before use.

Table 2.1: Source, stock concentrations, solvents and working concentrations of reagents used for E. coli cell culture

Reagents	Source	Stock Concentration	Solvent	Working Concentration
Carbenicillin	ForMedium	50 mg/mL	De-ionized water	50-100 µg/mL
Ampicillin	ForMedium	50 mg/mL	De-ionized water	50 µg/mL
Tetracycline	Sigma	5 mg/mL	Ethanol	12.5 µg/mL
IPTG	Sigma	600 mM	De-ionized water	600 µM

2.1.3 Buffers

The composition of all buffers used in this study is listed in Table 2.2. All buffers were filter-sterilized before use. All chemical components for the buffers were obtained from Sigma. For all Tris-based buffers, the pH was adjusted by addition of hydrochloric acid (HCl) to the mixture. 2-(N-morpholino) ethanesulfonic acid (MES)-based buffer was adjusted to the desired pH using sodium hydroxide (NaOH). For all potassium phosphate buffer desired concentrations were prepared for KH_2PO_4 (dibasic; pH ~ 4.4) and K_2HPO_4 (monobasic; pH ~8.0) separately. The desired pH was reached by gradually adding the dibasic solution to the monobasic.

Table 2.2: Composition of buffers used in this study

Buffer ID	Composition
A	50 mM Tris, 1 mM EDTA, pH 7.2
B	50 mM Tris, 1 mM EDTA, 0.5 M KCl pH 7.2
C	25 mM KPi, pH 6.5
D	50 mM Tris, 1 mM EDTA, pH 7.2, 50 % glycerol
E	100 mM KPi, pH 7.0
F	50 mM KPi, pH 7.0
G	5 mM KPi, pH 7.0
H	50 mM KPi, 0.1 M KCl, pH 7.0
I	50 mM MES 0.2 M NaCl, pH 7.0
J	0.1 M Triethanolamine, pH 8.0
K	0.1 M Tris, pH 8.5

2.1.4 Chromatography Columns

The different columns used in this study are listed in Table 2.3. The ceramic hydroxyapatite column (and matrix) was obtained from Bio-Rad (Hemel Hempstead, UK) while the other columns (and matrices) were purchased from GE Healthcare (Herts, UK).

Table 2.3: Chromatography methods and resins used in this study

Column ID	Chromatography Type	Matrix	Internal Diameter (mM)	Bed Volume (mL)
DEAE-Sepharose Fast Flow	Weak anion exchange	Diethylaminoethyl (DEAE)-cellulose	50	104
Q-Sepharose Fast Flow	Strong anion exchange	Quaternary amine (Q)-Sepharose	26	50
HA	Affinity chromatography	Ceramic hydroxyapatite (HA)	26	30
S-200 10/300 GL	Gel filtration	Cross-linked agarose and dextran	10	24
PD-10	Desalting/Gel filtration	Sephadex G-25	10	8.3

2.1.5 Analytical Gel Electrophoresis

2.1.5.1 Agarose Gel Electrophoresis

After the purification of plasmid DNA using a QIAprep Spin mini-prep kit, the DNA samples were resolved using 0.8% agarose gel electrophoresis to visualize the presence, purity and approximate concentration of the samples. The stages are as follows:

Casting the gel: 25 mL of 0.8% agarose gel was prepared by weighing 0.2 g of agarose powder into a Duran glass bottle and adding 25 mL of 1X TAE (containing 40 mM Tris base, 20 mM acetic acid and 1 mM EDTA) buffer. The mixture was heated in a microwave oven for short intervals with mixing until the agarose dissolved. The sample was allowed to cool slightly and 3 µM ethidium bromide was added to the mixture, following which it was poured into the casting tray and allowed to set. The comb and spacers were removed and the tray containing the gel was placed in the electrophoretic chamber pre-filled with 1 X TAE buffer.

Sample preparation: The sample solutions contained 5 µL DNA (typically ~ 1µg) sample and 2 µL 6 X loading dye made up to volume (12 µL) by adding 5 µL deionized water. The standard solution was prepared by mixing 1 µL of 1 kb DNA ladder (NEB, Herts, UK) with 2 µL 6 X loading dye and the volume was adjusted to 12 µL with deionized water.

Running the gel: The prepared solutions were loaded into the wells and the gels run using a sub-cell GT system (BioRad, Herts, UK) at 80 mV X 130 mA until the DNA migrated a sufficient distance away from the wells.
The DNA bands were visualized using an ultraviolet transilluminator.

2.1.5.2 Sodium Dodecyl Sulfate Polyacrylamide Gel Electrophoresis (SDS-PAGE)

12% SDS-PAGE gels were used to visualize the expression and purity of the enzymes while 6% and 10% SDS-PAGE gels were used to check for cross-linking in full length BM3 enzymes and the P450/reductase domains, respectively. Further pre-cast 4-12 % horizontal Gebagel gels purchased from Generon Ltd (Berks, UK) were also used to check for the extent of cross-linking in full length BM3 enzyme. The composition of the 6, 10, and 12% resolution and 5% stacking gels were as shown in Table 2.4.For both resolution and stacking gels, the polymerizing solutions (freshly prepared 10% w/v ammonium persulphate [APS] and 0.1% v/v TEMED) were added just before pouring into the gel plates. The manually prepared gels were run in 1 X running buffer (containing 25 mM Tris, 192 mM glycine and 0.1% w/v SDS) using a Mini-Protean III vertical gel electrophoresis system at 180 volts for 1 hour, while the precast gels were run at 160 volts for 1 hour. Samples were prepared in 6 X sample buffer (containing 10% w/v SDS, 10 mM DTT, 20% w/v glycerol, 0.2 M Tris, 0.05% w/v bromophenol blue). Gels were stained using Coomassie Blue for 5-10 minutes and the gels destained

with de-ionized water. The resulting protein and molecular weight marker bands were visualized using a white light transilluminator.

Table 2.4: Composition of SDS-PAGE gels used in this study

10 mL RESOLUTION GELS			
Composition	**6% (mL)**	**10% (mL)**	**12% (mL)**
Sterile Water	5.3	4.3	3.3
30% (w/v) Acrylamide Mix	2.0	3.0	4.0
1.5 M Tris, pH 8.8	2.5	2.5	2.5
10% (w/v) SDS	0.1	0.1	0.1
10% (w/v) Ammonium persulphate (APS)	0.1	0.1	0.1
TEMED	0.008	0.008	0.008
3 mL STACKING GELS			
Composition	**5% (mL)**		
Sterile Water	2.1		
30% (w/v) Acrylamide Mix	0.5		
1.0 M Tris, pH 8.8	0.38		
10% (w/v) SDS	0.03		
10% (w/v) Ammonium persulphate (APS)	0.03		
TEMED	0.003		

2.1.6 Transformation of Plasmid DNA

The plasmids pBM25 (based on the vector pUC118) and pBM20 (based on vector pUC119) were freshly transformed into *E. coli* TG1 cells for the expression of full length P450 BM3 enzyme and the P450 domain respectively (*7, 178*), while plasmid P450 BMR/pET-11d (based on vector pET11d) was transformed into *E. coli* BL21 (DE3) cells for expression of the reductase domain (*157*). For plasmid preparation, the desired plasmid was transformed into the tetracycline resistant *E. coli* strain, XL1 blue for the pBM20 and 25 constructs. However, supercompetent XL1 blue cells were used for plasmid preparation for the reductase domain construct P450 BMR/pET-11d.

2.1.6.1 Competent cell transformation

Prior to transformation, a single colony of the required strain was picked from a LB agar plate and inoculated in 5 mL sterile LB medium (containing 12.5 µg/mL of tetracycline) and incubated at 37 ºC overnight with shaking in an orbital incubator. 100 µL of the overnight sample was then sub-cultured in 5 mL LB medium as done previously, and the sample incubated as before for 5 hours. A 1 mL aliquot of the fresh culture was pipetted into a 1.5 mL microtube (Sarstedt, Leicester, UK) and centrifuged at 13,000 RPM using a benchtop centrifuge. The supernatant was discarded and the

pellet was resuspended in 0.5 mL of ice cold 50 mM $CaCl_2$. The cells were re-pelleted and resuspended as above. The suspension was then incubated on ice for an hour after which 1 µL (typically containing ~1 µg of DNA) of the desired plasmid was added to the suspension and incubation done for a further hour. The mixture was heat-shocked at 42 ℃ for 45 seconds and re-incubated on ice for a further 2 minutes. 800 µL of sterile LB medium was then added to the mixture and it was incubated at 37 ℃ for 1 hour with shaking. The mixture was centrifuged under the same conditions as before and the supernatant was discarded, leaving about 100 µL for re-suspension of the pellet. The suspension was spread onto a LB agar plate containing antibiotic selective for the relevant plasmid (prepared as in section 2.1.1) and the plate incubated at 37 ℃ overnight.

2.1.6.2 Pre-prepared competent cell transformation

For transformation of competent cells obtained from commercial suppliers, 20 µL of competent cells (XL1 blue cells for plasmid preparations) were pipetted into a microtube and defrosted on ice.1 µL (typically containing ~1 µg of DNA) of the desired plasmid was added to the cells and the mixture incubated on ice for 5 minutes. The mixture was subsequently heat-shocked at 42 ℃ for 30 seconds and returned to ice for a further 2 minutes. 80 µL SOC medium was added to the microtube, and mixed by pipetting up and down. The mixture was spread onto a LB agar plate (prepared as in section 2.1.1) and the plate incubated at 37 ℃ overnight.

2.2 ENZYME PREPARATION

2.2.1 Plasmid Construction

The construction of plasmids used in this study was described previously (*7, 157, 178*). Plasmids pBM20, pBM25 and P450 BMR/pET-11d (Figure 2.1) were used for the expression of the BM3 P450 domain, full length enzyme and the reductase domain, respectively. While the expression of the original full length BM3 construct (pBM23) was under the control of the Bacillus promoter, the expression of the re-cloned full length BM3, BMP (heme domain) and BMR (reductase domain) constructs is regulated by IPTG (Isopropyl-beta-D-thiogalactopyranoside)-inducible lac/tac and T7 promoter systems, respectively. As shown *e.g.* in Figure 2.1C, the reductase domain plasmid (P450 BMR/pET-11d) contains an origin of replication, an ampicillin resistance gene

(β-lactamase), the target gene (BMR), a T7 promoter (not shown), a *lac* operator just downstream of the promoter (not shown) and a *lacI* gene which codes for the natural lac repressor (which prevents transcription). The T7 promoter is recognized by the T7 RNA polymerase encoded in the chromosome of the host cell and transcription of target gene is initiated. IPTG causes displacement of the repressor from the operator site in the plasmid (allowing transcription of the target reductase gene) and on the chromosome (allowing transcription of the T7 RNA polymerase) to facilitate concerted gene induction. In the BM3 and heme domain constructs, a similar induction process results in expression from the chromosomal *E. coli* RNA polymerase, and also involving the displacement of the lac repressor from its plasmid binding site. However, it was found that high levels of production of both the intact BM3 and the BMP domain were achieved without IPTG addition, likely as a consequence of the "leaky" gene expression on both plasmids.
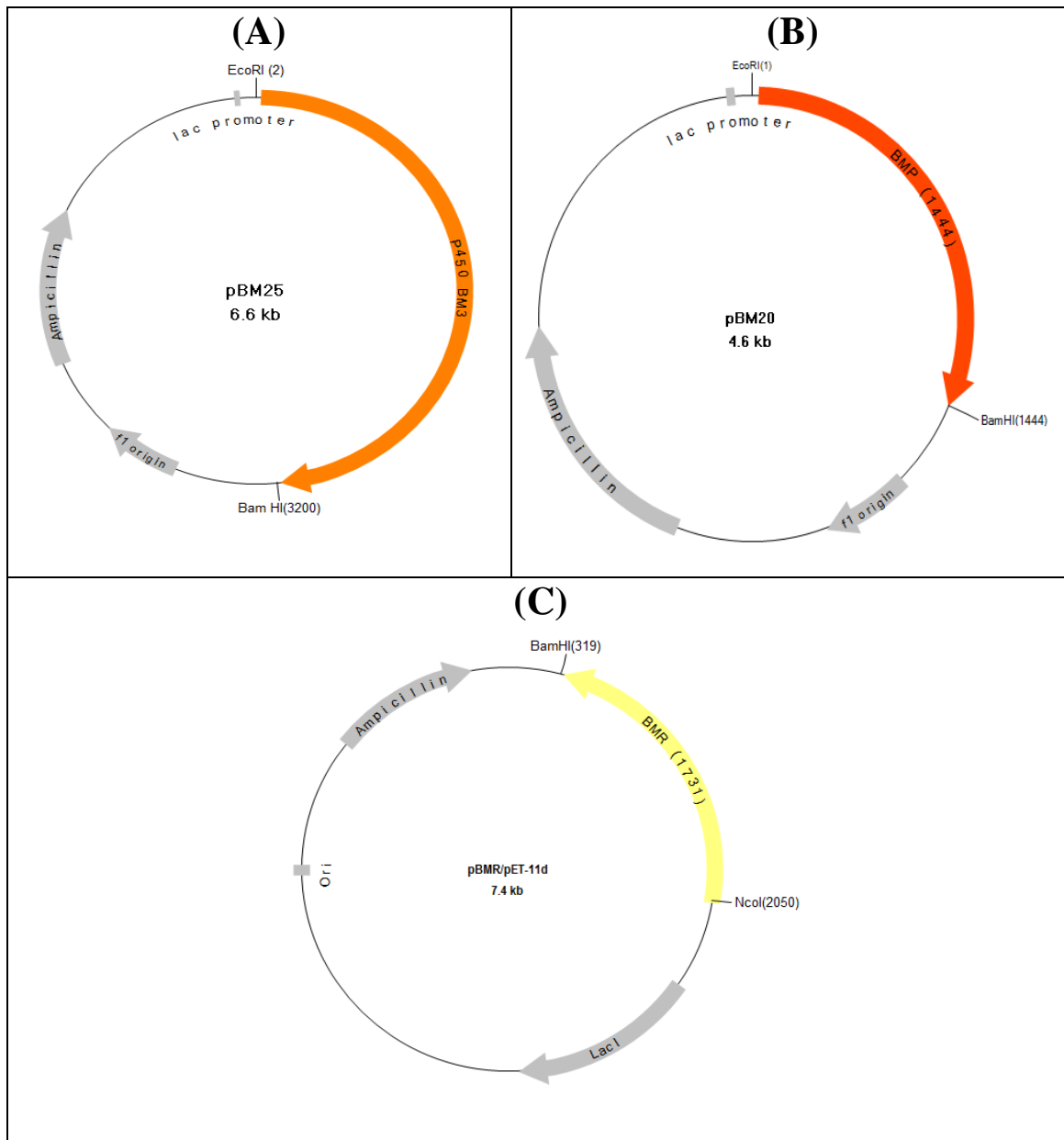
Figure 2.1: Plasmid vector maps for the full length (A), P450 domain (B) and reductase domain (C) of P450 BM3. *The plasmids for the full length BM3 (pBM25), its P450 domain (pBM20) and the reductase domain (pET-11d) are discussed in references (7), (178), and (157) respectively. The various restriction enzyme sites used for gene cloning are shown. All three plasmids have the ampicillin resistance region.*

2.2.2 Plasmid DNA Preparation and Purification

An *Escherichia coli* strain known to maintain a high plasmid copy number, XL1 Blue, was used for plasmid preparation. 1 µg plasmid was transformed into XL1 Blue cells, and the cells were plated on LB agar containing 100 µg/mL of carbenicillin, and incubated at 37 °C overnight. A colony of the transformed cells was picked and inoculated into 150 mL LB medium containing 50 µg/mL of carbencillin and incubated

at 37 °C with agitation overnight. The culture was divided into four portions; the cells were harvested and used for purification of large amounts of DNA using a QIAprep Spin Miniprep Kit from Qiagen (West Sussex, UK), scaled up to 37.5 mL volume. The stages include cell lysis to extract the DNA, precipitation of the chromosomal DNA, DNA binding to an ion-exchange spin column, washing the column to remove excess buffer and impurities, and finally eluting the plasmid DNA. The purified plasmid DNA, which was eluted in a concentrated form, was stored at -20 °C for further use. The four different preparations were analyzed by 0.8% agarose gel electrophoresis (with ethidium bromide staining) against known standards to visualize the purity and concentration of plasmid DNA prepared.

2.2.3 C773A Site-Directed Mutagenesis (Reductase Domain)

Amino acid substitution at the C773 position in the reductase domain (amino acid residues 473–1048 of full-length BM3 enzyme) was carried out using the QuikChange II site-directed mutagenesis kit (Stratagene). The oligonucleotide primers used were C773A Forward, 5'-CAATGGCTGCTAAAACGGTC<u>GCC</u>CCGCCGCATAAAGTAGAG-3' and C773A Reverse, 5'- CTCTACTTTATGCGGCGG<u>GGC</u>GACCGTTTTAGCAGCCATTG-3' (Eurofins MWG Operon, UK; mutated codon underlined). The PCR reaction mixture contained 125 ng primers; 5 µL of 10x P*fuUltra* buffer; 200 µM dNTPs; 2.5 units of P*fuUltra* polymerase and 5, 50 and 100 ng reductase plasmid as template (in different reactions), made up to 50 µL with distilled water. The PCR was carried out under the following conditions:

Pre-cycle denaturation:	1x	95 ºC, 30 seconds
Denaturation:	18x	95 ºC, 30 seconds
Annealing:	18x	55 ºC, 1 minute
Extension:	18x	68 ºC, 7 minutes
Post-cycle extension:	1x	68 ºC, 10 minutes

Following PCR, template DNA was degraded by the addition of 10 units of D*pn*I to the reaction mixture. The digestion reaction was then incubated at 37 ºC for 1 hour. 1 µL of the resulting mixture was transformed into supercompetent XL1-Blue cells and plated

on LB agar plates containing 100 ng/µL carbenicillin. 6 colonies were selected and subcultured into 5 mL LB medium, grown overnight at 37 ℃ and subsequently mini-prepped to harvest DNA (Qiagen; Section 2.2.2). DNA samples were sent to Geneservice (Nottingham, UK; Source Bioscience) for sequencing in both forward and reverse directions to confirm the presence of the desired mutations and check for the absence of unwanted mutations.

2.2.4 Overxpression and Purification of Full Length P450 BM3 Enzyme, the P450 and Reductase Domains and the Mutant Reductase Domain

For expression of the full length enzyme and the P450 domain, the plasmids pBM25 and pBM20, respectively, were transformed into the *E. coli* strain TG1. Expression of intact BM3 and the P450 domain was under the control of a lac promoter. The host strain used for overexpression of the reductase domain was BL21 (DE3). Expression of the reductase protein and mutant were under the control of an IPTG inducible T7 RNA polymerase/promoter system.

Transformant colonies picked from LB agar plates containing 100 µg/mL of carbencillin were first grown in a small scale (usually 250 mL conical flasks) in LB medium containing 50 µg/mL of carbencillin at 37 °C with agitation overnight. For the full length enzyme and the P450 domains, large scale cell cultures were grown in 2 L conical flasks containing 1 L of sterile terrific broth (TB) medium, 50 µg/mL of ampicillin, and inoculum (1% v/v) from small scale overnight cultures of the transformants. The cultures were grown at 37 °C with agitation at 200 rpm for approximately 38 hours. For the reductase domain and mutant, cultures from transformed overnight small scale cultures were inoculated into a 2 L conical flask containing 600 mL sterile LB medium with 50 µg/mL of ampicillin. The cultures were then incubated at 37 °C with shaking at 200 rpm until the OD at 600 nm reached 1.0. The cells were then induced with IPTG (up to a final concentration of 600 µM), the temperature decreased to 30 °C and growth was allowed to continue for another 12-15 hours. In all preparations, cells were harvested by centrifugation at 6,000 rpm for 10 min using a Beckman JLA 8.1 rotor at 4 °C. Cells were washed by resuspension in buffer A (50 mM Tris, 1 mM EDTA, pH 7.2) and re-centrifuged as before. Pellets were then stored at -20 °C until further use. All further handling of cells or enzyme preparations was conducted on ice or at 4 °C.

Cell pellets were thawed and resuspended in 3-4 volumes of buffer A containing the protease inhibitors benzamidine (hydrochloride salt) and PMSF (phenylmethylsulphonylfluoride), both at 1 mM. For the full length enzyme and the P450 domain, the resuspended cells were subjected to 10-15 pulses of ultrasonication on ice at maximum power for 5 seconds, with a 55 second delay between pulses using a Bandelin Sonopuls sonicator. For the wild type and mutant reductase domains, the resuspended cells were lysed by passage twice through a Thermo electron corporation French press cell disrupter at 1000 PSI and then transferred to the ultrasonicator, where maximum lysis was achieved after 5-7 pulses.

Cell lysates were centrifuged at 18,000 rpm using a Beckman JA 25.50 rotor for 15 min at 4 °C. The resulting supernatant was passed through two successive stages (0-30% and 30-60%) of ammonium sulphate precipitation. Ammonium sulphate was slowly added at 4 °C with stirring, and the supernatant was retained after the 30% ammonium sulphate cut and the pellet after the 60% cut. The precipitated material was separated by centrifugation at 18,000 rpm for 10 min after each cut. The 60% pellet was then resuspended in buffer A and dialysed against a large volume of buffer A for approximately 2 hours. The dialysis process was repeated 4-5 times with fresh buffer to ensure that the resulting enzyme preparation was effectively desalted.

For the full length enzyme and the P450 domain, the enzyme preparation was first loaded on a DEAE-Sepharose column with an internal diameter of 50 mm and a bed volume of 104 mL (GE Healthcare, Herts, UK) pre-equilibrated in buffer A. After washing with approximately 3 column volumes of buffer A, the proteins were eluted with a linear salt gradient of buffer A against elution buffer B (50 mM Tris, 1 mM EDTA, pH 7.2, 500 mM KCl). Fractions were checked for purity by measuring the heme absorbance at 418 nm for the heme domain/ full length BM3 and the total protein at 280 nm. The purity ratio was then calculated by dividing the resulting absorbance at 418 nm by that at 280 nm. The less pure fractions were stored frozen in glycerol for further purification, while the higher quality fractions ($A_{418}/A_{280} > 1.0$, for heme domain and $A_{418}/A_{280} > 0.15$ for full length BM3) were concentrated using a YM-30 Centriprep ultrafiltration device (Millipore). The concentrated protein was then set to dialyse again against buffer A before loading on to a Q-Sepharose column with an internal diameter of 26 mm and a bed volume of 50 mL. Samples were eluted against a salt linear

gradient (from 0 to 500 mM KCl in buffer B) and pure fractions were also selected based on co-factor absorbance to total protein absorbance ratios ($A_{418}/A_{280} > 1.2$ for heme domain and $A_{418}/A_{280} > 0.3$ for full length BM3).

Dialysis was conducted against buffer C (25 mM potassium phosphate [KPi] at pH 6.5) before loading proteins onto a hydroxyapatite column with an internal diameter of 26 mm and a bed volume of 30 mL (GE Healthcare). The proteins were eluted in a linear gradient (500 mL) of buffer C to 500 mM KPi at the same pH. The higher quality fractions at this stage ($A_{418}/A_{280} > 1.5$ for heme domain and $A_{418}/A_{280} > 0.55$ for full length BM3) were pooled.

The same procedure was used to purify the wild type and mutant reductase domains, but a column order of (i) DEAE, (ii) hydroxyapatite, with a final step of (iii) Q-Sepharose yielded pure proteins. The purity ratio was calculated by dividing the co-factor absorbance at 456 nm (arising from the oxidized FAD and FMN cofactors) by the total protein absorbance at 280 nm. Pure sample fractions after DEAE and Q-Sepharose column runs had purity ratios (A_{456}/A_{280}) > 0.04 and 0.08, respectively.

Final purity was assessed by SDS-PAGE and the resulting blood red (full length and P450 domain) and golden yellow (reductase domain) pure protein fractions were pooled, concentrated (to >500 μM) and dialysed in buffer D (50 mM Tris, 1 mM EDTA and 50 % [v/v] sterile glycerol, pH 7.2). These samples were then stored in small volumes using Eppendorfs at -80 °C until required. Purification tables were constructed using these data to quantify the protein yield.

Freshly purified FAD and FMN domains used for size exclusion chromatography with light scattering (SEC-MALLS) and small angle X-ray scattering (SAXS) experiments (see section 2.3.1) were obtained from Dr. Adrian Dunford (University of Manchester). Since the FAD domain is suspected to aggregate (via disulfide linkages) the enzyme was further purified using gel filtration (Superdex 200 10/300; GE Healthcare) just before use for SEC-MALLS and SAXS studies.

2.2.5 Determination of Protein Concentration

A bench-top Cary 50 UV-vis spectrophotometer (Varian) was used for measuring protein absorption and to enable estimation of protein concentrations. For the homogenous full length P450 BM3 and the P450 domain, the concentrations were

determined using the method of Omura and Sato (*276*). Spectra were collected for the ferric resting form of the enzymes, a few grains of sodium dithionite were added and the cuvette sealed to create an anaerobic environment, yielding the ferrous form. Finally, a ferrous CO adduct was generated by gently bubbling the sample with CO. A difference spectrum was generated by subtracting the spectrum for the dithionite reduced ferrous heme from that of the reduced-plus-CO adduct. Beer-Lambert's Law was used to determine the hemoprotein concentration, *c,* according to Equation 2.1

$$A = \varepsilon \text{ x } c \text{ x } L \tag{2.1}$$

Equation 2.1: Beer-Lambert's law for estimating protein concentration. *A is the measured absorbance, ε is the extinction coefficient (in units of $mM^{-1} \, cm^{-1}$) and L is the path length through the solution in cm. The cuvettes used in this experiment have a path length of 1 cm.*

The extinction coefficients used for the full length and P450 domains of BM3 were 105 and 95 $mM^{-1} \, cm^{-1}$ for the Soret absorption of the oxidized (low-spin) forms of these proteins at 418 nm. These coefficients were derived with respect to the concentrations of enzymes determined using the method of Omura and Sato (*276*), and by comparing the absorption spectra of the oxidized forms of the intact BM3 and P450 domain with those for their ferrous-CO complexes. For the reduced/CO complexes, the absorption difference between 450 and 490 nm was measured and a coefficient of $\Delta A_{450\text{-}490} = 91$ $mM^{-1} \, cm^{-1}$ was used for the difference between this wavelength pair in reduced/CO-bound and reduced forms of the enzymes. However, it should be noted that formation of an inactive (P420) CO complex can occur due to cysteine thiolate heme ligand protonation and that this may lead to underestimation of total P450 heme concentration by this method. For this reason, the extinction coefficients used for the oxidized enzymes were derived from studies in which the ferrous-CO complexes of intact BM3 and its heme domain were near-completely in the thiolate-bound (P450) form. The concentration of the reductase domain was calculated using an extinction coefficient of 21.2 $mM^{-1} \, cm^{-1}$ at 456 nm (*116*).

2.3 ACTIVITY STUDIES IN FLAVOCYTOCHROME P450 BM3

2.3.1 Materials

All items used in activity studies including lauric acid, arachidonic acid, imidazole, 4-phenylimidazole, NADPH, horse heart cytochrome *c* and potassium ferricyanide (FeCN), but with the exception of N-palmitoylglycine (NPG), were purchased from Sigma-Aldrich and used without further purification. NPG was synthesized from N-hydroxysuccinimidyl fatty acid and glycine as described by Haines *et al.* (*113*).

2.3.2 Substrate/Ligand Binding and Steady State Analysis for Enzyme Activity

2.3.2.1 Substrate/Ligand Binding to full length BM3 and the P450 Domain

The affinity of different substrates and inhibitors for the enzyme was measured at equilibrium by optical titration. For ligand binding to the P450 domain, substrates used included lauric acid and NPG, while the inhibitors were imidazole and 4-phenylimidazole (4-PI), obtained from Sigma-Aldrich and used without further purification. Substrate binding to the full length BM3 enzyme was studied using arachidonic acid. All ligand binding assays were carried out under aerobic conditions at 30 °C using a bench-top Cary 50 UV-vis spectrophotometer and a 1 cm pathlength cuvette. The final volume of the reaction mixture was 1000 µL containing ~5 µM proteins in assay buffer E (100 mM potassium phosphate buffer, pH 7.0). Ligands were titrated from the stock concentrations detailed in Table 2.5 in 0.1 µL aliquots, with spectral acquisition after each addition until no further shifts were observed. The stock concentrations, solvents and different concentration ranges for the substrates and inhibitors were as shown in Table 2.5.

Table 2.5: Ligands/substrates used for P450 optical binding assays. *The stock concentrations prepared in their respective solvents and the concentration ranges used in this study are shown.*

Ligand	Stock Concentration (mM)	Solvents Used	Concentration Range
lauric acid	50	Acidified Ethanol	0-1400 μM
N-palmitoylglycine	10	50 mM K$_2$CO$_3$	0-8 μM
imidazole	1000	Buffer E	0-20 mM
4-phenylimidazole	50	Buffer E	0-100 μM
arachidonic acid	33	Ethanol	0-25 μM

Absorbance difference spectra for data analysis were obtained by subtracting the absolute absorbance spectrum for the substrate-free form from that of the substrate/ligand-bound form of P450 enzymes. The resulting change in absorbance was plotted against the substrate concentration and fitted to either a quadratic or a hyperbolic ligand binding function (Equation 2.2 and 2.3) using Origin 7.0 (OriginLab, Northampton MA) to generate the dissociation constants (K_d values). All K_d values shown result from fitting of a single experimental data set. Standard errors associated with the data fitting are also given in the relevant result sections.

$$A = \{A_{max}/(2*E_t)\}*\{(S + E_t + K_d) - (S + E_t + K_d)^2 - (4*S*E_t)\}^{0.5} \tag{2.2}$$

Equation 2.2: Quadratic ligand binding function. *A and A_{max} are the observed absorbance and maximum absorbance respectively, S is the substrate concentration, E_t is the total enzyme concentration used and K_d is the dissociation constant of the enzyme-substrate/ligand complex.*

$$A = \frac{A_{max}[S]}{K_d + [S]} \tag{2.3}$$

Equation 2.3: Hyperbolic ligand binding function. *A and A_{max} are the observed absorbance and maximum absorbance respectively, [S] is the substrate concentration and K_d is the dissociation constant of the enzyme-substrate/ligand complex.*

2.3.2.2 Steady-State Kinetics of Full Length BM3 and Reductase Domain

The steady-state activity of the intact P450 BM3 enzyme was assayed via substrate-dependent NADPH oxidation with lauric acid as the fatty acid substrate. NADPH consumption was monitored by the change in UV-vis absorption at 340 nm using an extinction coefficient of 6.21 mM^{-1} cm^{-1} to follow the absorption decrease. The assay

was carried out at 30 °C in a reaction mixture containing 102 nM intact enzyme and lauric acid in buffer E, making up a final volume of 1000 μL. Reactions were initiated by the addition of 500 μM NADPH (saturating conditions) which was added last to avoid the reductive inactivation of the reductase domain (see section *1.2.4.2*). Lauric acid concentrations were varied from 0-500 μM.

Steady-state kinetics of NADPH-dependent reduction of artificial exogenous electron acceptors (cytochrome *c* and ferricyanide) by flavocytochrome P450 BM3 reductase (BMR) was determined. Stock solutions (1 mM each of cytochrome *c* and FeCN) were prepared in buffer E (Table 2.2). Steady state cytochrome *c* reductase activity was measured at a temperature of 30 °C and at a wavelength of 550 nm using an extinction coefficient of 22.64 mM^{-1} cm^{-1} for the reduced minus oxidized cytochrome *c* to follow the absorption increase on cytochrome *c* reduction. The final volume of the reaction mixture was 1000 μL containing 17 nM BMR, 500 μM NADPH (saturating conditions), and 0-50 μM cytochrome *c* in buffer E. For comparison purposes, the cytochrome *c* reductase activity of the full length enzyme was also determined under the same conditions with an enzyme concentration of 23 nM. The order of addition of reactants is also important, with NADPH added last to prevent any accumulation of FMN hydroquinone in the reductase domain, since rates of electron transfer between FMN semiquinone/FMN hydroquinone and cytochrome *c* may be different.

Similarly, steady-state FeCN reductase activity was measured at a temperature of 30 °C and at a wavelength of 420 nm using an extinction coefficient of 1.02 mM^{-1} cm^{-1} for the reduced minus oxidized FeCN absorption (absorbance decrease on FeCN reduction). Reactions were performed in buffer E containing 0.015 nM BMR, 500 μM NADPH (saturating conditions), and 0-600 μM FeCN, up to a final volume of 1000 μL. Once again, NADPH was added last to initiate the reaction.

Table 2.6: Stock concentrations of ligands and electron acceptors used in steady-state kinetics of full length BM3 and its reductase domains.

Substrate	Stock Concentration (mM)	Solvents Used	Concentration Range
NADPH	20	Buffer E	500 μM
lauric acid	50	Acidified ethanol	0-500 μM
ferricyanide	1	Buffer E	0-600 μM
cytochrome *c*	1	Buffer E	0-50 μM

For data analysis, the concentration of substrates reduced was calculated, using a form of Beer's law, from the change in sample absorbance with time and the extinction coefficient according to equation 2.4.

$$c = \frac{\Delta A}{\varepsilon \times L}$$

(2.4)

Equation 2.4: Beer's law for estimating sample concentration. *The parameters are defined as follows: c is the concentration of reduced substrate (mM), ΔA is the change in sample absorbance, ε is the accompanying extinction coefficient in $(mM^{-1} cm^{-1})$ and L is the path length, which is given as 1 cm.*

The rates (in units of min^{-1}) at which the enzyme reduced its substrates were then calculated by dividing the resulting rates of change of concentrations of the reduced substrates (mM min^{-1}) by the total enzyme concentration used per assay (mM). These observed rates for each reaction were plotted against the relevant concentrations of the substrates. Data were fitted using the Michaelis-Menten equation (Equation 2.5) to obtain the catalytic rate constants (k_{cat}) and Michaelis constant (K_m) for the reductase and intact enzymes with relevant substrates. Rate constants obtained are a representative of at least three separate measurements at each substrate concentration.

$$v = \frac{V_{max}[S]}{K_m + [S]} = \frac{k_{cat}[E_T][S]}{K_m + [S]}$$

(2.5)

Equation 2.5: The Michaelis-Menten equation. *The equation parameters are defined as follows: v is the observed initial enzyme velocity; V_{max} represents the maximum velocity; K_m is the Michaelis constant; k_{cat} is turnover number; and [S] and [E_T] represent the substrate and total enzyme concentrations respectively. The Michaelis constant measures the apparent affinity of the substrate for the enzyme (the substrate concentration at which enzyme rate is 0.5 x V_{max}) and, under steady state conditions, the Michaelis constant approximates the apparent dissociation constant of the enzyme-substrate complex.*

2.3.3 Stopped-Flow Analysis of Domain Interactions

Stopped-flow techniques were used to characterize weak interactions between the P450 and reductase domains of the P450 BM3 enzyme. All stopped-flow analyses of transient changes associated with binding of CO to the reduced heme iron were carried out using an Applied Photophysics SX.17 MV stopped-flow spectrophotometer under anaerobic

conditions at 25 °C. The sample handling units of the stopped-flow device was contained within a glove box (Belle Technology, Portesham, Dorset, U.K.) under a nitrogen atmosphere. All buffers were thoroughly filtered and deoxygenated by bubbling oxygen-free nitrogen through them, and then placed in the glove box overnight before use. Transient kinetics experiments were performed in carbon monoxide saturated buffer F (50 mM potassium phosphate, pH 7.0) containing a near-saturating concentration (88 µM) of arachidonic acid with varying concentrations (0-1 M) of KCl. Stopped-flow multiple wavelength studies were carried out using a photodiode array (PDA) detector and X-SCAN software (Applied Photophysics Ltd, Surrey, U.K.). In single wavelength studies, formation of the ferrous-CO adduct was measured at 450 nm.

Firstly, flavin-to-heme electron transfer in the full length enzyme was measured and spectra were collected over 200 milliseconds. Syringe A contained 5 µM BM3 while syringe B contained NADPH in excess (500 µM); both in CO-saturated buffer F containing 88 µM of arachidonic acid and with the ionic strength varied from 0 to 0.8 M KCl. Formation of the ferrous-CO adduct was measured at both 418 and 450 nm. Further, to ensure that the rate constants obtained from these studies are independent of flavin reduction rate constants, single wavelength studies of flavin reduction at the same conditions were performed and the flavin reduction was observed at 475 nM. The reactant composition in the stopped-flow syringes was the same as above, and spectra were collected over 50 milliseconds. In addition, a pH-dependence study was conducted under the same conditions in the absence of KCl with the pH varied from 6 to 8.

Secondly, flavin-to-heme electron transfer between the separate P450-BM3 domains was then measured at up to 50 (single wavelength) and up to 1000 (PDA) seconds in the presence and absence of dithiothreitol (DTT, 10 mM). In both cases, syringe A contained 5 µM each of the reductase and P450 domains while syringe B contained 500 µM of NADPH, both in CO-saturated buffer F with 88 µM arachidonic acid. Furthermore, the dependence of the observed rate on enzyme concentration was measured at 0.2 M KCl by fixing the concentration of the heme domain at 5 µM and varying the reductase concentration (from 0 to 20 µM) in buffer F.

Thirdly, the rate at which the ferrous-CO complex was formed in the absence of the reductase domain was measured up to 1000 seconds using the PDA system. Syringe A contained 10 µM P450 domain while syringe B contained NADPH in excess (500 µM), both in CO-saturated buffer F with 0.2 M KCl.

Analysis of both single and multiple wavelength stopped-flow data was carried out using both Applied Photophysics ProK software and Origin (OriginLab), both of which use non-linear regression least squares fitting procedures. Traces were fitted using a standard double-exponential function (Equation 2.6) to obtain estimates of the apparent rate constant (k_{obs1} and $_2$) for the formation of the CO-ferrous complex of the P450. The stopped-flow traces for CO complex formation could not be fitted accurately using a single exponential function but were fitted well using a double exponential function. These rate constants were plotted against the salt concentration to establish their dependence on ionic strength. The rate constants shown (for single wavelength studies) are representatives of at least three separate determinations at each condition.

$$A_t = \Delta A_1 e^{-k_{obs1}t} + \Delta A_2 e^{-k_{obs2}t} + A_f \tag{2.6}$$

Equation 2.6: Double exponential equation. *The parameters are defined as follows: A_t represents the observed amplitude at any time t; ΔA_1 and ΔA_2 are the amplitudes for first and second components of the reaction; k_{obs1} and k_{obs2} are the observed first order rate constants for the first and second reaction components; A_f represents the final value of the absorbance.*

2.4 BIOPHYSICAL STUDIES FOR WEAK PROTEIN-PROTEIN INTERACTIONS (PPIs) IN BM3

2.4.1 Size Exclusion Chromatography with Multi-Angle Laser Light Scattering (SEC-MALLS)

SEC-MALLS measurements were made using a size exclusion chromatography column (*SEC*; Superdex 200 10/300; GE Healthcare) in series with a Wyatt multi-angle laser light scattering (MALLS) Dawn Heleos-II detector and a Wyatt quasi-elastic light scattering (QELS) detector installed at the 13th position of the MALLS detectors (Wyatt Technology, Santa Barbara, CA). Samples with volumes of 200 or 500 µL were injected on the Superdex 200 10/300 GL column by a Dionex GS50 gradient pump (Dionex Corp, Sunnyvale, CA) using a mobile phase flow rate of 0.71 mL/min. Absorbance was measured using a Jasco UV 2077 plus visible spectrophotometer (Jasco Inc, Easton, MD). Protein concentration was also determined using an in-line Wyatt Optilab rEX refractometer (differential refractometer used to measure the difference in refractive

index of a protein solution and the pure solvent) with a value of *dn/dc* for the protein equal to 0.186 mL/g. Wyatt Astra 5.3.4.13 software was used for data collection and analysis to give the peak protein concentration, molecular weight and hydrodynamic radius (See Appendix A for theories and principles of SEC-MALLS). Buffer F was used for all SEC-MALLS experiments while the ionic strength was varied from 0 to 800 mM KCl. Prior to all measurements, each sample was purified using the same procedure described above to remove any aggregates. Injected sample concentration was varied between 0.1 and 2.5 mg/mL.

SEC-MALLS analysis was conducted for the full length enzyme (BM3) and the respective domains: heme domain (BMP), reductase domain (BMR), reductase mutant (C773A), the FMN domain, and the FAD domain. Further, the effect of fatty acid binding on BM3 self-interaction was evaluated in two different buffers G (5 mM KPi, pH 7.0) and H (50 mM KPi, 0.1 M KCl, pH 7.0). The purified BM3 was split into two fractions. The first fraction was subjected to SEC-MALLS analysis immediately without any further modifications. 50 µM NPG was added to the second fraction, the sample mixed and incubated at room temperature for one hour. The modified sample was then centrifuged and subjected to SEC-MALLS analysis as above.

Similarly, in order to determine whether the dimerization of the various domains of BM3 were caused by intermolecular disulfide bond formation, the BM3, BMR and FAD domains were further modified (reduced and alkylated). The samples were first run down the Superdex 200 10/300 GL column to remove any aggregates. The purified dimeric fractions were split into two. The first fraction was subjected to SEC-MALLS analysis immediately without any further modifications. 10 mM DTT was added to the second fraction, the sample was mixed and incubated at 37 °C for one hour. The sample was then cooled to room temperature, mixed with 50 mM iodoacetamide and incubated in the dark at room temperature for 30 minutes. The modified sample was then centrifuged and subjected to SEC-MALLS analysis as above.

2.4.2 Analytical UltraCentrifugation (AUC)

All AUC experiments were performed on an Optima XLA using 2-sector epon centrepieces with quartz glass windows (See Appendix B for theories and principles of AUC). Prior to all measurements, each sample was applied to a Superdex 200 10/300 GL column to remove any aggregates. Sedimentation velocity experiments were

performed (for BM3 and BMR) with a protein concentration of 1 µM in buffer H at 20 °C and at 40,000 RPM, scanning at 230 nm every 1 minute 30 seconds until the sample was fully depleted. The scans were imported into Ultrascan (*277*) for model fitting with finite element solutions to the Lamm equation (*278*). Statistical analysis was performed with 2000 Monte-Carlo bootstrap simulations. Sedimentation velocity experiments were also carried out on NPG-bound BM3 prepared as discussed in section 2.3.2. Similarly, sedimentation velocity experiments were carried out on reduced and alkylated BMR (prepared as discussed in section 2.4.1) for comparison purposes.

Sedimentation equilibrium was performed using a 180 µL solution of BM3 and BMR at concentrations of 0.18, 0.36, 0.85 µM and at salt concentrations of 0.05, 0.15, 0.3, 0.6 and 1 M in buffer F. Equilibrium was reached after 15 hours at 10,000 rpm, and scans were taken at 280 and 230 nm. The dissociation constant was determined from fitting the data using non-linear regression of a monomer-dimer equilibrium model with the program *sedphat* developed by Peter Schuck (*279*).

2.4.3 Static Light Scattering (SLS)

SLS (also known as multi-angle-laser light scattering; MALLS) experiments were carried out in batch using a DAWN Heleos-II obtained from Wyatt Technology Corporation, Santa Barbara (CA 93117). A purified BM3 sample was collected from the SEC column (see section 2.3.1) and was diluted to generate 8 or 10 different samples with varying protein concentration from 0.05 to 1.0 mg/mL. The dilutions were performed with the same salt solution containing buffer F as used for the mobile phase in the SEC column. The samples were then pre-filtered using an on-line Whatman 0.02 µm anotop 10 sterile filter (obtained from VWR International) and continuously injected into the light scattering instrument using a multiple speed syringe pump (model A99) obtained from Razel Scientific instruments (See Appendix C for theories and principles of SLS). The infusion rates used were 17.5 mL/hr for 2.5 mL samples and 20.1 mL/hr for 5 mL samples.

The SLS set-up is similar to that of the SEC-MALLS, excluding the size exclusion column. The light scattering detector is connected in series to an Optilab rEX refractometer and a Jasco UV 2077 plus visible spectrophotometer (Jasco Inc, Easton, MD); the refractometer and spectrophotometer were used for estimating sample concentration. A refractive index increment (*dn/dc*) equal to 0.186 mL/g was used to

estimate concentrations from the differential refractive index data while extinction coefficients of 120 mM^{-1} cm^{-1} and 105 mM^{-1} cm^{-1} were used to estimate BM3 concentrations at 280 and 418 nm respectively. All data were collected and analyzed using Microsoft Excel and Wyatt Astra 5.3.4.13 software. The Zimm equation given below was used to calculate the second osmotic virial coefficient (B_{avg}) and the weight average molecular weight (M_w).

$$\frac{Kc_t}{\bar{R}_\theta} = \frac{1}{M_w} + 2B_{avg}c_t \tag{2.7}$$

Equation 2.7: General light scattering equation. *The parameters are defined as follows: K is the light scattering constant (which depends on the refractive index increment of the salt measured at constant solvent chemical potential), B_{avg} is the second osmotic virial coefficient which is averaged over all types of interactions occurring between all protein species in solution, R_θ is the measured light scattering intensity minus that of the solvent, c_t is the total mass concentration of the protein, and M_w is the weight average molecular weight. The left hand side of Equation 2.7 is plotted versus protein concentration; the value of B_{avg} is equal to one half of the slope, and the weight average molecular weight is given by the inverse of the y-intercept. For a one component protein solution where there is no oligomerization, the weight average molecular weight is equal to the monomer value and the B_{avg} is equal to the pure component osmotic virial coefficient often denoted by B_{22}.*

2.4.4 Composition Gradient Multi-Angle Laser Light Scattering (CG-MALLS)

CG-MALLS technique is an automated version of SLS using a Calypso system developed by Wyatt Technology. This system includes a programmable triple-syringe pump with in-line filters (0.1 µM pore size Millipore polycarbonate) and degassers set to deliver a controlled gradient of protein concentrations into the Dawn Heleos-II static light scattering detector for concurrent measurement of light scattering signals. A Waters 2487 dual wavelength (Waters, Milford, USA) UV detector was used to monitor protein concentration.

BM3 samples were centrifuged at 13,000 rpm using a microfuge 5430 (Eppendorf, New York, USA) for 10 minutes and triple filtered using Whatman 0.02 µm anotop 10 filters (Sigma-Aldrich, USA) to remove large aggregates before injection. Buffer F with varying KCl concentrations ranging from 0-to-800 mM were prepared, filtered and degassed prior to each experiment and passed through a 0.02 µm Whatman anotop filter before use. To effectively capture BM3 behaviour at low and high protein

concentrations, stock solutions of 0.25 mg/mL and 2.5 mg/mL of BM3 were prepared in the running buffer and each was placed in a separate syringe on the Calypso. The third syringe contained the running buffer, which was used to generate 20 serial dilutions with each of the syringes containing protein solutions. Data analyses for determination of K_d and B_{22} required fitting the light scattering data using a multi-component light scattering equation (See Appendix D for theories and principles of CG-MALLS).

CG-MALLS was used to examine the monomer-dimer equilibrium of the BM3 enzyme. In addition, protein formulations always contain a small fraction of irreversibly formed large aggregates, which need to be removed using an SEC step prior to CG-MALLS. However, it is not always possible to remove all the aggregates and as a consequence, these also need to be included in the light scattering analysis. Thus Equation 2.8 includes the effects of higher molecular weight aggregates as well as the individual monomer-dimer and dimer-dimer interaction parameters. In this case, the M_w is given by

$$M_w = \sum_i w_{i,irrev} M_{i,irrev} + w_m M_m + w_d M_d \tag{2.8}$$

Equation 2.8: Definition of light scattering weight average molecular weight. *w_i is the mass fraction of the ith sized aggregate with molecular weight given by M_i. Subscripts m and d represent monomer and dimer respectively.*

A constant fitting parameter $I=\sum_i w_{i,irrev} M_{i,irrev}$ represents the irreversibly formed high molecular weight aggregates. B_{avg} in equation 2.7 accounts for all possible types of self and cross interactions between the monomer and dimer species*:*

$$B_{avg} = \frac{1}{M_w^2} \sum_i \sum_j M_i M_j w_i w_j B_{ij} = \frac{M_d^2}{M_w^2} w_d^2 B_{dd} + \frac{M_m M_d}{M_w^2} w_d^2 B_{md} \tag{2.9}$$

Equation 2.9: Definition of average second osmotic virial coefficient. *Subscript m and d corresponds to monomer and dimer respectively. In equation 2.9, the contribution from the monomer-monomer virial coefficient has been neglected because this term is very small for systems with dissociation constant on the order of micromolar.*

Combining Equations 2.7-2.9, the light scattering equation can be re-written as a function of the measured variables- (c_t), the fitting parameters (I, B_{dd}, K_d), and constants (M_m, M_d).

$$\frac{Kc_t}{\bar{R}_\theta} = \frac{1}{M_w(c_t, K_d, I)} + \frac{M_d^2}{M_w^2(c_t, K_d, I)} w_d^2 (c_t K_d) B_{dd} c_t \qquad (2.10)$$

Equation 2.10: Light Scattering Equation used for CG-MALLS data fitting. *This equation can be used for fitting the parameter to the light scattering data obtained as a function of protein concentration.*

The dimer mass fraction, w_d, can be written in terms of c_t and K_d as follows:

$$w_d = 1 + \frac{K_d M_m^2}{2 c_t M_d} - \sqrt{\frac{K_d M_m^2}{c_t M_d}\left(1 + \frac{K_d M_m^2}{4 c_t M_d}\right)} \qquad (2.11)$$

Equation 2.11: Light scattering dimer mass fraction. *Where equation 2.12 is derived from considering the monomer-dimer equilibrium K_d which is given as*

$$K_d = \frac{K_d M_m^2}{4 c_t M_d}. \qquad (2.12)$$

Equation 2.12: Dissociation constant from light scattering

2.4.5 Cross-Linking

All cross-linkers were freshly prepared in their appropriate solutions just before use (See Appendix E for mechanism of action of crosslinkers). Protein samples were exchanged into the reaction buffer H using PD-10 desalting columns (GE Healthcare, Hemel Hempstead, UK) and further diluted to the desired concentration in the reaction buffer. Cross-linked BM3 samples were run on precast 4 – 12 % gradient (Generon, Berks, UK) or on a 6% SDS-polyacrylamide gel (*i.e* by SDS-PAGE; with Coomassie blue staining) using high molecular weight protein standards (HiMark™ Pre-stained Protein Standard, Invitrogen) to assess the extent of cross-linking. Similarly, cross-linked BMR and BMP samples were run on a 10% SDS-polyacrylamide gel (with Coomassie blue staining) using Broad Range Protein Marker (2–212 kDa; New England Biolabs, Herts, UK). SEC-MALLS analysis (Section 2.2.1) was carried out on BM3 samples cross-linked with formaldehyde and glutaraldehyde. The cross-linkers used are listed below:

Formaldehyde: All cross-linking experiments with formaldehyde were carried out at room temperature. Initial trials in formaldehyde cross-linking involved varying the amount of formaldehyde (0.5-4% volume by volume, V/V) added to 50 µM of purified BM3 prepared in buffer H. Following this trial, the ratio of pure BM3 to formaldehyde

was fixed at 3% V/V while the duration of cross-linking was varied between 5 and 80 minutes, quenching the reaction with a final concentration of 200 mM glycine and incubating on ice until the SDS-PAGE analyses. This time-dependent formaldehyde cross-linking was repeated at various fixed ratios of pure BM3 to formaldehyde ranging from 0.01% V/V to 1% V/V.

Formaldehyde cross-linking was also attempted for BMR (in the presence and absence of DTT) and BMP at 0.5% and 1% V/V, with BMP and BMR concentrations at 100 µM each. The cross-linking reactions were also quenched with a final concentration of 200 mM glycine before SDS-PAGE analysis.

To further assess the effects of formaldehyde cross-linking, SEC-MALLS analysis was performed on formaldehyde cross-linked BM3 samples in buffer H. A concentrated BM3 sample was first run through the SEC column to remove aggregates. The eluent was then divided into two equal halves of 1 mg/ml BM3. The first half was run immediately without any further modifications. Excess formaldehyde (200 µL of 4% formaldehyde) was added to the second half (200 µL of 1 mg/mL BM3) and incubated at room temperature. The cross-linking reaction was quenched with 100 µL of 1M glycine after 10 minutes and incubated on ice until it was loaded onto the SEC column.

Glutaraldehyde: Glutaraldehyde cross-linking experiments were performed in a similar way to those with formaldehyde. For preliminary runs, 50 µM BM3 was mixed with glutaraldehyde at 1% and 2% V/V ratios and incubated at room temperature. The cross-linking reaction was stopped after 10 minutes by adding 50 µL of 1 M Tris-HCl pH 8.0 and run on SDS-PAGE after 10 minutes. In subsequent reactions, the amount of glutaraldehyde used was reduced to a range of 0 − 1% V/V while the duration of the cross-linking reaction with BM3 was varied between 0 and 10 minutes.

SEC-MALLS analysis was also carried out on glutaraldehyde cross-linked samples. A concentrated BM3 sample was first run through the SEC column to remove aggregates. The eluent was then divided into two equal halves of 1 mg/mL BM3. The first half was run immediately without any further modifications. 100 µL of 1% glutaraldehyde was added to the second half and incubated at room temperature for 10 min. The reaction was quenched with 100 µL of 1 M glycine after 10 minutes and incubated on ice until the sample was loaded onto the SEC column.

1-Ethyl-3-[3-dimethylaminopropyl]Carbodiimide Hydrochloride (EDC): A stock solution of 200 mM EDC (Pierce) was made up in buffer I (50 mM MES, 0.2 M NaCl, pH 6.0). 50 µM BM3 (in buffer H) was mixed with varying concentrations of EDC (5-20 µM) and incubated at room temperature for 10 minutes. The cross-linking reaction was stopped by adding 4 µL of 0.5 M β-mercaptoethanol (BME) up to a final concentration of 20 mM. In the following reactions, the concentration of EDC used was increased to 50 µM and cross-linking was attempted with 50 µM BMR and 50 µM BMP.

1,5-Difluoro-2,4-dinitrobenzene (DFDNB): Stock solutions of 5 mM DFDNB (Pierce) and BM3 were prepared in the reaction buffer H. Over a 100-fold excess (final concentrations of 1 and 1.6 mM) of DFCNB was added to 2.5 µM BM3 and mixtures incubated at 4 ºC for 30 minutes. The cross-linking reaction was quenched using 100 µL of 1 M glycine (final concentration of 0.1 M) and samples run on SDS-PAGE after 10 minutes.

Bis(sulfosuccinimidyl) suberate (BS³): A 5 mM stock solution of BS³ (Pierce) was prepared in distilled water. For initial trials, 0.25 – 1 mM BS³ was mixed with 50 µM BM3 and incubated at room temperature for 30 minutes. The reaction was quenched with 10 µL of 1 M glycine. In subsequent reactions, the concentration of BM3 was reduced to 25 µM while that of BS³ was reduced to 20-60 µM.

Dimethyl pimelimidate dihydrochlride (DMP): A 10 mM stock solution of DMP was prepared in buffer J (0.2 M triethanolamine, pH 8.0). 50 µM BM3 was mixed with 0.5-2.0 mM DMP, while 25 µM BM3 was mixed with 40-80 µM DMP and incubated at room temperature for 10 minutes. The reaction was stopped by adding 10 µL of 1 M glycine up to a final concentration of 0.1 M.

Table 2.8: Solvents, stock concentration and reaction quenchers of cross-linkers used in this study. All cross-linkers, buffers, and quenchers were freshly prepared immediately before use.

Cross-Linker	Solvent	Stock Concentration	Working Concentration Range	Final Concentration of Quencher
Formaldehyde	Buffer H	5% V/V	0-4 % V/V	200 mM glycine
Glutaraldehyde	Buffer H	5% V/V	0-2 % V/V	200 mM glycine
EDC	Buffer I	0.2 M	5–20 μM	20 mM BME
DFDNB	Buffer H	5 mM	0-1.6 mM	100 mM glycine
BS^3	Sterile water	5 mM	0-1 mM	1 M glycine
DMP	Buffer J	10 mM	0-2 mM	1 M glycine

2.4.6 Crystallization Trials with BM3 Reductase Mutant C773A

The C773A mutant of the BM3 reductase was expressed and purified as described in section 2.1.3. Preceding crystallization studies, C773A reductase was applied to a gel filtration column (Superdex 200 10/300; GE Healthcare) for further purification in buffer K (10 mM Tris-HCl, pH 7.5). Purest fractions were collected and concentrated using a 30 kDa cutoff vivaspin ultrafiltration device (Generon, Berkshire) to 36 mg/mL. Crystallization trials were carried out using the sitting drop method at 20 ºC using MRC 96-well crystallography plates containing one large well (for mother liquor) and two small wells (wells A and B) which contain the drops. Initial screening was performed using Crystal Screens I and II; Morpheus; PACT premier; and JCSG-Plus (Molecular Dimensions, Suffolk, UK). Wells A contained 200 nL of mother liquor and 200 nL of 12 mg/mL C773A reductase, while wells B contained 200 nL of mother liquor and 200 nL of 12 mg/mL reductase pre-mixed with 500 μM NADP$^+$. The automated liquid handling robot, a Mosquito (Molecular Dimensions), was used to pipette the precise volumes of mother liquor and samples into the wells.

Following initial screening, crystal growth was assisted using the seeding technique (see Appendix F for Seeding protocol). Further, crystallization conditions were optimized by varying the amount of potassium thiocyanate, buffer and PEG (PEG 6000, PEG 20000, and PEG MME 550) making up to 1 mL volumes using buffer K in 96 X 1.5 mL deep well blocks.

2.4.7 Small Angle X-Ray Scattering

SAXS measurements were carried out on the EMBL beamline X33 located at the light source facilities DORISIII at HASYLAB/DESY (Hamburger Synchrotronstrahlungslabor/ Deutsches Elektronen-Synchrotron; Hamburg, Germany) using a MAR345 image plate. Scattering profiles were collected using an exposure time of 30 seconds and a sample-to-detector distance of 2.4 metres, covering a momentum transfer interval of 0.10 nm^{-1} < q < 5.0 nm^{-1} (where q = $4\pi\sin\theta/\lambda$, λ is the wavelength and 2θ is the angle between the incident and scattered radiation). Calibration of the q-range was performed with silver behenate powder which has a diffraction spacing of 58.38 Å. Further information on SAXS theory and principles are discussed in appendix G.

BM3 samples were exchanged into the reaction buffer H (50 mM KPi, 0.1 M KCl, pH 7.0) using PD-10 desalting columns (GE Healthcare, Hemel Hempstead, UK) and further diluted or modified to the desired concentration in the reaction buffer. Data were collected at a range of concentrations for BM3 (1, 2, 4 and 6 mg/mL); BM3 with 1 mM NADP^{+} (1, 3, and 6 mg/mL); and BM3 with 100 µM NPG (1, 3, 6 and 8 mg/mL). BMR and FAD domain samples were run through a gel filtration column (Superdex 200 10/300; GE Healthcare) preceding SAXS data collection to remove aggregates. Data were collected at 5.5 mg/mL and 5.0 mg/mL for BMR and FAD domains, respectively, in buffer H. All measurements were taken at a fixed temperature of 10 ºC.

Radial averaging of scattering images and subtraction of buffer scattering intensities were automatically carried out using the *AUTOMAR* and *AUTOSUB* software (*280*), respectively. Estimates of molecular mass (scattering normalized to BSA) and radius of gyration (*Rg*) were obtained using the *AUTORG* software (*280*). The indirect Fourier transform program, *GNOM*, (*281*) was used to calculate the *Rg*, intra-particle distance distribution function [*p(r)*], and the forward scattering intensity (I_o). *DAMMIN (282)* was used to generate 20 independent but similar molecular shapes *ab initio*, each at different orientations and symmetry. These *ab initio* shapes were then combined and filtered to produce an average model using the *DAMAVER* software (*283*). For the FAD domain, scattering profiles from the crystal structure were generated and compared to the SAXS scattering profiles using *CRYSOL (284)*.

Rigid-body refinement of the experimental SAXS data for the reductase domain was done using SASREF (*285*) with rigid body models generated from the crystal structures of the BM3 FAD and FMN domains already published (*114, 115*). Constraints were applied by varying the inter-flavin distances within the reductase dimer. The generated reductase model was then used as a rigid body model along with the heme domain (*111*) for a further modeling to match the SAXS data collected of the full length enzyme, by also using SASREF and inter-flavin distance constraints.

2.4.8 Further Data Analysis

2.4.8.1 Hydrodynamic bead modeling

Hydrodynamic bead modeling is used to compare the crystal lattice structure to the conformation of the molecule in solution. The modeling uses the algorithm *AtoB* which allows the construction of bead models from the atomic coordinates of the crystal structure. *Ab initio* and rigid-body models (PDB files) generated in SAXS studies were fed into the HYDROPRO (*286*) software to generate bead models. Interpretation of these bead models by the software yields hydrodynamic and solution scattering parameters, including translational diffusion coefficient, hydrodynamic radius (r_H), rotational diffusion coefficient, radius of gyration (R_g), sedimentation coefficient ($s_{20,w}$), frictional coefficient, intrinsic viscosity and maximum distance. These theoretical parameters were compared to the experimental ones obtained using the various techniques in this study: SEC-MALLS, sedimentation velocity and equilibrium, and experimental SAXS.

2.4.8.2 Relating monomer-dimer equilibrium to BM3 function

Equations (2.15) and (2.16) derived below were used to estimate the percentage of monomers and dimers, which was then correlated with measured electron transfer kinetics of intact BM3. The K_d used for this analysis was derived from the sedimentation equilibrium studies.

The equilibrium dissociation constant (K_d) for a self-associating dimer system is defined as:

$$K_d = \frac{[M]^2}{[D]} \qquad\qquad (2.13)$$

where [M] and [D] are the molar concentration of monomers and dimers, respectively.

Also, assuming a sample solution comprising only of monomers and dimers, the total concentration [T] is given as

$$[T] = [M] + 2[D] \tag{2.14}$$

where [M] and [D] represent the molar concentrations of monomers and dimers, respectively.

Equations 2.13 and 2.14 can be combined to give:

$$[D] = \frac{4[T] + K_d - \sqrt{8[T]K_d + K_d^2}}{8} \tag{2.15}$$

and

$$[M] = \frac{-K_d + \sqrt{8[T]K_d + K_d^2}}{4} \tag{2.16}$$

Equations 2.13-2.16: Equations for obtaining monomer and dimer concentrations from Kd.

CHAPTER 3

Biochemical Characterization of Flavocytochrome P450 BM3 and Its Domains

CHAPTER THREE: BIOCHEMICAL CHARACTERIZATION OF FLAVOCYTOCHROME P450 BM3 AND ITS DOMAINS

3.0 INTRODUCTION

As detailed in the Introduction section, the flavocytochrome P450 BM3 system is a multi-domain flavocytochrome enzyme that is a model system in the P450 enzyme superfamily. The major aims of this PhD thesis are to provide a detailed analysis of the structural properties of this enzyme, its aggregation state and inter-domain interactions. To facilitate these studies, methods were established to express and purify intact BM3 and its component domains. This chapter reports the underpinning studies done to produce intact P450 BM3 enzyme and its major heme and diflavin domains, to be used in biochemical, biophysical and structural studies that are reported in this chapter, as well as the later chapters.

Equilibrium optical titration analysis and steady-state kinetics were used to determine binding affinities of flavocytochrome P450 BM3 (BM3) and its P450 domain (BMP) for various substrates and inhibitors. Further, these methods were also used to characterize reduction of non-physiological electron acceptors by BM3 through its reductase (BMR) domain. In addition, the interactions between the BMP and BMR domains for both the intact BM3 and for the isolated (reconstituted) domains were examined using stopped-flow analytical techniques. The results of these experiments are presented in this section.

3.1 PLASMID DNA PREPARATION AND ENZYME PURIFICATION

3.1.1 Plasmid DNA preparation and purification

3.1.1.1 Full-length BM3 and Domains

Plasmids required for the expression of intact BM3 enzyme and its constituents domains were freshly prepared as described in Materials and Methods (section 2.2.2). Transformed cells containing the plasmid of interest (encoding the reductase domain, heme domain or intact P450 BM3) were harvested and used for producing large amounts of DNA using scaled-up mini-prep techniques (QIAprep Spin Miniprep Kit,

Qiagen). For each construct, 5 mL of fresh transformant culture were transferred into four different 1.5 mL microtubes (approximately 1.25 mL per microtube) and mini-prepped separately. 1 µL each of the purified DNA was analyzed by 0.8 % agarose gel electrophoresis for purity and concentration. A typical ethidium bromide-stained gel for BMP and reductase BMR domains is shown in Figure 3.1. The concentration of the DNA produced was quantified by comparing the sizes of one of the plasmid bands with the marker band. For BMP, the 3.0 kb marker band contains 125 ng of DNA, thus the preparations shown were estimated to contain ~1.5 µg DNA in 1 µL of plasmid. On the other hand, the 8.0 kb marker band for the BMR gel contains 42 ng of DNA yielding ~ 200 ng DNA in 1 µL of plasmid. Plasmid quantification results obtained for the full length enzyme were similar to that of the BMP domain (data not shown).
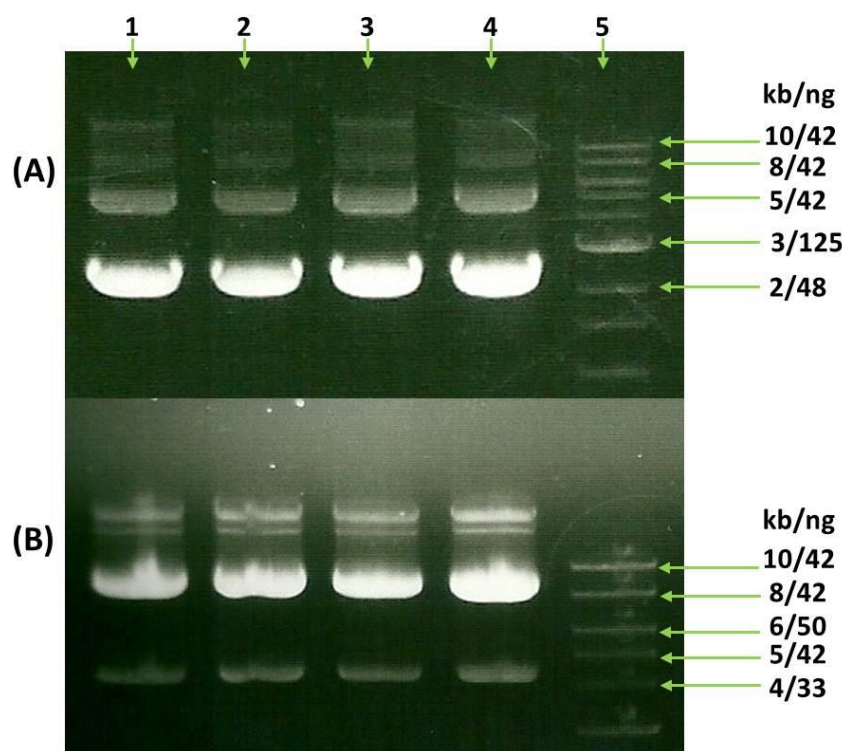
Figure 3.1: Plasmid DNA preparation for the BMP (A) and BMR (B) domains. A 0.8 % agarose gel stained with eithidium bromide showing four independent preparations (1 µL) of plasmid DNA encoding the BM3 heme and reductase domains are shown in lanes 1-4. Lane 5 shows a 1 kb DNA ladder from New England Biolabs. Each microlitre of BMP plasmid was estimated to contain ~ 1.5 µg DNA, while the BMR plasmid was estimated to contain ~200 ng DNA. Further, each microtube contained ~ 50 µL of purified plasmid DNA. The same procedure was used for the preparation of the intact BM3 plasmid, where similar yields as for the BMP plasmid were observed (data not shown).

3.1.1.2 BM3 Reductase C773A Mutant

Replacement of a cysteine residue with alanine within the BM3 reductase domain (position 773 in the full length enzyme of 1048 residues; C773A) was achieved using the QuikChange II site-directed mutagenesis kit (Stratagene). Varying volumes (1-5 µL) of freshly prepared pET-11d plasmids were resolved on a 0.8 % agarose gel (Figure 3.2 A(i)) to estimate the plasmid concentration prior to mutagenesis. Mutation reactions were carried out at three different quantities of the reductase plasmid (5, 50 and 100 ng) in a total reaction volume of 50 µL. The resulting mutant reaction mixtures were transformed into supercompetent XL1-Blue cells and plated on LB agar plates containing 100 µg/mL of carbenicillin. The successful amplification of plasmid using mutagenic primers was confirmed by agarose electrophoresis post mini-prep (Figure 3.2 A(ii)) and the DNA sequence chromatograms at the three different reductase concentrations studied (Figures 3.2 B-D) confirmed the desired mutation. In all three cases, the chromatograms show that the cysteine codon (TGC) was successfully replaced by the alanine codon (GCC). The DNA sequence chromatograms also show that no secondary mutations were introduced by the PCR reaction.
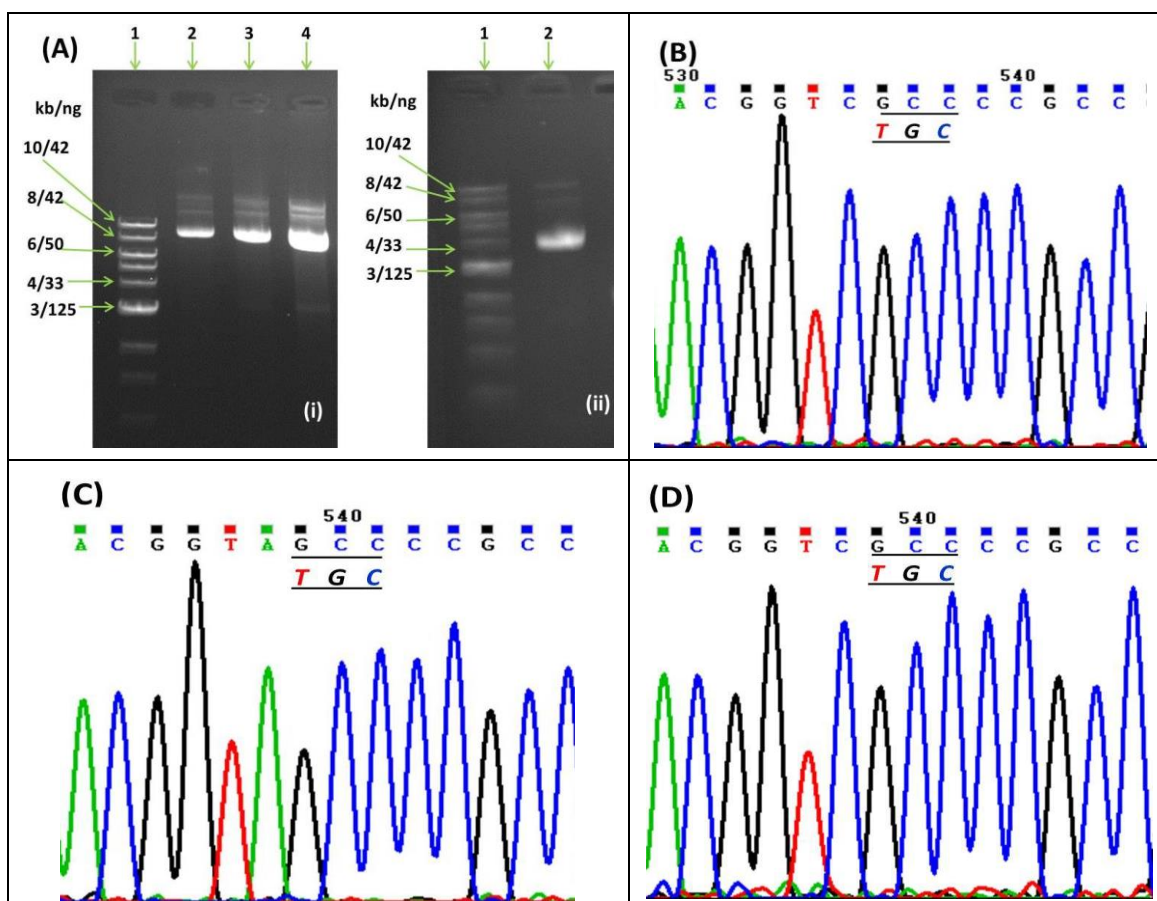
Figure 3.2: Agarose gel electrophoresis and DNA sequence analysis for C773A reductase plasmid. (A)*: Ethidium bromide stained gels showing the mini-prepped BM3 CPR plasmid before (i) and after (ii) mutagenesis to generate a C773A reductase variant plasmid. 1 µL of 1 kb DNA ladder from NEB (Lane 1) was used as the DNA protein marker and the plasmid volumes used were 1, 3 and 5 µL (Lanes 2, 3, and 4 respectively) corresponding to 150, 300 and 750 ng DNA, respectively. The estimated concentration of the wild type reductase plasmid from gel (i) was 150 ng/µl while the estimated concentration of the C773A plasmid from gel (ii) was 130 ng/µl. (****B-D)****: DNA sequence chromatograms from three different preparations of resulting C773A mutants from 5, 50 and 100 ng reductase plasmid mutation reactions, respectively. Results show that the alanine codon underlined (GCC) has successfully replaced the cysteine codon also underlined beneath (TGC) in all three plasmid samples studied.*

3.1.2 Over-Expression and Purification of Intact BM3 and its Domains

The *E. coli* strain TG1 was used as the expression host following transformation of plasmids pUC119 and 118 encoding the full length BM3 and BMP, respectively. Following a 3-step purification protocol as described in section 2.2.4, large quantities of blood red BM3 and BMP were obtained. Purity was monitored by obtaining the Reinheitzahl (Rz) value from comparing the heme absorbance at ~418 nm to the absorbance of aromatic amino acids at 280 nm (A_{418}/A_{280}; Figure 3.3 A). Purity was

assessed (at every stage) by running the samples on SDS-PAGE (Figure 3.3B). Results shown here are for BMP, and similar results were obtained for intact BM3 with respect to increased Soret absorption by comparison to A_{280} during purification steps.
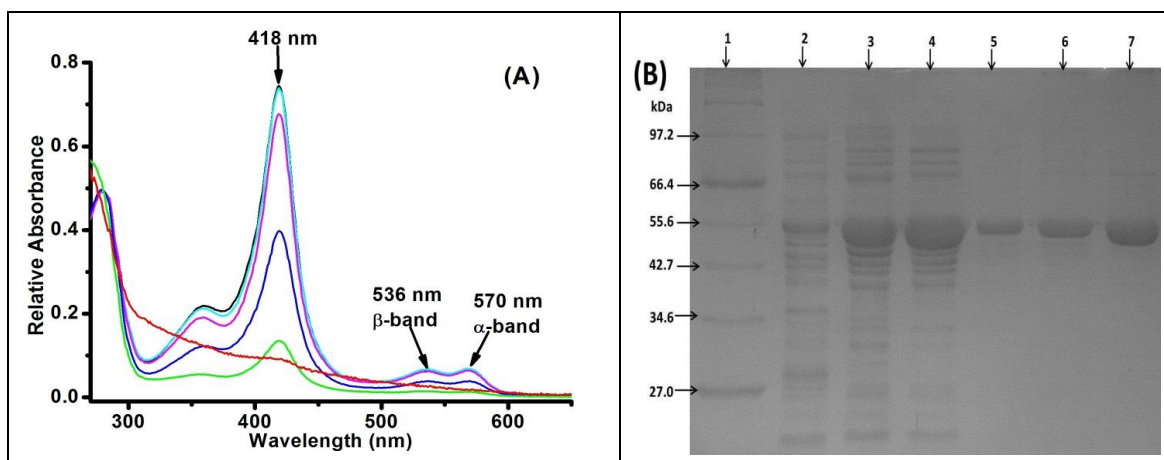
***Figure 3.3: Relative absorption spectra (A) and SDS-PAGE gel (B) for all purification stages of BMP.** (A) The relative absorption spectra were collected and gel run for BMP after lysis (Red-lane 2); ammonium sulphate precipitation (green-lane 3); ion-exchange chromatography on DEAE (Blue-lane 4) and Q-Sepharose (Magenta-lane 5) columns; affinity chromatography using hydroxyapatite column (Cyan – lane 6) and gel filtration (Black – lane 7). (B) NEB Broad range protein marker (2-212 kDa) was used as a standard (lane 1) and the pure BMP protein band is observed at ~55 kDa. Fixing the absorbance measured at 280 nm, the increase in absorbance at 418 nm shows that the protein is progressively purified by the chromatographic steps.*

Similarly, wild type and the C773A mutant pET-11d BMR expression plasmids were transformed into the *E. coli* strain BL21 (DE3) for expression of the BM3 reductase domain (BMR) and its C773A mutant. Purification of these domains was carried out as described in section 2.2.4 to obtain substantial quantities of bright yellow BMR and C773A mutant. Purification was assessed spectrophotometrically using the absorption ratio value for the oxidized flavins relative to aromatic acids (A_{456}/A_{280}) and SDS-PAGE was done as described for BM3 and BMP (Figure 3.4 A-B). Results shown here are for the WT BMR. Similar results were obtained for C773A, where flavin content was not affected by the mutation.

Reinheitzahl values (A_{418}/A_{280} for BM3 and BMP) and flavin/protein ratios (A_{456}/A_{280} for BMR) for the pure forms of BM3, BMP and BMR were calculated from UV-visible spectra of pure proteins (Figure 3.5) as 0.61, 1.50 and 0.13 respectively.
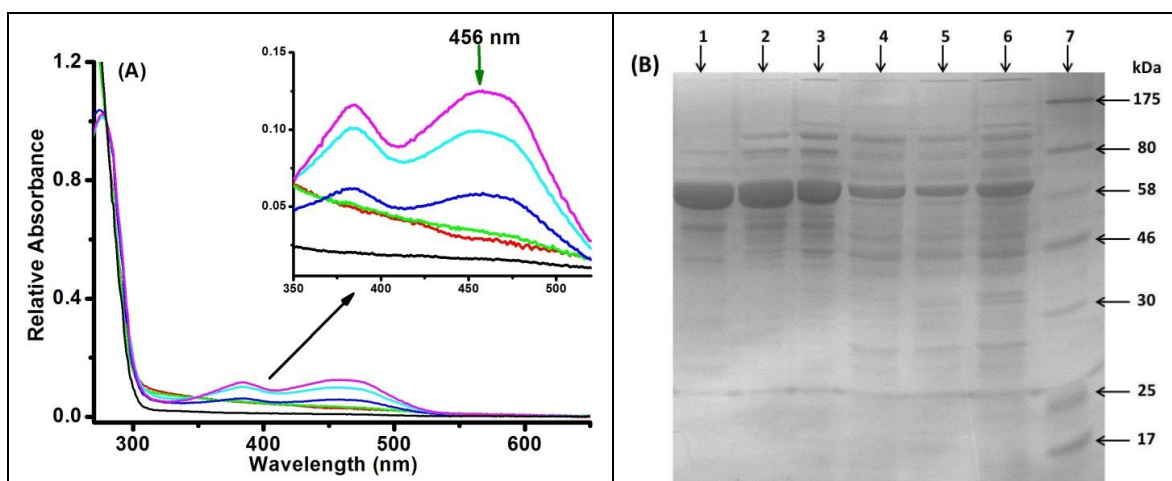
Figure 3.4: Relative absorption spectra (A) and SDS-PAGE gel (B) for all purification stages of BMR. *(A) The relative absorption spectra were collected and gel run for BMR after lysis (Red-lane 6); 0-30% ammonium sulphate precipitation (black-lane 5); 30-60% ammonium sulphate precipitation (green-lane 4); ion-exchange chromatography on DEAE column (Blue-lane 3); affinity chromatography using a hydroxyapatite column (Cyan – lane 2) and another ion-exchange chromatography step using a Q-Sepharose column (Magenta-lane 1). (B) NEB Broad range protein marker (2-212 kDa) was used as a standard (lane 7) and the pure BMR band is observed at ~65 kDa. Fixing the absorbance measured at 280 nm, the increase in absorbance at 456 nm shows that the protein is progressively purified by column chromatography steps (see inset).*
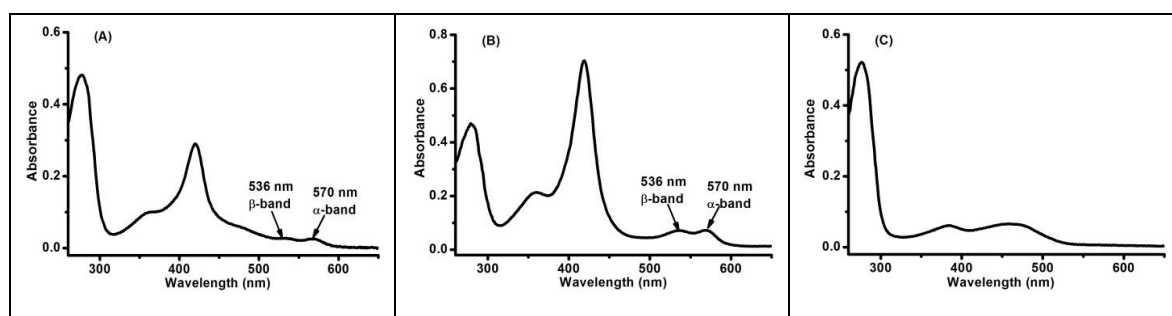
Figure 3.5: Absorption spectrum of purified BM3 (A), BMP (B), and BMR (C). *Approximate concentrations of BM3, BMP and BMR are 3 μM, 7 μM and 3 μM, respectively. BM3 and BMP have their absorption maxima at 418 nm while the BMR domain peaks at 456 nm. Further, the presence of the reductase domain in the full length BM3 makes the alpha (570 nm) and beta (536 nm) bands of the heme less pronounced as a consequence of the contributions of the oxidized FAD and FMN flavins. The Rz values for BM3, BMP and BMR obtain from these spectra are 0.61, 1.50, and 0.13 respectively.*

3.2 EQUILIBRIUM ANALYSIS OF LIGAND BINDING AND STEADY STATE ENZYME ACTIVITY IN BM3 AND ITS DOMAINS

3.2.1 Substrate Binding to the P450 Domain

The P450 domain of BM3 (BMP) was purified as described in section 2.2.4. UV-visible spectral properties of the P450 domain are shown in Figure 3.5A. To assess the binding affinity of the substrates lauric acid and N-palmitoylglycine (NPG) for the BMP, equilibrium optical titration of the enzyme with the substrate was carried out at 30 °C. In the ligand-free form, the BMP domain exhibits spectral features typical of other cytochromes P450 with an intense Soret band at 418 nm and alpha/beta bands in the visible region at 570 and 536 nm. As shown in Figure 3.6, binding of NPG results in a type I (blue) shift of the Soret peak from 418 nm to ~393 nm. Figure 3.7 shows a similar, but less extensive, absorbance change in the case of laurate.
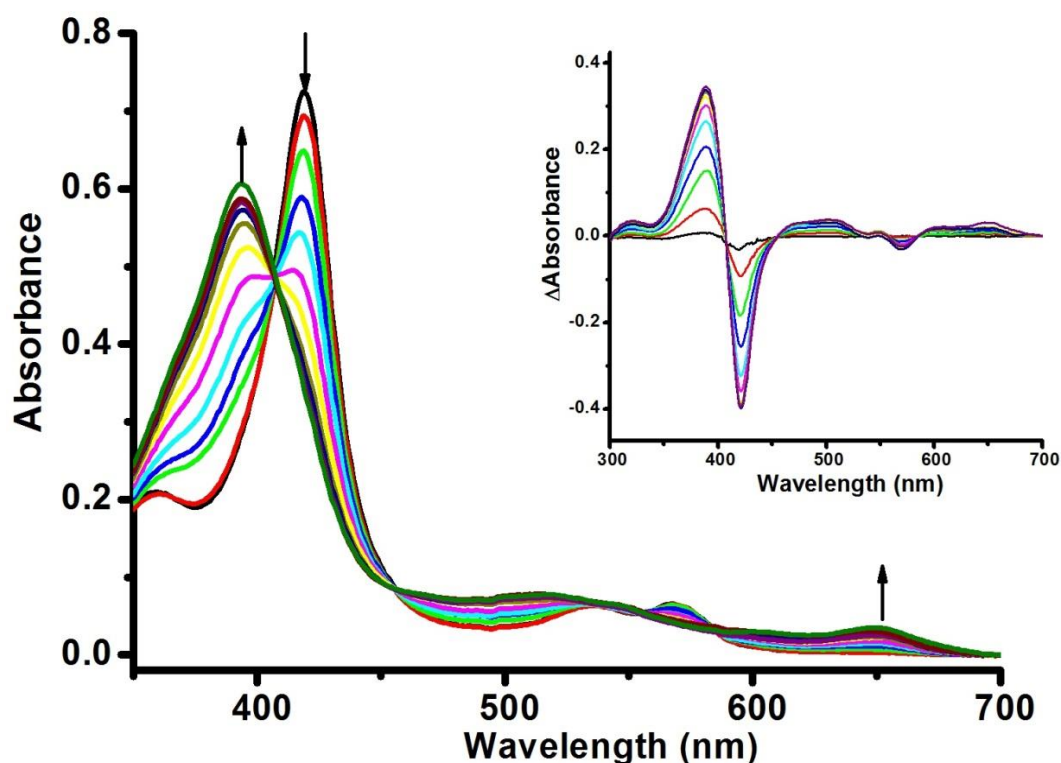
Figure 3.6: NPG binding to the BM3 P450 domain. *Absorption spectra show the titration of BMP (7.5 μM) with NPG in 100 mM KPi, pH 7.0 at 30 °C. Arrows indicate directions of absorption change at selected wavelengths. The inset shows the absorption difference spectra generated by subtracting the ligand-free spectrum from each BMP-NPG absolute spectrum. Spectrum were generated by successive additions of 0.4 μM NPG from a 20 mM stock. Selected spectra shown in the main panel correspond to 0 (black), 0.4 (red), 1.6 (green), 2.8 (blue), 4.0 (cyan), 5.2 (magenta), 6.4 (yellow), 7.6 (dark yellow), 8.8 (navy), 10.0 (purple), 11.2 (wine) and 15.2 μM NPG (olive).*

Moreover, Table 3.1 shows that laurate binding is weaker than that for NPG. Near-complete conversion to the high-spin form is seen for NPG, but the same extent is not observed for laurate binding. However, a characteristic decrease in intensity of the Soret peak at 418 nm and an increase in intensity at 393 nm were observed for both substrates. These absorbance changes are indicative of a conversion in spin state of the heme iron from a six-coordinated low-spin to five-coordinated high-spin form (*129, 287*).
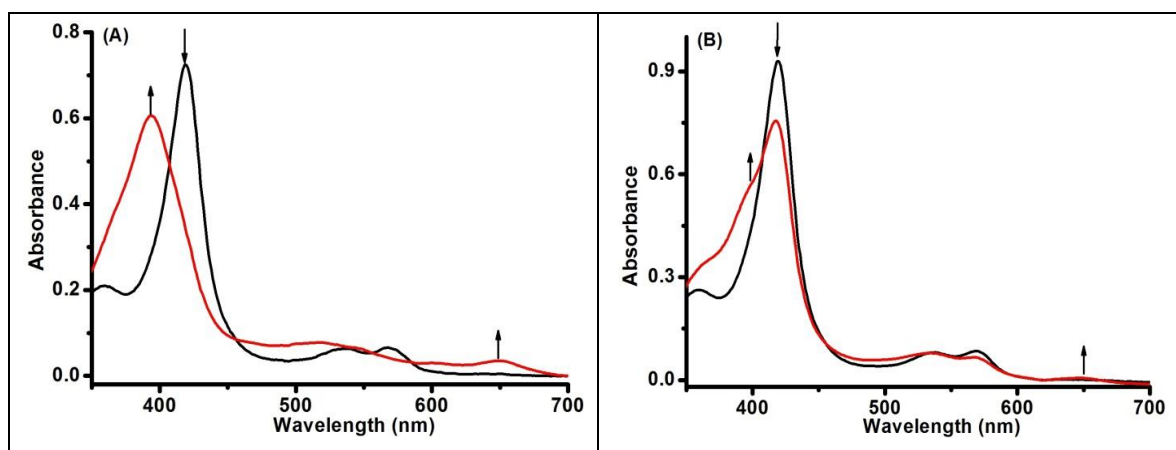
Figure 3.7: Spectral analysis of substrate binding to BMP. *Absorption spectra show the substrate-free (black) and substrate-saturated (red) BM3 P450 domain (ca 8 μM and 10 μM, respectively) with (A) 15.2 μM NPG (B) 1390 μM Lauric acid. Arrows indicate directions of absorbance change on substrate addition at selected wavelengths.*

A plot of the dependence of the change in heme absorbance versus the concentration of lauric acid or NPG (Figure 3.8A, B) allows for the estimation of the dissociation constants of the substrates. In each case, difference spectra were used to identify peak and trough wavelengths following substrate addition, and the absorption difference between this wavelength pair was plotted against substrate concentration to enable data fitting (as described in section 2.3.2.1). The calculated binding constants are given in Table 3.1 and data fits shown in Figure 3.8. The much lower value of the dissociation constant equal to 0.13 μM for NPG when compared to a value of 185 μM for lauric acid indicates that NPG has a higher affinity for the enzyme than lauric acid and hence binds more tightly. The difference in affinity and extent of high spin shift for the two substrates for the enzyme is further seen in the increase in intensity of the high spin charge transfer band at 650 nm, which is less conspicuous in the lauric acid binding spectra compared to those for binding of NPG. This band is characteristic of high-spin ferric heme proteins (*129*). This demonstrates a greater conversion to high spin when binding NPG than for lauric acid. All K_d values determined for substrate/inhibitor

binding to P450 BM3 or BMP are consistent with other values reported in the literature. For example, NPG – 0.262 μM (*113*); 4-PI – 0.85 μM (*136*); imidazole - > 5mM (*136*); lauric acid - 241 μM (*5*); arachidonic acid – 3.6 μM (*5*).

Table 3.1: Binding affinities of various substrates/inhibitors for the P450 domain of flavocytochrome P450 BM3

LIGAND	K_d (μM)	Inference
N-Palmitoylglycine (NPG)	0.127 ± 0.003	Tightest
4-Phenyl Imidazole (4-PI)	3.36 ± 0.47	Tight
Lauric acid	185 ± 15	Weak
Imidazole	8230 ± 240	Weakest
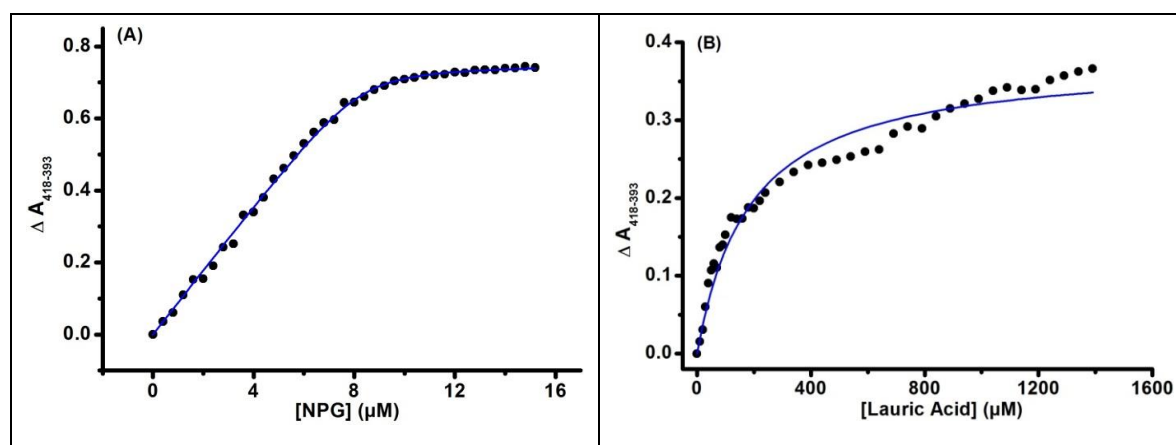
Figure 3.8: NPG (A) and Lauric acid (B) binding to BMP. Maximum absorbance changes between peak and trough were calculated from difference spectra (inset Fig. 3.6) and plotted against the corresponding substrate concentration. Fitting of data was as described in section 2.3.2.1. Data were fitted using equation 2.2 for NPG and equation 2.3 for lauric acid, producing K_d values of 0.127 ± 0.003 μM (NPG) and 185 ± 15 μM (lauric acid).

3.2.2 Inhibitor Binding to the P450 Domain

Weak and tight binding affinities of ligands for BMP were also observed with the inhibitors used in this study. On saturation with imidazole and 4-phenyl imidazole, there was a red-shift in the Soret band from 418 to 425 nm, characteristic of a type II spectral shift (Figures 3.9 and 3.10). As with the substrates, the red-shift was accompanied by a decrease in Soret peak intensity at 418 nm, although there was a large difference in the

percentage of intensity decrease between the inhibitors. A decrease of ~40% was observed for imidazole while a decrease of ~19% was observed for its derivative, 4-PI. This sort of absorbance change is consistent with inhibitor binding to cytochromes P450 involving ligation to the heme. Generally, inhibition of cytochromes P450 by imidazole is not unexpected since the azole functionality has a nitrogen atom which is able to coordinate to the P450 heme iron (*288*).

By fitting the absorbance changes using a quadratic function (equation 2.2) describing bimolecular association reactions, dissociation constants of 823 ± 24 µM and 3.36 ± 0.47 µM were derived for imidazole and 4-PI respectively (Figure 3.11). The variations in optical intensity decrease between imidazole and 4-PI are not related to differences in extent of binding, since both ligands were titrated until there was no further optical change noted. This implies that 4-PI and imidazole induce slightly different absorption changes, despite the fact that the coordinating group imidazole is the same in each case.
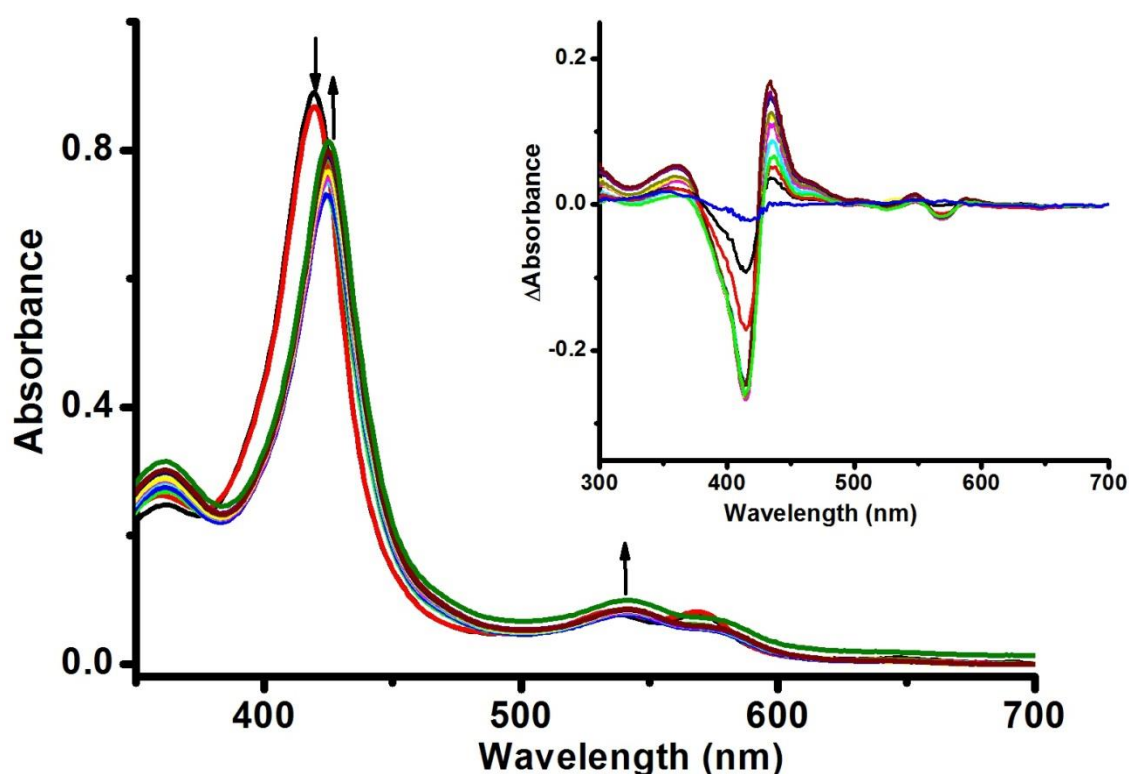
Figure 3.9: 4-phenyl imidazole binding to BMP. *Absorption spectra show the titration of BMP (8.5µM) with 4-phenyl imidazole in 100 mM KPi, pH 7.0 at 30 °C. The inset shows the absorption difference spectra generated by subtracting the inhibitor-free spectrum from each BMP-4-PI absolute spectrum. Arrows indicate direction of absorbance shift induced on 4-PI addition. Each spectrum was generated by the successive addition of 2.5 µM 4-PI from a 25 mM stock. Selected spectra in the main panel correspond to 0 (black), 0.25 (red), 12.5 (green), 22.5 (blue), 32.5 (cyan), 42.5*

(magenta), 55.0 (yellow), 65.0 (dark yellow), 75.0 (navy), 85.0 (purple), 95.0 (wine) and 100.0 μM 4-phenyl imidazole (olive).
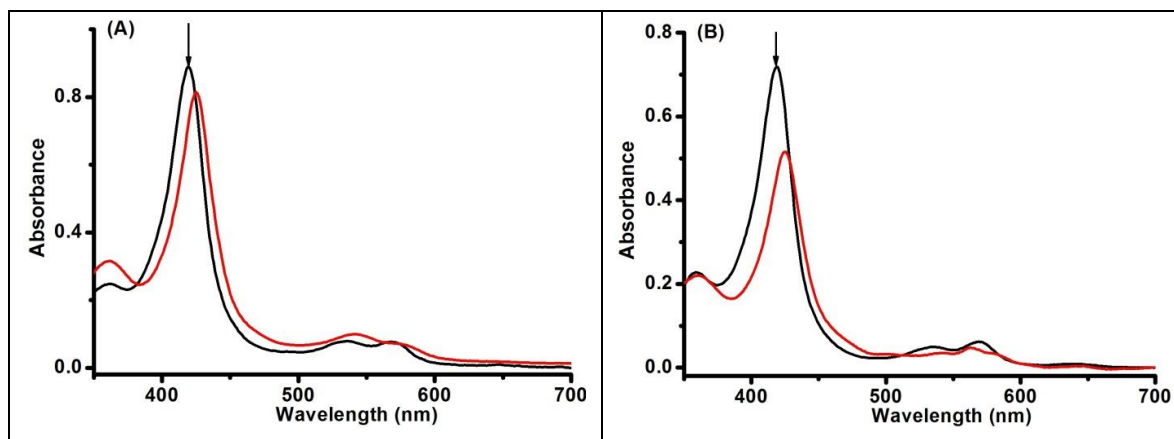
Figure 3.10: Spectral analysis of inhibitor binding to BMP. *Absorption spectra show the inhibitor-free (black) and inhibitor-saturated (red) P450 domain (ca 8.5 μM and 7 μM, respectively) with (A) 100 μM 4-phenyl imidazole and (B) 15 mM imidazole.*
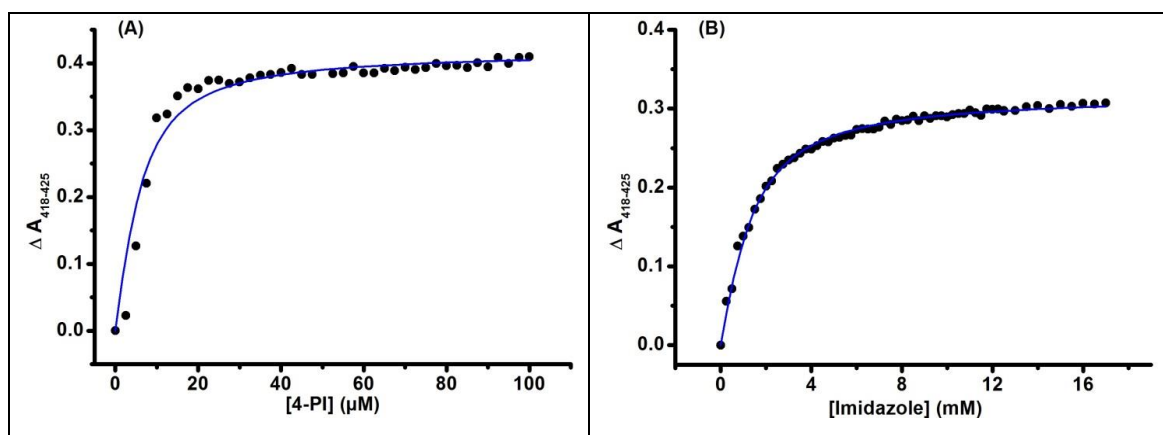
Figure 3.11: Inhibitor ligand binding to BMP. *The plots show binding of 4-phenyl imidazole (A) and imidazole (B) to BMP. Maximum absorbance changes were calculated from difference spectra (inset Fig. 3.9) and plotted against the corresponding concentration of inhibitor. Fitting of data was done as described in section 2.3.2.1. Data were fitted using equation 2.2, producing K_d values of 823 ± 24 μM (imidazole) and 3.36 ± 0.47 μM (4-PI).*

3.2.3 Intact P450 BM3: Affinity and Activity with Fatty Acids

An assessment of the affinity and activity of the intact P450 BM3 enzyme with fatty acids was conducted at equilibrium (optical binding titrations) and under steady-state conditions, respectively. The binding of arachidonic acid to full length BM3 was studied via titration of arachidonic acid from a 33 mM stock in 0.1 μL aliquots at 30 °C in 100 mM potassium phosphate, pH 7.0 buffer (Buffer E). As with the P450 domain

(BMP), a characteristic peak at 418 nm (the low-spin Soret band) is seen in the ligand-free form. Binding of a substrate resulted in a blue shift of the Soret to a wavelength of 393 nm (Figure 3.12A). A decrease in intensity at 418 nm with the accompanying increase at 393 nm was also observed, representing a shift in the ferric heme iron spin-state equilibrium from low-spin towards high-spin. Fitting the resulting data (absorption peak minus trough data, using wavelengths generated from difference spectra) using a quadratic function (equation 2.2) in Origin gave a dissociation constant (3.04 ± 0.29 µM) characteristic of tight binding of the substrate to the enzyme (Figure 3.12B). Moreover, the small increase in absorbance at 650 nm is a further indication of the formation of a high-spin ferric species (a thiolate-to-high-spin ferric heme charge transfer band). Thus, the characteristics of substrate binding near the heme of the P450 domain are similar to those of the intact BM3 enzyme. It should be noted that the starting spectrum for the "as-purified" form of BM3 already has a proportion of high-spin heme iron that likely arises from co-purification of the enzyme with a small amount of one or more *E. coli* fatty acids (likely palmitic acid). Thus, the K_d value for arachidonic aid is probably even tighter than the 3.04 µM estimated from this titration.
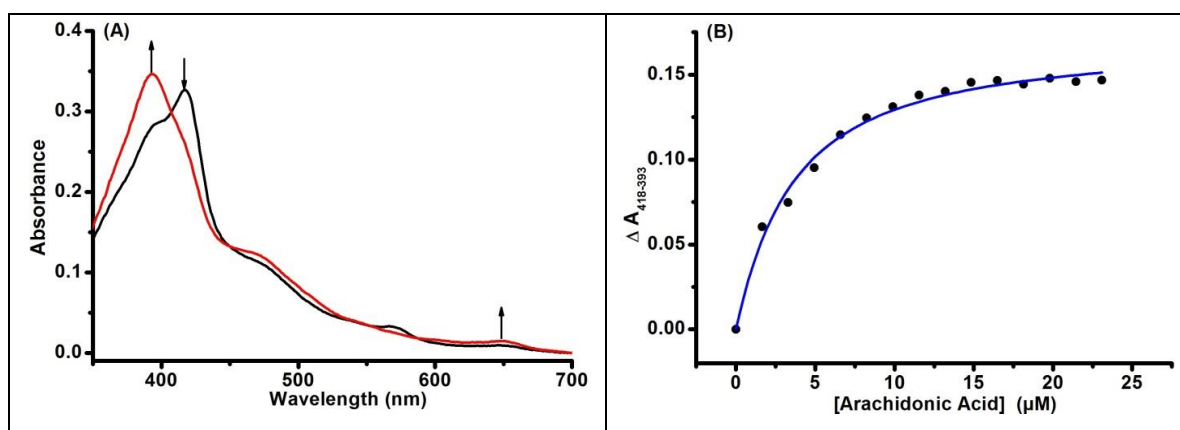
Figure 3.12: Arachidonic acid binding to intact BM3. *(A) Absorption spectra for the as-purified (black) and arachidonic acid-saturated (red) intact BM3 enzyme (ca 4 µM). (B) Maximal changes in absorbance versus arachidonic acid concentration were calculated from difference spectra, which were generated by subtracting the substrate-free spectrum from subsequent spectra collected in the arachidonic acid titration. The K_d value determined by fitting data using equation 2.2, and was 3.04 ± 0.29 µM.*

Furthermore, lauric acid-dependent oxidation of NADPH by intact enzyme was used to assess the activity of the full length BM3 enzyme in substrate-dependent NADPH oxidation using steady state kinetics. The rate of NADPH oxidation was measured spectrophotometrically by monitoring the change in UV-visible absorbance at 340 nm

using an extinction coefficient of $\varepsilon_{340} = 6.21$ mM^{-1} cm^{-1} for the oxidation of NADPH to NADP$^+$. The rates obtained were plotted against the relevant concentrations of lauric acid and data fitted to the Michaelis-Menten equation to obtain the catalytic rate constant (k_{cat}) and the apparent binding affinity of the enzyme for the substrate (K_M; Figure 3.13). A relatively weak binding is indicated by the resulting K_M (which under steady state conditions approximates the apparent dissociation constant) of 111 ± 4 μM. The corresponding k_{cat} is 26.05 ± 0.34 s^{-1} (Table 3.2). The k_{cat} for lauric acid is thus ~11-fold lower than that with arachidonic acid (285 s^{-1}) under similar conditions (*131*).
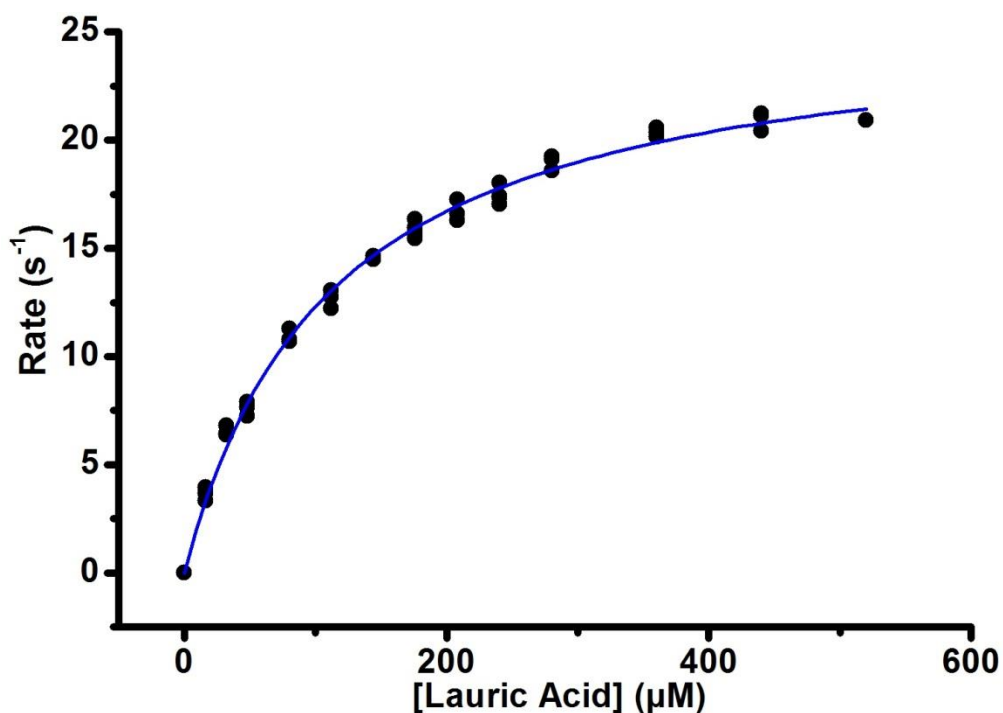
Figure 3.13: Steady-state analysis of P450 BM3 during catalysis of lauric acid-dependent NADPH oxidation. The plot shows the rate of lauric acid-dependent oxidation of NADPH by flavocytochrome P450 BM3 at 30 °C. Data were fitted using the Michaelis-Menten function (equation 2.5) to yield a k_{cat} of 26.05 ± 0.34 s^{-1} and a K_m of 111.6 ± 4.1 μM.

3.2.4 Activity and Affinity for Electron Acceptors in Intact BM3 and its Reductase Domain

A suitable assay for understanding the catalytic activities of redox enzymes is by characterizing the rate of electron transfer to physiological and non-physiological electron acceptors. Here, electron transfer to, and subsequent reduction of, two non-physiological electron acceptors – cytochrome *c* and potassium ferricyanide (FeCN) was assayed. The choice of electron acceptors reflects differences in the mode by which

electron transfer occurs in the reductase. Electrons are transferred from NADPH through both flavins to cytochrome *c* (i.e. to FAD, then FMN, and onto the cytochrome *c* from the FMN). For FeCN, however, the electrons do not pass obligatorily through the FMN cofactor, as FeCN accepts electrons directly from the FAD cofactor preferentially in BM3 and other diflavin reductases (*157, 289, 290*). These experiments were conducted under steady-state conditions.

Cytochrome *c* reduction was assayed under aerobic conditions at 30 °C in 100 mM potassium phosphate buffer (pH 7.0) containing near-saturating concentrations (500 µM) of NADPH. For assays with the intact enzyme the reaction mixture contained 0.023 nM of BM3, while for assays with the reductase domain, 0.017 nM of BMR was used. The data for the dependence of catalytic rate on substrate concentration describe Michaelis-Menten kinetic behaviour in the case of both BM3 and BMR.
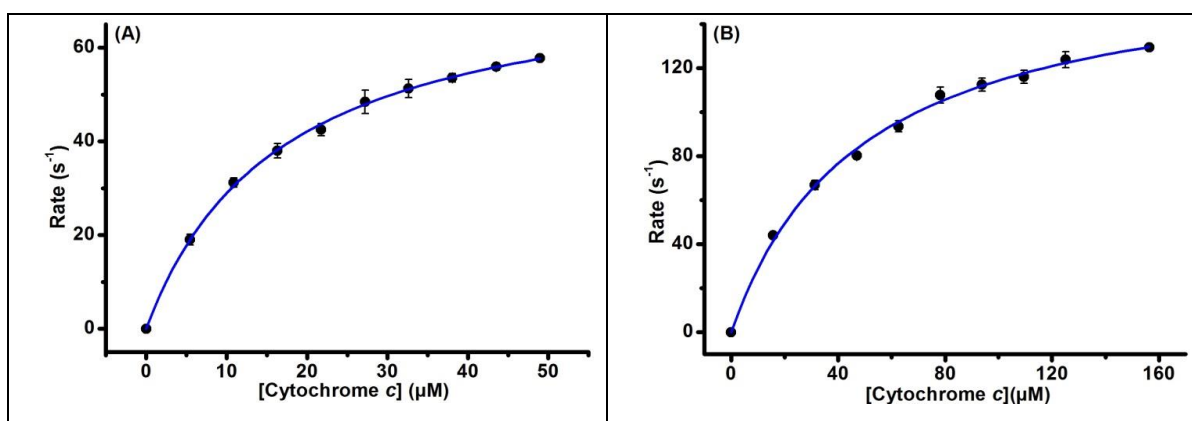
Figure 3.14: Steady state reduction of cytochrome c catalyzed by intact P450 BM3 (A) and the reductase domain (B). *Reaction rates were determined spectrophotometrically, by monitoring at 550 nm and using a difference extinction coefficient of 22.64 mM^{-1} cm^{-1}. The resulting data were fitted using the Michaelis-Menten function (equation 2.5) to yield the binding (K_M) and catalytic constants (k_{cat}). Each point shows the mean and standard error of data obtained from three independent readings. The k_{cat} and K_M values are given in the following text.*

Figure 3.14 shows a plot of the resulting catalytic rates of reduction of cytochrome *c* by both BM3 and BMR as a function of cytochrome *c* concentration. The K_M values of BMR and BM3 for cytochrome *c* were observed to be 48.6 ± 3.0 µM and 16.7 ± 0.7 µM respectively. The turnover numbers as indicated by k_{cat} values for the reduction of cytochrome *c* by BM3 and BMR were 77.3 ± 1.1 s^{-1} and 169.9 ± 4.0 s^{-1} respectively (Table 3.2). Although the intact enzyme has a slightly higher affinity for cytochrome *c*

than does BMR, more molecules of cytochrome *c* are converted to product with the reductase domain than with the intact enzyme in unit time at saturating substrate concentration. However, an estimation of the catalytic efficiencies of these enzymes shows that BM3 with a k_{cat}/K_M of 4.63 μM^{-1} s^{-1} has a slightly higher catalytic efficiency for cytochrome *c* than BMR with a k_{cat}/K_M of 3.50 μM^{-1} s^{-1}. Furthermore, the observed k_{cat}/K_M value for BMR obtained here is lower when compared to the results of Roitel *et al* [k_{cat}/K_M was reported to be 12.7 $\pm$ 1.5 μM^{-1} s^{-1} *(63)*]. This is possibly due to the higher salt concentration used here (100 mM KPi as opposed to 50 mM KPi). This argument is supported by the observed decrease in BMR-cytochrome *c* reductase activity with increasing ionic strength reported in previous studies (*176*).

Table 3.2: Catalytic properties of BM3 and its reductase domain. *The K_M and k_{cat} values show the affinities and activities of the intact enzyme and the reductase domain of flavocytochrome P450 BM3. The values are derived from Michaelis-Menten fits of data sets, where individual data points were each recorded in triplicate. The k_{cat} and K_M values are indicated as mean ± standard deviations. *data from Govindaraj and Poulos (291). Data were obtained at a saturating concentration of NADPH (500 µM).*

SUBSTRATE/ ELECTRON ACCEPTORS	REDUCTASE (BMR)		INTACT ENZYME (BM3)	
	k_{cat} (s^{-1})	K_M (µM)	k_{cat} (s^{-1})	K_M (µM)
Lauric Acid	nd*	nd*	26.1 ± 0.3	111.6 ± 4.1
Cytochrome *c*	169.9 ± 4.0	48.6 ± 3.0	77.3 ± 1.1	16.7 ± 0.7
Ferricyanide	286.4 ± 7.5	41.3 ± 4.9	299.3 ± 1.6*	>50*

Similarly, an assay of the reduction of ferricyanide (FeCN) by P450 BM3 reductase domain was carried out under the same conditions. With an enzyme concentration of 0.015 nM, the reaction followed Michaelis-Menten kinetics (Figure 3.15). Higher rates of FeCN reduction (k_{cat} of 286 s^{-1}) were observed compared to cytochrome *c* reduction. This might be expected as FeCN is a small molecule, and there is a greater likelihood of productive electron transfer interactions with the reductase flavins than might be the case of cytochrome *c*. Furthermore, the preferred channel of electron flow to FeCN (NADPH-FAD-FeCN) is short compared to that for cytochrome *c* (NADPH-FAD-FMN-cytochrome *c*), and movement of the FMN-binding domain may be required for productive interactions with cytochrome *c*. Thus, reduction of cytochrome *c* could be limited by rates of events such as FAD-to-FMN electron transfer and FMN domain motion. The k_{cat} results are in good agreements with those of Roitel *et al.* (*63*), however the K_M and k_{cat}/K_M value were slightly lower in this study (K_M and k_{cat}/K_M values reported by Roitel *et al* were 21.5 $\pm$ 1.7 µM and 12.7 $\pm$ 1.5 μM^{-1} s^{-1} respectively). This

discrepancy is attributable to the difference in ionic strength of buffers used. With FeCN, however, the discrepancy is more pronounced with the K_M (48 %) than with the k_{cat} (4 %). There is a possibility that the ionic strength has a great effect on the interaction between the enzyme and substrates, as indicated by the large difference in K_M observed.
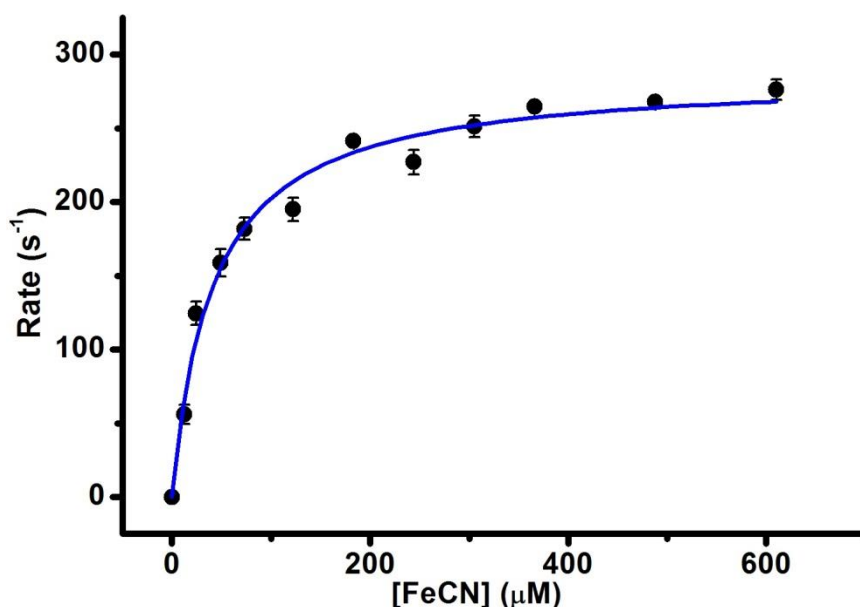
Figure 3.15: Steady state reduction of ferricyanide catalyzed by P450 BM3 reductase. *Ferricyanide reduction was determined spectrophotometrically, monitoring the reaction at 420 nm and using an extinction coefficient of 1.02 mM^{-1} cm^{-1}. The resulting data were fitted using the Michaelis-Menten function (equation 2.5) to yield the binding and catalytic constants (see Table 3.2).*

3.3 STOPPED-FLOW ANALYSIS OF P450 BM3 DOMAIN INTERACTIONS

One of the major objectives of this study is to characterize the weak interactions between the reductase and the P450 domains of BM3 when these domains are not covalently bound to each other. One approach is to study the electron transfer (e.t.) rate between these domains across a range of different salt concentrations. As seen in section 1.2.4, electron flow in flavocytochrome P450 BM3 is from NADPH to the FAD-binding domain and then on to the FMN-binding domain, and finally to the P450 domain. There is a general consensus that the rate at which the P450 domain is reduced by the FMN semiquinone is the major rate limiting step of the P450 cycle (section 1.2.4.4). Direct measurement of this FMN to heme e.t. rate is not easily monitored as subsequent oxygen binding and further stages of the catalytic cycle makes measurements

complicated. However, since the P450 domain has to be reduced before binding of oxygen or carbon monoxide (CO), the rate at which a ferrous-CO adduct is formed (Figure 3.16) can be used as an indication of the electron transfer rate between the FMN and the P450 domain. Measurement of CO binding to BM3 has been studied previously (*292*) and this rate is observed to be significantly faster than that for flavin-to-heme electron transfer.
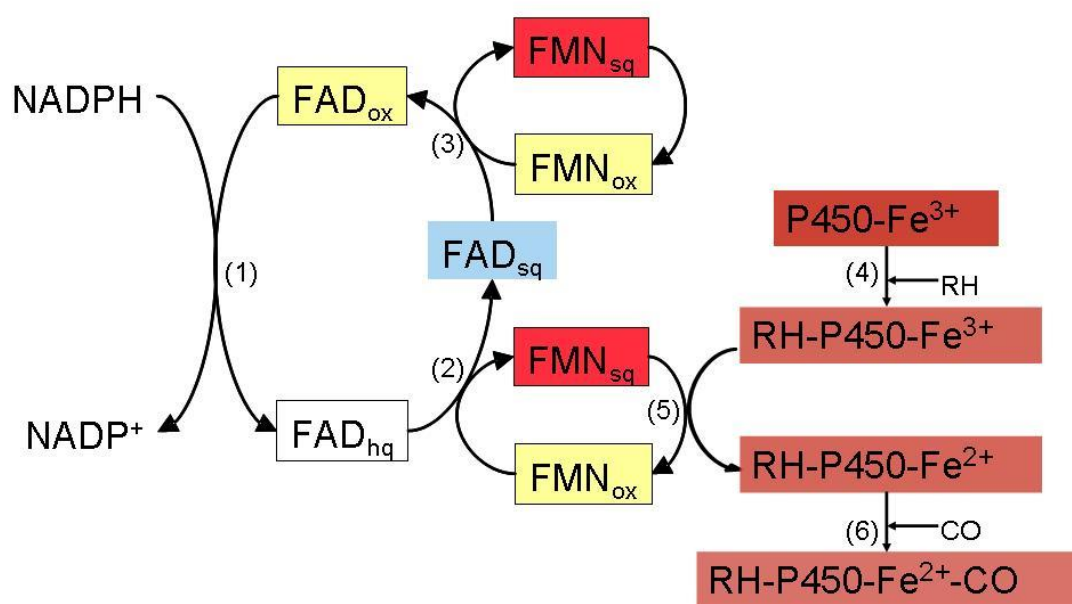
Figure 3.16: Electron transfer between the BM3 domains. *The cofactor colour in the respective redox states in solution is as indicated. The process involves hydride transfer from NADPH to FAD (1) and two one-electron transfer steps from FAD to FMN (2, 3). Substrate binding to the heme domain (4) creates a thermodynamically favourable environment for reduction of ferric heme to ferrous heme by FMN_{sq} (5) which in turn facilitates binding of CO to the ferrous heme (6). The uppermost cycle of reduction of FMN to its (red) semiquinone is relevant only for the catalytic situation, where the second of the two consecutive single electron transfer reactions to the heme iron is required for substrate oxidation.*

3.3.1 Principle of Stopped-Flow Spectroscopy

Stopped-flow spectroscopy is one of the most frequently used rapid kinetics techniques for measuring fast reactions in solution. The typical single-mixing stopped-flow device is as shown in Figure 3.17. Essentially, syringes A and B contain the reaction solutions.

Small volumes of the solutions are simultaneously and rapidly driven from the high performance syringes into a high efficiency mixing chamber to initiate a fast reaction. The resultant mixture quickly flows through a measurement flow cell into a stopping syringe. As the stopping syringe fills up, the plunger hits a block causing the flow to stop instantaneously. The 'stop' triggers data acquisition which, in this case, is output as a change in absorbance of the reaction mixture with time.

This change in absorbance can be measured at single or multiple wavelengths. For simultaneous multi-wavelength measurements from a single stopped-flow drive, photodiode array (PDA) detectors are employed (*293*).
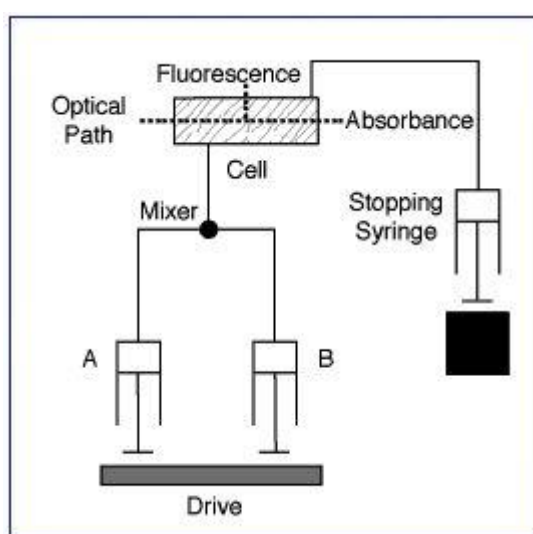
Figure 3.17: A Schematic Representation of a Single-Mixing Stopped Flow Device (Source: TgK Scientific; (293))

3.3.2 Intact P450 BM3- Reduction of Heme and Flavins

3.3.2.1 Measurements of Rate Constants and Amplitudes at 418 and 450 nm

The effects of ionic strength on the rate of electron transfer between the reductase and P450 domains of intact flavocytochrome P450 BM3 (BM3) was first investigated in the full length enzyme. The rate of formation of the ferrous-CO adduct was measured at a wavelength of 450 nm and at 418 nm in buffer containing 50 mM potassium phosphate with 88 μM arachidonic acid at pH 7.0 and 25 °C and at various salt (KCl) concentrations. The data at 418 nm was collected to check that it correlates with the 450 nm data. That is, the appearance of the ferrous-CO band at 450nm should be concomitant with the decrease of the ferric band at 418 nm (loss of low spin ferric

heme). As described in section 2.3.3, the change in absorbance was monitored for 200 milliseconds. Absorbance traces were obtained at each salt concentration and the rate constants were determined by fitting the average of traces taken at different KCl concentrations to a double exponential function (equation 2.6) using the Applied Photophysics software. The absorbance traces (with a characteristic kinetic trace and fit) for this measurement process and plots of the observed rate constants (k_{obs}) and amplitudes for both phases and wavelengths against the salt concentration are shown in Figure 3.18.
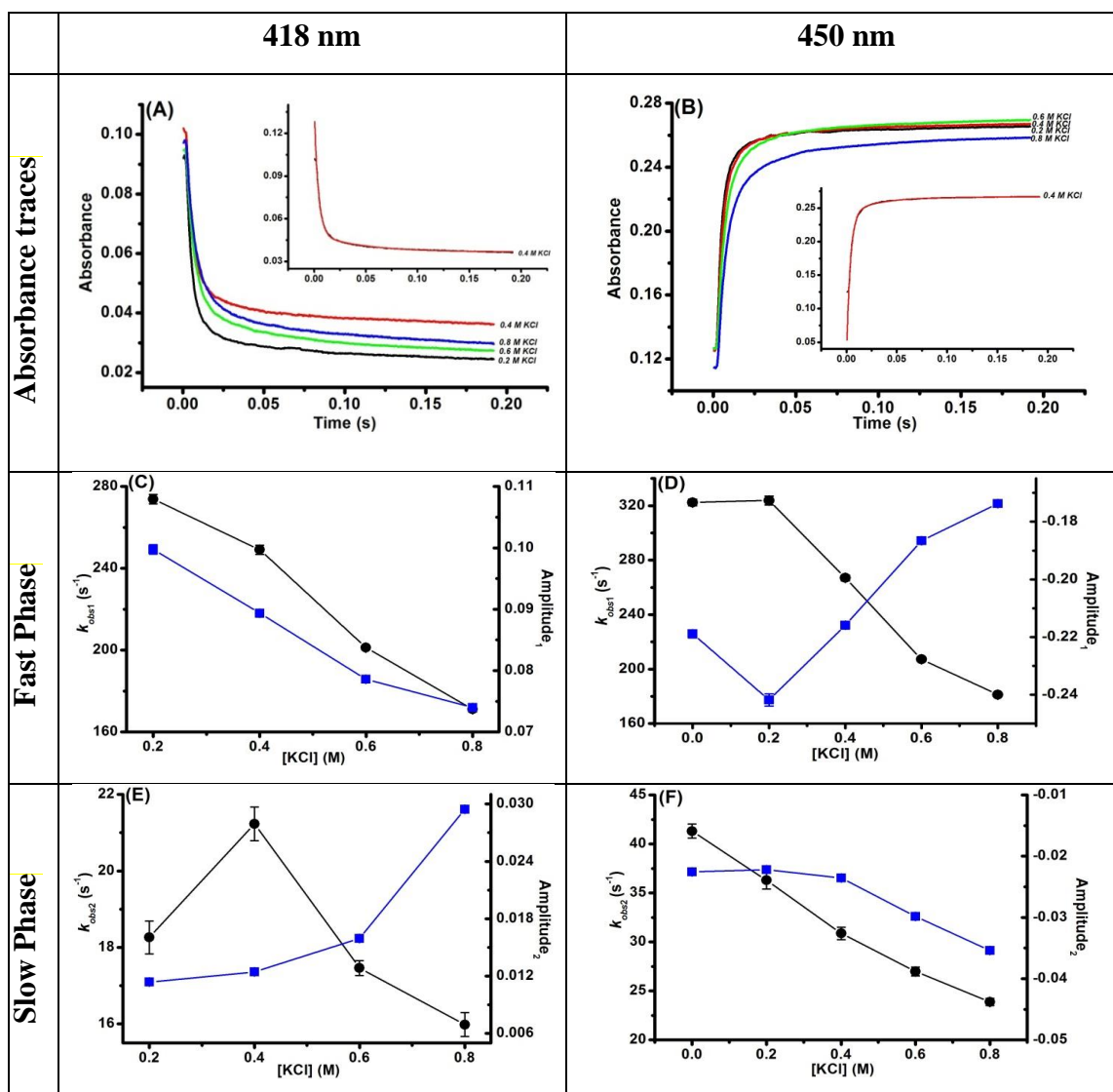
Figure 3.18: Kinetic analysis of heme reduction in intact BM3. *(A-B): Absorbance traces for the reduction of intact BM3 by NADPH and the subsequent binding of CO monitored at 418 and 450 nm (ΔA_{418} and ΔA_{450}) respectively. Insets show a characteristic kinetic trace (black) and double exponential fit to the trace (red) measured at 0.4 M KCl. The observed rate constants (black circles) and amplitudes (blue squares) for the FMN-to-heme electron transfer in intact BM3 as a function of salt concentration for the fast phase (C-D) and the slow phase (E-F) at 418 and 450 nm*

respectively, are also shown. Experiment was conducted at 25 °C in buffer containing 50 mM potassium phosphate, pH 7.0 over a period of 200 milliseconds.

The insets in Figures 3.18A-B show that the kinetic traces fitted well to a double exponential (but not to a single exponential function) function yielding two rate constants in each case. The process of forming the CO complex involves the reduction of the FAD in the reductase domain, electron transfer through the FMN and onto the heme iron, followed by CO binding to the ferrous heme. The latter step may also be affected by the position of the fatty acid in the active site. For these reasons, it is not surprising that the reaction is not monophasic. For the fast phase (k_{obs1}), there was no significant change in k_{obs1} between 0 and 0.2 M KCl (Figure 3.18D, black circles). However, there was a large decrease as the salt concentration increased above 0.2 M. On the other hand, electron transfer for the slower phase (k_{obs2}) was found to decrease consistently as ionic strength was increased from 0-0.8 M KCl (Figure 3.18F). Furthermore, comparing the amplitudes measured for both phases at 450 nm (blue squares - Figure 3.18 D, F), most absorbance change occurs in the fast phase, indicating that the majority of the Fe^{2+}-CO complex formation occurs in this phase. In the absence of salt, the apparent rate constants for electron transfer between the flavin and heme domains were approximately $k_{obs1} = 320$ s^{-1} and $k_{obs2} = 41$ s^{-1}. The k_{obs1} rate constant is thus similar to that previously reported by Munro *et al* with myristic acid (223 s^{-1}; (*116*)). Assuming that the k_{obs1} value most accurately represents the true rate of electron transfer to the P450 heme iron (since k_{obs2} is lower than the steady-state turnover rate reported with arachidonate (*5*)) it may be the case that k_{obs2} is associated with (for instance) slower heme reduction in a proportion of the heme domain occupying a different conformational state, or e.g. heme iron being reduced by FMN hydroquinone (rather than semiquinone). A similar trend is observed with the fast and slow rates obtained with measurements at 418 nm, again suggesting that the fast phase might represent the rate of electron transfer to the heme iron from the FMN (anionic) semiquinone rather than from the hydroquinone.

3.3.2.2 Flavin Reduction in Intact cytochrome P450 BM3

To confirm if the observed rates are not limited by NADPH-dependent flavin reduction rates (which are fast; and >700 s^{-1}(*116*)), the dependence of flavin reduction rate constants across the same range of salt concentration used in this study was also monitored at 475 nm in intact BM3. Reaction transients were again fitted most

accurately using a biexponential expression. No major change was observed in the fast reaction rate constant (k_{obs1}) for flavin reduction (Figure 3.19). The k_{obs2} value (which was much lower) showed some apparent dependence (increase) with ionic strength. The highest k_{obs1} value was equal to 570 ± 7 s^{-1} (which presumably reflects the majority of electron transfer to the FMN, since it is faster than the rate constant for Fe(II)CO complex formation which involves electron transfer from FMN, see Figure 3.18).
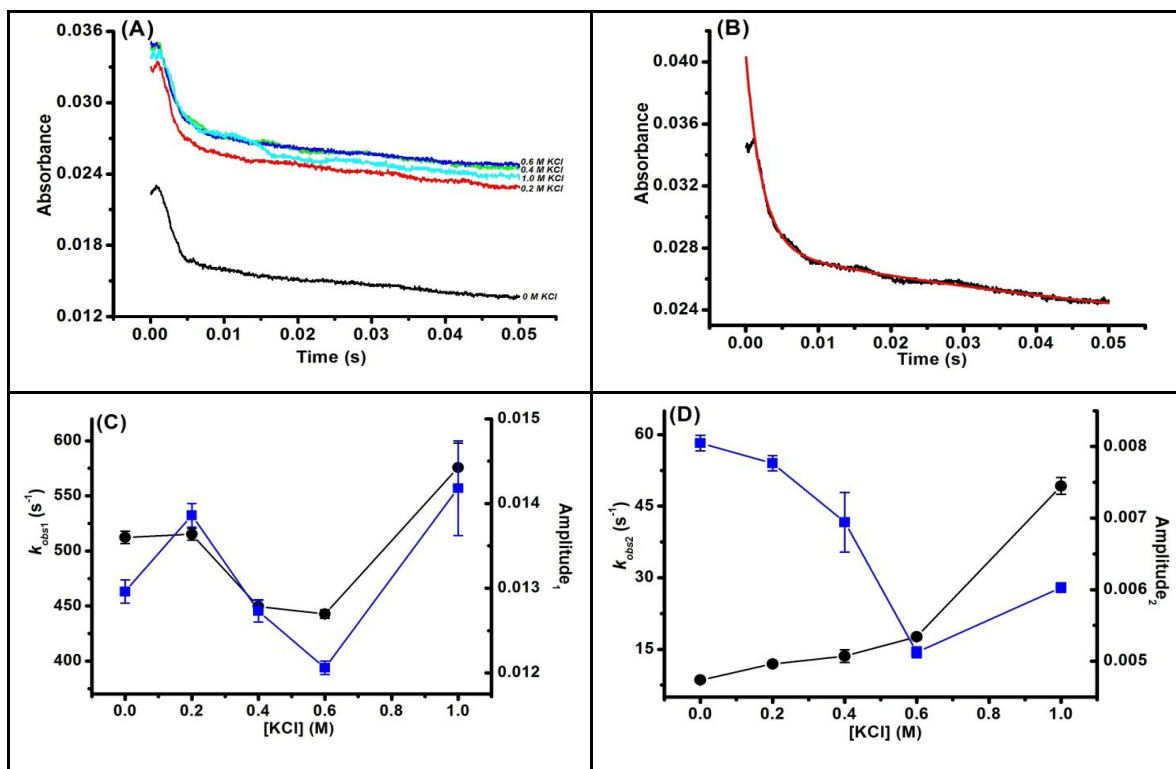
Figure 3.19: Kinetic analysis of flavin reduction in intact BM3. *(A) Absorbance traces at 475 nm and at the various KCl concentrations studied; (B) A characteristic kinetic trace (black) and double exponential fit to the trace (red) for the reduction of flavins in intact BM3 by NADPH at 0.4 M KCl. Plots showing the dependence of flavin reduction rate constants (black circles) and amplitudes (blue squares) in intact BM3 on salt concentration for the fast (C) and slow (D) phases. The experiments were conducted at 25 °C in 50 mM potassium phosphate buffer, pH 7.0 over a period of 50 milliseconds.*

As seen in Figure 3.19, reaction transients observed for flavin reduction in intact BM3 were fitted most accurately using a double exponential function. Typically, the data were not fitted as accurately when compared to the fits for heme reduction. However, reaction rate constants for flavin reduction were clearly much faster than those for heme reduction, and approaching the limit of the stopped-flow instrument, explaining the greater difficulty in obtaining highly accurate fits. Moreover, there was no significant pattern of change in the rate of flavin reduction for the fast phase (k_{obs1}), although the

slower reaction phase (k_{obs2}) did show some apparent increase in rate with higher salt concentration. The apparent rate constants for heme reduction show a different pattern of ionic strength dependence compared to those for the flavin reduction, with heme reduction rate decreasing (for both phases) as ionic strength increases, while the flavin reduction rate constants do not show any clear pattern of change for k_{obs1}, and a clear increase for k_{obs2} as ionic strength is elevated. The mechanistic origin of the slower k_{obs2} phase is unclear, but could be related, for instance, to dissociation of NADP$^+$ or to altered electrostatic interactions of the reductase flavin domains. Ionic strength could also affect heme reduction rate by disfavouring interaction of reduced FMN domain with the heme domain as ionic strength is elevated. The data collected are also consistent with the first flavin-to-heme electron transfer being the rate-limiting step in catalysis (it is much slower than flavin reduction and close to the maximal steady-state turnover rate reported for BM3) (*5*).

3.3.2.3 pH-Dependent Electron Transfer in Intact BM3

The effects of pH on the rate of electron transfer between the heme and reductase domain in the full length BM3 enzyme was also investigated under similar conditions as those for the ionic strength dependent experiments. Measurements of the rates and amplitudes were carried out in 50 mM KPi at a wavelength of 450 nm and a temperature of 25 ºC for 100 milliseconds while the pH was varied between 6.0 and 8.0 (Figure 3.20A). As seen in the ionic strength dependence measurements, data could only accurately be fitted using a double exponential equation (Figure 3.20B), resulting in fast and slow rate constants (Figure 3.20 C and D). Although there is no apparent dependence of the measured rate constants and amplitudes across the pH range studied, it was observed that the highest k_{obs1} rate constant was obtained at pH 7.0 (357.9 ± 4.2 s^{-1}).
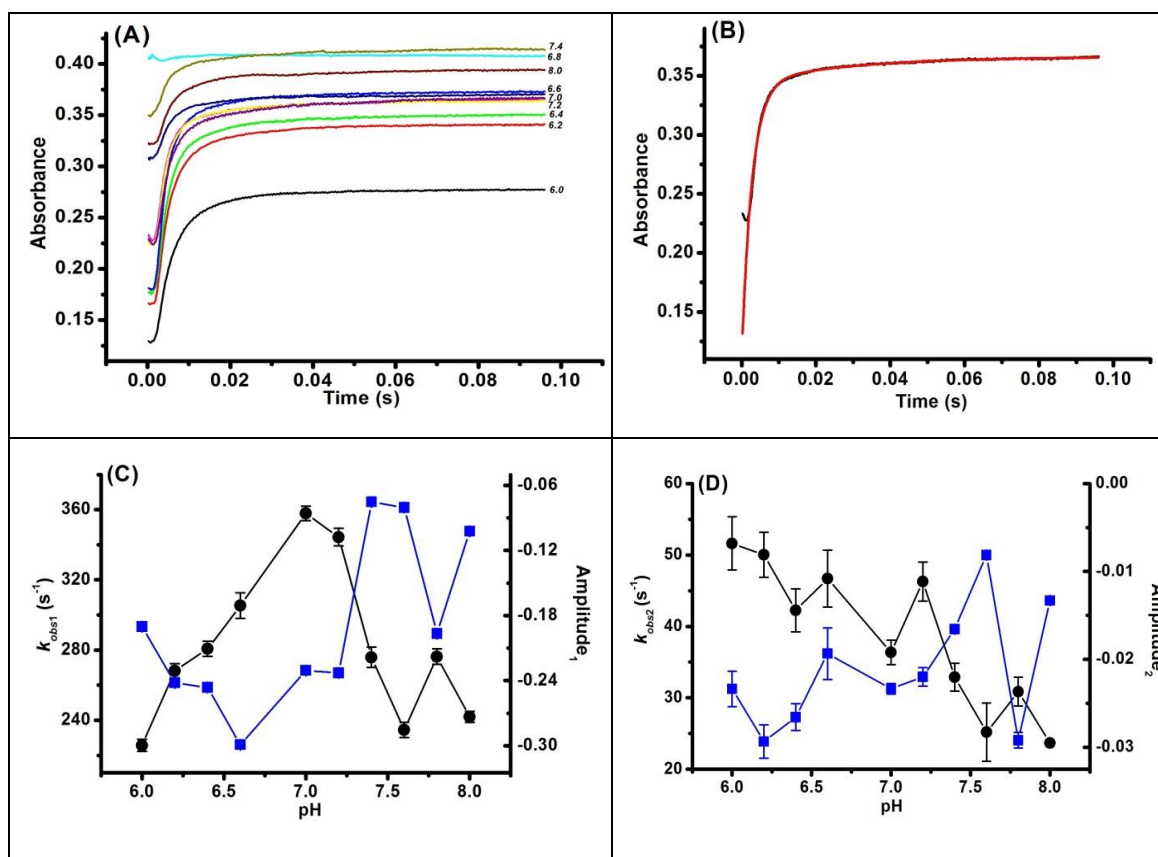
Figure 3.20: pH-dependent kinetic study of heme reduction in intact BM3. *(A) Absorbance traces at 450 nm and at the various pH values studied; (B) A characteristic kinetic trace (black) and double exponential fit to the trace (red) for heme reduction in intact BM3 at pH 7.0. The dependence of heme reduction rate constants (black circles) and amplitudes (blue squares) in intact BM3 on pH for the fast (C) and slow (D) phases are also shown. For the fast phase, the highest rate constant (357.9 ± 4.2 s^{-1}) was obtained at pH 7.0. The experiment was conducted at 25 °C in 50 mM potassium phosphate buffer over a period of 100 milliseconds.*

3.3.3 Electron Transfer in a Reconstituted BM3 Enzyme

3.3.3.1: BMR-to-BMP Electron Transfer in a Reconstituted BM3 System

The first electron transfer event between the BMR and BMP domains of P450 BM3 for the reconstituted system was examined by monitoring the rate of formation of the Fe^{2+}-CO complex at a wavelength of 450 nm. 5 µM each of BMP and BMR were mixed together in a CO-saturated 50 mM potassium phosphate buffer containing 88 µM arachidonic acid with 500 µM NADPH at pH 7.0 and absorption change was measured at 25 °C over 50 seconds. Kinetic traces (Figure 3.21A-B) showing the absorbance change (ΔA_{450}) over time indicated that data were fitted well using a double exponential function, implying that the reaction (as also observed with the intact enzyme) is biphasic. Furthermore, the observed rate constants in the absence of salt for the fast

(k_{obs1}) and slow (k_{obs2}) phases were 0.471 ± 0.040 s^{-1} and 0.09 ± 0.01 s^{-1}, respectively for the reconstituted domains. Although around a thousand fold slower than that observed with the full length enzyme, these rate constants were also seen to decrease with increasing concentration of KCl (Figure 3.21C-D).
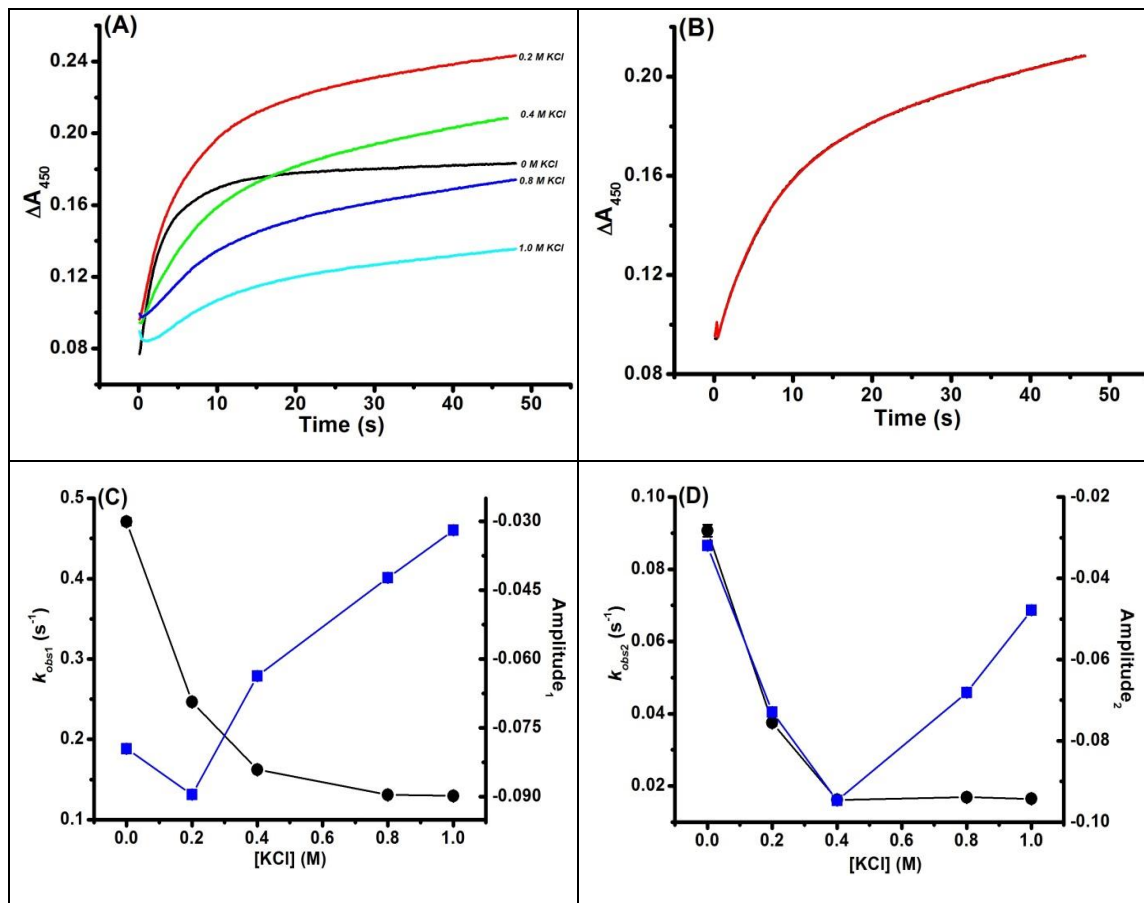
Figure 3.21: Kinetics of electron transfer between BMR and BMP domains. Absorbance traces (A) and a representative kinetic trace (black) and biphasic fit to the trace (red) (B; measured at 0.4 M KCl) showing the change in absorbance with time for the first electron transfer between the reductase and heme domains (and formation of the Fe(II)CO complex at 450 nm) in a reconstituted BMR/BMP system. Plots showing the dependence of observed rates and amplitudes on salt concentration for the fast (C) and slow (D) phases are also shown. The highest rates were obtained in the absence of KCl and the values are 0.471 ± 0.040 s^{-1} and 0.09 ± 0.01 s^{-1} respectively. A similar change in amplitude (~0.06) was observed for both phases. The experiments were conducted at 25 °C in buffer containing 50 mM potassium phosphate, pH 7.0 over a period of 50 seconds.

Both slow and fast phases exhibit similar trends in the dependence of the observed rate constants on KCl concentration. Moreover, a comparison of the data obtained for the intact enzyme with the reconstituted domains reveal that while nearly a 70 % decrease in k_{obs1} was observed with the reconstituted enzyme domains, only a 43 % decrease was

observed with the intact enzyme across the same range of ionic strength. This implies a much greater ionic strength effect on the rate of electron transfer between the reconstituted domains. It further suggests that, although the linker plays an important role in positioning the domains for proper electron transfer, there is likelihood that other factors are also relevant. Some non-covalent forces almost certainly come into play in facilitating this interaction between the reductase and the heme domains of BM3, and these are affected by changes in ionic strength for both intact BM3 and the isolated BMP/BMR domains.

3.3.3.2: BMR-BMP electron transfer in a reconstituted BM3 system over an extended timescale

Although the kinetic trace shown in Figure 3.21B fits well to a double exponential function, it is evident that the reaction has not come to an end, reflecting the much slower transfer between the isolated domains. Thus the experiment was left to run over 900 seconds under the same operating conditions and the resulting absorbance traces with representative double exponential fits to the data are shown in Figure 3.22 A-C.
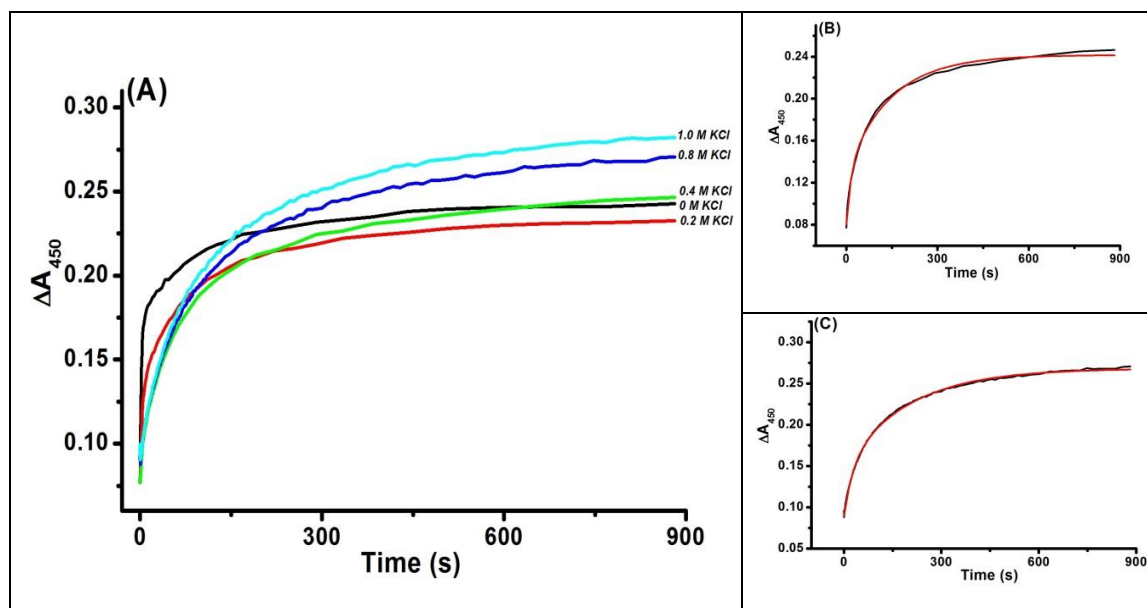
Figure 3.22: BM3 BMR–to-BMP electron transfer over an extended time scale. The resulting absorbance traces (A) and representative kinetic transient (black) and double exponential data fit (red) measured at 0.4 M KCl (B) and 0.8 M KCl (C) showing the change in absorbance with time for the first electron transfer between the reductase and heme domains (forming a Fe(II)CO complex in a reconstituted BM3 system). Experiments were conducted at 25 °C in buffer containing 50 mM potassium phosphate, pH 7.0 with data accumulation for 900 seconds.

Since the experiment was conducted using a PDA (photodiode array attachment enabling rapid capture of multi-wavelength data) the data were fitted using the accompanying Applied Photophysics ProK software (which fits the whole data set at all wavelengths by global analysis) and using Origin software (which fits only single wavelength data). To fit in Origin, the data were exported as CSV files; the trace at 450 nm singled out, and then fitted using a double exponential function (representative traces shown in Figure 3.22B-C). There is good agreement between the fits obtained from both data analysis tools (data not shown).

Comparing the traces in Figures 3.21A and 3.22A, the reaction does not go to completion at 50 seconds, but to near-completion at 900 seconds. Thus, experiments for the isolated domains need to be run for a longer period of time to ensure that the data set collected is more complete. While the fast rate constants (k_{obs1}) observed for both timescales are similar, the slow rate constants (k_{obs2}) are significantly higher for measurements made over 50 seconds (Figure 3.23A-B). Also, the value obtained for k_{obs1} (0.471 ± 0.005 s^{-1}) is slightly higher at 900 seconds (0.493 ± 0.013 s^{-1}) when compared to k_{obs1} at 50 seconds. The variability in apparent rate constants determined over the two timescales suggested that factor(s) other than direct reduction of BMP and BMR might influence the reaction over extended reaction times. The most obvious of these could be direct reduction of heme iron by NADPH. To eliminate the contribution of non-specific background rates contributing to the observed rate constants measured at 900 seconds (i.e. any direct heme reduction by NADPH), further experiments were conducted under the same conditions in the absence of the reductase domain. This is discussed in the following section.
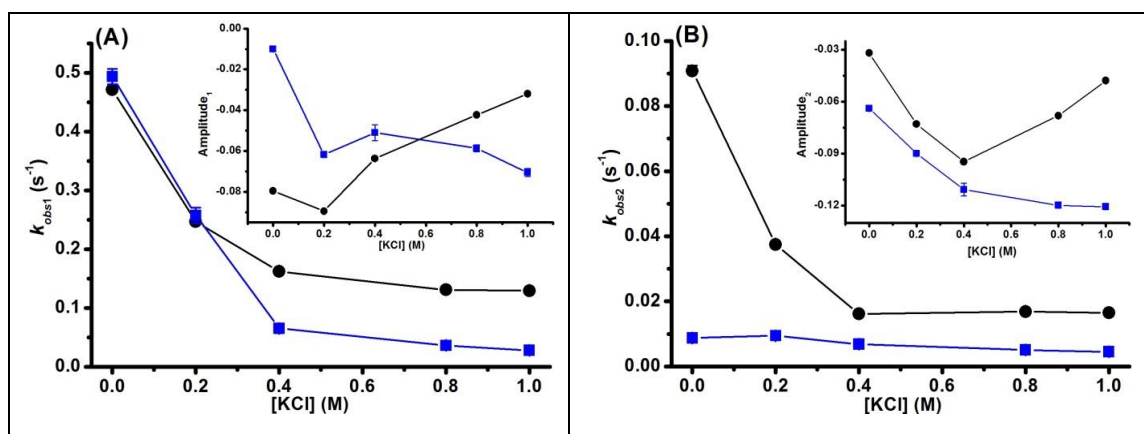
Figure 3.23: A comparison of the observed rate constants and amplitudes for A450 development following in the interaction between BMR and BMP domains of P450 BM3. The plots show fits obtained from measurements at 50 seconds (black circles) and 900 seconds (blue squares) for k_{obs1} (A) and k_{obs2} (B) at different KCl concentrations while insets show corresponding amplitude measurements.

3.3.3.3 NADPH-Dependent Reduction of BMP Heme in the Absence of the BMR Domain

In order to ensure that the rate constants obtained for the reduction of BMP domain (given that they were much slower for experiments done using BMR/BMP compared to those in the intact BM3) were not affected by direct reduction by the coenzyme (NADPH), an experiment was conducted to investigate direct reduction of BMP by NADPH in the absence of the reductase domain. Stopped-flow analysis was carried out at 25 °C over 1000 seconds in CO-saturated 50 mM potassium phosphate also containing 88 µM arachidonic acid at pH 7.0. The first syringe contained 500 µM NADPH while the second had 10 µM BMP. As seen in the singled-out absorbance traces at 450 nm (Figure 3.24A), an exponential reaction occurs with increasing A_{450}, similar to that seen in the presence of the BMR domain (See Figure 3.22A). This is characteristic of the formation of a Fe^{2+}-CO complex. As shown in Figure 3.16, CO-binding occurs once the heme iron has been reduced from the ferric to the ferrous form. This figure further indicates that the heme iron accepts an electron from the reduced FMN, reducing it from the ferric to ferrous form, and enabling binding of CO. Thus, for a ferrous-CO adduct to be formed, it should be the case that the BMP's reductase domain (fused or separate) should be present. However the absorbance data in Figure 3.24 show that the formation of a Fe^{2+}-CO complex can occur with NADPH in the absence of the reductase, as well as in the presence of BMR. Thus the heme iron can be

directly reduced by NADPH in the absence of the reductase domain, albeit only when the experiment is conducted over a long period of time.
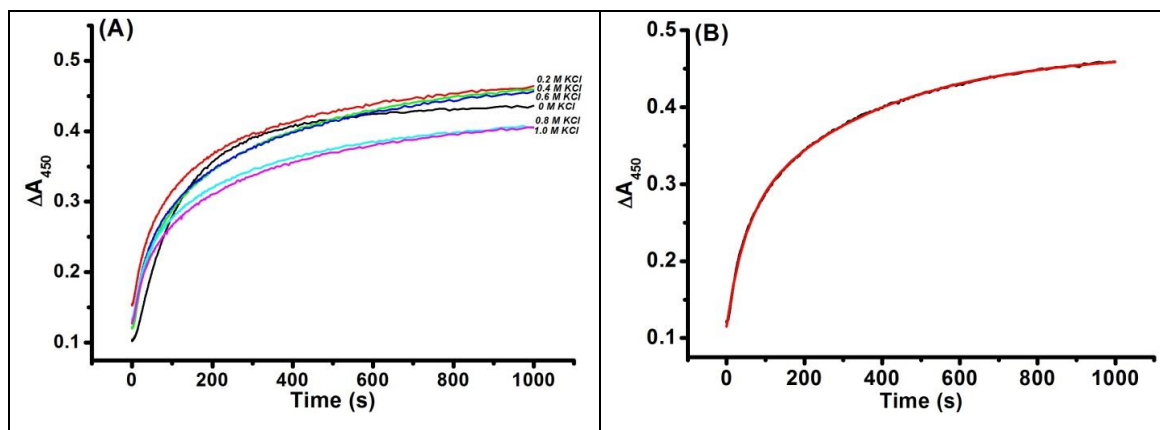
Figure 3.24: Direct reduction of BMP by NADPH. *Stopped-flow absorption traces (A) and a double exponential fit to the trace measured at 0.4M KCl (B) showing the reduction of 10 μM BM3 P450 domain by excess (500 μM) NADPH in the absence of reductase, monitored over 1000 seconds. Experiments were conducted at 25 °C in 50 mM potassium phosphate buffer, 600 mM KCl, pH 7.0.*

Fitting the resulting data using any form of exponential function (single or multiple) posed a great challenge. Attempts to fit the data using single, double and even triple exponential functions using the global analysis software (Applied Photophysics ProK), to fit full spectral changes were unsuccessful. The process was possibly complicated by the changing spectral contributions from both NADPH and BM3 heme domain during the reaction. In attempts to solve this issue, using Origin, the traces only at 450 nm were fitted using a single exponential function (for the 0 M KCl concentration) and a double exponential function (for other data set collected from 0.1-1.0 M KCl). Although the reaction transients (Figure 3.24B) were fitted well using a double exponential function, relatively small changes in the amplitudes of the transients used for fitting resulted in changes to the rate constants, likely indicating that the reactions had not progressed to completion over the timescale used. This may result from factors such as the long duration of time over which the absorbance changes were monitored, back electron transfer from BMP heme to FMN (in reactions using BMR), or dissociation of CO/oxidation of heme iron. The rate constants and amplitudes obtained for reduction of the heme domain directly (by NADPH) and in the presence of reductase domains are compared in Figure 3.25. According to the data collected, the rate constants and amplitudes obtained for the reduction of heme in the presence of reductase are much higher (up to 90% in the fast phase at low KCl concentration; Figure 3.25A) than those

obtained in the absence of reductase. It can be deduced from these data that in electron transfer reactions between BMR and BMP a proportion of the electron transfer to the heme is directly from NADPH while the remainder occurs via the reduced reductase domain. Again this conclusion is drawn with some caution given the complexities associated with estimating the rates for direct reduction of heme by NADPH.
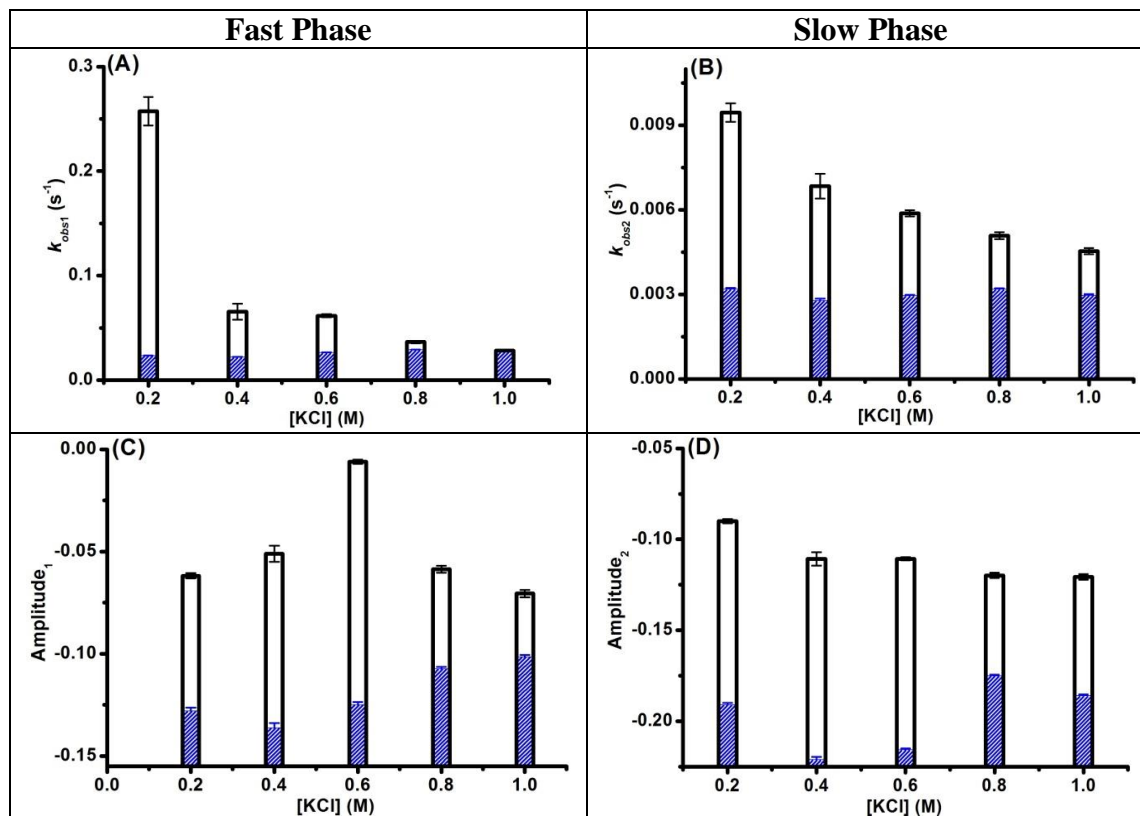
Figure 3.25: A comparison of electron transfer rate constants (A-B) and amplitudes (C-D) obtained for direct reduction of heme by NADPH in the presence of reductase (white bars) and in the absence of reductase (blue striped bars).

3.3.3.4 Effects of DTT on Electron Transfer between BMP and BMR in Reconstituted BM3

As reviewed in section 1.2.7, research suggests that the presence of disulfide bonds in the FAD and BMR domains play a major role in its dimerization and might also be important in the dimerization of the full length enzyme. Thus, measurements of electron transfer from the BMR to the BMP domains in reconstituted BM3 were also carried out in the presence of 10 mM DTT for comparison purposes. The experiment was conducted using 5 µM each of the BMP and BMR domains in CO-saturated 50 mM potassium phosphate buffer containing 88 µM arachidonic acid with 500 µM NADPH

at pH 7.0, with the change in absorbance monitored at 450 nm and at 25 °C over 100 seconds. The resulting absorbance traces fitted well to a double exponential equation. The comparison plot (Figure 3.26) shows that there is no major change in the rate constants determined at low KCl concentration (below 0.2 M KCl) for both the slow and fast phases. However as the ionic strength increases, higher rate constants are obtained for measurements in the presence of DTT for both phases. Further, higher amplitudes were recorded for experiments conducted in the presence of DTT for both the slow and fast phases.
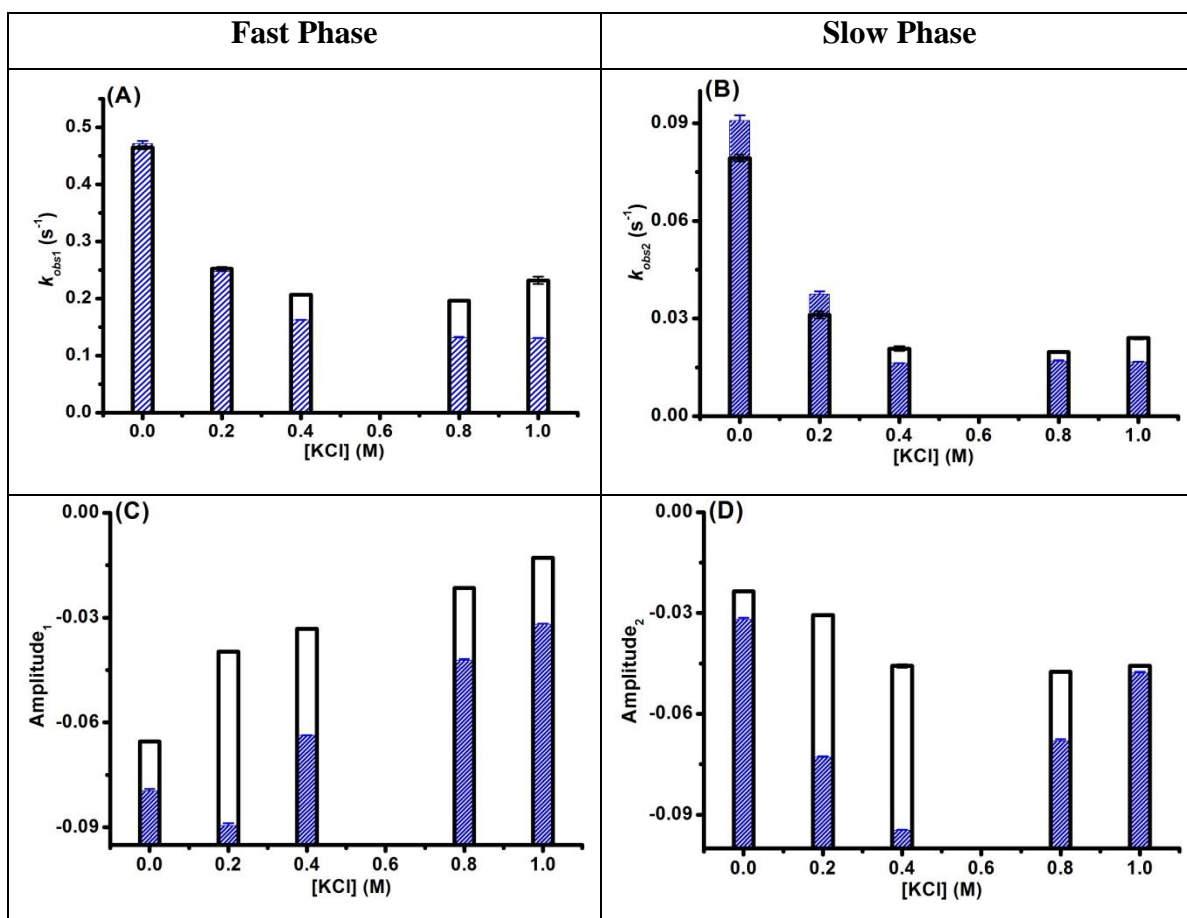
Figure 3.26: A comparison of electron transfer rate constants (A-B) and amplitudes (C-D) for A450 (Fe(II)CO complex) development following the interaction between the reconstituted BMP and BMR domains of P450 BM3 in the presence of DTT (white bars) and in the absence of DTT (blue striped bars).

3.3.3.5 Electron Transfer in Reconstituted Domains – Is it a Bimolecular Reaction?

The rate of unimolecular reactions does not depend on the concentration of the reactants. Using this as the basis, an experiment was conducted to establish that the reaction between the reconstituted BMP and BMR domains was bimolecular. This was done by examining the dependence of the observed electron transfer rate constants on the concentration of the reductase domain while the concentration of the P450 domain was fixed. This experiment was conducted in 50 mM phosphate buffer with 0.2 M KCl at pH 7.0, and at a temperature of 25 °C for 100 seconds.

According to the law of mass action, the dissociation constant for protein binding to a ligand (or to another protein) is calculated using the equation:

$$K_d = \frac{k_{off}}{k_{on}}$$

(3.1)

Equation 3.1: Dissociation constant for equilibrium binding: *where* K_d *is the dissociation constant in M,* k_{off} *is the dissociation (unimolecular) rate constant in units of* s^{-1}*, and* k_{on} *is the association (bimolecular) rate constant of the complex in units of* $M^{-1} s^{-1}$*.*

This concept is often applied in enzyme kinetic studies to estimate the dissociation constant from a plot of the rate constant for formation of an enzyme-substrate (or protein-protein) complex against the concentration (varied) for the substrate (protein).

Figure 3.27 shows the resulting reaction transients alongside the rate constants and amplitudes observed. Experimental results indicate a linear dependence of the fast reaction rate constants (i.e. k_{obs1} for Fe(II)CO complex formation) on the concentration of BMR at 0.2 M KCl (Figure 3.27 C). Fitting the k_{obs1} data for Fe(II)CO complex formation versus [BMR] to a linear function gave k_{off} (intercept of the linear graph on Y-axis) and k_{on} (slope of the linear graph) values of 0.1203 ± 0.0015 s^{-1} and 0.0162 ± 0.0002 $\mu M^{-1}s^{-1}$ respectively. Applying these values to equation 3.1 resulted in a dissociation constant of 7.68 ± 0.13 μM. The observed linear dependence is an indication that electron transfer between the FMN and heme domains of the reconstituted enzyme occurs via a bimolecular reaction mechanism.
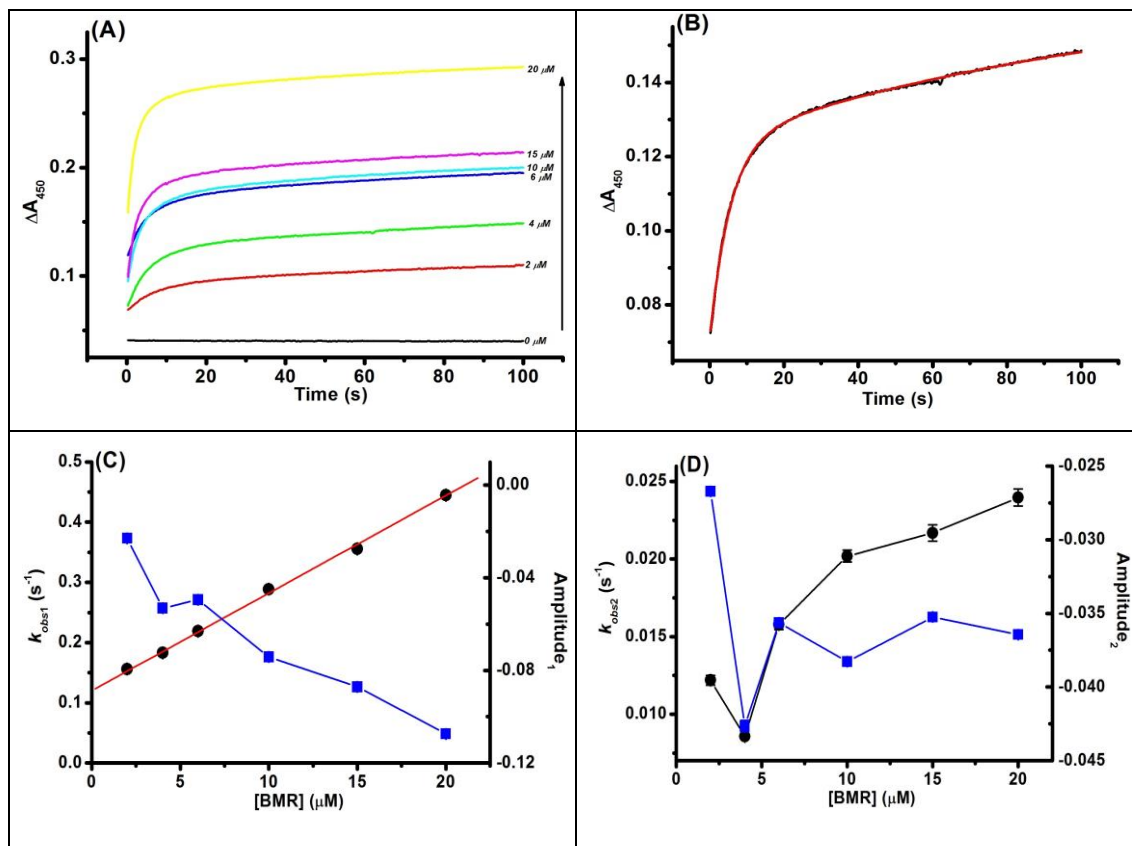
Figure 3.27: Dependence of BMP Fe(II)CO complex formation on [BMR]. *ΔA_{450} reaction transients showing the reduction of 5 µM P450 BM3 heme domain by 0-20 µM BM3 reductase domain (A) and a characteristic double exponential fit (red) for the trace measured at 4 µM BMR (black). Arrow shows increasing concentration of reductase domain. The double exponential fits yield rate constants (black circles) and amplitudes (blue squares) for the fast (C) and slow phases (D). A linear dependence of the electron transfer rate (k_{obs1} for ΔA_{450}) on BMR concentration is observed which fits accurately to a linear equation (red line in C) yielding k_{off} and k_{on} of 0.1203 ± 0.0015 s^{-1} and 0.0162 ± 0.0002 µM^{-1}s^{-1} respectively. Experiment was carried out at 25 °C in 50 mM potassium phosphate buffer, 0.2 M KCl, pH 7.0 for 100 seconds.*

3.4 DISCUSSION

3.4.1 UV-Visible Analysis of Ligand Binding to P450 BM3 Heme Domain

In studies to measure the dissociation values for substrates and inhibitors binding to the BM3 heme domain, absorbance spectra were generated at different ligand concentrations. Comparing the spectra obtained for substrate-bound enzyme with those for inhibitor-bound enzyme, two significant differences are observed. First, there was no increase in the peak at 650 nm on binding of inhibitors like those observed with the substrate binding. This implies that there was no formation of high-spin ferric species

with the inhibitor binding leaving the heme iron in the low-spin ferric form, as expected from studies on a large number of other cytochromes P450 with imidazole/azole-based inhibitors of the type used in these studies on BM3 (*153, 154*). Second, the magnitudes of the Soret band shift for both substrate- and inhibitor-bound forms are not the same. While a 7 nm (or even 5 nm as observed by (*154*)) shift in wavelength is observed for both weakly- and tightly-bound azole inhibitors (a red shift), the shift for NPG is observed to be about 28 nm (a blue shift). These types of inhibitor- and substrate-induced shift to longer and shorter wavelengths, respectively, were also noticed with P450cam and with numerous other P450 enzymes (*288*), and are referred to as type II and type I P450 shifts, respectively.

Inhibitor binding studies showed that association of imidazole resulted in a substantial decrease in Soret intensity, while 4-phenyl imidazole did not give such a significant decrease. This difference in the extent of the decrease in absorption intensities for the two inhibitors used in this study was also observed by Smith *et al.* (*153*) who used resonance Raman (RR) spectroscopy to study the effects of imidazole and imidazolyl derivatives on the enzyme structure. Structural information on the effects of inhibitors on heme centres can be obtained from RR spectroscopy, which is used to measure the vibrational characteristics of these centres characterized by specific wavenumbers that generally correlate with heme iron oxidation, spin or coordination state, and/or with heme conformational properties. In their studies, Smith *et al.* (*153*) observed "small but appreciable differences in the magnitude of the change in intensities" of two peaks between the RR spectra obtained for the imidazole-bound BM3 and the 4-PI/1-PI imidazole-bound BM3. This observation led to the suggestion that the inhibitors might exhibit differing steric effects on the enzyme's active site. In addition, with the recently solved crystal structure of N-fatty acylated imidazole-BMP (i.e when bound to N-(12-imidazolyldodecanoyl)-L-leucine(*154*), a more open conformation (when compared with the substrate-bound form) was observed (Figure 3.28) and steric clashes between the imidazole ring and some active site residues were confirmed.
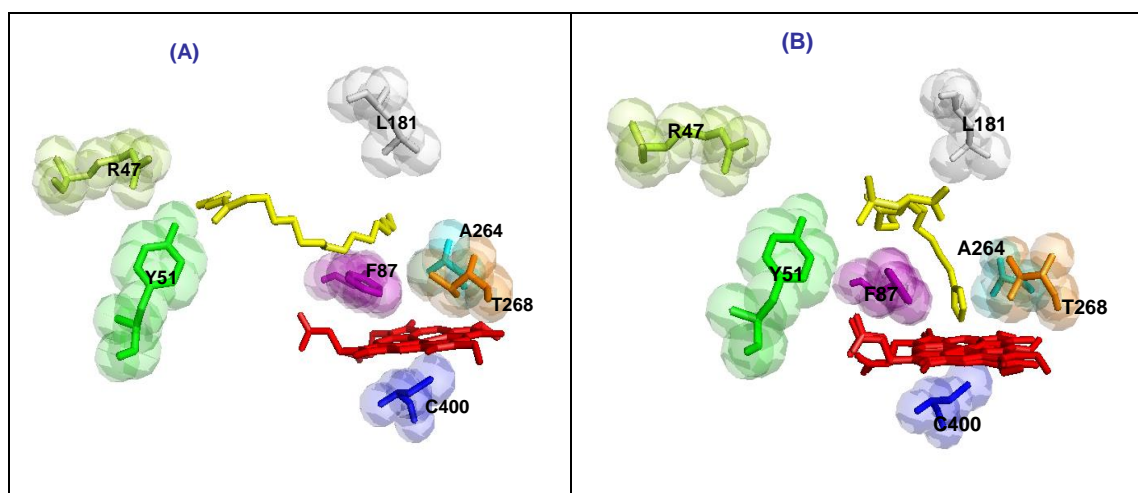
Figure 3.28: Active site of BM3 heme domain in N-palmitoyl glycine and N-(12-imidazolyldodecanoyl)-L-leucine complexes. The images show the active site conformations of substrate-bound (A) and inhibitor-bound (B) P450 domain of BM3. The substrate (N-palmitoyl glycine, NPG) and inhibitor (N-(12-imidazolyldodecanoyl)-L-leucine) are coloured yellow and the heme coloured red. Key active site residues involved in substrate binding (Y51, R47, L181), control of iron-oxo intermediate protonation/regioselectivity of substrate oxidation (A264, T268, F87) and heme iron ligation (C400) of BM3 are shown. Differences in conformation of various amino acid side chains are observed, and the heme domains occupy different conformational states.

Measured values of dissociation constants indicate that 4-PI binds more tightly to BM3's active site/heme iron than does imidazole. This tighter binding has also been observed with other imidazolyl derivatives. For long chain fatty acids incorporating an imidazole moiety, tight binding was observed, with dissociation constants in the region of 0.2 to 30 μM (*294*). Addition of fatty acid head groups to imidazoles (with the carboxylic acid group in place) resulted in an increased inhibitor potency with dissociation constants of ~1.2 to 18 μM depending on the fatty acids used (*154*). The fatty acid carboxylic group likely 'docks' in the substrate carboxylate binding position, stabilized by the side chains of Arg47 and Tyr51, and high affinity for these molecules is also due to other stabilizing interactions formed by the alkyl chain of the modified azoles with the P450 active site, as well as from the binding of the azole group to the heme iron (*5*).

As pointed out by Sevrioukova and Peterson (*176*), literature results on the rates at which BMR and intact P450 BM3 reduce cytochrome *c* are quite confusing, since different rates are reported by different authors. This discrepancy is mainly attributed to the differences in the reaction conditions used. At a salt concentration of 300 mM KPi and pH 7.0, Li *et al* (*295*) noticed a higher turnover number of BMR-cytochrome *c*

reductase activities when compared to that of BM3. On the other hand, Oster *et al.* (*296*) using a buffer condition of 20 mM MOPS, 0.1 M KCl, pH 7.0 observed that the cytochrome *c* reductase activity of BMR was approximately 50 % that of BM3 under the same conditions. With the addition of excess FMN, this reductase activity of BMR increased (by nearly 50%) up to the value obtained for BM3, suggesting that cytochrome *c* can accept electrons from both the reductase domains and free FMN. In both cases, however, the activity of BM3 was higher than that of BMR. Under the same pH and buffer conditions, Munro *et al.* (*116*) also observed a slightly higher activity for BM3 than for BMR. Running the same experiment at the same pH across a range of potassium phosphate concentrations (2-300 mM KPi), Sevrioukova and Peterson (*176*) showed that, irrespective of the ionic strength of the buffer, the cytochrome *c* reductase activities of BM3 are higher than that of BMR. All of the studies mentioned above were conducted under steady-state conditions.

The rates obtained in this study are in good agreement with those of Li *et al.* (*295*), as cytochrome *c* reductase activities of BMR are doubled when assayed with the intact BM3 enzyme. Taking into consideration both the K_M and k_{cat} values, the relative catalytic efficiencies of the intact enzyme are higher than the reductase domain in cytochrome *c* reduction catalysis. Moreover, based on the K_M, the apparent binding affinity of BM3 for cytochrome *c* is tighter than that for BMR. This might support the hypothesis that the presence of the heme domain (with BM3) prevents unsuccessful collisions between the FMN domain and cytochrome *c* (*176*), or that the heme domain promotes binding of cytochrome *c* in the correct configuration(s) for its reduction.

3.4.2 Stopped-flow kinetic analysis of BM3 electron transfer reactions

Analysis of the effects of ionic strength on the reaction rates and affinities between redox partners is useful in understanding the mode of interaction between these partners. In cytochromes P450, these studies have been conducted for single (*i.e.* P450 and other reductases) and mixed reconstituted systems (*i.e.* P450-P450 and other reductases). Among the most widely characterized are the interactions between cytochrome P450 reductase (CPR) and its partners the P450s, and cytochromes *c* and b_5. The studies of salt effects coupled with chemical modification of charged residues on the surfaces of CPR and the cytochromes have shown that charge pairing plays a dominant role in the binding and electron transfer between these redox partners (*261,*

262, 297-299). Furthermore, the influence of ionic strength on the rates of electron transfer between a number of bacterial P450s and their redox partners (P450cam and putidaredoxin; and P450cin and cindoxin) has also been investigated. The results obtained in both cases suggested the involvement of electrostatic interactions in the association (*300-302*). Davydov *et al.* (*261*) used FRET (fluorescence resonance energy transfer) to examine the mode of interaction between the P450 (BMP) and reductase (BMR) domains of BM3, and observed electrostatic repulsion and low affinity between the proteins.

In this work, stopped-flow techniques were employed to investigate the mode of interactions between the P450 and reductase domains of BM3 by analyzing the dependence of electron transfer rates between BMR and BMP domains as a function of varying ionic strength and pH. The electron transfer rate was found to be around a thousand fold faster in the intact enzyme than with the reconstituted domains. This observation is consistent with the results of Munro *et al.* and of Miles *et al.* (*7, 178*) that showed the rates of NADPH oxidation and fatty acid hydroxylase activities, respectively, of the reconstituted domains were approximately a thousand-fold lower than those for intact BM3. This affirms the role of the linker region in efficient functioning of the BM3 system. Moreover, the massive decrease in electron transfer rates between the two systems indicate that BMP-BMR interactions in the reconstituted system are weak and hence a perfect model for analyzing the weak interactions between these systems, which is a major goal of this study.

Despite the differences in electron transfer rates for the intact flavocytochrome and the reconstituted systems, a decrease in electron transfer rate is observed as the ionic strength is increased in both cases (Figures 3.18 and 3.21). Using an online bioinformatics tool, the isoelectric points (where the net charge on the protein is zero) of BMP and BMR are estimated at 6.17 and 5.02 respectively (protein calculator version 3.3) (*303*). Usually, when the pH of a buffer solution is increased above the isoelectric points of proteins in the solution, there is a net increase in the negative charges on the protein surfaces. Using the same tool, the net charges on the surfaces of BMP and BMR at pH 7 (pH used in this study) are estimated at -6.9 and -27.5. It is thus expected that since both BMR and BMP have the same net (negative) charges on their surfaces, electrostatic repulsive interactions will dominate, and that these interactions will be screened as the salt concentrations are increased. Page *et al.* (*304*), via electron

tunneling analyses on redox proteins, observed that electrons can only "jump" up to a maximum of 14 Å between two redox centres. Thus, screening of the surface charges on both proteins with increasing salt concentrations should minimize the repulsive effects of the surface charges, enabling domain interactions, thus enhancing the inter-protein electron transfer rates. Hence, the decrease in electron transfer rate as a function of salt concentration observed in this study is rather unexpected. This decrease was also observed for the second electron transfer between putidaredoxin (pdx) and its partner, P450cam (*300*). In this case, the authors suggested that there was apparently no net repulsion between the complexes, which is expected given that both proteins also had the same isoelectric points. They attributed the decrease to an electrostatic effect on the proteins. However, this suggestion may not be applied in the case of BMP-BMR, as preliminary light scattering studies on the complex showed electrostatic repulsion between the domains, which became attractive as the salt concentration was increased (*305*). Further, using a combination of FRET and kinetic modeling analyses, electrostatic repulsion was observed for BMP-BMR complex (*261*). It is important to point out that studies confirming electrostatic repulsion were carried out with the oxidized domains of BM3, and that those on electron transfer rates were conducted with the reduced domains of the enzyme. Thus, the behaviour of the domains may be different in the oxidized and reduced enzyme forms. Certainly, the relative conformations of the FAD- and FMN-domains of the reductase likely change according to the redox state of this domain. Studies on the BM3 enzyme have shown that, when the FMN domain is reduced (and possibly as a consequence of NADP(H) binding and debinding), the FMN domain likely re-arranges its conformation to sit in a position where electrons can transfer more efficiently from the FMN cofactor to the heme (*163*). This implies that the distance between these two domains (BMP and BMR) is crucial for electron transfer. An alternative explanation for the decreased electron transfer rates with increasing salt concentration is that repulsive effects are indeed screened, but that this leads to a promotion of non-specific interactions between BMP and BMR domains that are non-productive with respect to FMN-to-heme reduction. It is likely that the productive docking of BMR with BMP results in the exposed FMN dimethyl group region contacting the proximal face of the heme in the region of the cysteine-iron bond to enable electron transfer.

 Using laser flash photolysis, direct reduction of BMP by NADPH was induced at a very fast rate on the microsecond time scale (*292*). In this work, it was observed that the

same end effect can be achieved without laser induction when electron transfer is monitored spectroscopically following stopped-flow mixing for a period of 1000 seconds. In the laser photoexcitation studies, the ultimate reductant is likely a hydrated electron or a coenzyme radical formed by laser irradiation of NADPH. The mechanism of the slow reduction of the P450 heme by non-irradiated NADPH remains unclear, although a much less efficient photo-induced reduction cannot be ruled out at this stage. The data presented in Figure 3.25 suggest that a proportion of the BMP heme iron is reduced directly from NADPH, while the remainder is reduced by the NADPH-reduced reductase domain. However, data presented in Figure 3.27 are consistent with productive electron transfer reactions involving electron transfer from the reductase domain. Thus, the balance is likely heavily in favour of BMP reduction by BMR and direct reduction of BMP by NADPH is a very slow process. Davydov *et al.* (*261*) studied the kinetics of electron transfer between BMR-BMP and rabbit liver CPR-BMP for approximately 4000 seconds in the presence of NADPH. Based on this study, the authors inferred that "the electron transfer in the flavoprotein-P450 complex is determined mostly by the nature of the flavoprotein". While this might be true, it is advisable that care should be taken when interpreting results derived from such experiments over a long period of time, as there may be other contributing factors (e.g. direct reduction of the coenzyme), as seen in this study.

In summary, substrate binding to BM3 results in blue, type I Soret spectral shifts, while binding of inhibitors (i.e. those that coordinate to the heme iron) results in red, type II Soret shifts. The observed shift direction and magnitude is consistent with studies on other cytochromes P450. Further, results have shown that the electron transfer rate between BMR and BMP domains in the reconstituted system is about a thousand fold less than the rate observed in the intact enzyme. This may also be a consequence of the dimeric state of the intact BM3, which enables efficient interactions between relevant FMN/BMP domains on opposite monomers (*9*). Moreover, the observed decrease in the electron transfer rates as a function of salt concentration is unexpected and is inconsistent with light scattering results (*305*) and data in the literature (*261*). However, this inconsistency could be explained by the fact that, while the literature data report studies conducted on the oxidized forms of the enzyme, studies in this report were carried out with the reduced forms of the enzyme; or (possibly and more likely) that high salt conditions screens repulsive inter-domain interactions, but at the expense of promoting non-specific interactions between BMR and BMP. Direct reduction of BMP

by NADPH in the absence of the reductase domain has been reported for the first time in this work, and was most noticeable when the experiment was conducted over 1000 seconds. This brings to fore the need to take caution while interpreting results obtained from studies on incubation of BM3 enzyme with NADPH over a long period of time, and particularly in relation to the relatively inefficient interactions between the dissected BMP and BMR domains. It should also be noted that NADPH-dependent reduction of the BM3 BMR domain will result (within a few seconds) in the accumulation of FMN hydroquinone, and that this form of the flavin is a less effective reductant of the BM3 heme iron (*4, 306*).

Having observed the effects of salt on electron transfer rates in the intact and domain-dissected forms of the enzyme, it is pertinent to conduct an elaborate analysis on the interactions between both reduced and oxidized forms of these enzymes. This is the focus of the following chapters where techniques such as Analytical Ultracentrifugation (AUC) and various light scattering techniques are employed to further investigate interactions within the different domains and the full length enzyme. In addition, these techniques are extended to the examination of the oligomerization states of BM3 enzyme in solution and further information on the nature of these oligomers will be drawn from detailed structural analysis using scattering techniques such as small angle X-ray scattering (SAXS).

CHAPTER 4

Biophysical Characterization of Flavocytochrome P450 BM3 and Its Domains

CHAPTER FOUR: BIOPHYSICAL CHARACTERIZATION OF FLAVOCYTOCHROME P450 BM3 AND ITS DOMAINS.

4.0 INTRODUCTION

The major aim of this study is to understand the structure of flavocytochrome P450 BM3 via characterization of the weak protein-protein interactions that occur between the various domains of BM3. In the previous chapter, the various steps leading to the production of very pure full length BM3 (BM3) and its P450 (BMP) and reductase (BMR) domains required for all assays were demonstrated. Further, steady-state kinetics and stopped-flow assays were employed in the study of the binding and kinetics of full length BM3, BMP and BMR.

As reviewed in section 1.2.3.1, flavocytochrome P450 BM3 is a self-sufficient multi-domain enzyme with its P450 and reductase domains tethered together on a single polypeptide chain of 119 kDa. Further, the reductase domain can be separated into the FAD and FMN domains (*62*). Electron transfer occurs across the three domains in the order FAD-to-FMN-to-P450. Fortunately, these three domains have all been crystallized, but crystal structures for the full length enzyme and the reductase domain are not available yet. This in turn hinders full understanding of the structural properties of BM3 and the reductase domain, in relation to its function.

In this chapter, the structural properties of BM3 will be examined with focus on identification and characterization of the oligomerization states of BM3, BMP, BMR and subdomains of BMR (FAD and FMN domains). SEC-MALLS was used for the initial examination of the oligomeric states. More detailed analysis required using sedimentation velocity and equilibrium methods, and static and dynamic light scattering, and cross-linking was used for further characterisation of the resulting oligomers. Further, the role of disulfide linkages in the dimerization of BM3, BMR and FAD domains, as previously reported (*107, 109*), is investigated and discussed in this chapter.

BM3 has been shown to be a self-sufficient fatty acid hydroxylase and its fastest activity (17,100 min^{-1}) was recorded with arachidonic acid (*119*). Also, NPG has been

demonstrated to exhibit high binding affinity (in terms of dissociation constant) for full length BM3 (K_d of 290 nM; (*307*)) and for the heme domain (K_d of 63 nM; Table 3.2). Moreover, NADPH-dependent lauric acid oxidation studies have indicated that the dimeric form of BM3 is the catalytically active form for fatty acid hydroxylation. Thus it is pertinent to evaluate the effects of fatty acid binding (using NPG) on the dimerization of BM3 as measured by SEC-MALLS and AUC in this chapter.

4.1 SEC-MALLS ANALYSIS ON BM3 AND ITS DOMAINS

Characterization of the oligomeric states of flavocytochrome BM3 and its domains were initially carried out using size exclusion chromatography (SEC) in series with an on-line multi-angle laser light scattering (MALLS) detector with a quasi-elastic light scattering (QELS) detector installed at an angle of 135 degrees, and refractive index and UV detectors for concentration measurements. SEC is a widely used technique for determining the oligomeric states of macromolecules in solution. More precise and accurate results are obtained by coupling of SEC to MALLS, as used in this study.

The SEC-MALLS-QELS technique was used to look at the distribution of species in the P450 BM3 enzyme (which is mainly dimeric) and its domains (some of which also oligomerize). The molecular weight estimates that come from MALLS are reported in order to show that the methodology can give reasonably accurate estimates of mass, but not to provide an exact mass – which is known already from the amino acid sequences of the protein and previous mass spectrometry studies in the area. SEC-MALLS-QELS provides hydrodynamic information about the sample analysed – including hydrodynamic radius and radius of gyration. Mass spectrometry methods are not available that provide such data.

Prior to all measurements, a size-exclusion Superdex 200 10/300 GL column was pre-equilibrated with the required buffer and samples were applied (at a flow rate of 0.71 mL/min) to the column to remove any aggregates or smaller molecules. The purified fraction was then used in the SEC-MALLS experiment following the experimental procedure outlined in section 2.4.1. Samples were injected onto the size exclusion column using a 200 or 500 µL loop and the set-up was run at a flow rate of 0.71 mL/min. Data collection and analysis were carried out using the accompanying ASTRA 5.3.4.13 software.

4.1.1 SEC-MALLS on Full Length Flavocytochrome P450 BM3

4.1.1.1 Dimerization of BM3

The oligomeric state of full length BM3 was initially determined by SEC-MALLS with an injection of 500 µL containing 1.8 mg/mL BM3 using a mobile phase of 100 mM KCl and 50 mM potassium phosphate buffer (pH 7). The chromatogram shown in Figure 4.1 indicates that BM3 eluted as a single broad peak. The weight average molecular weight of the protein contained in the resulting peak was estimated from the MALLS data to be approximately 198.6 ± 12.3 kDa while a peak concentration of 1.6 mg/mL was obtained. A dynamic light scattering detector was used to measure the average hydrodynamic radii (r_H) of the BM3 sample and a value of 5.73 ± 0.36 nm was obtained.
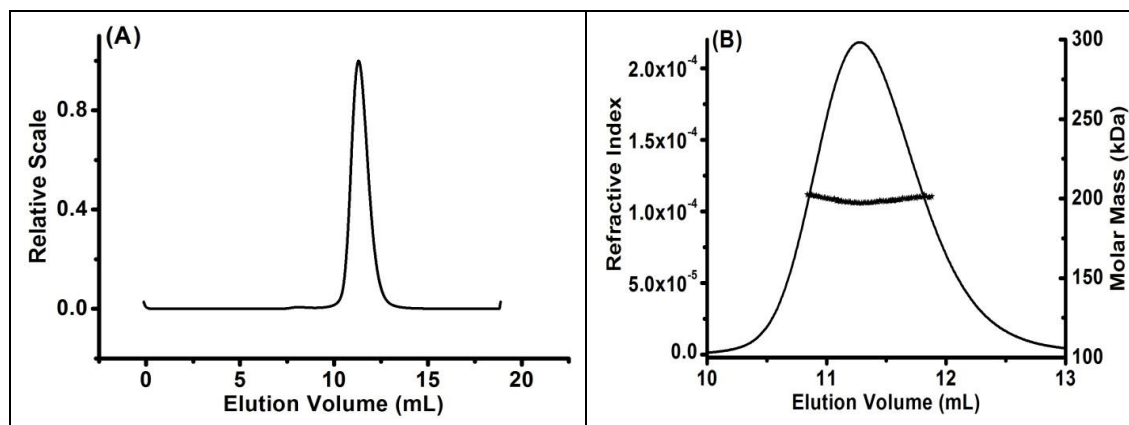
Figure 4.1: SEC-MALLS chromatographs of full length BM3*. Measurement of the oligomerization state of wild type full length flavocytochrome P450 BM3 using size exclusion chromatography coupled with multi angle laser light scattering and refractive index measurements. (A) Elution profile of BM3 showing the MALLS trace at detector 11. (B) A chromatogram representing the refractive index measurements (left-hand scale) of 1.6 mg/mL BM3 in buffer containing 50 mM KPi, 0.1 M KCl at pH 7.0. The right- hand scale represents the average molecular weights of the peak slices as estimated by the ASTRA software. The chromatograms show that BM3 elution peaks are broad and an average molecular weight of 198.6 ± 12.3 kDa was obtained in 50 mM KPi, 100 mM KCl, at pH 7.0.*

The observed weight average molecular weight of 198.6 kDa is nearly double the sequence molecular weight of BM3, indicating that BM3 exists as a dimer in solution. However, a fully dimerized BM3 enzyme is expected to have a molecular weight of 238 kDa which is significantly higher than the values obtained using this technique. The lower-than-expected molecular weights could indicate the dimerization is weak enough

such that the peak contains a mixture of monomer and dimer. Further characterization involved investigating the effects of altering the buffer ionic strength on the resulting molecular weight and the dimerization strength of the BM3 enzyme.

4.1.1.2 Effects of ionic strength on dimerization of BM3

The salt-dependent behaviour of BM3 was characterized by SEC-MALLS analysis conducted across a range of ionic strengths ranging from very low salt concentration (5 mM potassium phosphate buffer) to potassium chloride concentrations of 600 mM in 50 mM potassium phosphate buffer at pH 7. Table 4.1 shows the resulting weight average molecular weights across the ionic strengths studied. The dimerization of BM3 is highly dependent on the ionic strength of the buffer. At a very low buffer ionic strength (5 mM potassium phosphate), the dimerization does not occur as the observed weight average molecular weight of 117.1 kDa is very close to the monomer molecular weight of BM3 (119 kDa). The molecular weight increases with increasing ionic strength up to 150 mM KCl where an average molecular weight of 235 kDa was observed (close to the dimer molecular weight of 238 kDa). The measured molecular weight then starts declining as the ionic strength is increased from 200 mM KCl up to 600 mM KCl.

Table 4.1: Average molecular weights for BM3 obtained from SEC-MALLS. *All experiments were carried out at a fixed temperature of 25ºC and pH of 7.0*

BUFFER CONDITION	Avg. M_w (kDa)
5 mM KPi, pH 7.0	117.1 ± 3.1
50 mM KPi, pH 7.0	186.9 ± 4.1
50 mM Kpi, pH 7.0, 0.1 M KCl	198.6 ± 12.3
50 mM Kpi, pH 7.0, 0.15 M KCl	235.7 ± 5.6
50 mM Kpi, pH 7.0, 0.2 M KCl	195.0 ± 6.7
50 mM Kpi, pH 7.0, 0.4 M KCl	171.6 ± 6.2
50 mM KPi, pH 7.0, 0.6 M KCl	150.9 ± 9.3

The observed monomeric state of the enzyme at low salt concentration can be attributed to the presence of repulsive electrical double-layer forces between monomeric proteins. At low ionic strength (ca 5 mM) the double layer forces have a range of almost 5.0 nm leading to a very long-ranged repulsive force, which prevents protein self-association (B_{22}; see Section 1.3.1.3). Further, increasing salt concentration to give an ionic strength of 150 mM decreases the range of the force to 0.8 nm, lowering the repulsion and allowing dimerization to occur. The further lowering of the molecular weight with increasing ionic strength above 150 mM suggests that the dimerization is controlled by

attractive electrostatic interactions that can occur between patches of opposite charge. Furthermore, the monomer-dimer equilibrium is weak and reversible as increasing salt concentration shifts the equilibrium to the monomeric state.

4.1.1.3 Effect of fatty acid on dimerization of BM3

The study was extended to investigate if the observed molecular weights of BM3 changes in the presence of excess NPG under the same salt and buffer conditions. As described in Section 2.4.1, purified BM3 was split into two equal fractions (of ~0.2 mg/mL). The first fraction was subjected to SEC-MALLS analysis immediately without any further modifications. The second fraction was modified with the addition of 50 μM NPG and then subjected to MALLS analysis. As seen in Table 4.2, binding of NPG to wild type BM3 does not extensively change the measured weight average molecular weight. BM3 remains a monomer at low ionic strength even with the addition of fatty acids.

Table 4.2: Average molecular weights for BM3-NPG obtained from SEC-MALLS. All experiments were carried out at a fixed temperature of 25ºC and pH of 7.0.

BUFFER CONDITION	Avg. M_w (kDa)
5 mM KPi, pH 7.0	117.1 ± 3.1
5 mM KPi, pH 7.0 + 50 μM NPG	107.8 ± 2.3
50 mM KPi, pH 7.0, 0.1 M KCl	197.0 ± 15.7
50 mM KPi, pH 7.0, 0.1 M KCl + 50 μM NPG	200.1 ± 4.9

4.1.2 SEC-MALLS on the domains of P450 BM3

4.1.2.1 The heme domain

Various crystal structures of the wild type BMP and mutants have been published alongside inhibitor- and substrate-bound structures (*135, 154*). In all cases, BMP was crystallized as a monomer (section 1.2.3.1). In this study, SEC-MALLS was used to investigate the oligomerization state of BMP at very high (12 mg/mL; concentrations in this range are routinely used for BMP crystallization (*135*)) and low (1.5 mg/mL) BMP concentrations in buffer containing 50 mM KPi, 0.1 M KCl, pH 7.0. Chromatograms shown in Figure 4.2 indicate that BMP eluted as a single monomeric peak with weight average molecular weights of 47.4 ± 1.6 kDa at high BMP concentration and 49.7 ± 1.5 kDa at low BMP concentration. The resulting molecular weights are close to the

sequence molecular weight of BMP (55 kDa) in both cases and no considerable difference is observed as the concentration of BMP is varied. An average hydrodynamic radius of 3.51 ± 0.13 nm was obtained at high BMP concentration but was not determined for low BMP concentration.

The first peak in Fig 4.2 A occurring at ~ 8 mL is termed the void volume. High molecular weight aggregates (often caused by minor impurities, or some aggregation of the target protein itself) or bubbles in the solution that are too big to fit into the stationary phase usually elute with the mobile phase as the void volume. In the data presented, these are clearly non-BM3 (and non-protein) related signals since there is no refractive index (red line) signal associated.
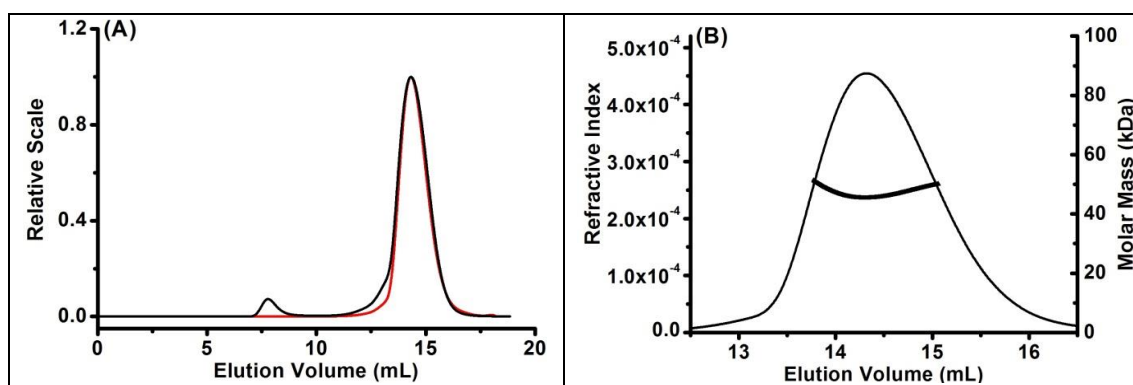
***Figure 4.2: SEC-MALLS chromatographs of BM3 heme domain**. (A) Elution profile of BMP showing the MALLS trace at detector 11 (black line) and the refractive index trace (red line). (B) A chromatogram representing the refractive index measurements (left-hand scale) of 12 mg/mL BMP in buffer containing 50 mM KPi, 0.1 M KCl at pH 7.0. The right-hand scale represents the average molecular weights of the peak slices as estimated by the ASTRA software. The resulting weight average molecular weight was estimated at 47.4 ± 1.6 kDa for BMP. Similar elution profiles and traces were obtained for measurements at 1.5 mg/mL BMP.*

4.1.2.2 The reductase domain and subdomains

The reductase domain of BM3 (BMR) is a 64 kDa subunit (residues ~ 471-1048) which can be further truncated into a 19 kDa FMN domain and a 45 kDa FAD domain. Within the reductase domain, two electrons derived from NADPH are transferred (one at a time) from the FAD hydroquinone to the FMN domain forming a semiquinone as the active species that passes electrons one at a time to the heme iron (Figure 1.13; (*131*)). Having ascertained that BM3 exists as a dimer in solution, there is a likelihood that one of the domains of BM3 (BMP or BMR) might also exist as a dimer in solution. In the

previous section, we have seen that BMP eluted as a single monomeric peak. The next step is to determine whether BMR exists as a dimer (or higher oligomers) in solution and, if so, then to identify whether either of the FAD or FMN domains is oligomeric. In this section, the oligomeric states of BMR, FAD and FMN domains were examined using SEC-MALLS. In addition, the ionic strengths of the buffers were varied to study the effects of electrostatics on the oligomer equilibrium.

For SEC-MALLS with BMR, FAD and FMN domains, 2.5 mg/mL of sample was injected onto the column pre-equilibrated with buffer containing 50 mM KPi, 100 mM KCl at pH 7. Results indicate that all three domains studied eluted as a single peak (Figure 4.3) with weight average molecular weights of 98.1 ± 2.2, 86.4 ± 3.8, and 18.5 ± 0.9 kDa for BMR, FAD and FMN domains respectively. However, the FAD peak was a lot broader than that of the other domains. The molecular weights indicate that the BMR domain exists in solution as a near dimer (similar to BM3) and the FAD domain is predominantly dimeric in solution while the FMN domain is monomeric.
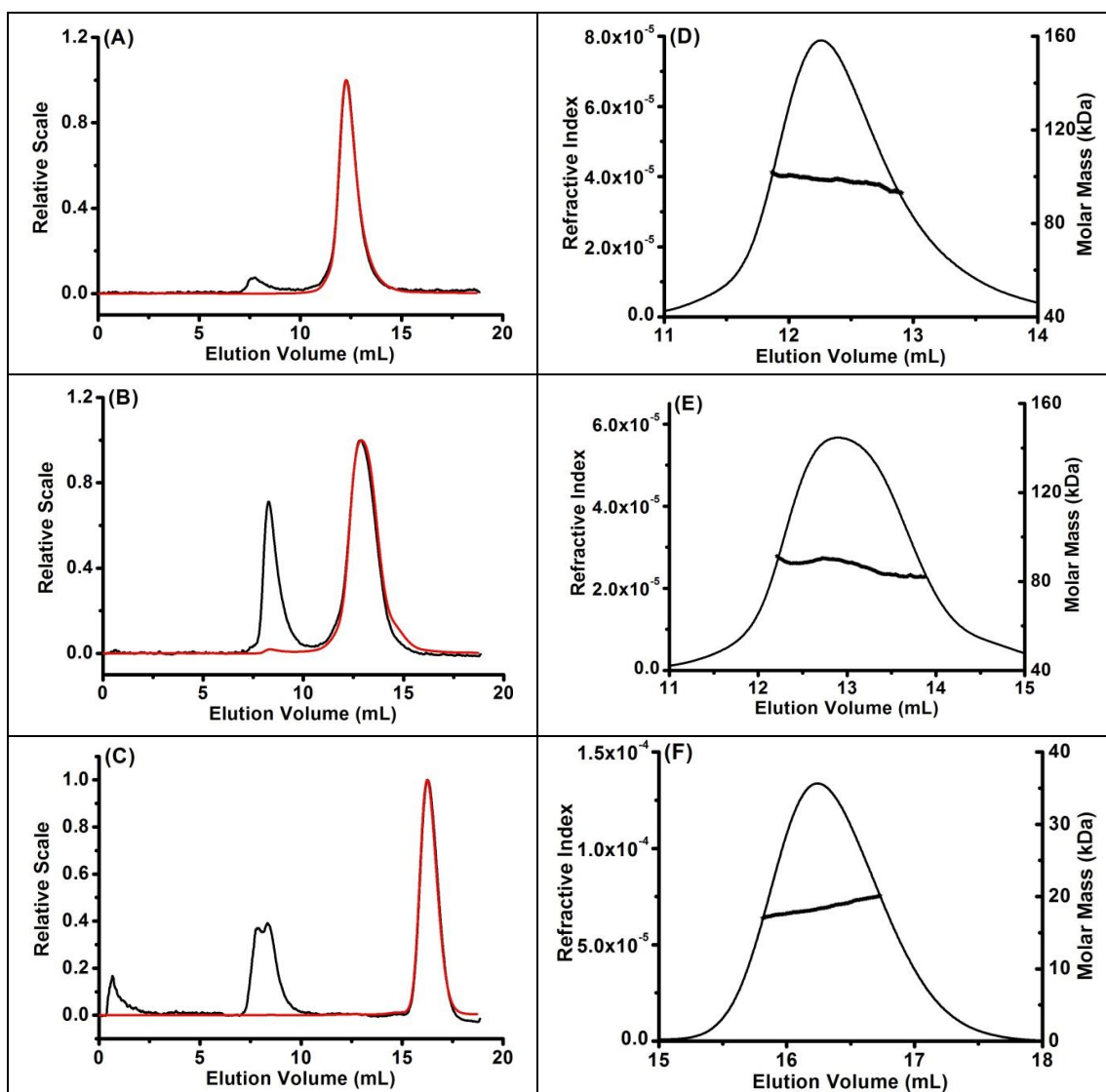
Figure 4.3: SEC-MALLS chromatographs of BM3 reductase, FAD and FMN domains. *Elution profiles of BMR, FAD and FMN domains (A-C) showing the MALLS trace at detector 11 (black line), and the refractive index trace (red line). The chromatograms representing refractive index measurements (left-hand scale) of 2.5 mg/mL BMR, FAD and FMN domains, respectively, in buffer containing 50 mM KPi, 0.1 M KCl at pH 7.0 are also shown (D-F). The right-hand scale represents the average molecular weights of the peak slices as estimated by the ASTRA software. The resulting weight average molecular weights obtained for BMR, FAD and FMN domains were 98.1 ± 2.2, 86.4 ± 3.8, and 18.5 ± 0.9 kDa respectively. The MALLS signal seen at ~ 8 minutes in panels A-C in this figure (and in Figure 4.2 A and 4.4 A-B) is the void volume. This signal likely originates from small gas bubbles rather than from high molecular weight protein aggregates – since there is almost no refractive index signal associated with the MALLS signal (red line) for the void volume.*

A comparison of the SEC-MALLS molecular weights for BM3 and its domains with the sequence molecular weight is shown in Table 4.3. The resulting SEC-MALLS molecular weights for BM3, BMR and FAD are above the sequence monomer molecular weight and approaching the dimer molecular weight. Further, comparing the SEC-MALLS molecular weights with the sequence molecular weights, BM3 and BMR do not dimerize fully (83% and 77% respectively) and the FAD dimer was about 97% complete. For the FAD dimer, the resulting molecular weight value is a little less than the expected dimer molecular weight but if corrected for experimental errors, this value could result in a molecular weight value equivalent to a full dimer. These results suggest that BM3 and BMR may have similar behaviour in solution. Indeed, if the interactions driving the dimerization of BM3 are the same as for BMR or the FAD, then we would similarly expect that the BMR or FAD dimerization can be weakened by changing the ionic strength. Thus SEC-MALLS of 2.5 mg/mL of BMR and FAD domains were repeated in the same buffer but with increased ionic strengths (0.5 M KCl and 0.8 M KCl respectively).

Table 4.3: Comparison of SEC-MALLS and sequence molecular weights for BM3 and its domains. *All measurements were carried out in buffer containing 50 mM KPi, 0.1 M KCl, pH 7.0.*

ENZYME	SEQUENCE MOL.WT (kDa)	SEC-MALLS MOL.WT (kDa)
BM3	119	198.6 ± 12.3
BMP	55	47.4 ± 1.6
BMR	64	98.1 ± 2.2
FAD	45	86.4 ± 3.8
FMN	19	18.5 ± 0.9

The results indicate that BMR and FAD also eluted as single peaks (albeit, slightly broader) with average molecular weights of 87.4 ± 2.0 and 86.8 ± 3.0 kDa (at ionic strength equal to 0.5 and 0.8 M, respectively). Thus, there was a reduction in the average molecular weight obtained for BMR (similar to what happened with BM3), but no change in the molecular weight obtained for FAD, although the elution peak remained broad. This suggests that electrostatic interactions might play a role in dimerization of the BM3 and BMR domain, but not the FAD domain. These results raised further questions: if electrostatics doesn't play a major role in dimerization of the FAD domain, could it be due to disulfide linkages as previously reported (*107, 109*)? Could the disulfide linkages contribute to the dimerization of the BM3 and BMR

domains alongside the electrostatics? These were investigated and reported in the next section.

4.1.3 Role of disulfide linkages in the dimerization of BM3, BMR and FAD domains.

The contributions to dimerization of BM3, BMR and FAD by the presence of disulfide linkages in the FAD or BMR domain were investigated by SEC-MALLS analysis on reduced and alkylated samples prepared as described in Section 2.4.1. Further, a mutant of the reductase domain (C773A, Section 2.2.3) created for crystallization studies was also subjected to SEC-MALLS analysis to also evaluate the effect of disulfide linkages on dimerization of BMR once one of the key cysteine residues has been mutated.

4.1.3.1 Reduction and Alkylation of BM3, BMR and FAD domains

Samples were first run on the gel filtration column (section 2.4.1) to remove high molecular weight aggregates. Pure samples were then split into three; the first fraction was run immediately without any further modification in 50 mM KPi, 100 mM KCl, pH 7.0 (low salt) while the second fraction was reduced with 10 mM DTT and alkylated with 50 mM iodoacetamide in the same buffer. The third fraction was also reduced and alkylated as described above and run in a high salt buffer (addition of 500 mM KCl for BM3 and BMR, and 800 mM KCl for FAD) to evaluate the effect of combined electrostatics and disulfide linkages on dimerization of the enzymes. The resulting weight average molecular weight and hydrodynamic radii are shown in Table 4.4.

For BM3 measurements, 0.2 mg/mL of sample was injected for the first run in low salt buffer without modification. The results show that BM3 eluted as a single peak comparable to measurements with high concentration of BM3 (1.8 mg/mL; Section 4.1.1.1) with a weight average molecular weight of 202.9 ± 6.7 kDa. It was also observed that reduction and alkylation of the BM3 sample led to a drop (~ 20% towards monomer molecular weight) in the measured weight average molecular weight while a further ~20% drop was recorded when the sample was run in high salt buffer. There was however no change in the resulting BM3 peak size for the three separate runs. Comparing these results to those obtained for the dependence of BM3 molecular weights on ionic strength (Table 4.1), it can be deduced that while disulfide linkages

might play a small role in the dimerization of BM3, the role of electrostatics seems to be dominant.

Measurements with BMR were carried out using injections containing 2.5 mg/mL of sample and results obtained followed similar trends to those observed for BM3. Reduction and alkylation of the sample led to a decrease in the resulting weight average molecular weight (towards the sequence monomer molecular weight). Further, at high salt concentration, a molecular weight of 78.7 kDa was obtained. This is a lot closer to the monomer molecular weight (64 kDa) than the dimer molecular weight (128 kDa). These results suggest that reduction of BMR shifts the monomer-dimer equilibrium towards monomers with less dimer present. Further, comparing BMR molecular weights measured at high salt without modifications (87.4 kDa; Section 4.1.2.2) with the reduced BMR also measured at high salt (78.7 kDa; Table 4.4), it can be deduced that disulfide linkages and electrostatics might play roles in the dimerization of the BMR domain. However, the reduction in molecular weight could also be attributed to the effects of alkylation since the change in molecular weight is quite small.

*Table 4.4: Average molecular weight (Mw) for reduced and alkylated BM3 and its domains obtained from SEC-MALLS. Samples were run in 50 mM KPi, 100 mM KCl, pH 7.0 (low salt); 50 mM KPi, 500 mM KCl, pH 7.0 (high salt for BM3 and BMR) and 50 mM KPi, 800 mM KCl, pH 7.0 (high salt for FAD domain). Samples were reduced and alkylated as described in Section 2.4.1. *(R+A) represents reduced and alkylated. Reduction and alkylation of BM3 and BMR leads to a reduction in the resulting dimer weight average molecular weight (values tabulated are in kDa), while that for FAD domain results in splitting of the dimer peak into dimer and monomer components.*

ENZYME	LOW SALT	LOW SALT (R+A)*		HIGH SALT (R+A)	
BM3	202.9 ± 6.7	180.2 ± 18.1		158.4 ± 5.8	
BMR	98.1 ± 2.2	88.3 ± 3.5		78.7 ± 2.7	
FAD	86.4 ± 3.8	86.3 ± 5.6 (dimer, 76%)	44.0 ± 2.1 (monomer, 24%)	84.4 ± 3.7 (dimer, 79%)	42.7 ± 1.1 (monomer, 21%)

Figure 4.4 shows results for SEC-MALLS measurements carried out with an injection of 2.5 mg/mL reduced and alkylated FAD in both low (100 mM KCl) and high (800 mM KCl) salt concentration buffer. Comparing the refractive index trace for unmodified FAD domain run in low salt buffer (see Figure 4.3E) with the DTT-reduced profile (run in the same buffer as shown in Figure 4.4C), reducing and alkylating the FAD domain has split the broad FAD elution peak into a dimer peak (with Mw equal to 86.6 ± 5.8

kDa) and a monomer peak (with Mw equal to 43.5 ± 1.2 kDa) containing 76% and 24% of the total protein, respectively. This ratio of protein under the peaks changed slightly to 79% for the dimer peak and 21% for the monomer peak when the buffer KCl concentration was increased from 100 mM to 800 mM. However, the resulting dimer and monomer molecular weights did not vary as the KCl concentration was increased. This implies that, unlike in BM3 and BMR, the dimerization of FAD domain is highly influenced by the presence of disulfide bond formation between cysteine molecules of the FAD domain. Further, there is likely no effect of electrostatic interactions in the dimerization of the FAD domain.
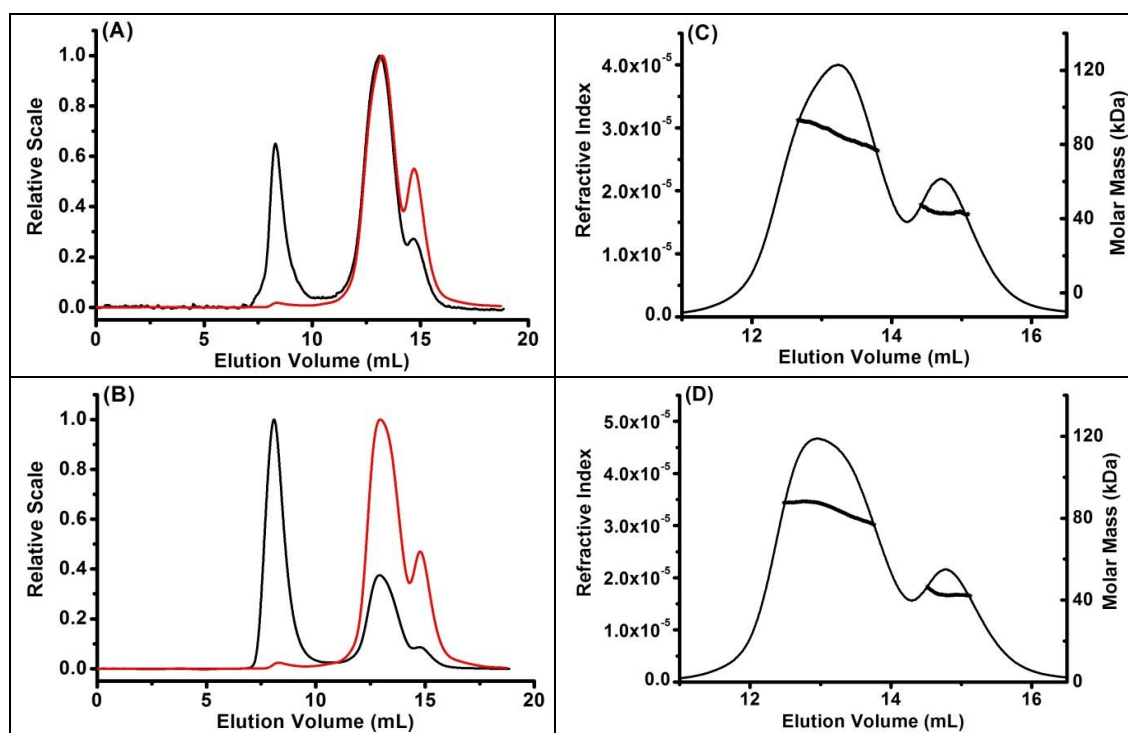
Figure 4.4: SEC-MALLS chromatographs of DTT-reduced FAD domain*. Elution profiles of 2.5 mg/mL FAD domain run in 50 mM KPi, 100 mM KCl, pH 7.0 (low salt; A) and 50 mM KPi, 800 mM KCl, pH 7.0 (high salt; B) showing the MALLS trace at detector 11 (black line), and the refractive index trace (red line). The corresponding chromatograms representing refractive index measurements (left-hand scale) of FAD domain measured in both low (C) and high salt (D) are also shown. The right-hand scale (Figures C and D) represents the average molecular weights of the peak slices as estimated by the ASTRA software.*

4.1.3.2 BM3 reductase mutant – C773A

The crystal structures of BM3 and its reductase domain are yet to be solved. The only available structure of the FAD domain is that of a double mutant (C773A/C999A) where two cysteine residues were mutated to alanine (*115*). Moreover, we have shown in this study that disulfide bonds play an important role in the dimerization of the FAD domain and that the FAD dimer is stabilized mainly by disulfide bonds. In view of these findings, a cysteine residue at position 773 (C773A) in the reductase domain was mutated to alanine as described in Section 2.2.3 for SEC-MALLS analysis as well as crystallization studies in an attempt to characterize and solve the crystal structure of the BMR domain. The SEC-MALLS result is discussed in this section while the crystallization trials are discussed in Section 4.5.

Pure samples of 2.7 mg/mL C773A were injected into the SEC column pre-equilibrated with buffer containing 50 mM KPi, 100 mM KCl, pH 7.0 (low salt). Results show that the samples eluted as a single peak with average molecular weight of 95.2 ± 4.5 kDa. This observed molecular weight is quite similar to that obtained for wild type BMR (98.1 ± 2.2 kDa; Table 4.3) under the same conditions. Further, results obtained at high salt (buffer contains 500 mM KCl) do not vary significantly with that of the wild type (Table 4.5). This indicates that the cysteine residue at position 773 may not play a role in the dimerization of the BMR domain. Moreover, further reduction of the C773A mutant (with DTT) did not result in any significant change in the resulting average molecular weight and hydrodynamic radii (Table 4.5).

Table 4.5: Average molecular weight (Mw) and hydrodynamic radii (r_H) for C773A obtained from SEC-MALLS.

C773A	Low salt	Low Salt (R+A)	High Salt	High Salt (R+A)
Mol. Wt (kDa)	95.2 ± 4.5	96.0 ± 3.4	86.9 ± 4.0	87.6 ± 2.1
Avg. r_H (nm)	4.4 ± 0.5	4.3 ± 0.6	4.2 ± 0.5	4.2 ± 0.6

4.1.4 Summary of SEC-MALLS results

In this section, the SEC-MALLS technique was employed to characterize the oligomeric states of flavocytochrome P450 BM3 and the respective domains, as well as a reductase mutant C773A. The measured weight average molecular weights shown in Table 4.3 indicate that BM3 and BMR eluted as single near-dimeric peaks, the FAD

domain eluted as a single dimeric peak, and BMP and FMN domains eluted as single monomeric peaks. Further, the presence of fatty acids in the buffer did not have any significant effects on the resulting molecular weights for BM3. On the contrary, BM3 is a monomer at very low ionic strength (5 mM KPi) and increasing the ionic strength of the buffer gradually increased the resulting molecular weight and a full-dimeric molecular weight (235 kDa) was attained at 0.15 M KCl. Further increase in the ionic strength (up to 0.6 M KCl), resulted in the screening of attractive electrostatic interactions on BM3 and, consequently, a decline in the resulting weight average molecular weight to a value closer to that of the monomer than the dimer (151 kDa). This behaviour is suggestive of a monomer-dimer equilibrium which gets shifted towards dimer or monomer when the ionic strength is varied. Treatment of pure BM3 with DTT (to prevent disulfide bond formation) had very little effect on the BM3 dimer, indicating that disulfide bond formation may not contribute as much as electrostatics to the dimerization of BM3.

Similarly, increasing the buffer ionic strength for BMR led to a reduction in the weight average molecular weight. This also suggests a monomer-dimer equilibrium which could be skewed by the presence of electrostatics. On the contrary, the FAD dimer is not affected by any variation in the buffer ionic strength, but the dimer peak gets split into dimer (76%) and monomer (24%) peaks when the sample is treated with DTT. Thus, disulfide bond formation by free cysteine thiols might have an exclusive effect on FAD dimerization, less effect on BMR, and negligible effect on BM3. This deduction is in agreement with a very recent publication by the Munro laboratory where two cysteine residues in the FAD domain of BM3 were mutated to alanine (C773A/C999A). SEC-MALLS analysis of this double mutant showed that it eluted as a single peak with an average molecular weight of 42.0 ± 2.5 kDa (*115*), close to the sequence molecular weight of FAD (45 kDa). Moreover, the influence of disulfide bond formation on FAD dimerization implies that the dimerization process is irreversible.

The presence of a reversible dimerization observed for BM3 and BMR is further supported by considering the shape of the chromatogram peaks. Using theoretical chromatographs, Yu et al (*308*) demonstrated that reversible dimerization in SEC can result in splitting, merging, fronting and tailing of the chromatograph peaks. The refractive index chromatograms obtained for BM3 across some of the ionic strengths studied are shown in Figure 4.5 A-F. All the chromatograms (with the exception of A

and D) are characterised with peak tailing which is in agreement with the near-dimer molecular weights observed and also describes intermediate association and dissociation with dimers being predominant. A similar trend is observed with BMR chromatograms at both low and high ionic strengths (Figure 4.5 G-H), and even with DTT-reduced samples (Figure 4.5I). On the other hand, peak merging is observed with BM3 measurements at 0.15 M KCl (Figure 4.5 D) where a full-dimer molecular weight was observed.
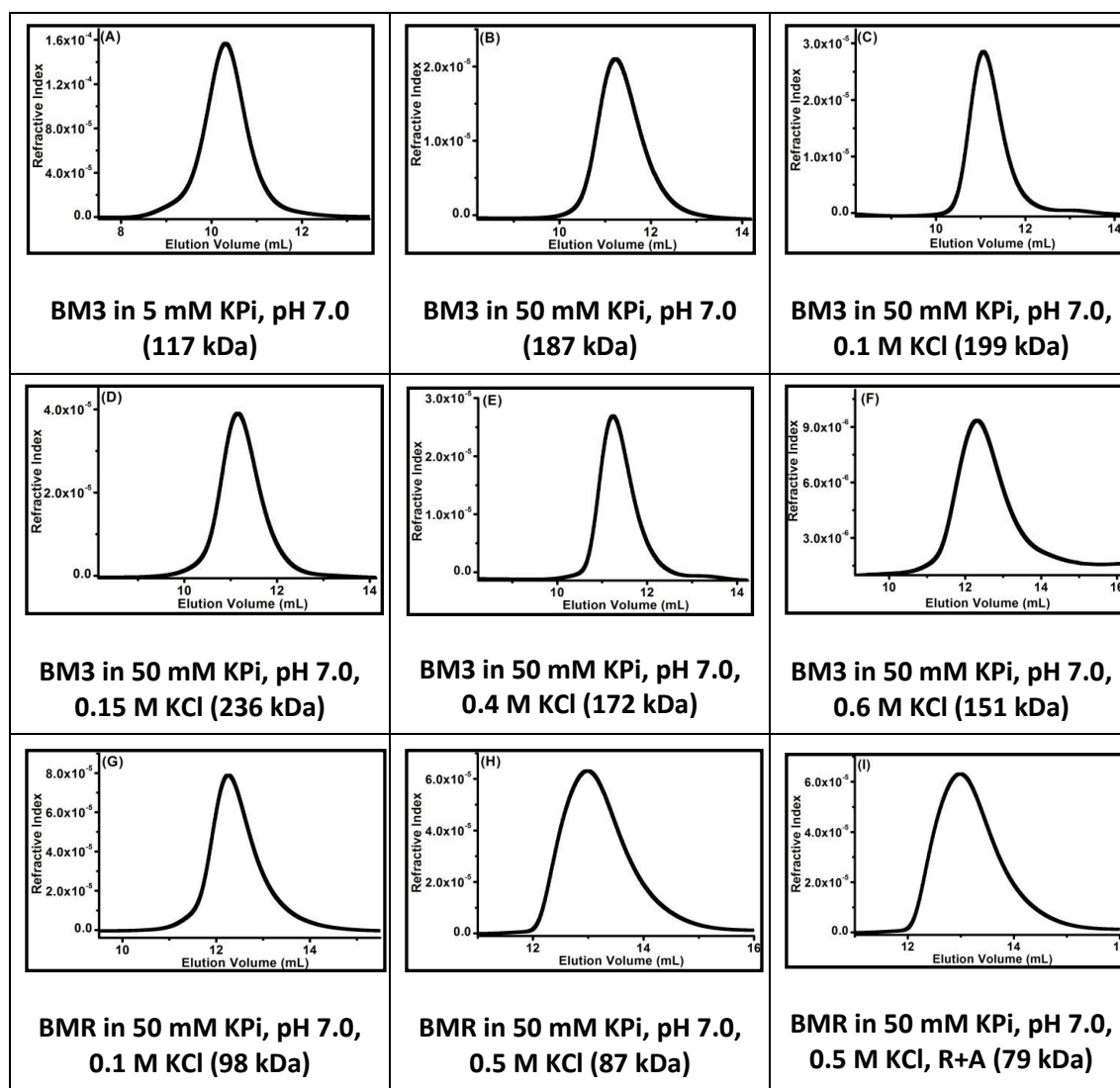
Figure 4.5: SEC-MALLS chromatograms of BM3 and BMR showing peak tailing, fronting and merging. *The buffer conditions and molecular weights obtained are shown under each chromatogram. The effect of reversible dimerization (which is proposed to be the mechanism of action of BM3 and BMR) can be seen in the merging (D) and tailings of the chromatogram peaks (B, C, E-I). It is worth noting that at 5mM KPi the chromatograms exhibit slight fronting rather than tailing or merging. This is in agreement with the observed molecular weights which suggest all monomers.*

Another striking observation with all the SEC-MALLS studies carried out for BM3 and BMR is that a polydispersity index of 1.0 was obtained in all cases. This implies that there is predominantly a single species present, which we hypothesised, is the dimer. Sedimentation velocity and equilibrium were used to test this hypothesis and to investigate the monomer-dimer equilibrium suggested to be the natural state of BM3. The results of this analysis are discussed in the next section.

4.2 AUC STUDIES ON BM3 AND BMR

In the previous section, SEC-MALLS analysis indicated that BM3, BMR and FAD domains exist predominantly as dimers in solution and this dimerization is likely reversible for BM3 and BMR and irreversible for FAD. AUC is an often-used method for characterizing protein structural and hydrodynamic properties including the oligomeric state, shape and details of macromolecule association (Appendix B). Here, sedimentation velocity was used to further characterize the hydrodynamic shape and size of the dimers formed by BMR and BM3, while sedimentation equilibrium was used to investigate and verify the proposed reversible monomer-dimer equilibrium in BM3 and BMR. Both sedimentation velocity and equilibrium experiments were carried out using an Optima XL-A analytical ultracentrifuge (Beckman Coulter) furnished with absorbance optics.

4.2.1 Sedimentation velocity studies on BM3 and BMR

Sedimentation velocity experiments for BM3 and BMR were carried out using post-gel filtration samples in their respective buffers. Centrifugation of both buffer and sample was carried out at 40,000 rpm and at 4°C with the sedimentation boundaries monitored at 230 nm every 90 seconds until the scans were depleted. Approximately 200 scans were generated in each case and these scans were imported into SEDFIT (*309*) to model the concentration distributions to the Lamm equations to produce the required s-values for c(s) maxima (s_{app}). SEDNTERP (*310*) was then used to derive the standard sedimentation coefficient ($s_{20,w}$), frictional ratio (f/f_o) and hydrodynamic radius (r_H) from the SEDFIT derived s_{app}, along with the sequence molecular weight, buffer viscosity and buffer density.

4.2.1.2 Sedimentation velocity analysis of ligand-free and ligand-bound BM3

Sedimentation velocity studies on ligand-free BM3 were carried out at three different BM3 concentrations (1, 4 and 5 µM). SEC-MALLS studies on BM3 showed that BM3 eluted as a single near-dimeric peak with no peak splitting. The SEDFIT c(s) analysis showing the species distribution for BM3 is presented in Figure 4.6. It is clearly seen that the single near-dimeric peak observed in SEC-MALLS has been further resolved into a 94% dimeric peak with estimated molecular weight of 235 ± 9.0 kDa, a 2% monomeric peak, and a 4% trimeric peak. The c(s) analysis shown here represents scan analysis for measurement taken at 4 µM BM3. Similar scans were obtained for measurements at 1 µM and 5 µM BM3 although more dimers (96%) and less trimers (1%) were observed at 5 µM BM3. Further analysis using the SEDNTERP software yielded more hydrodynamic parameters including the sedimentation coefficient corrected to 20ºC and density of water ($s_{20,W}$), the frictional ratio and the hydrodynamic radius as shown in Table 4.6.
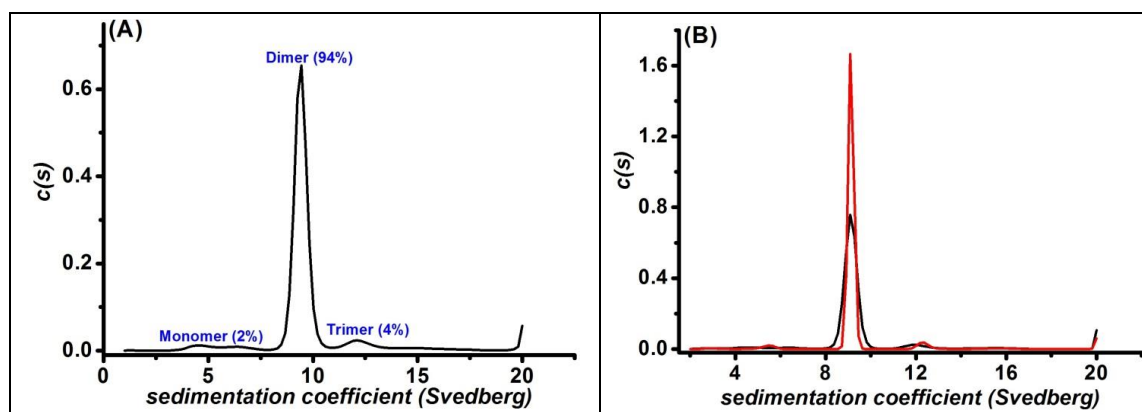
Figure 4.6: Sedimentation velocity plot [c(s) analysis] for SEC-purified wild type and NPG-bound BM3. *The species distribution was calculated using sedfit from ~200 sedimentation scans. (A) Measurement was conducted with 4 µM substrate-free BM3 in 50 mM KPi, 0.1 M KCl, pH 7.0. The monomer, dimer and trimer peaks gave s_{app} values of 4.51, 9.43, and 12.09 respectively. Similar distribution plots were obtained for measurements at 1 and 5 µM BM3. (B) Comparison plot for 4 µM substrate-free (black line) and NPG-bound BM3 (red line).*

Table 4.6: Hydrodynamic parameters for BM3 obtained from sedimentation velocity studies

Molecule	[BM3] (µM)	s_{app} (x 10^{-13}s)	$s_{20,w}$ (x 10^{-13}s)	r_H (nm)	f/f_o
BM3	1.0	9.35	9.65	5.73	1.40
BM3	4.0	9.44	9.74	5.68	1.39
BM3	5.0	9.50	9.81	5.64	1.38
BM3 NPG	4.0	9.44	9.74	5.68	1.39

This result further supports our hypothesis that BM3 is predominantly dimeric in solution. A combination of $s_{20,w}$ value of 9.74, r_H value of 5.68 and f/f_o value of 1.39 suggests that the BM3 dimer is compact and relatively globular in shape. It is also interesting to observe that these hydrodynamic parameters vary only slightly (most likely within experimental errors) with BM3 concentration. Further, the SEDNTERP derived hydrodynamic radius (5.68 nm) is in good agreement with that obtained from SEC-MALLS (5.70 nm).

Moreover, addition of 100 µM NPG to the BM3 sample did not affect the BM3 species distribution or the resulting hydrodynamic parameters (Figure 4.6B, Table 4.6). This is consistent with SEC-MALLS result where the presence of fatty acids in the buffer did not affect the resulting weight average molecular weights.

4.2.1.3 Sedimentation velocity analysis of free and modified BMR

Here, BMR and C773A sedimentation velocity studies were carried out under the same buffer conditions as used in SEC-MALLS (50 mM KPi, 0.1 M KCl, pH 7.0) and the effects of DTT-reduction on BMR were investigated. SEC-MALLS result indicted that BMR is primarily dimeric at low ionic strength (i.e. 100 mM) and the dimerization was weakened with increasing ionic strength leading to part monomer formation. However, there was no significant change observed between native BMR and DTT-reduced BMR. There was also no effect on dimerization when removing a surface accessible cysteine in the C773A mutant.

Two post-SEC fractions at high (~5 µM) and low (~3 µM) BMR concentrations were subjected to sedimentation velocity and the resulting scans were analysed by SEDFIT as shown in Figure 4.7. The relative area under the monomer peak is greater than observed for BM3 samples at both concentrations studied. Further, with reducing protein concentration, the percentage of monomers increases from 24% to 46% whereas there is a decrease in dimer percentage from 74% to 53%. The ability to partially separate the dimers from monomers and the increase in monomer at lower concentration of BMR supports our hypothesis that there is a reversible monomer-dimer equilibrium observed in BMR. This reversible equilibrium is similar to that observed in BM3, albeit weaker.
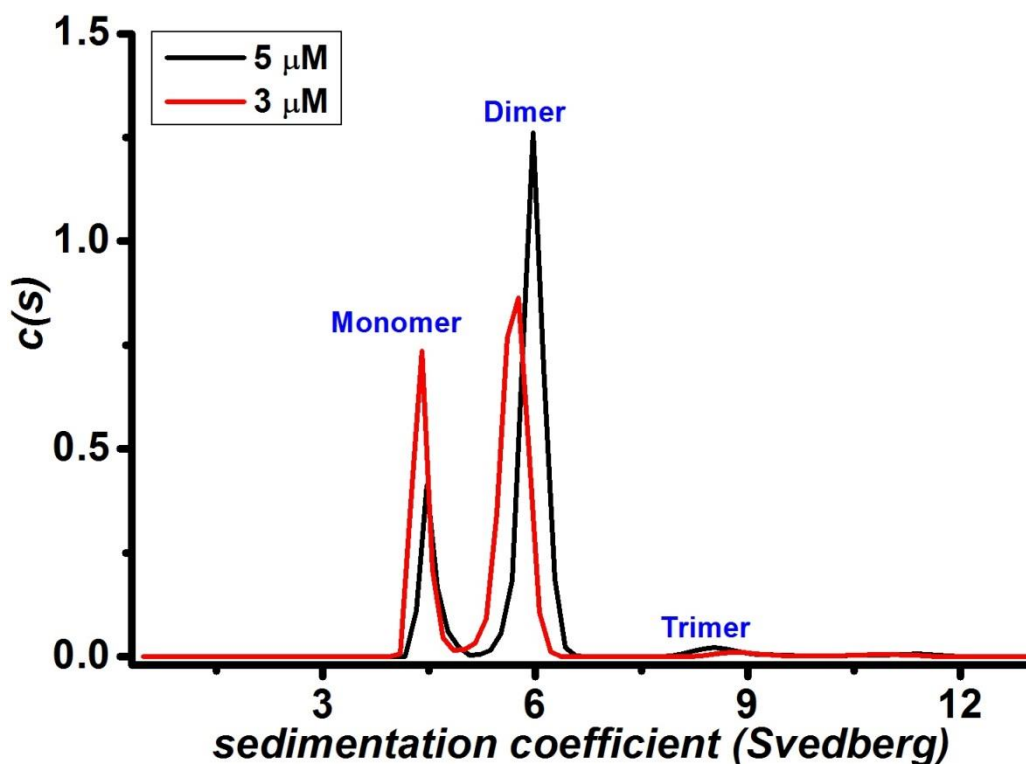
Figure 4.7: c(s) analysis for SEC-purified BMR. *The species distribution was calculated using sedfit from ~200 sedimentation scans for 5 μM BMR (black line) and 3 μM BMR (red line) in 50 mM KPi, 0.1 M KCl, pH 7.0. Three peaks were observed in both cases, proposed to be the monomer, dimer and trimer peaks. The s_{app} values obtained in each case for all peaks are shown in Table 4.7.*

The $s_{20,w}$, r_H, and f/f_o values obtained for BMR at both concentrations are shown in Table 4.7. The hydrodynamic radii and frictional ratio are slightly lower at high concentration for both BMR monomers and dimers (probably within experimental error of each other), while the standard sedimentation coefficient values obtained are slightly higher. Further, the r_H observed for the BMR dimer here (~5.0 nm) is similar to that seen with DLS after an SEC step (~5.2 nm). Another interesting observation is that the hydrodynamic radius for BMR dimer is not so far from that obtained for BM3 dimer (~5.7 nm) from both SEC-MALLS and sedimentation velocity studies. This suggests that the BMR may adopt a different shape in isolation from the BM3, as supported by the difference in the frictional ratio between the BMR and BM3 dimers. While that of the BM3 dimer (1.39) is suggestive of a compact structure, the frictional ratio of BMR dimer (1.52) indicates a more extended structure (likely ellipsoidal). This is understandable given that the BMR has to give electrons to the heme domain and as such, might have to assume a more compact shape when tethered to the heme domain for efficient electron transfer.

Table 4.7: Hydrodynamic parameters for BMR and C773A obtained from sedimentation velocity studies. *R+A: DTT-reduced and alkylated with iodoacetamide. ± M refers to monomer and ^D refers to dimer.*

Molecule	[BMR] (μM)	s_{app} ($\times 10^{-13}$s)		$s_{20,w}$ ($\times 10^{-13}$s)		r_H (nm)		f/f_o	
		$M^{\pm}$	$D^{\wedge}$	M	D	M	D	M	D
BMR Low	3.0	4.39	5.76	4.60	6.04	3.31	5.0	1.25	1.52
BMR High	5.0	4.47	5.97	4.69	6.26	3.25	4.87	1.23	1.46
BMR R+A*	5.0	4.61	5.97	4.83	6.26	3.15	4.87	1.12	1.46
BMR C773A	1.0	4.07	5.61	4.38	5.88	3.57	5.18	1.35	1.56

Subsequent studies were carried out with 3 μM DTT-reduced BMR and 1 μM C773A BMR under the same buffer conditions. As seen in the SEDFIT analysis plot (Figure 4.8A), pre-incubation of BMR with DTT does not seem to affect the c(s) plot, implying that disulfide bonds are not important for BMR dimerization. On the other hand, the c(s) plot for the C773A mutant gives less conclusive findings as the peaks are not very defined (Figure 4.8B). However, it appears that the mutation might have a slight effect on the conformation of the BMR dimer. Further, the hydrodynamic parameters obtained are the same in all three cases investigated here. These results are in good agreement with SEC-MALLS studies and further support our hypothesis that disulfide linkage may not play a role in dimerization of BMR.
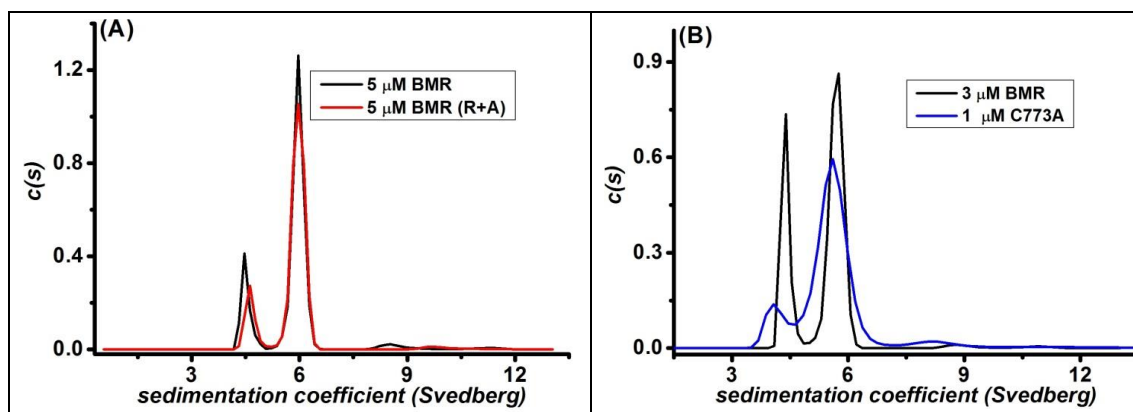
Figure 4.8: Comparative [c(s) analysis] plot for SEC-purified wild type BMR, reduced and alkylated BMR, and C773A mutant. *(A) Comparative plot for 5 μM BMR (black line) and 5 μM BMR DTT-reduced and alkylated BMR (red line). (B) Comparison plot for 3 μM ligand-free BMR (black line) and 1 μM C773A BMR (blue line). All measurements were carried out in 50 mM KPi, 0.1 M KCl, pH 7.0.*

In summary, the sedimentation velocity results for both BM3 and BMR do not differ from those obtained from SEC-MALLS studies. Reversible dimerization is observed for both BM3 and BMR, but that of BMR is shown to be weaker as the relative monomer concentration observed using sedimentation velocity experiments is much greater for BMR than for BM3. In the next section, sedimentation equilibrium is employed to further characterize this reversible equilibrium and to derive dissociation constants in each case.

4.2.2 Sedimentation equilibrium studies on BM3

Sedimentation equilibrium experiments were conducted for BM3 to further measure the proposed reversible monomer-dimer equilibrium as described in section 2.4.2. The centrepieces containing the sample and reference solutions were centrifuged at three different speeds and scans were collected at 230 nm and 280 nm. Global data analysis was carried out using the SEDPHAT software (*279*).

BM3 sedimentation equilibrium data were collected at 3 different protein concentrations (0.18, 0.36, and 0.85 µM), at 3 different speeds (6,000; 10,000 and 17,000 rpm) and absorbance data was collected at wavelengths of 230 and 280 nm. We studied solutions with buffer containing 50 mM KPi, pH 7.0 and KCl concentrations ranging from 0.05 to 1 M. The sedimentation equilibrium data were fitted using various global analysis models including the monomer-dimer and monomer-trimer self-association models. The best fit to the data (*i.*e the model which gives the most random distribution of residuals) was obtained with the monomer-dimer model and the resulting global fit dissociation constants (K_d) and average masses are plotted in Figure 4.9. The global fit represents a fit of three rotor speeds and three BM3 concentrations used for each ionic strength, with the mass for the monomer fixed and the association constant (K_a) floated Although the data were fitted globally (*i.e.* for a given ionic strength, fit is to a set of data generated by different rotation speeds and protein concentrations), residuals were obtained for the various speeds for the ionic strengths studied. In Figure 4.10, residuals obtained for data collected at medium speed at 0.15 M and 0.3 M KCl are shown.
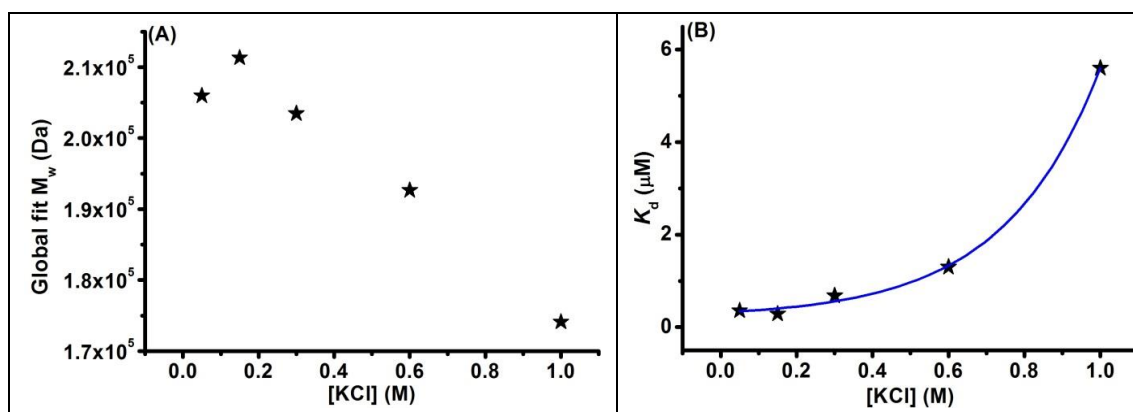
Figure 4.9: Global fit BM3 molecular weights and dissociation constants from sedimentation equilibrium. (A) Weight average molecular weights and (B) dissociation constants with Boltzmann fit (blue line) derived from all three BM3 concentrations and all three speeds per ionic strength. The highest molecular weight (211 kDa) and lowest K_d (0.29 μM) were obtained at 0.15 M KCl.

The resulting molecular weight trend agrees with previous data collected for BM3 using SEC-MALLS (Table 4.1). Also, the values of weight average molecular weight and dissociation constant indicate the dimerization is strongest at an ionic strength of 0.15 M KCl. The relatively strong BM3 dimerization (K_d of 0.29 μM) is weakened as the ionic strength increases. However, the Boltzmann fit shows that full monomer is not obtained at the highest ionic strength studied here (1 M KCl), but can only be obtained at an ionic strength of 2.7 M KCl (x_0=2.68). This suggests that dimerization of BM3 is not fully modulated by electrostatic interactions, but that there might be additional contributions from other factors such as hydrogen bonding and hydrophobic interactions.

The highest average mass obtained with sedimentation equilibrium is 211 kDa, which is below the expected dimer molecular weight of 238 kDa. Further, extrapolating the Boltzmann fit to zero concentration does still give an apparent K_d of 0.30 μM, also implying there is still a reasonable amount of monomer at this stage. This could be attributed to partial unfolding of the monomers to form a dimer. If this is the case, some of the monomers do not quickly refold to form dimers, leading to the presence of some monomers within the solution.
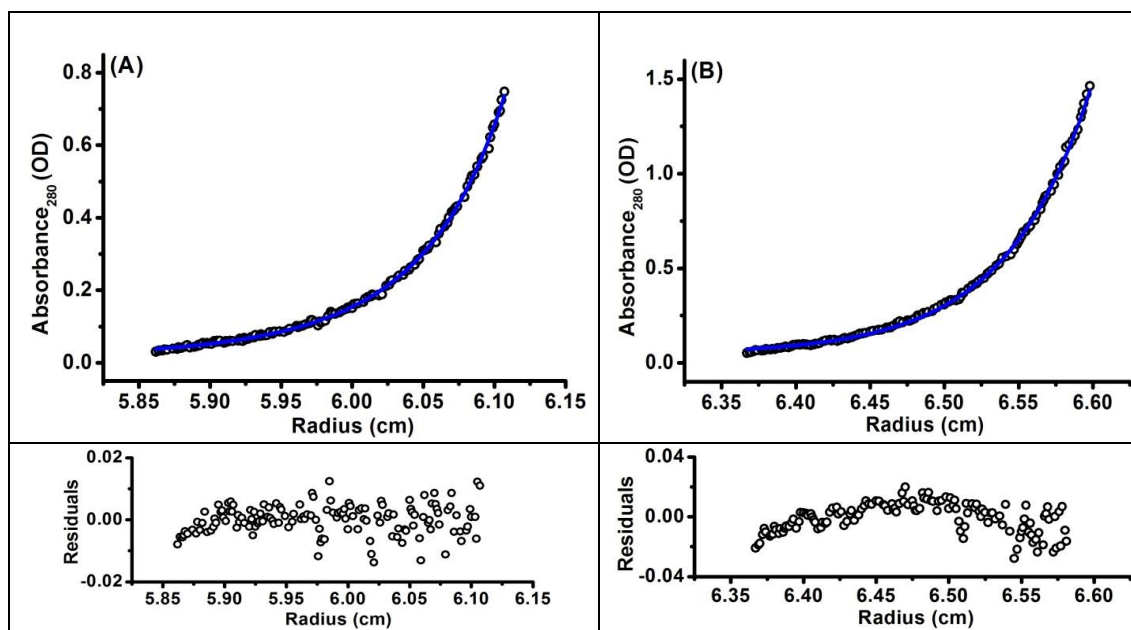
Figure 4.10: Global data analysis for BM3 sedimentation equilibrium data. Absorbance measurements (open back circles) with fits (blue line) and residuals (below) for measurements carried out at medium speed and 0.15 M KCl (A) and 0.3 M KCl (B).

4.3   BATCH MALLS ANALYSIS ON FULL LENGTH BM3

Multi angle laser-light scattering (MALLS) is a biophysical technique that has been used for accurate measurements of protein solution behaviour for many decades. As discussed in Section 1.3.1.3, this technique, originally developed for characterisation of weak non-specific protein-protein interactions, can be used for precise characterization of molecular interactions with affinities ranging from nanomolar to millimolar.

From SEC-MALLS and sedimentation velocity studies, it has been demonstrated that BM3 is predominantly dimeric in solution. Further characterization of BM3 self-association using sedimentation equilibrium indicated that the dimerization process is reversible, and measured dissociation constants indicate that the dimerization is weakened with increasing ionic strength. Light scattering can also be used to characterize the energetics of protein dimerization directly from the dependence of the measured weight average molecular weight on protein concentration as outlined by equations 2.7 to 2.12. Furthermore, the same experiment can be used to deduce the non-specific protein-protein interactions in terms of the osmotic second virial coefficient (*237, 311*).

In this section batch MALLS (Section 2.4.3) experiments were initially used to measure the weight average molecular weight, the dissociation constant, and the osmotic second virial coefficients for solutions of BM3. However, this technique relies on obtaining exact concentration measurements in order to determine accurate values for the weight average molecular weights and the average osmotic second virial coefficient (see below). This problem is overcome by using the CG-MALLS technique (with the Calypso system), which has been designed to automate exact dilutions and generate varying protein concentrations for better accuracy. The dilutions are very precise such that protein concentrations can be determined from the known dilution factors instead of by using absorbance detectors, which are sometimes not sensitive enough to measure low protein concentration accurately. Using dilutions has permitted accurate light scattering data to be obtained at micromolar concentration of protein which, in turn, has made it possible to measure the dissociation constants. The results obtained using concentrations measured by absorbance and by exact dilutions are discussed below.

4.3.1   Static light scattering studies on P450 BM3

Batch static light scattering studies on full length BM3 were carried out using the Wyatt DAWN Heleos-II connected in series to a UV detector and a refractometer as described in section 2.4.3. Pure BM3 samples just exiting the SEC-column were diluted into 10 different samples (of 5 mL volumes) with increasing concentration from 0.05 mg/mL to 1.0 mg/mL and injected into the system. The light scattering, UV and differential refractive index data were exported into Excel for analysis to calculate apparent weight average molecular weights ($M_{w,app}$; See Equation 2.8) as a function of BM3 concentration. The values of $M_{w,app}$ are equal to the true weight average molecular weight of BM3 plus a correction factor which is related to an averaged virial coefficient describing the non-specific protein-protein interactions between all protein species. These studies were conducted at 5 different ionic strengths ranging from 0.1 M to 1.0 M KCl in buffer containing 50 mM KPi, pH 7.0. The resulting molecular weight trend across the various BM3 concentrations measured at 0.2 M and 0.5 M KCl are shown in Figure 4.11 A and B, respectively.
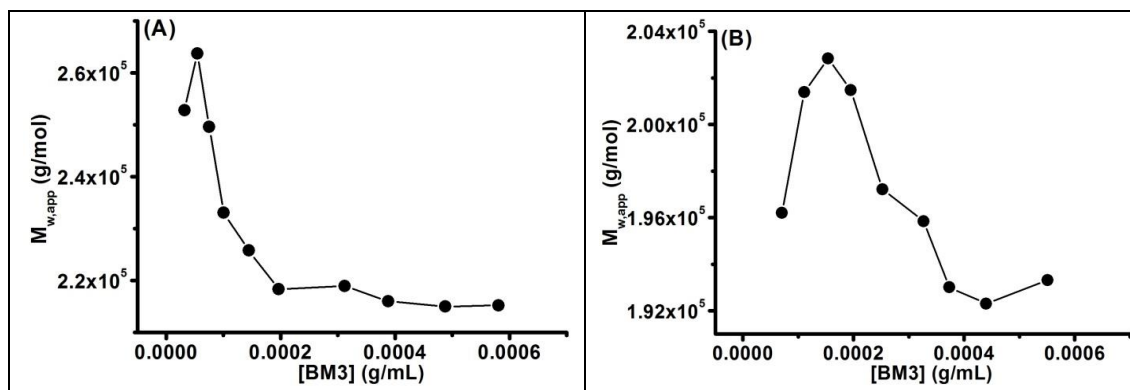
Figure 4.11: Weight average molecular weights obtained from batch static light scattering in solutions of 50 mM KPi, pH 7 and (A) 0.2M or (B) 0.5 M KCl.

The resulting molecular weight measurements are in agreement with data obtained from SEC-MALLS and AUC, indicating that BM3 is predominantly dimeric at concentrations of 0.1 g/L and higher. Furthermore, there is a slight increase in protein molecular weight with initially increasing protein concentration, possibly reflecting a reversible dimerization; according to Le Chatelier's principle, increasing protein concentration leads to increased dimerization. Above a critical protein concentration, the apparent molecular weight begins to decrease, which reflects the contribution from the averaged virial coefficient. A decrease indicates a positive second virial coefficient or repulsive protein-protein interactions. The effect of increasing ionic strength is to shift the critical protein concentration to higher values and to decrease the molecular weights. This trend supports the observation that increasing ionic strength screens the interactions between monomers resulting in less dimer formation.

Fitting the data to the light scattering given by Equation 2.7 to obtain the average molecular weights (M_w) and interactions between the BM3 dimer (in terms of osmotic second virial coefficient, B_{avg}) did not produce good fits. The B_{avg} and M_w obtained at 0.2 M KCl were 6.85 X 10^{-4} mLmol/g^2 and 248 kDa respectively, while those obtained at 0.5 M KCl were 2.42 X 10^{-4} mLmol/g^2 and 202 kDa respectively. The inability to fit the data using a non-associating model suggests a reversible equilibrium involving different kinds of interactions such as monomer-monomer association (defined in terms of the dissociation constant, K_d) and dimer-dimer interactions (defined by the osmotic virial coefficient B_{dd}, Equation 2.10).

However, obtaining accurate enough data for determining K_d, requires accessing very low protein concentration which is beyond the sensitivity of the UV detector and the DAWN system. On the other hand, high protein concentration measurements are

required for accurate estimation of the dimer-dimer second virial coefficient (B_{dd}) and also to determine whether higher oligomers (such as trimers and tetramers) are formed at higher protein concentrations. Further, various issues arose with obtaining accurate measurements of high protein concentration. UV data were collected at 280 and 418 nm for comparison purposes. Absorbance at 280 nm could only be used for measuring protein concentration up to 2 g/L; whereas we found that absorbance at 418 nm was not linear with respect to protein concentrations (data not shown). Consequently, more detailed light scattering studies were conducted with the Calypso system which has the added advantage of delivering a controlled gradient of protein concentrations via automation, hence eliminating errors associated with manually diluting the samples before injecting onto the light scattering equipment. This permitted accessing protein concentrations from known dilution factors instead of by using absorbance. The results of the CG-MALLS studies are discussed in the following section.

4.3.2   CG-MALLS analysis on full length BM3

Composition gradient-multi-angle light scattering measurements were carried out using the light scattering facilities at Wyatt Technology, Santa Barbara. At the time of conducting this experiment, the laboratory was not equipped with a size exclusion column, which is necessary (as used in all SEC-MALLS, AUC, and SLS) to remove high molecular weight aggregates prior to CG-MALLS analysis. Thus, all stock protein samples dissolved in the experimental buffer were centrifuged and triple filtered with a 0.02 micron filter before use as described in Section 2.4.4. The Calypso system contains three automated syringe delivery systems. Two of the syringes were filled with protein solutions at concentrations of 0.25 mg/mL and 2.5 mg/mL needed to generate concentration gradients to effectively capture BM3 behaviour at low and high protein concentrations. The third syringe contained the experimental buffer (50 mM KCl pH 7.0, with varying concentrations of KCl), which was used to generate 20 serial dilutions at high and low protein concentrations. For accuracy, 2-3 separate measurements were carried out for the low concentration range (up to 0.25 mg/mL) data while two separate measurements were taken for the high concentration range data (up to (2.5 mg/mL) at every ionic strength studied. UV data were also collected at wavelengths of 280 nm and 418 nm.

4.3.2.1 BM3 concentration measurements at 280 and 418 nm

Precise concentration measurements are needed for accurate determination of the K_d and B_{dd}. Having observed discrepancies in the UV data measured at 280 nm and 418 nm for static light scattering studies, this phenomenon was investigated further using the Calypso, which had the additional benefit that concentrations could be determined from the dilution factors When calculating concentrations from dilutions, small errors might occur at the beginning of an experiment as some of the protein in the initial sample can get adsorbed on the tubing and consequently, a lower concentration than expected would occur in the light scattering cell. Otherwise, the concentration change between successive samples should be a constant as equally spaced dilution factors were used for each experiment. If we are to assume constant dilutions, we need to have a value for the dilution factor which is defined here in equation 4.1.

$dil = C_n/n$ 4.1

Equation 4.1: Dilution factor for concentration estimation

where C_n is the concentration at the nth injection assuming that concentrations are in ascending order.
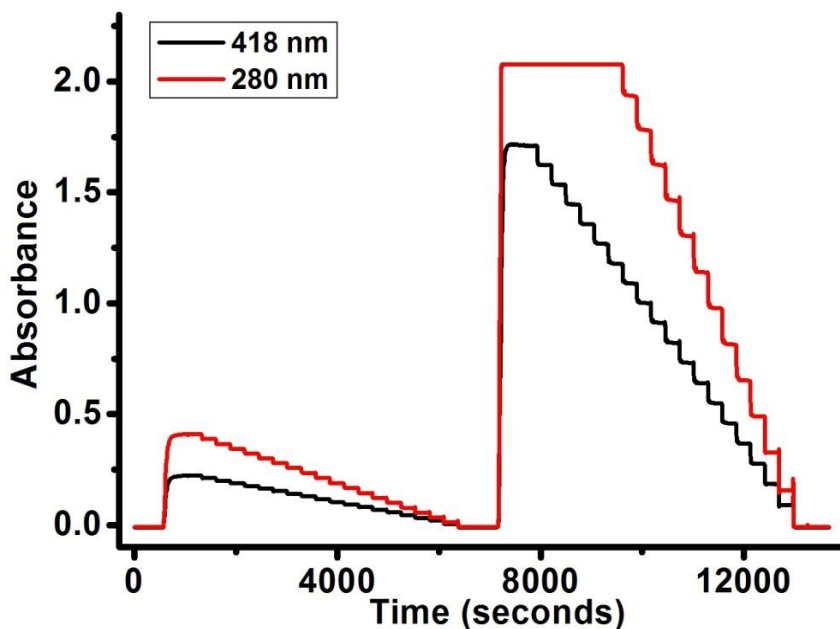
Figure 4.12: Absorbance measurements for BM3 at 280 nm and 418 nm. *The plot shows the noiseless absorbance data obtained for BM3 run 1 at 418 nm (red) and 280 nm (black) for both low and high concentration ranges in solutions with 0.2 M KCl. Similar noiseless data was obtained for runs 2 and 3 as well as for the light scattering and refractive index data. BM3 concentrations for the 19 dilutions were calculated from the plateaus.*

The absorbance data collected for the first run using protein concentration ranges up to 0.25 g/L (low) and 2.5 g/L (high) in buffer containing 0.2 M KCl are shown in Figure 4.12. The data collected were noiseless; similar plots were obtained for all other runs across the ionic strengths studied. In order to examine the accuracy of concentration measurements, the changes in protein concentration for successive dilutions were calculated from the plateau values of the absorbance measured at 280 nm and 418 nm. The results for the experiment with 0.2 M KCl are shown in Figure 4.13. For measurements at 280 nm over the low protein concentration range (Figure 4.13A), there is a spike in the plot (at ~ 0.00015 g/mL), which occurred for each of the three runs. This spike was observed at a similar BM3 concentration for most of the ionic strengths studied (data not shown). Using the concentrations obtained from 280 nm absorbance readings in generating the light scattering plot for $M_{w,app}$ (Figure 4.14) results in a discontinuity at the same protein concentration where the spike occurs in the concentration differences. The discontinuity is not physically realistic so must arise from either an error in the light scattering measurement or an error in the concentration measurement. The error is due to some systematic error in the UV detector, as exact dilutions should produce equally spaced protein concentrations. Thus, the use of BM3 concentration estimated from this measurement for light scattering analysis is not advisable. Samples at high protein concentrations were not in the linear region for using the Beer-Lambert law, which is reflected by the decrease in the plot of concentration difference at high protein concentration shown in Figure 4.13B for the absorbance readings at 280 nm. Furthermore, the maximum absorbance limit of the UV detector is attained halfway through the dilutions. For these reasons, none of the concentration measurements made at 280 nm can be used for BM3 light scattering analysis.
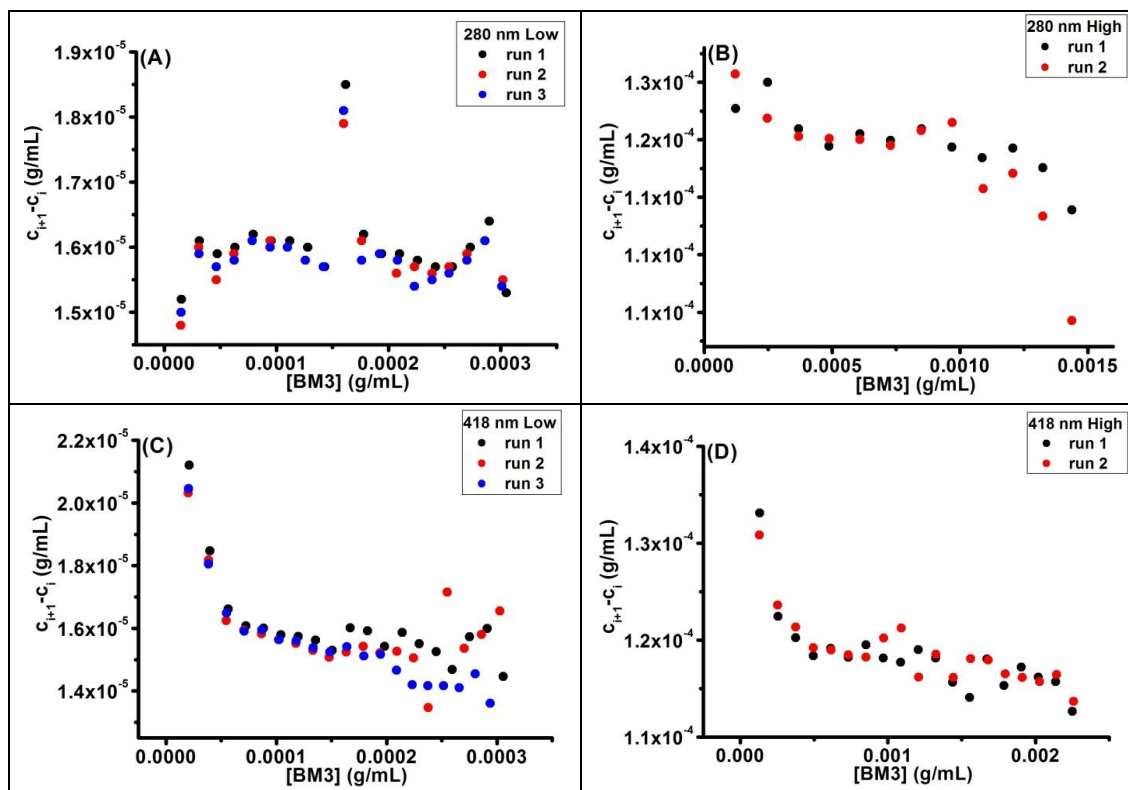
Figure 4.13: Plots of the differences in BM3 concentration over successive samples from light scattering runs at an ionic strength of 0.2 M KCl. The differences shown in the plot were obtained from measurements at 280 nm within the low and high protein concentration ranges (A and B respectively), and measurements at 418 nm for the low and high protein concentration ranges (C and D respectively).

Next, the accuracy of using absorbance measurements at 418 nm for concentration estimation was examined. The results at 418 nm shown in Figure 4.13 C and D indicate that the concentration difference in successive samples is decreasing, especially at low protein concentration. A similar trend was observed previously, in which case absorbance measurements at 418 nm overestimated concentrations when compared with the measurements at 280 nm for low protein concentration. The reason for this behaviour is most likely due to a difference in the extinction coefficients of the BM3 monomer and the dimer; in which case, the extinction coefficient would change with protein concentration as the fraction of dimerization also changes. Because absorbance readings at 418 nm and 280 nm were not reliable, the data analysis was carried out using the dilution method.

For the low concentration range measurement data, the dilution factor was obtained using the absorbance readings at 280 nm of the most concentrated protein sample. For the experiments at high protein concentration, the dilution factor was estimated from the

absorbance measurements taken at 280 nm for the samples at protein concentration less that 1 g/L. The absorbance measurements from the 418 nm detector were not used in the analysis to determine the values of K_d and B_{dd}.
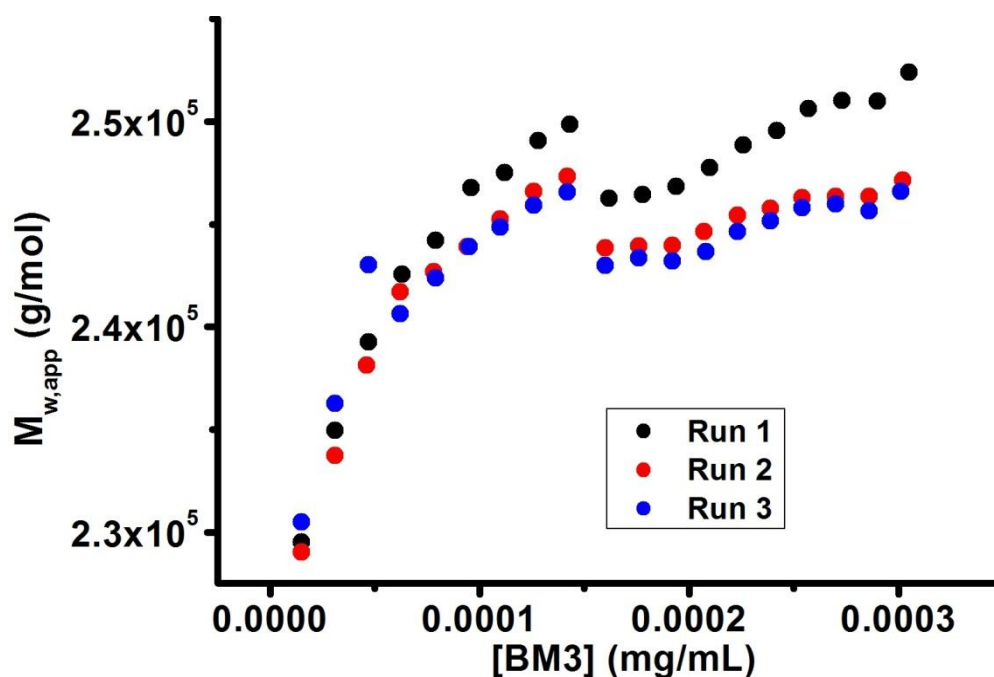
Figure 4.14: Light scattering plots for BM3 using the three low concentration measurements collected at 280 nm. *The apparent molecular weights in this plot were estimated from concentrations shown in Figure 4.13A using equation 4.1. It can be seen that the blip in the concentration measurements causes a discontinuity in the light scattering plot.*

4.3.2.2 Measuring weak protein-protein interactions in BM3 using CG-MALLS

The dissociation constants (K_d) were first determined from analyzing CG-MALLS data taken for samples with protein concentrations up to 0.25 g/L, which corresponds to a range over which a significant fraction of monomers and dimers exist in equilibrium. The light scattering data (Kc/R_θ) were fitted using an equation given by substituting Equation 2.11 into Equation 2.10. The fitting parameters are the dissociation constant K_d, the dimer-dimer osmotic second virial coefficient (B_{dd}) and a parameter reflecting the amount of irreversible protein aggregation, denoted here as *I*. The contribution of the monomer-dimer interaction (B_{md}) was also varied but unrealistic fits were obtained except when the value was near to zero, in which case the fit was not sensitive to the value of B_{md}. As a consequence, the parameter was set to zero. The monomer molecular weight was fixed at the value calculated from the amino acid sequence equal to 119,000

g/mol. The results of the fitting were not sensitive to the choice of monomer molecular weight.

For the low concentration range data, the fitting was carried out for all three runs and the best fit K_d values chosen. The fitting of low protein concentration runs is insensitive to the value of B_{dd} as this term only makes significant contribution to data taken at higher protein concentrations. Representative light scattering fits at low concentration are shown in Figure 4.15 for studies conducted at 0.1 M and 0.8 M KCl. The resulting molecular weights in the light scattering studies are higher than those obtained previously with SEC-MALLS and AUC analysis, predominantly because no SEC column was available to remove all aggregates from the sample. The effects of high molecular weight aggregates in the fitting procedure were included by using the parameter I of Equation 2.10. The data also support the hypothesis that BM3 is dimeric in solution. The increase in molecular weight with protein concentration reflects the monomer-dimer equilibrium. The lines shown in Figure 4.15 correspond to the best fit to the light scattering equation without any virial coefficient terms. As alluded to above, the contributions from the second virial coefficients are negligible at protein concentrations up to 0.25 g/mL. The fit values of the light scattering data correspond to K_d values of 0.05 and 1.1 micromolar at the ionic strengths of 0.1 and 0.8 M.
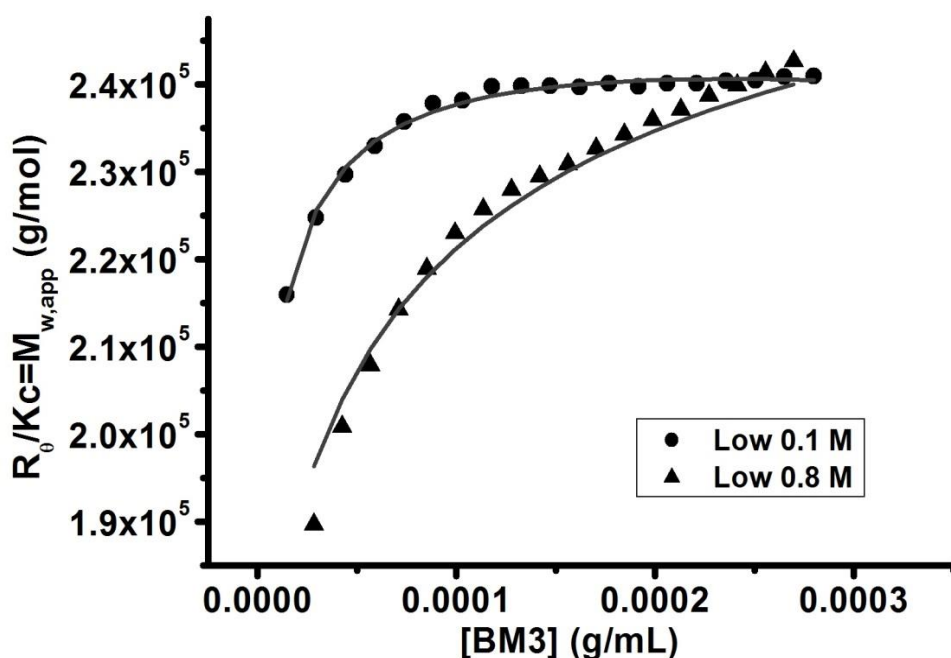
Figure 4.15: Light scattering fits to BM3 CG-MALLS data obtained for low protein concentration range in solutions at 0.1 and 0.8 M KCl. *Fits were obtained without any virial coefficient terms and the K_d values obtained were 0.5 μM and 1.1 μM at 0.1 M KCl and 0.8 M KCl respectively.*

The values of K_d obtained for all fits at a particular ionic strength were averaged and the results are presented in Figure 4.16 and Table 4.1. The dimerization of BM3 is weakened with increasing salt concentration, as also observed in sedimentation equilibrium studies (Figure 4.15). This result is also consistent with our initial observations from the SEC-MALLS in which case the average molecular weight decreased with increasing salt concentration. The main effect of increasing salt concentration over an ionic strength range of 0.1 to 1.0 M is to be to screen electrostatic interactions between proteins. The finding that dimerization is weakened suggests that the dimer is stabilized by attractive electrostatic interactions. Previous work has established that electrostatic interactions stabilize hetero-association between heme and reductase domains in systems where the partners are not covalently attached to each other (*261*). In contrast, here we find electrostatic-driven self-association, which is most commonly observed for proteins in solutions near to the isoelectric point. In this case, the repulsive monopole-monopole interaction is weakened sufficiently that attractive interactions can be formed between surfaces containing charged patches of opposite sign to each other. For instance, β-lactoglobulin undergoes a reversible dimerization near its isoelectric point (*312*).
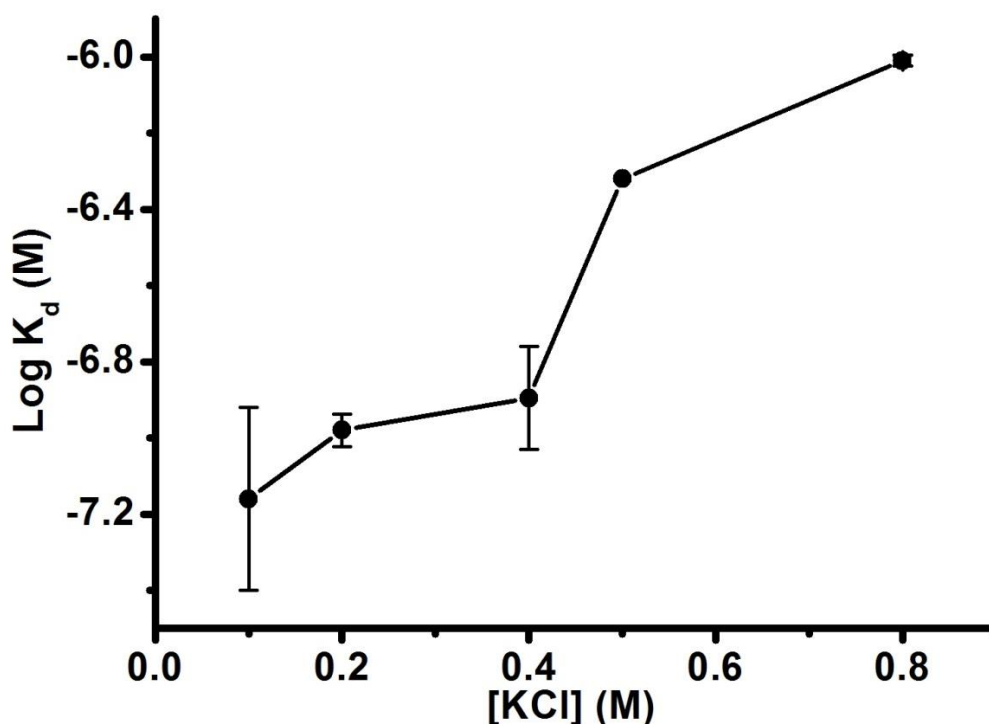
Figure 4.16: Dissociation constants obtained for BM3 at low protein concentration range using CG-MALLS.

Table 4.1: Dissociation constants and dimer-dimer virial coefficients for BM3 obtained from CG-MALLS analysis.

[KCl] (M)	K_d (Low Range, μM)	K_d (High Range, μM)	B_{dd} (x 10^{-4})
0.1	0.08 ± 0.04	0.09 ± 0.03	1.19 ± 0.19
0.2	0.115 ± 0.02	0.13 ± 0.01	1.71 ± 0.01
0.4	0.13 ± 0.04	0.14 ± 0.01	1.21 ± 0.01
0.5	0.48 ± 0.01	N/D	N/D
0.8	0.99 ± 0.04	1.025 ± 0.07	1.65 ± 0.15

The dimer-dimer virial coefficients (B_{dd}) were measured from analysing CG-MALLS data taken at the high protein concentration range (up to 2.5 mg/mL). As before, the data were fitted using a model where B_{md} is set to zero and the fit parameters are B_{dd}, K_d, and I. The results for the fittings at high BM3 concentration range for measurements taken at 0.1 M and 0.8 M KCl are shown in Figure 4.17. As observed in both figures 4.15 and 4.17, the peak in the light scattering signal corresponds to a weight average molecular weight of slightly greater than the value expected for the dimer. This discrepancy could be due to the reversible formation of higher order oligomers or due to the presence of a small fraction of irreversibly formed aggregates. But as seen in the light scattering data for more concentrated protein solutions (Figure 4.17), the reversible formation of oligomers greater than dimer does not occur. As a consequence, a small fraction of the light scattering signal can be attributed to irreversibly formed aggregates (most likely due to intermolecular disulfide bond formation).
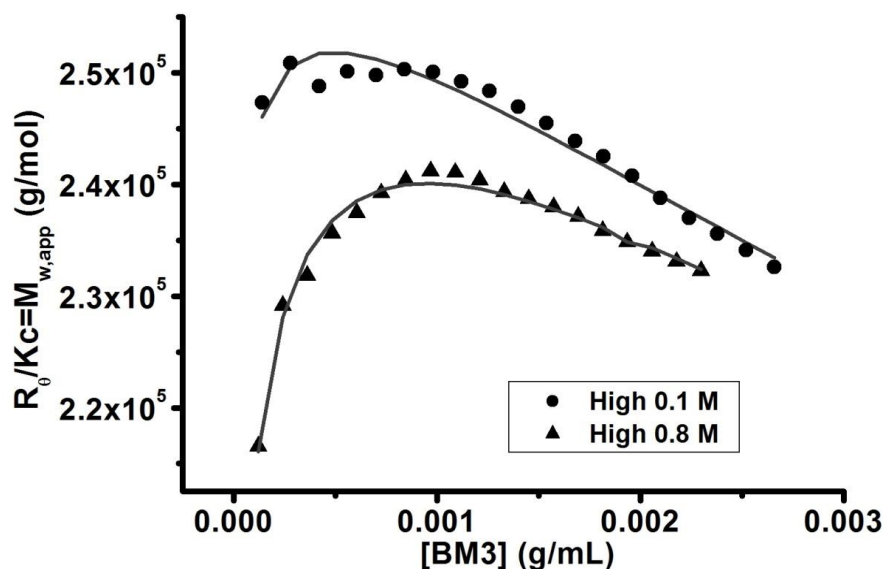
Figure 4.17: Light scattering fits to BM3 CG-MALLS data obtained for high protein concentration range at 0.1 and 0.8 M KCl. The K_d values obtained from fitting the data are similar to those obtained for the low protein concentration range. The fit B_{dd} values indicate that the dimers are repulsive and there is no possiblilty of higher oligomer formation.

The lines shown in Figure 4.17 are the best fit to the data using Equations 2.7 and 2.9 with the B_{md} set to zero. The results indicate the monomer-dimer equilibrium is almost saturated at the concentrations of 0.0005 g/mL for the experiment at 0.1 M ionic strength, whereas at 0.8 M ionic strength, there is still a detectable change in the monomer-dimer equilibrium up to concentrations of 0.001 g/mL. The dimer-dimer virial coefficient is determined from the slope of the light scattering at higher protein concentrations. The results also clearly show that there is no higher order oligomerization. If higher oligomers were forming, one would expect to see an increase in molecular weight with increasing protein concentration according to Le Chatelier's principle. The best fit values for B_{dd} obtained from the plots are 1.5 x 10^{-4} and 1.0 x 10^{-4} mL mol/g^2 for the ionic strengths of 0.1 and 0.8 M, respectively. The results of the fitting are sensitive to the choice of B_{md}, which we have set to zero. Similar fits to the data can be obtained by systematically changing the value of B_{md} and K_d.

However, as seen in Figure 4.18 and Table 4.1, the K_d values obtained at high protein concentration when setting B_{md} equal to 0 are consistent with those obtained from fitting the data at low protein concentration. This provides support that the monomer-dimer virial coefficient is very close to zero.
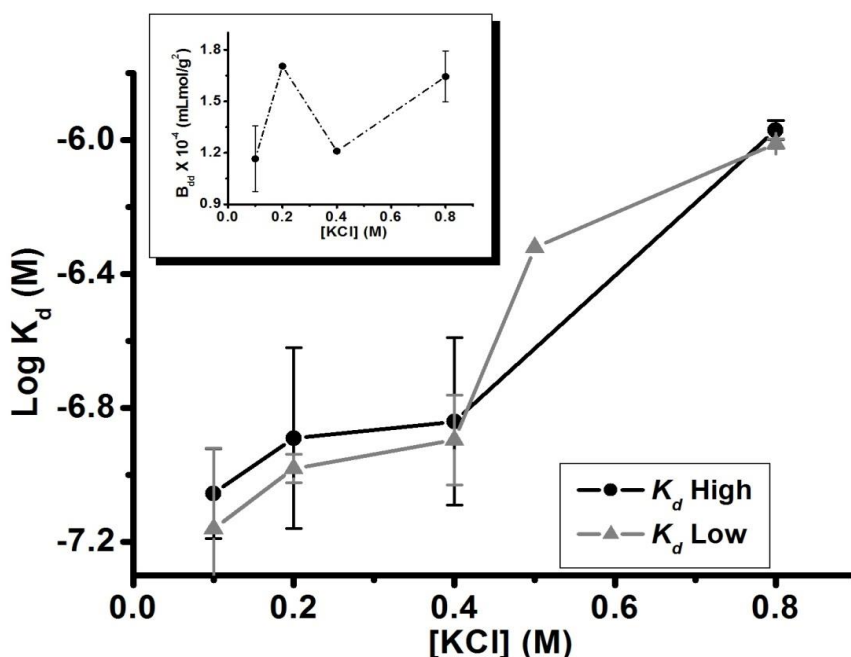
Figure 4.18: Dissociation constants and dimer-dimer virial coefficient obtained for BM3 at both high and low protein concentration range using CG-MALLS. Inset shows dimer-dimer virial coefficient (B_{dd}) plotted versus ionic strength. The B_{dd} values indicate that dimer-dimer interaction is repulsive.

The osmotic second virial coefficients (B_{dd}) are related to an averaged protein-protein interaction between the dimers: positive values reflect repulsive forces, whereas negative values correspond to weakly attractive interactions. The finding that B_{dd} values are always positive indicates that the formation of oligomers with sizes greater than dimer does not occur. The insensitivity of B_{dd} to changes in salt concentration over the range of 0.1 to 0.8 M indicates that electrostatic forces do not make a large contribution to the dimer-dimer interaction. In the absence of repulsive electrostatic interactions, the main contribution to repulsive forces between proteins arises from excluded volume effects. In this case, the value of B_{dd} is equal to the volume about a dimer made inaccessible to other protein dimers. Excluded volume interactions should be independent of ionic strength as long as the protein size is invariant, which is also consistent with our finding that the values of B_{dd} do not change much with salt concentration.

4.3.3 Summary of SLS and CG-MALLS studies on BM3

The results obtained in this section provide further support that BM3 exists in a monomer-dimer equilibrium with dissociation constants in the micromolar region. It is also clear that the interactions in the solutions with ionic strengths equal to 0.5 M and

0.8 M are weaker than those that occur in 0.1 to 0.4 M ionic strength. The interactions at high ionic strength appear to have K_d values on the order of 1 micromolar and those in the lower ionic strengths appear to be on the order of 0.1 micromolar. This agrees with SEC-MALLS and AUC studies and indicates that the BM3 dimer is stabilized by electrostastic interactions. Further, the repulsive dimer-dimer virial coefficient suggests that no higher oligomers are formed in BM3. Further characterization of the BM3 dimer was attempted using cross-lonking studies, as will be discussed in the following section.

4.4 CROSS-LINKING STUDIES ON BM3 AND ITS DOMAINS

Cross-linking has been one of the most applied techniques to characterization of weak interactions in cytochrome P450 systems (see Section 1.3.4). The interaction site(s) between cytochromes P450 and their partners (or other cytochromes) can be identified using a combination of cross-linking and tandem mass spectrometry. In one approach, SDS-PAGE analysis is conducted on the cross-linked samples after which the complex bands are excised and digested (usually via trypsinolysis). In another approach, the cross-linked samples are immediately digested without SDS-PAGE analysis. In either approach, tandem mass spectrometric analysis is used to identify the bonds formed by the cross-linking reactions, which are then used to identify the protein contact sites.

In this study, we aimed to identify interaction sites within the BM3 dimers by using a similar procedure. Initially, cross-linking was attempted using various cross-linkers before SDS-PAGE analysis to identify complexes (preferably containing dimers) on the gel. Cross-linking experiments with formaldehyde and glutaraldehyde were further subjected to SEC-MALLS analysis to examine the formation of higher oligomers. All SDS-PAGE analyses were carried out as described in section 2.1.5.2. These results are discussed in the following sections.

4.4.1 Cross-linking Studies using Formaldehyde with BM3 and Other Domains

Cross-linking studies using BM3 and formaldehyde were carried out at room temperature in buffer containing 50 mM KPi, 0.1 M KCl, pH 7.0. Initial reactions involved ascertaining the best concentrations of formaldehyde to be used, the reaction duration and the resolution gel required. All formaldehyde reactions were quenched with 200 mM glycine and incubated on ice prior to SDS-PAGE analysis.

4.4.1.1 SDS-PAGE analysis of BM3 cross-linking with formaldehyde

For the first trial, 50 µM BM3 was prepared with varying concentrations (0.5 – 4.0 % v/v) of freshly prepared formaldehyde to ascertain at what formaldehyde concentrations higher oligomers are formed. The mixture was incubated for 10 minutes before quenching by adding glycine to a final concentration of 200 mM. Results (not shown) indicate that no higher oligomers were formed for all the formaldehyde concentrations studied. For subsequent reactions, the formaldehyde concentration was fixed at 0.5% and 3% v/v and a time-dependent (5 – 80 minutes) reaction was run using 6% and 10% gels. This was to determine the appropriate incubation time for BM3-formaldehyde mixture as well as to investigate the best resolution gel to be used for further experiments. As seen in Figure 4.19, a better resolution of bands is obtained using the 6% gel. As a result, all subsequent cross-linking studies were carried out using a 6% resolution gel. Further, there was no difference in mobility observed with bands across the various incubation periods studied, or with the bands containing either 0.5% v/v or 3% v/v formaldehyde. In all cases, higher oligomers were not observed. However, the bands very close to the wells indicate the presence of high molecular weight aggregates above the resolution capacity of the marker. This implies that the cross-linking reaction is non-specific and leads to indefinite association of the molecules.
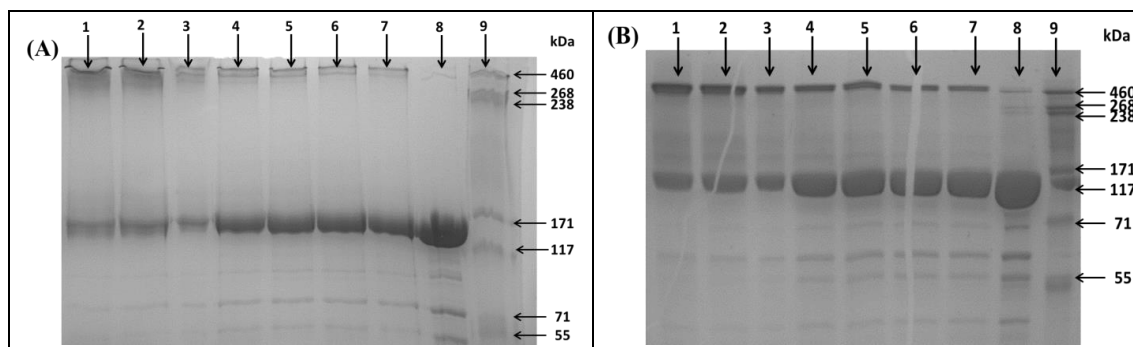
Figure 4.19: SDS-PAGE gel for BM3-Formaldehyde cross-linking studies. *(A) 6% and (B) 10% resolution gel for mixture containing 50 µM BM3 and 3% v/v formaldehyde after an incubation time of 80 minutes (lane 1); 60 minutes (lane 2); 40 minutes (lane 3); 20 minutes (lane 4); 15 minutes (lane 5); 10 minutes (lane 6) and 5 minutes (lane 7). Lane 8 contains pure non-modified BM3 sample while lane 9 contains the HiMark^{TM} pre-stained high molecular weight protein standard (30 – 460 kDa).*

4.4.1.2 SEC-MALLS analysis of BM3-formaldehyde cross-linking

Since no dimers were observed on the SDS-PAGE analysis for BM3-formaldehyde mixture (as expected), the mixture was run using SEC-MALLS to examine if any higher oligomers are formed that could not be detected using SDS-PAGE. The experiments were conducted at two different BM3 concentrations. Unreacted BM3 in buffer containing 50 mM KPi, 0.1 M KCl, pH 7.0 was purified with SEC and then post gel filtration samples were reacted with formaldehyde and one sample was run without further modification for comparison purposes. In one reaction, 200 µL of purified BM3 at 1 mg/mL BM3 was added to 200 µL of 4% formaldehyde and the mixture incubated at room temperature before quenching by adding 100 µL of 1 mM glycine and subsequently incubated on ice. The total 500 µL mixture was run on SEC-MALLS. For the second experiment, 200 µL of 4% v/v formaldehyde was added to 200 µL of 10 mg/mL post gel filtered BM3, quenched by adding 100 µL of 1 mM glycine and run on SEC-MALLS as described above. The SEC-MALLS results at high (4 mg/mL) and low (0.4 mg/mL) BM3 concentrations are shown in Figure 4.20.
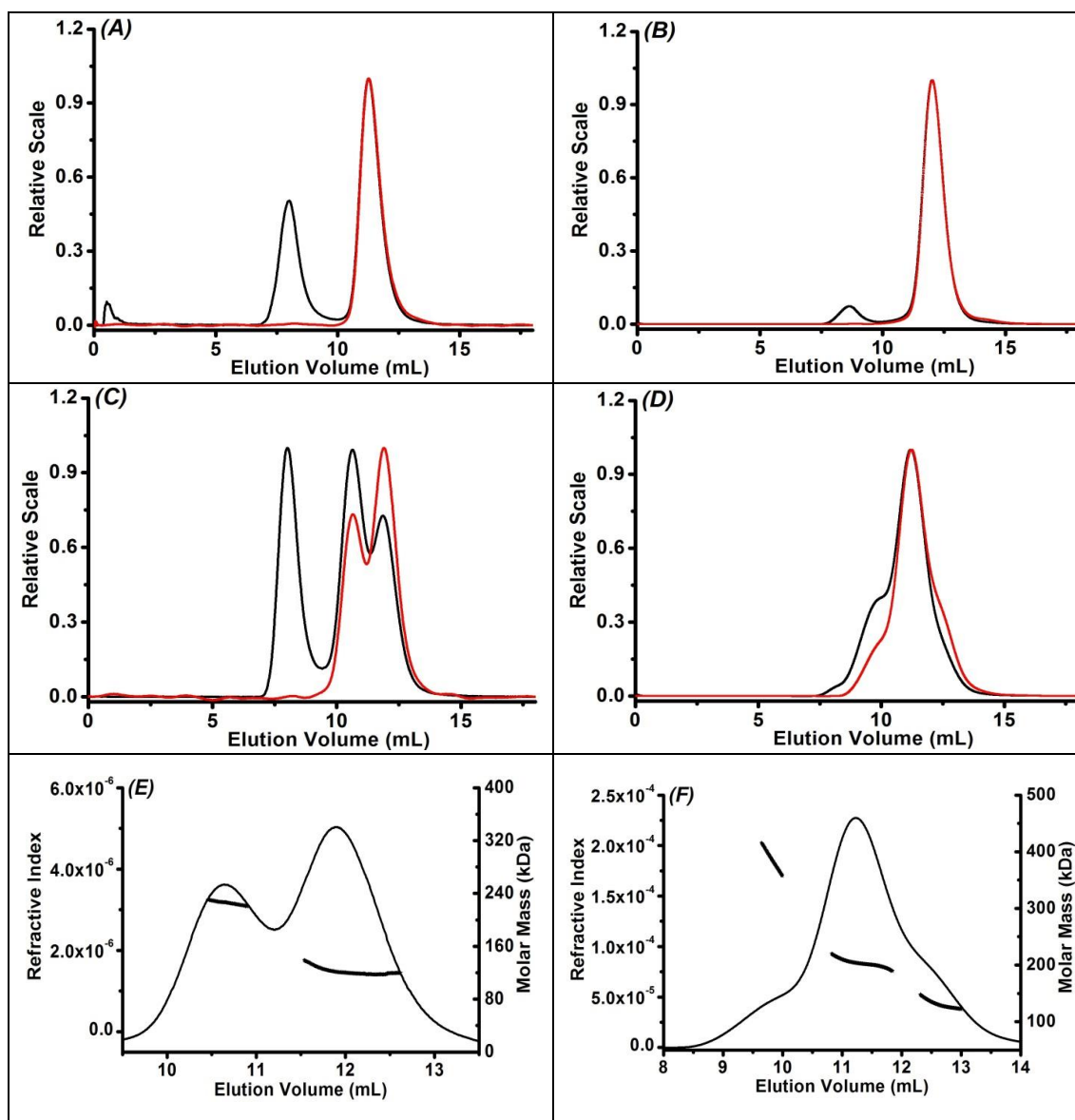
Figure 4.20: SEC-MALLS chromatographs of BM3-formaldehyde complex. *Elution profiles of unmodified BM3 at (A) low (0.4 mg/mL) and (B) high (4 mg/mL) concentrations; with 4% v/v formaldehyde at (C) low and (D) high BM3 concentrations showing the MALLS trace at detector 11 (black line), and the refractive index trace (red line). The corresponding chromatograms representing refractive index measurements (left-hand scale) of BM3 with 4% v/v formaldehyde measured at both (E) low and (F) high BM3 concentrations are also shown. The right- hand scale (Figures E and F) represents the average molecular weights of the peak slices as estimated by the ASTRA software. At low BM3 concentration, monomers (58% of total peak corresponding to 122 kDa) and dimers (42% of total peak corresponding 226 kDa) were observed while at high BM3 concentration, monomers (15% of total peak corresponding to 125 kDa), dimers (76% of total peak corresponding to 203 kDa) and trimers (9% of total peak corresponding to 386 kDa) were observed. Unmodified BM3 eluted as 100% dimers with weight average molecular weights of 202.9 and 202.2 kDa at low and high BM3 concentrations respectively.*

The unmodified BM3 samples at both high and low concentration eluted as single dimeric peaks with weight average molecular weights of 202.9 ± 6.7 and 202.2 ± 5.9 kDa, respectively. The chromatograms (Figure 4.20 A-B) and resulting molecular weight is in good agreement with previous SEC-MALLS studies under the same conditions (Figure 4.1). On the other hand, in the cross-linking mixture at low BM3 concentration 42% of the BM3 formed a dimer and 58% formed a monomer with average molecular weights of 225.7 ± 2.8 and 122.1 ± 5.6 kDa respectively. Although no higher oligomers were observed in this case, it was interesting to observe that the presence of formaldehyde led to the isolation of monomers. At high BM3 concentration, trimers (386.2 ± 17.3 kDa) were observed in addition to monomers (125.4 ± 2.1 kDa) and dimers (203.3 ± 7.0 kDa).

The mechanism for the formation of monomers, dimers and trimers is not fully understood at this point. One possibility is that formaldehyde causes the P450 domain to dissociate and the reductase domain (sequence molecular weight equals 64 kDa) associates to form dimers (128 kDa), tetramers (252 kDa) and higher oligomers, also explaining the weight average molecular weights obtained. On the other hand, the formaldehyde could cause the active dimers observed in the non-modified samples to dissociate into monomers and then cause the monomers to re-associate by converting the free carboxylic groups to permanent amines leading to the formation of dimers and trimers. Further, the presence of fewer monomers (at 15% of total peak) for measurements carried out at high BM3 concentration compared to measurements at low BM3 concentration (at 58% of total peak) suggests that the isolated monomers could reversibly associate to form stable dimers. To test this, the monomer peak from the high concentration experiment was split into two equal fractions. One fraction was re-run on the SEC-MALLS under the same buffer conditions and the result is shown in Figure 4.21, while the other fraction was subjected to further analysis using sedimentation velocity (section 4.4.1.3).
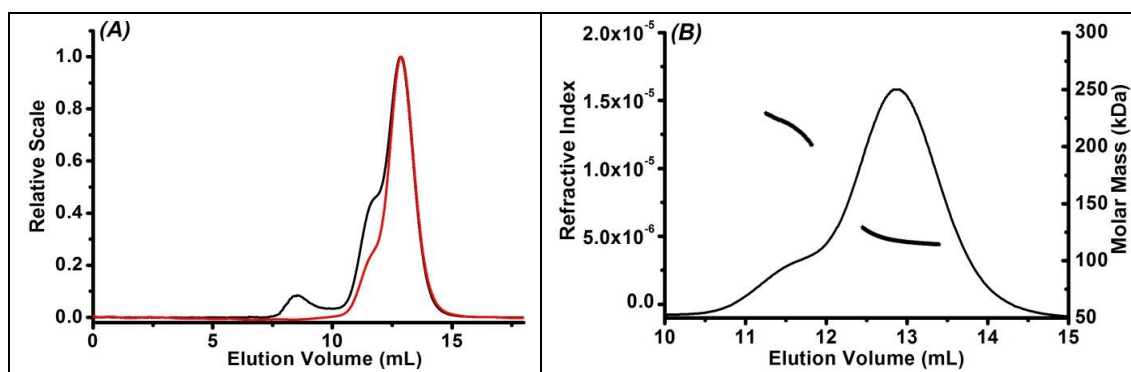
Figure 4.21: SEC-MALLS chromatographs of BM3 monomer. *(A) Elution profiles of formaldehyde BM3 monomer showing the MALLS trace at detector 11 (black line), and the refractive index trace (red line). (B) The corresponding chromatograms representing refractive index measurements (left-hand scale) of BM3-formaldehyde are also shown. The right-hand scale (Figure B) represents the average molecular weights of the peak slices as estimated by the ASTRA software. A predominantly monomeric peak (88%, 118.5 kDa) and a dimeric shoulder (12%, 218 kDa) were observed.*

As seen in Figure 4.21, a re-run of the monomeric peak from Fig 4.20F still produced a high percentage of monomers (88% of total peak) with an average molecular weight of 118.5 ± 4.0 kDa and a dimeric shoulder (12% of total peak) with average molecular weight of 218.3 ± 7.7 kDa. No trimer peaks or shoulders were observed. This again suggests either the formation of a stable BM3 monomer or a BMR dimer (where the BMP domain has been lost). Sedimentation velocity experiment was conducted on this monomer for further evaluation, as discussed in the following section.

4.4.1.3 AUC analysis on formaldehyde generated BM3 monomer

Sedimentation velocity on the formaldehyde modified BM3 (3 µM) was conducted under the same conditions for unmodified BM3 and BMR as described in section 4.2. The resulting sedimentation velocity plot (Figure 4.22) indicates that four peaks are observed with s_{app} values 3.69 S (3%), 5.61 S (79%), 7.24 S (10%), and 8.91 S (8%). The predominant peak with s_{app} value of 5.61 was further analysed using SEDNTERP to generate the hydrodynamic parameters. Further, the c(s) plot for the formaldehyde modified form of BM3 and the generated hydrodynamic parameters were compared to those obtained for wild-type BM3 and BMR as shown in Figure 4.22B and Table 4.8. The formaldehyde BM3 peak is at the same position as the BMR dimer peak and has similar hydrodynamic values to the BM3 dimer. This provides further support that the peak observed in SEC-MALLS and AUC for formaldehyde modified BM3 could be

that of a BMR dimer after the heme domain has been lost. It is important to note that the loss of heme domain is very unlikely but not impossible.
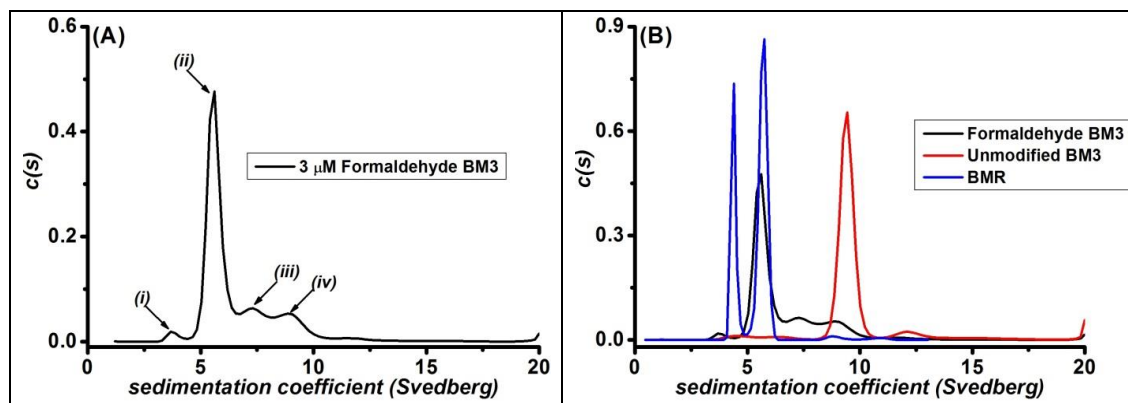
Figure 4.22: Sedimentation velocity plot [c(s) analysis] for proposed BM3 monomer. *The species distribution was calculated using SEDFIT from ~200 sedimentation scans. (A) c(s) analysis plot for 3 µM BM3 monomer peak from SEC-MALLS in 50 mM KPi, 0.1 M KCl, pH 7.0. Four peaks were observed (i-iv) and the s_{app} values obtained were 3.69, 5.61, 7.24, and 8.91. (B) Comparison plot for formaldehyde modified BM3 (black line), unmodified BM3 (red line), and unmodified BMR (blue line).*

Table 4.8: Hydrodynamic parameters for BM3 formaldehyde-treated and unmodified BM3/BMR sedimentation velocity studies

Molecule	[BM3/BMR] (µM)	s_{app} (x 10^{-13} s)		$s_{20,w}$ (x 10^{-13} s)		r_H (nm)		f/f_o	
BM3	4.0	9.44		9.74		5.68		1.39	
BM3 formaldehyde	3.0	5.63		5.81		4.76		1.47	
BMR	3.0	4.39	5.76	4.60	6.04	3.31	5.0	1.25	1.52

4.4.1.3 Formaldehyde cross-linking of BMR and BMP

Formaldehyde cross-linking was also attempted for the BMR (in the presence and absence of DTT) and BMP domains. 100 µM each of BMR and BMP were cross-linked with 0.5% v/v formaldehyde and the reaction was allowed to proceed for 10 minutes. After quenching with a final concentration of 200 mM glycine, the mixture was subjected to SDS-PAGE analysis as described for BM3. According to the resulting gel (not shown) the formaldehyde modified BMP and BMR had exactly the same migration patterns as the wild type BMP and BMR, respectively, implying that no higher oligomers were formed. Subsequent studies were then carried out using other cross-linkers as discussed in the following section.

4.4.2 Cross-linking Studies on BM3 with Glutaraldehyde and Other Cross-Linkers

As discussed in section 2.4.5, further cross-linking attempts were carried out with BM3 and several other cross-linking agents. While some interesting results were observed with glutaraldehyde, most other cross-linkers did not yield any higher oligomers and the gel migrating patterns of these cross-linked mixtures were not different from that of the wild-type BM3. Here, only the results for glutaraldehyde and EDC (1-Ethyl-3-[3-dimethylaminopropyl]Carbodiimide Hydrochloride) are shown as a representative of the migrating patterns for all cross-linkers studied.

4.4.2.1 SDS-PAGE analysis of BM3 cross-linking with glutaraldehyde and EDC

Cross-linking experiments with glutaraldehyde were carried out in a similar way to those with formaldehyde. The concentration of glutaraldehyde was varied between 0 and 2% v/v while BM3 concentration was fixed at 50 µM. The reaction was quenched with excess Tris-HCl, pH 8.0 (final concentration of 500 mM) and incubated on ice before SDS-PAGE analysis. The concentration of EDC was varied between 0 and 50 µM. The cross-linking reaction was quenched by adding a final concentration of 20 mM β-mercaptoethanol and incubated on ice prior to SDS-PAGE analysis. Irrespective of the concentration of glutaraldehyde and EDC used, similar gel migration patterns were observed for each cross-linker as shown in Figure 4.23. Although the samples were overloaded, the gel shows that no higher oligomers were obtained with EDC as the gel migration pattern was the same as the unmodified BM3 sample. However, the glutaraldehyde samples did not migrate past the loading wells. Is it possible that the cross-linking was too efficient and generated higher oligomers beyond tetramers? This phenomenon was investigated further by running the cross-linked mixture on SEC-MALLS as discussed in the next section.
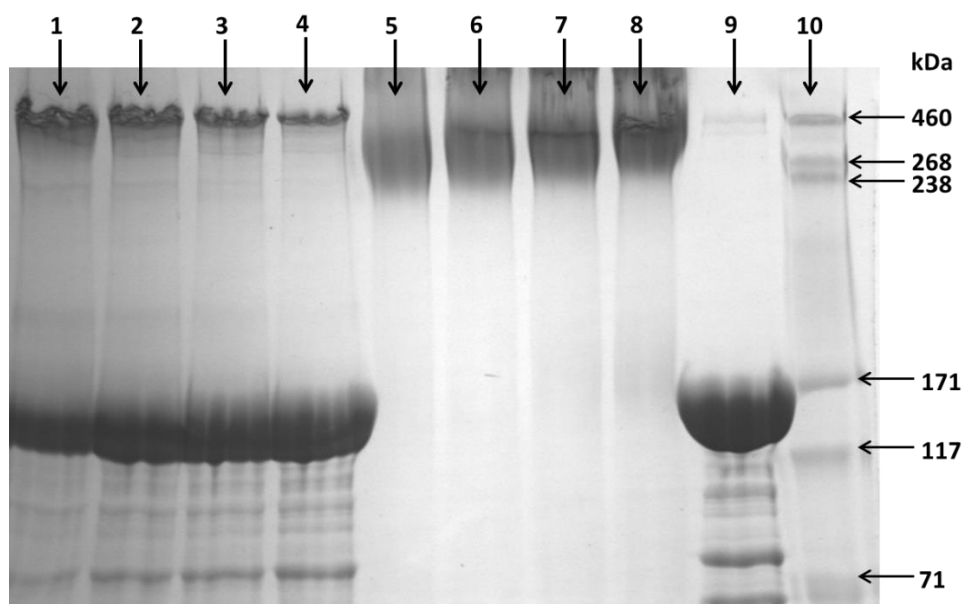
Figure 4.23: SDS-PAGE gel for BM3-glutaraldehyde and BM3-EDC cross-linking. *A 6% resolution gel for mixture containing 50 µM BM3 and 10 µM EDC (lane 1); 20 µM EDC (lane 2); 30 µM EDC (lane 3); 40 µM EDC (lane 4); 0.2% v/v glutaraldehyde (lane 5); 0.4% v/v glutaraldehyde (lane 6); 0.6% v/v glutaraldehyde (lane 7) and 1.0% v/v glutaraldehyde (lane 8). Lane 9 contains pure non-modified BM3 sample while lane 10 contains the HiMark^{TM} pre-stained high molecular weight protein standard (30 – 460 kDa).*

4.4.2.2 SEC-MALLS analysis of BM3-glutaraldehyde cross-linking

For SEC-MALLS analysis, 100 µl of 1% v/v glutaraldehyde was added to 100 µL of 1 mg/mL post gel-filtered BM3 and incubated at room temperature for 10 minutes. The reaction was quenched with 100 µL of 1 M glycine and the sample was loaded onto the size exclusion column. The resulting elution profile and chromatogram is shown in Figure 4.24. The mixture is shown to elute as a predominantly dimeric peak (90% of the total peak) with a weight average molecular weight of 251.8 ± 3.4 kDa and a near-dimeric shoulder (10% of a total peak) with molecular weight of 153.3 ± 7.1 kDa. The dimer molecular weight obtained in this case is higher than the expected dimer molecular weight (238 kDa) and those obtained with non-modified BM3 under the same conditions (198.6 ± 12.3 kDa; see Table 4.3). This might suggest the presence of trimers under the same peak. Further, comparing the molecular weight obtained in the absence of glutaraldehyde (198 kDa) with that obtained in the presence of glutaraldehyde (251 kDa), it appears that glutaraldehyde has a stabilizing effect on the dimer formed. In addition, the molecular weight resulting from the shoulder (153 kDa) is higher than that

expected for a monomer (118 kDa) and much lower than that expected for the dimer. This also suggests a mixture of monomers and dimers under the same shoulder.
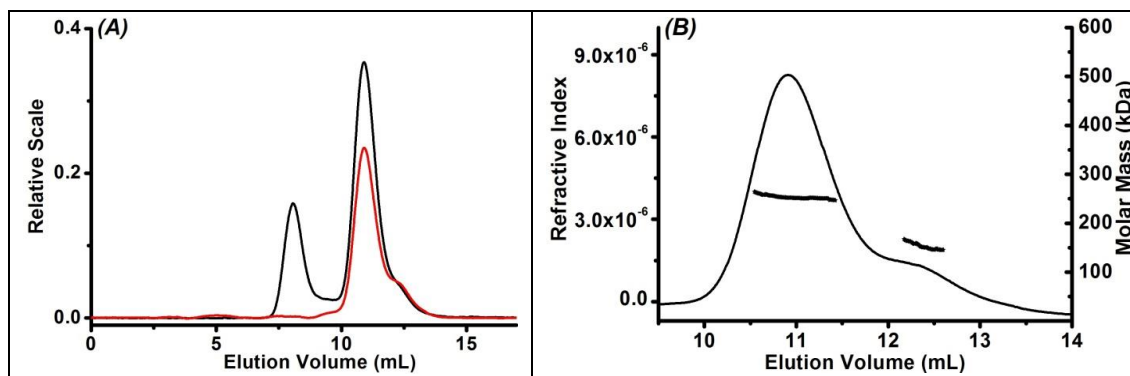
Figure 4.24: SEC-MALLS chromatographs of BM3-glutaraldehyde mixture. *(A) Elution profiles of mixture containing 1% v/v glutaraldehyde with BM3 showing the MALLS trace at detector 11 (black line), and the refractive index trace (red line). (B) The corresponding chromatograms representing refractive index measurements (left-hand scale) of BM3-glutaraldehyde are also shown. The right-hand scale (Figure B) represents the average molecular weights of the peak slices as estimated by the ASTRA software. A predominantly dimeric peak (90% of total peak corresponding to 251.8 kDa) and a near-monomeric shoulder (10% of total peak corresponding to 153.3 kDa) were observed.*

4.4.3 Summary

Although some cross-linked BM3 dimers were observed from SEC-MALLS studies with formaldehyde, these could not be seen on SDS-PAGE gels with formaldehyde or other cross-linkers. As a result, the cross-linking studies could not be continued to examine the contact points within the BM3 or BMR dimer. A possible reason for not obtaining stable dimers using SDS-PAGE analysis could be that the cross-linked sample was reduced prior to applying onto the gel. However, this does not explain the presence of monomers on SEC-MALLS with the formaldehyde mixtures, but not with glutaraldehyde mixtures. That notwithstanding, future studies with non-reduced samples is recommended for verification purposes.

4.5 CRYSTALLIZATION TRIALS WITH C773A BMR

The biophysical and hydrodynamic characterization of the reductase mutant, C773A, has already been described in sections 4.1.3.2 and 4.2.1.3. SEC-MALLS and sedimentation velocity analysis revealed that there was no significant difference in all

the hydrodynamic parameters deduced between the wild type reductase domain and the C773A mutant. In this section, results from crystallization trials with C773A are discussed.

For initial screening, 200 nL of 12 mg/mL of post-gel filtered BM3 reductase (in the presence and absence of $NADP^+$) was mixed with 200 nL of different commercially available screens (Crystal Screens I and II; Morpheus; PACT premier; and JCSG-Plus) using the sitting drop method as discussed in section 2.4.6. Crystals were obtained from Crystal Screen II condition H12B (containing 0.15 M potassium thiocyanate, 0.1 M Tris pH 8.5, 15% w/v PEG 6K, 12 mg/ml C773A, 500 μM NADPH); Crystal Screen II condition D1B (containing 0.1 M sodium cacodylate pH 6.5, 40% V/V MPD, 12 mg/ml C773A, 500 μM NADPH); and Morpheus condition D5A (containing 0.12 M alcohols, 0.1 M sodium HEPES:MOPS pH 7.5, 37.5% PEGMME:PEG20K, 12 mg/ml C773A). The crystals obtained were, however, not of good-diffraction quality. The process was repeated and crystal growth was assisted using the seeding technique (See Appendix F for Seeding protocol). More crystals were obtained at conditions shown in Table 4.9.

Table 4.9: Conditions for crystal growth for BM3 reductase mutant, C773A, at 20ºC with seeding to assist crystal growth

Screen	Crystal Shape	Precipitant	Buffer (pH)	Ligand/Salt
Morpheus D5	Hexagon	PEGMME550; PEG 20K	7.5	Alcohols
Morpheus D9	Needle	PEGMME550; PEG 20K	8.5	Alcohols
Morpheus D12	Hexagon	Racemic MPD; PEG 1K, PEG 3350	8.5	Alcohols
Morpheus E9	Needle	PEGMME550; PEG 20K	7.5	Ethyleneglycols
Morpheus F9	Needle	PEGMME550; PEG 20K	8.5	Monosaccharides
Clear Strategy H12	Chunky	PEG 6K	8.5	Potassium Thiocyanate

The screen with the highest diffraction-qualities was clear strategy H12. Thus, optimization was attempted by varying the amount of C773A, potassium thiocyanate, buffer and PEG. More crystals were produced as shown in Figure 4.25, but unfortunately these crystals did not diffract beyond ~9 Å.
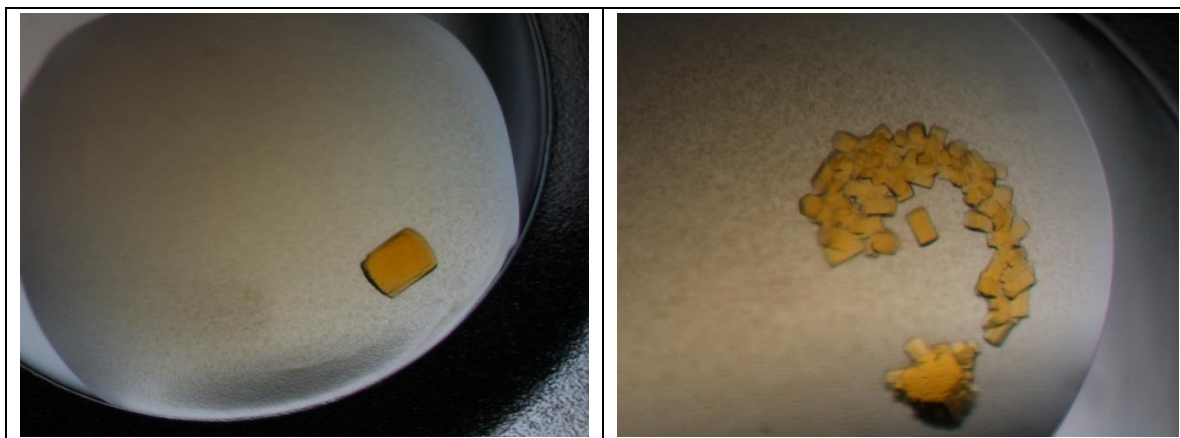
Figure 4.25: Some images of C773A crystals. *These crystals were obtained using 25 mg/mL C773A, 0.12 M 1-butanol, 30% PEG 550 MME, in buffer containing 0.1 M Tris pH 8.5 (left) and 25 mg/mL C773A, 0.15 M methanol, 30% PEG 550 MME in buffer containing 0.1 M Tris pH 8.5 (right).*

4.5 DISCUSSION

4.5.1 Determination of the oligomeric states of flavocytochrome P450 and its domains

In this chapter, various biophysical techniques were employed to determine and characterize the oligomeric states of flavocytochrome P450 BM3 and its domains. The elucidation included molecular weight measurements from a range of techniques and enzyme sedimentation coefficient determination. The weight average and single species molecular weights observed for all BM3 and the domains were comparable.

Flavocytochrome P450 BM3 has been shown in this chapter to be near-dimeric in solution. A comparison of the sequence molecular weight of BM3 to the resulting molecular weight obtained from various biophysical techniques reported in this chapter is shown in Table 4.10. The comparison clearly shows that the weight average molecular weights obtained in all the cases are almost double that of the sequence molecular weight indicating that BM3 is dimeric in solution, albeit with a molecular weight slightly less than that calculated from the dimer amino acid sequence. The lower molecular weights could be as a result of one or a combination of the following. First, we have observed a rapidly forming and dissociating monomer-dimer equilibrium suggesting that a full dimerization weight average molecular weight cannot be obtained at any point in all the experiments. Second, average molecular weights are estimated from SEC-MALLS data using an assumption that there are no repulsive interactions

between the samples, hence setting the second virial coefficients (B_{22}) to zero. However, studies using CG-MALLS (see section 4.3.2.2) indicate a slightly strong repulsive interaction in the sample. Although B_{22} is negligible at concentrations less than 0.5 mg/ml and hence does not explain the results at lower protein concentration; the strong repulsion could significantly decrease the apparent molecular weight observed at higher BM3 concentrations. Third, recent work has shown that resulting SEC chromatogram peak shapes can be rationalized in terms of reversible dimerization (*308*). Using the dimerization constants (K_{12}) obtained from sedimentation equilibrium analysis and CG-MALLS along with the injected BM3 sample concentrations (C_{eM}; assuming all monomers), $K_{12}C_{eM}$ values between 0.1 and 50 were studied in the SEC runs here (with a greater majority in the range of 1 to 10). This is a range where monomers and dimers are found to co-exist. In our studies, the SEC chromatograms had characteristic tailing peaks (Figure 4.5) which, when combined with the $K_{12}C_{eM}$ values obtained, suggests relatively fast association and dissociation rates.

Table 4.10: Summary of BM3 molecular weight measurements obtained from various techniques discussed in this chapter. The molecular weights shown in this table represent measurements from low BM3 concentrations at KCl concentrations varying from 0.05 to 0.2 M.

TECHNIQUE	BM3 (kDa)
Sequence	119
SEC-MALLS	199
Sedimentation velocity	235
Sedimentation equilibrium (single species)	212
Sedimentation equilibrium (global fit)	206
CG-MALLS	215

Further, SEC-MALLS studies indicated that BM3 exists as only dimers in solution. This was also confirmed by sedimentation velocity studies as the SEC peak was further resolved into a 94% dimer peak and a 4% trimer peak (Figure 4.6). In the same vein, positive dimer-dimer virial coefficients were obtained from CG-MALLS analysis indicating that the dimers repel each other and there was no evidence of trimer or higher oligomer formation. Thus, these studies have shown that BM3 only exists as a dimer in solution and the presence of higher oligomers are unlikely. Further, addition of DTT to BM3 sample did not significantly change the resulting weight average molecular weight, signifying that disulfide linkages play little or no role in dimerization of BM3.

Under non-reducing conditions, BM3 was found to migrate only as monomers on SDS-PAGE but eluted only as dimers on FPLC (M_W = 230 kDa) and pre-incubation with DTT did not affect the resulting molecular weight (*107*). This is in agreement with the observations in this study confirming that disulfide linkages do not play a role in dimerization of BM3. On the contrary, earlier reports by Black and Martin (*109*) showed that BM3 eluted on HPLC as a combination of monomers, dimers, trimers, and higher oligomers (Table 4.11). However, pre-incubation with DTT resulted in the production of more dimers (94%). DTT was also observed to slightly alter the sedimentation velocity and equilibrium results but they concluded that these DTT effects do not imply the reduction of disulfide bonds. The sedimentation coefficient value obtained from our study (9.44) is similar to that obtained from the report by Black and Martin (9.244), which, when combined with the estimated sedimentation velocity molecular weights in both studies, indicate the presence of predominantly dimeric species.

According to Table 4.3, the BMP and FMN domains eluted as monomers while the BMR and FAD domains eluted as near-dimer and full dimer respectively. Further, it was observed that BMR and BM3 exhibit similar behaviours in solution, although the dimerization for BMR may not be as strong as that of BM3. The monomer-dimer equilibria for BM3 and BMR were further resolved by sedimentation velocity into a predominantly dimer peak (94%) and a dimer/monomer peak (53%/46%) respectively (Figures 4.6 and 4.7). From SEC-MALLS studies, a single peak was observed with molecular weight corresponding to values above the monomer molecular weight and below the dimer molecular weight (1.5-mer). On the contrary, an earlier report (Table 4.11) indicated that BMR eluted as two peaks using FPLC (corresponding to a 1.4-mer and a 2.5-mer) while the other study reported the presence of a 1.3-mer peak and other higher oligomers using HPLC. Further, in our study, we observed that pre-incubation of BMR with DTT does not significantly affect the resulting molecular weight, which implies that disulfide linkages do not contribute to the dimerization of BMR. This, however, is not the case with the FPLC studies reported above where pre-incubation with DTT led only to the formation of a 1.4-mer and the 2.5-mer peak disappeared. A common factor in these three studies is the presence of the ~1.4-mer, which suggests that BMR forms a reversible monomer-dimer equilibrium. During SEC-MALLS, the monomers and dimers could not be resolved and eluted as a single peak, whereas the equilibrium species could be resolved by sedimentation velocity.

Almost complete dimerization (1.9-mer) was observed for FAD in our study. However, upon reduction of the FAD domain by DTT, monomers could be resolved from dimers. Comparing this result to HPLC and FPLC studies as shown in Table 4.11, other oligomeric states (besides dimers) were observed for the FAD domain, but pre-incubation with DTT favoured the elution of mostly monomers. These findings indicate that dimerization of the FAD domain is mostly controlled by the formation of disulfide linkages which is also consistent with a study where the mutation of two surface cysteine amino acids to alanine in the FAD domain allowed for the crystallization of the protein (*115*).

*Table 4.11: Oligomerization states of BM3, BMR and FAD compared with available literature. * represents measurements from this study using SEC-MALLS; + represents measurements from HPLC studies by Govindaraj and Poulos (107); ^ represents measurements from FPLC studies by Black and Martin (109); NM means not mentioned in the paper.*

Enzyme	Sequence Mol. Wt. (kDa)	Mol. Wt. (kDa)/Percentage/Oligomerization state		
		SEC-MALLS*	HPLC[+] (*109*)	FPLC^(*107*)
BM3	119	198.6/100/1.7-mer	763.8/3.3/6.4-mer 360.6/17.8/3.0-mer 245.5/30.4/2.1-mer 173.4/47.5/1.5-mer	230/100/1.9-mer
BM3 + DTT		180.2/100/1.5-mer	NM/94/1.5-mer NM/6/Other higher forms	230/100/1.9-mer
BMR	64	98.1/100/1.5-mer	63.9/NM[$]/1.3-mer Other higher forms	159.5/65/2.5-mer 90/35/1.4-mer
BMR + DTT		88.3/100/1.4-mer	NM	90/most/1.4-mer
FAD	45	86.4/100/1.9-mer	NM/62.6/1.3-mer NM/26.9/2.3-mer NM/6.8/3.5-mer NM/3.6/4.9-mer	120/40/2.7-mer 42.9/60/0.95-mer
FAD + DTT		86.3/76/1.9-mer 44.0/24/1.0-mer	NM	Mostly monomers

In summary, BM3 has been observed to be monomeric at very low ionic strength (5 mM KPi) and predominantly dimeric at higher ionic strengths with no likelihood of higher oligomers present. BMR is also near-dimeric and exhibits similar behaviour with BM3 as both dimerizations are weakened by increasing ionic strength and unaffected in the presence of a reducing agent DTT. On the other hand, the FAD domain dimerizes almost completely in solution, but the dimerization is decreased in the presence of DTT, indicating that disulfide bonds are formed between FAD molecules. Since the FAD

domain dimerizes irreversibly, it is highly likely that FAD dimerization drives BMR dimerization. The BMP and FMN domains exist as monomers in solution. Further studies involved characterization of the BM3 and BMR dimers, as will be discussed in the following section.

4.5.2 Characterization of the BM3 and BMR dimers

The near-dimer molecular weights obtained for BM3 and BMR suggested the presence of a monomer-dimer equilibrium, which was further investigated by measuring dissociation constants and second virial coefficients. Data obtained from both sedimentation equilibrium and CG-MALS studies of BM3 could only be fitted to an interacting model consisting of a monomer-dimer equilibrium. For the sedimentation equilibrium studies, the highest K_d equal to 0.29 μM was measured in solutions containing 0.15 M KCl reflecting a relatively strong transient dimerization. Attempts to fit the data to other models did not give accurate fits. This result is not in agreement with that of Black and Martin who obtained excellent fits to the sedimentation equilibrium data for BM3 with a model representing monomer-dimer-trimer-tetramer equilibrium. Further, the BM3 frictional ratio obtained in their sedimentation velocity study (f/f_o = 1.50) was larger than what we obtained for BM3 (f/f_o = 1.39) but comparable to what we measured for BMR (f/f_o = 1.52) in this study. The measured frictional ratios suggest a near-spherical but asymmetric shape for BM3 and an ellipsoidal shape for BMR. These conformations are discussed further in the chapter 5. The differences observed between our study and that of Black and Martin could be attributed to the solution conditions used in both experiments. In our study, the buffer contained varying concentrations of potassium phosphate at pH 7 and the experiment was conducted at 4 ºC, while the buffer used in the studies by Black and Martin was at pH 7.4 and the experiment was conducted at 20ºC. Further running the samples through a gel filtration column prior to sedimentation velocity and equilibrium analysis as done in our studies (and not in the studies of Black and Martin) results in the removal of high molecular weight aggregates which could increase the measured hydrodynamic parameters.

The dependence of BM3 molecular weights, dissociation constants and dimer-dimer virial coefficients on ionic strength was also studied to determine the effects of electrostatic interactions on the BM3 dimer. For molecular weight measurements, SEC-

MALLS (Table 4.1) and sedimentation equilibrium (Figure 4.9A) studies both show reduction in resulting molecular weight as the ionic strength of the solution is increased. Although full monomers are not observed at the highest salt concentration studied here (1.0 M KCl), it can be observed that electrostatic interactions play a strong role in the dimerization of BM3.

Similarly, there is also an observed dependence of dissociation constants measured from sedimentation equilibrium (Figure 4.9B) and CG-MALLS studies (Figure 4.16/4.18) on ionic strength. This observed decrease in K_d with increasing ionic strength also supports our hypothesis that electrostatic interactions contribute significantly to stabilizing the BM3 dimer. Further, the values obtained from the sedimentation equilibrium experiments are slightly greater than the values obtained from CG-MALLS (Figure 4.26). This disparity could be as a result of the different experimental conditions in either case. The BM3 samples were gel-purified prior to sedimentation equilibrium analysis while the samples were only triple-filtered prior to CG-MALLS analysis. Also, sedimentation equilibrium studies were conducted at 4 ºC while the CG-MALLS studies were carried out at room temperature. Moreover, the fitting equation for CG-MALLS accounts for the presence of irreversible aggregates in the solution (Equation 2.10) which is not obtained with sedimentation equilibrium. However, in either case, the dimerization is weakened with increasing salt concentration and from CG-MALLS studies, full monomers could be obtained at 2.7 M KCl.
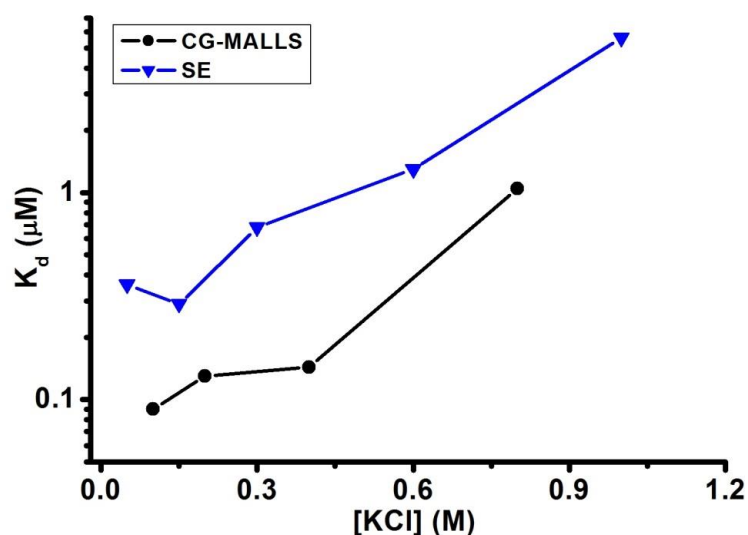
Figure 4.26: Comparison of dissociation constants obtained from sedimentation equilibrium (SE) and CG-MALLS. *The K_d values obtained from CG-MALLS studies (black circles) are lower than those obtained from sedimentation equilibrium (blue triangles).*

The decrease observed for molecular weights and dissociation constants as ionic strength increases is not observed with the dimer-dimer virial coefficient. This implies repulsive interactions between the dimers and also suggests that electrostatic forces might not contribute to the dimer-dimer interaction. In the absence of repulsive electrostatic interactions, the main contribution to repulsive forces between proteins arises from excluded volume effects. In this case, the value of B_{22} is equal to the volume about a dimer made inaccessible to other protein dimers. Calculating the excluded volume contribution to the virial coefficient requires knowledge of the shape of the protein. For a sphere, the excluded volume contribution is equal to four times the volume of the sphere divided by the molecular weight squared. Using the hydrodynamic size equal to 5.7 nm to approximate the sphere radius would give a value of the virial coefficient equal to 0.35 x 10^{-4} mLmol/g^2, which is significantly less than the value measured here. Spherical shapes provide a lower estimate to the virial coefficient as all other shapes (rods, discs) exclude more volume. In addition, a theoretical study of lysozyme has shown that assuming a smooth shape leads to underestimating the excluded volume contribution to the virial coefficient by up to 70 percent (*313*). Thus, it is not unreasonable that the measured values of B_{22} reported here are much greater than predicted for a smooth sphere. The results reported here are also consistent with a recent study of an intact monoclonal antibody, which has a similar size to the P450 BM3 enzyme (*314*).

In summary, the BM3 dimer has been characterized as an asymmetrical but near-spherical molecule whose dimerization is stabilized by electrostatic interactions. The dimerization constants obtained for the BM3 dimer is relatively strong with K_d values in the micromolar region. Similarly, the BMR dimer is an ellipsoidal molecule whose dimerization is also weakened with increasing ionic strength. In both cases, the presence of disulfide bonds does not contribute to the stabilization of the dimers.

4.5.3 Relating the dimerization of BM3 to its functions

Recent work has shown that the dimeric form of BM3 is the active form required for effective electron transfer from the FMN domain of one monomer to the P450 domain of the other monomer (*9*). Although the possibility of intra-monomer electron transfer from the FMN domain of one monomer to the P450 domain of the same monomer has not been ruled out, the inter-domain electron transfer from the FMN domain of one

monomer to the P450 domain of the other is believed to be responsible for the high fatty acid hydroxylase activity of BM3. In this study, the activity of BM3 is correlated with its functions using equations 2.13-2.16. Here, the K_d values obtained from sedimentation equilibrium studies are used to compute the percentage of monomer and dimer at concentrations used in the stopped-flow experiments. For these conditions, the rate constants and absorption amplitudes (accompanying heme reduction) form electron transfer between the FMN and the P450 domains (Section 3.3.2.1) within the the BM3 holo-enzyme at different ionic strengths are reported in Table 4.12. From the table, the percentages of dimers that contribute to the observed rates measured during the stopped-flow analysis have been estimated and it can be seen that this percentage decreases with increasing ionic strength. The rate of electron transfer between the FMN domain and the heme domain within the full length BM3 enzyme also decreases with increasing ionic strength. Further, at a high ionic strength (1.0 M KCl), the electron transfer rate constant is decreased by a magnitude of ~50% while the percentage of dimer was also observed to decrease by a similar magnitude. This correlation confirms that the dimeric form of BM3 is required for the fatty acid hydroxylase activity.

Table 4.12: Relationship of BM3 dimerization to rate constant for electron transfer between FMN and heme domains. The rate constant and amplitude data are for formation of the Fe(II)CO complex of P450 BM3, which reflects the rate constant for electron transfer between FMN and heme cofactors.

[KCl] (M)	Rate constant (s^{-1})	Amplitude	K_d (L/μM)	Dimer (%)	Monomer (%)
0.00	322.4	0.219	0.36	83	17
0.15	323.8	0.242	0.29	84	16
0.30	267.0	0.216	0.68	77	23
0.60	207.0	0.187	1.30	70	30
1.00	181.3	0.174	5.60	48	52

4.5.4 Cross-linking and crystallization studies

Cross-linking experiments were carried out with various cross-linking agents with different mechanisms of action. In all cases, no stable dimer was observed on a gel and, as a result, further analysis with mass spectrometry was not carried out to identify the cross-linking sites. However, SEC-MALLS and AUC analysis of the cross-linked samples yielded interesting results that might require further investigation. SEC-

MALLS experiments indicated that, when formaldehyde is used as a cross-linking agent, BM3 eluted as a mixture of monomers, dimers, and trimers, with the monomers and dimers being predominant. This suggests that formaldehyde could either cause the near-dimeric BM3 observed to dissociate into stable monomers which could re-assemble to form dimers and trimers; or that the formaldehyde caused the scission of the P450 domain leaving the reductase domains to re-associate into dimers, trimers and higher oligomers. When the peak corresponding to BM3 monomer molecular weight was isolated and re-run, greater than 90% BM3 monomers were observed, confirming that the monomers (or BMR dimers) formed from the BM3-formaldehyde mixtures are stable. Further, AUC analysis of the monomer peak resulted in 4 peaks and a re-run of the predominant peak yielded c(s) plots comparable to that of BMR, which suggests that the formaldehyde may have led to the scission of the P450 domain, resulting in the formation of a BMR dimer.

On the other hand, two peaks (corresponding to 2.1-mer (90%) and 1.3-mer (10%) of BM3) were observed from SEC-MALLS analysis of a BM3-glutaraldehyde mixture. The ability to obtain a full BM3 dimer (2.1-mer) with glutaraldehyde, which was not obtained for unmodified BM3 (1.7-mer; Table 4.11), suggests that glutaraldehyde stabilizes the BM3 dimer. Interestingly, no monomers were observed with glutaraldehyde, as were seen with formaldehyde, although both cross-linkers have a similar mechanism of action in which amine groups are cross-linked to form a methylene bridge. The difference, however, is that glutaraldehyde has two aldehyde groups while formaldehyde only has one group. There is a probability that addition of either cross-linking agent initially favours the observed monomer-dimer equilibrium towards monomers before a second cross-linking step where dimers are formed. However, the presence of two aldehyde groups on glutaraldehyde could cause the reaction to go more rapidly yielding stable dimers, while that of formaldehyde may be slow and could result in the formation of just more monomers that dimers. It is unfortunate that the dimers were not observed on reducing SDS-PAGE gels for further analysis using mass spectrometry. However, the observation of BM3 monomers is an interesting angle that needs to be explored further and might provide more insights into the dimerization mechanism of BM3.

Crystallization trials with C773A BMR yielded crystals that did not diffract beyond 9 Å. SEC-MALLS and AUC analysis on this mutant did not yield profiles significantly

different from the unmodified BMR, which has not been crystallized to date. However, recent studies have shown that a second mutation at C999A FAD resulted in the crystallization of the FAD domain (*115*). Thus, it is possible that creating this double mutant (C773A/C999A) in BMR could lead to easier crystallization of this domain and better quality diffraction data.

CHAPTER 5

Small Angle X-Ray Scattering and Modelling Studies on Flavocytochrome P450 BM3 and Its Domains

CHAPTER FIVE: SMALL ANGLE X-RAY SCATTERING AND MODELING STUDIES ON FLAVOCYTOCHROME P450 BM3 AND ITS DOMAINS.

5.0 INTRODUCTION

One of the major aims of this study is to structurally characterize the intact BM3 enzyme as well as its respective domains. While the crystal structures of full length BM3 (BM3) and the reductase domain (BMR) are yet to be solved, those of the heme domain (BMP), the FAD domain (FAD) and the FMN domain (FMN) are available. Using the recently resolved FAD structure, a homology model of BMR has been generated by docking the published FAD and FMN structures on rat cytochrome P450 reductase (CPR) structure (*115*). However, the solution structure of BM3 is not known due to only a limited number of hydrodynamic studies. This in turn has limited the understanding of structural determinants for BM3 fatty acid hydroxylase function, which has been reported to be the fastest among cytochrome P450s (*5*).

In the previous results chapters (Chapters 3 and 4), biochemical and biophysical characterization of BM3, BMP, BMR, FAD, and FMN domains were discussed. In these studies, BM3 and BMR were shown to be predominantly dimeric in solution. The dissociation constant for the BM3 dimer was estimated at 0.29 μM at an ionic strength of 0.15M KCl. The dimerization of BM3 was partly stabilized by electrostatic interactions, while the FAD domain was shown to be irreversibly dimerized in solution due to the formation of intermolecular disulfide bonds. BMP and FMN domains eluted as monomers on SEC-MALLS studies. Further, no higher oligomers were observed in any studies conducted with BM3, and the presence of fatty acids in the buffer did not affect the dimerization of BM3. Moreover, sedimentation velocity experiments indicated the BM3 hydrodynamic radii of ~ 5.7 nm and frictional ratio of ~1.39, suggesting that BM3 is relatively compact and globular in structure. Further, the BMR monomer and dimer peaks (from sedimentation velocity studies) corresponded to hydrodynamic radii of ~3.2 nm and ~ 5.0 nm, respectively, with frictional ratios of ~1.3 and ~ 1.5 respectively. While the BMR monomer results suggest a compact structure, the dimer results points towards a more elongated structure (ellipsoidal).

SAXS is an established method for determining oligomeric states, size, shape and quaternary structure of simple, flexible and complex macromolecules (See Appendix

G). From the scattering profile obtained as a function of wavevector, aggregation states can be determined in solution as well as low-resolution structures via *ab initio* and rigid body modelling (*315, 316*). The application of SAXS to the study of cytochromes P450 is limited in the literature, but SAXS was recently used to demonstrate that the oxidized form of human CPR is elongated while the reduced form is compact and spherical (*268*).

In this chapter, the application of SAXS to in-depth studies of full-length BM3 and its respective domains are discussed. In the first section, various SAXS data analysis programs are employed to determine the oligomeric states, sizes and shapes of BM3 and the domains. In the following sections, *ab initio* and rigid body modelling techniques are applied to develop various models describing the quaternary structures of the enzymes studied. Subsequently, scattering profiles and *ab initio* models obtained for the FAD domain from SAXS data are compared to the theoretical scattering profiles of the crystal structure while the generated SAXS hydrodynamic parameters are also compared to hydrodynamic data obtained in Chapter 4 using bead modelling techniques. The results obtained from SAXS and modelling studies are summarized in the last section.

5.1 SAXS PROFILE CONVERSIONS FOR BM3 AND DOMAINS

SAXS data were collected for BM3 in ligand-free solution (unmodified BM3), and in solutions containing either 1 mM NADP (BM3-NADP) or 100 µM NPG (BM3-NPG), and for solutions of unmodified BMR or FAD domains. 50 mM KPi, 0.1 M KCl, pH 7.0 buffer was used in all experiments. Prior to sample injections, a concentrated BM3 sample was buffer exchanged using a PD-10 column to remove high molecular weight aggregates while BMR and FAD samples were purified using a gel filtration column (Superdex 200 10/300). Data were collected at four different protein concentrations for experiments with unmodified BM3 and for BM3-NADP, while data collected for BM3-NPG experiment were at only one sample concentration as the other preparations at higher concentrations were damaged by radiation. Further, to ensure accurate data output and establish effects of ligands, NADP and NPG were added to buffers used for BM3-NADP and BM3-NPG sample data collection, respectively. The various scattering profiles obtained and the automated data processing at the beamline are discussed below.

5.1.1 SAXS Scattering Patterns and Beamline Automated Data Analysis

The sample concentrations used for each SAXS experiment are shown in Table 5.1. Data analysis at the beamline was carried out as previously described (*280*). Firstly, data collected were automatically reduced and normalised at the beamline using *AUTOMAR* (*280*) to generate the various scattering profiles shown in Figure 5.1. These SAXS profiles represent the scattering intensity as a function of the magnitude of the scattering wave-vector (*q*). In some cases, the shape of the molecule can be inferred from the SAXS scattering patterns, usually along with the pair distribution function of the molecule as will be discussed in section 5.1.4. Addition of NADP or NPG does not seem to change the BM3 scattering profiles (Figure 5.1D), and thus might not affect the overall shape of BM3 when these ligands are bound. It is important to note that conformational changes at atomic resolution are rarely detected in SAXS studies.
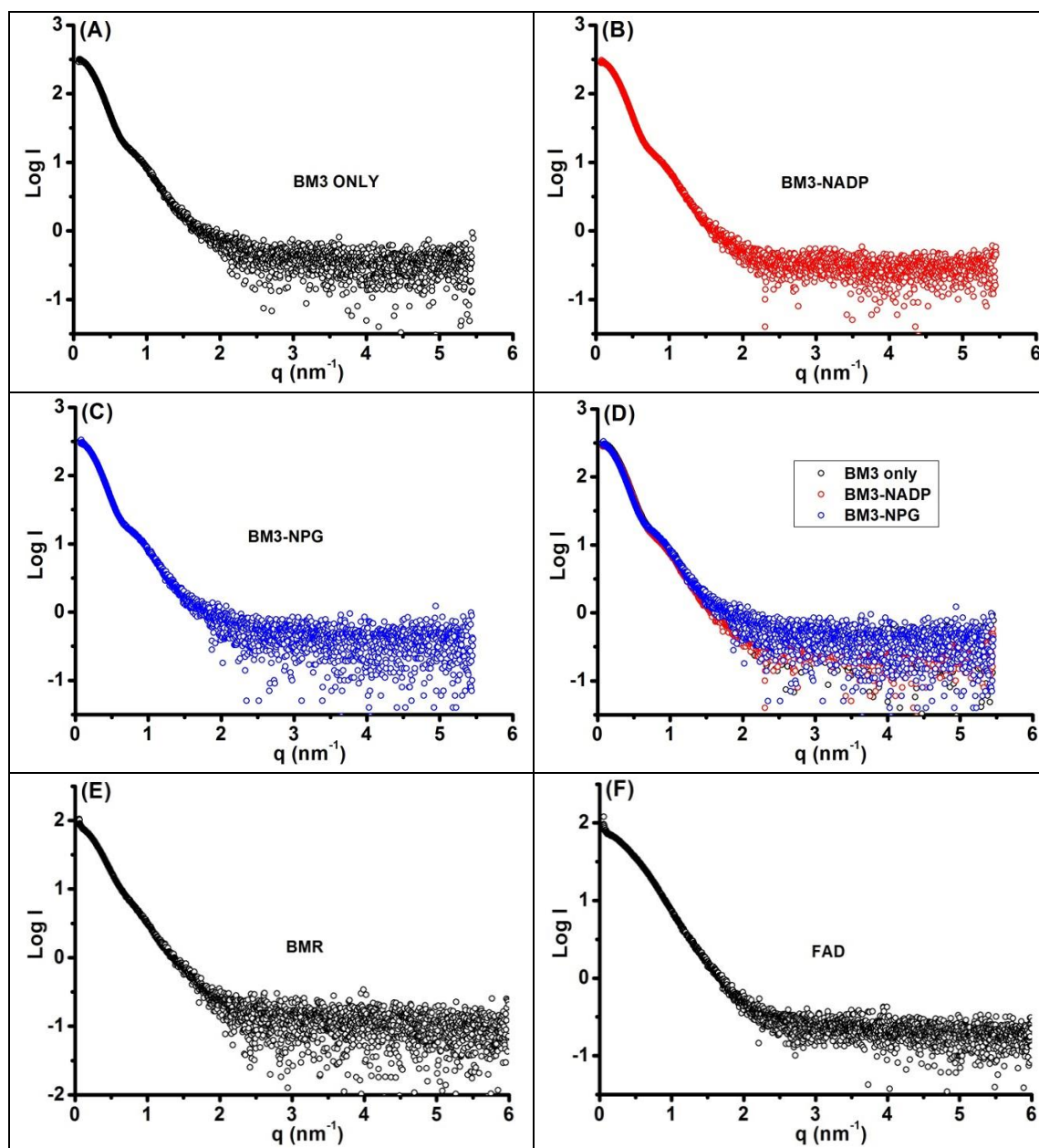
Figure 5.1: SAXS scattering profiles for BM3, BMR, and FAD. *The difference curves (buffer-subtracted) for 6 mg/mL BM3 (A), 8 mg/mL BM3-NADP (B) and 3 mg/mL BM3-NPG (C) have very similar profiles as shown in the overlay of the 3 profiles (D). The difference curves for 5.5 mg/mL BMR and 5 mg/mL FAD are also shown (E and F respectively). All measurements were carried out in solutions containing 50 mM KPi, 0.1 M KCl, pH 7.0.*

Secondly, subtraction of the background (buffer) was carried out using *AUTOSUB*, following which sample molecular weights (M_w) were automatically estimated (using BSA as reference). Further, preliminary analysis was also carried out on all buffer-subtracted data using *AUTOGNOM* and *AUTORG (281)* to determine the quality of the data obtained as well as to output the maximum molecule dimensions (D_{max}) and radius of gyration (R_g), respectively. The resulting M_w, D_{max}, and R_g, are shown in Table 5.1.

The data quality obtained in all cases are above 75% indicating that the data collected are of good quality, and that subsequent analysis (as will be discussed in the following sections) will be accurate.

Table 5.1: Automated data reduction at X33 beamline. **N/D represents not determined. The molecular weights were estimated automatically using BSA as a reference while the R_g and D_{max} were estimated using AUTOGNOM and AUTORG respectively. The data quality obtained in all the cases are above 75% indicating that that good quality data were obtained from the beamline. [+]The accuracy of the molecular weights is dependent on accurate concentration measurements and accurate determination of the calibration constant from solutions of BSA.*

Sample	Sample Concentration (mg/mL)	M_w (kDa)[+]	R_g (nm)	D_{max} (nm)	Data quality (%)
BM3	1.0	171	5.1 ± 0.1	16.8	77
BM3	2.0	157	5.1 ± 0.1	17.7	93
BM3	4.0	165	5.0 ± 0.1	17.4	81
BM3	6.0	167	4.9 ± 0.1	16.5	83
BM3-NADP	1.0	151	5.1 ± 0.1	17.1	88
BM3-NADP	3.0	157	5.1 ± 0.1	16.6	81
BM3-NADP	6.0	152	4.9 ± 0.1	15.7	92
BM3-NADP	8.0	154	4.8 ± 0.1	16.6	84
BM3-NPG	3.0	158	5.1 ± 0.1	17.8	88
BMR	5.5	106	4.5 ± 0.1	15.6	N/D*
FAD	5.0	94	2.9 ± 0.1	7.4	N/D

Molecular weights of 151-171 kDa were observed in all studies with BM3. These resulting molecular weights are higher than the expected BM3 monomer molecular weight of 119 kDa and lower than the expected dimer molecular weight of 238 kDa. A similar trend is observed with BMR where a measured molecular weight of 106 kDa was less than the expected dimer molecular weight of 128 kDa. Although only estimates, these molecular weight results are consistent with those obtained in previous biophysical studies (discussed in Chapter 4), indicating that while BM3 and BMR exist in solution as dimers predominantly; FAD exists in solution as a full dimer (expected dimer molecular weight is 90 kDa). This is also suggestive of monomer-dimer equilibrium in both BM3 and BMR.

Further, a radius of gyration of ~5 nm was observed in all BM3 samples, indicating that the overall size of BM3 is not affected by the addition of ligands. However, the radius

of gyration is observed to decrease, albeit slightly, with increasing BM3 concentrations. This suggests that the observed BM3 dimers are repelling each other, indicating that there is no possibility of higher oligomer formation. This is also in agreement with CG-MALLS studies where the B_{22} values indicated that no higher oligomers are observed with BM3. The R_g and D_{max} results obtained here for BM3 and the domains are discussed further in section 5.1.4.

Preliminary analysis revealed that accurate fits to the scattering profile data was obtained using *AUTOGNOM* for BM3, BM3-NPG, BM3-NADP while fits to data collected for BMR and FAD could be improved. Data for the FAD and BMR domains were subsequently re-analysed using *PRIMUS* and *GNOM* and the fits were improved for BMR by manually running *GNOM*, while no improvements were observed with the FAD domains. These solutions were then used for further data analysis to generate structural parameters and *ab initio*/rigid-body models of the enzymes, studied as discussed in the following sections.

5.1.2 Guinier Analysis

The Guinier plot is used usually to determine the polydispersity and aggregation states of proteins in solution. The logarithm of the scattering intensity (*lnI*) is plotted as a function of the square of the scattering vector (q^2). A linear dependence at small q-values indicates a monodisperse sample with no aggregation. The radius of gyration can also be obtained from the slope of this linear plot according to equations 5.1-5.2.

$$\ln[I(q)] = \ln[I(0) - \frac{q^2 R_g^2}{3}]$$
5.1

$$R_g = \sqrt{-3 * slope}$$
5.2

Equations 5.1 – 5.2: Guinier equation for calculating radius of gyration. $I(q)$ *represents scattering intensity as a function of q, I(0) represents scattering intensity at zero angle.*

The Guinier plots for 6 mg/mL BM3, 8 mg/mL BM3-NADP, 3 mg/mL BM3-NPG, 5.5 mg/mL BMR and 5 mg/mL FAD samples are shown in Figure 5.2 below. The values of the radius of gyration obtained from the slope are displayed in the respective plots. The Guinier plots are linear suggesting monodisperse samples with no aggregation. Further, the R_g values obtained for BM3 are similar to those obtained using the *AUTORG* software which also uses the Guinier approximation to determine R_g over an optimal

range of q. the R_g for BM3 increases slightly on addition of NADP and decreases slightly on addition of NPG. The R_g values obtained for BMR and FAD using the Guinier approximation also vary slightly from those obtained using the *AUTORG* software. The R_g values obtained using the *AUTORG,* Guinier and pair distribution functions are compared in section 5.1.4.
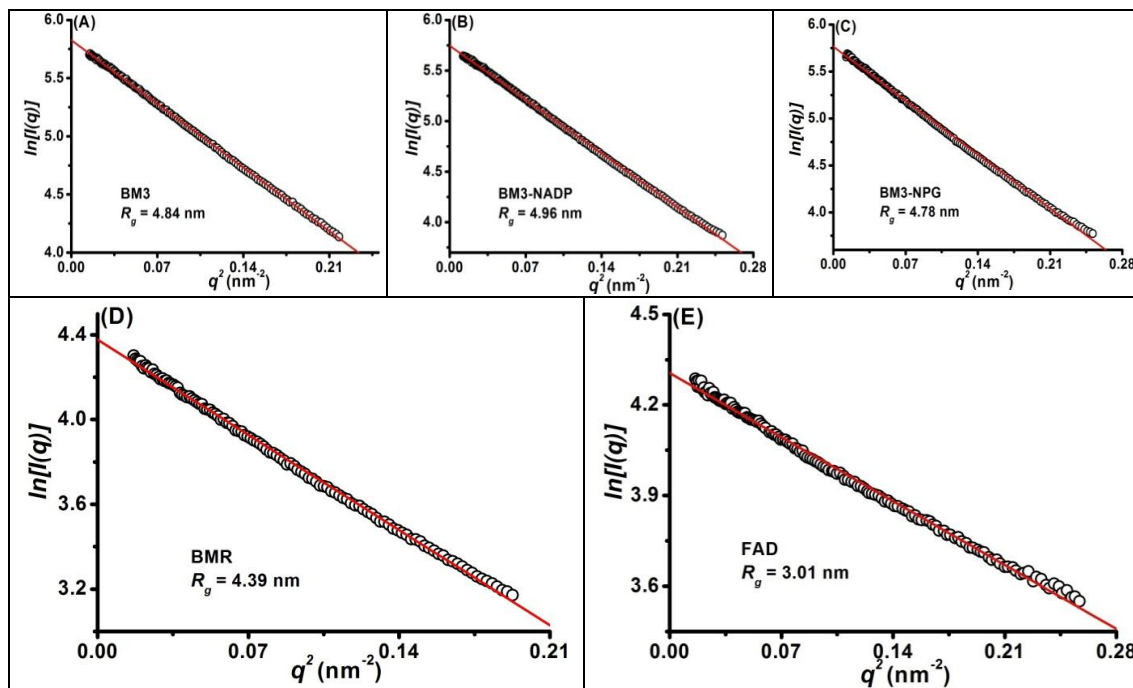
Figure 5.2: Guinier plots for BM3, BMR and FAD. *The plot shows scattering profiles at low q-region for 6 mg/mL BM3 (A), 8 mg/mL BM3-NADP (B), 3 mg/mL BM3-NPG (C), 5.5 mg/mL BMR (D) and 5 mg/mL FAD (E) samples. The red line represents the fit to the Guinier approximations from which the R_g values are derived, as displayed in the respective plots.*

5.1.3 Evaluating the shape of BM3 and domains: Kratky plots

A Kratky plot can be used to evaluate the folding of samples as well as the shape and flexibility of the macromolecule. The square of the scattering vector multiplied by the scattering intensity (q^2I) is plotted as a function of the scattering vector q. For folded globular proteins, a prominent peak is usually observed at low angles (low q) (*316*). The Kratky plots for free and modified BM3 as well as for BMR and FAD domains are shown in Figure 5.3 below.

The plots in Figure 5.4 all show prominent peaks at very low q-values (at ~ 0.35 nm^{-1} for free and modified BM3, at ~ 0.40 nm^{-1} for BMR and at ~ 0.65 nm^{-1} for the FAD domain) indicating that the enzymes are folded in solution. However, a second (albeit,

smaller) peak is observed at ~ 0.8 nm^{-1} for all BM3 and BMR samples studied (Figure5.3A-D) but absent in the Kratky plot for the FAD domain (Figure 5.3E). Very few SAXS profile of proteins show two prominent peaks at low angles as exhibited by BM3 and the BMR domain. This behaviour could be described by the presence of repeating units, such as in dimers or in a multi-domain enzyme with flexible linkers. Dimerization is most likely not the reason for the double peak as FAD has been shown to be dimeric in solution, but the second peak is not observed in the FAD domain Kratky plot.

Further, the two prominent peaks at low angles observed for studies on ligand-free and modified forms of BM3 could suggest that the enzymes are relatively compact or globular in solution. This might not be the case with BMR as the second peak is not very distinct, but continues into a tail suggesting a more elongated enzyme. On the other hand, the FAD domain appears to be quite compact in solution, also due to the prominent peak at low angles. The distance distribution function discussed in the next section is more sensitive to the shapes of macromolecules in solution and will be used to confirm the findings deduced from the Kratky plots. It is, however, noteworthy that the addition of NADP or NPG to the BM3 sample does not affect the configuration of BM3 as depicted by the Kratky plots.
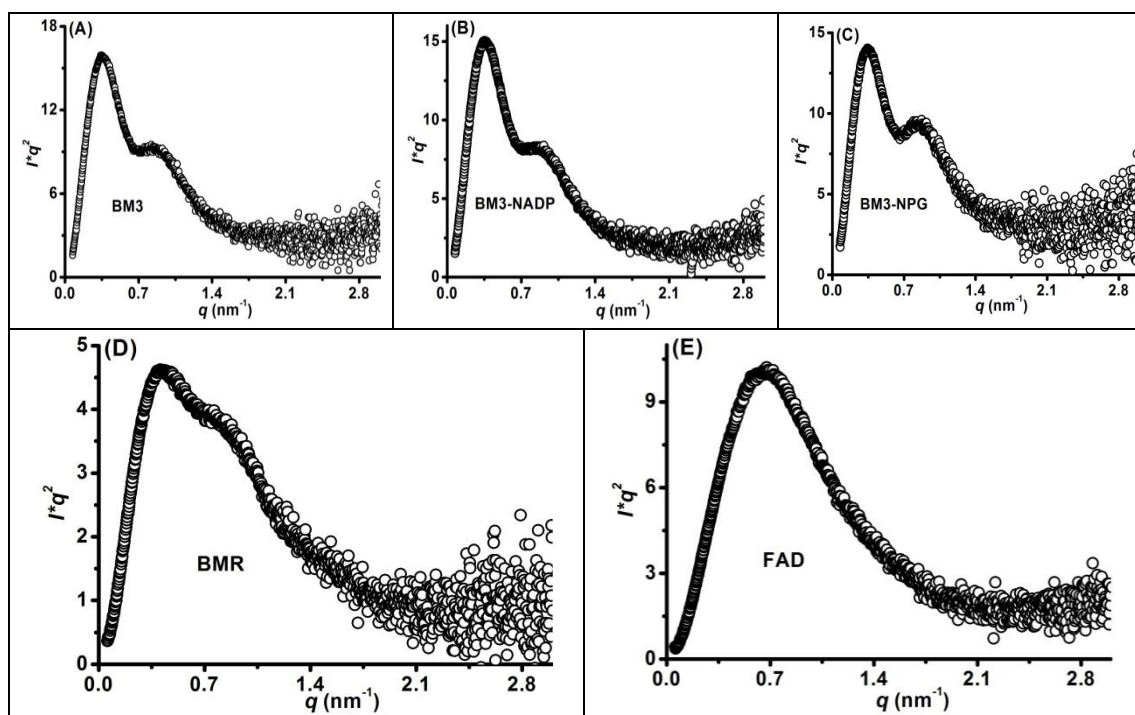
Figure 5.3: Kratky plots for BM3, BMR and the FAD samples. *The Kratky plots for 6 mg/mL BM3 (A), 8 mg/mL BM3-NADP (B), 3 mg/mL BM3-NPG (C), 5.5 mg/mL BMR (D) and 5 mg/mL FAD (E) samples are shown. The prominent peaks observed at low angles in all 5 plots indicate that the proteins are folded.*

5.1.4 Evaluating the shape of BM3 and its domains from the distance distribution function

The distance distribution function (also known as the *GNOM* plot or the *P(r)* function) is a graphical representation of the scattering profile (Figure 5.1) in real-space. The distance distribution function [*P(r)*] is a histogram of all distances between pairs of atoms in the protein. The radius of gyration (termed real-space R_g) can be obtained by integration of the *P(r)* function and the maximum dimension of the particle (D_{max}) can be determined from the point at which the *P(r)* function returns to zero. The shape of the macromolecule can be inferred from the shape of the *P(r)* function (*315, 316*). Further, conformational changes within a macromolecule are reflected by changes to the *P(r)* function since the distance distribution function is a sum of all the distances between atoms of the protein. Thus, considering the scattering profile along with the *P(r)* function can give an insight on the shape of the macromolecule studied.

Scattering intensities and distance distribution functions for typical geometric shapes are shown in Appendix G, but it is important to note that these are for defined geometric shapes. It is highly likely that macromolecules would either adopt a combination of

these shapes in solution or none of the described shapes. For guidance, globular particles display bell-shaped *P(r)* functions with a maximum at $D_{max}/2$, elongated and flattened particles show a distinct maximum at distances less than $D_{max}/2$, while multi-domain particles might contain more than one maximum.

The distance distribution functions for BM3, BM3-NADP, BM3-NPG, BMR, and the FAD domain are shown in Figure 5.4. Each of the *P(r)* functions appear to be bell-shaped and slightly elongated at longer *r*. For unmodified BM3, the skewed bell-shaped structure has a shoulder at 4.2 nm with a maximum at 6.3 nm, but the D_{max} is estimated at 15 nm. Thus, the maximum occurs at a distance slightly less than $D_{max}/2$ and the bell shape observed is not perfect, but asymmetric and skewed near the peak. This suggests that BM3 exists in solution as a compact and near-globular molecule. The bump observed at about 4.2 nm could be likened to the second peak observed in the Kratky plot (Figure 5.3A) also suggesting the presence of a flexible linker in a multi-domain enzyme. Further, the BM3 scattering intensity profile (Figure 5.1A) is skewed at shorter *q;* comparing the profile to the *P(r)* function suggests that BM3 is near-globular in solution.

The *P(r)* function for ligand-free BM3 (and the resulting D_{max}) does not differ from that of BM3 bound to NADP (Figure 5.4B). Further, the observed bump and maximum are also at the same value of *r*, suggesting that binding of NADP to the protein does not induce any conformational change to the overall structure of BM3. On the other hand, the *P(r)* function for BM3 bound to NPG is slightly more extended than that for BM3 alone. As seen in Table 5.2, the resulting D_{max} is marginally higher, indicating that binding of NPG to BM3 induces a conformational change, albeit minimal, to the BM3 conformation. The curve peaks at 6.97 nm while the maximum dimension observed is 16.05 nm; indicating that the maximum is also at a distance marginally less than $D_{max}/2$. This suggests that BM3 remains compact but somewhat more extended on binding to NPG. This minimal conformational change upon binding of NPG to BM3 was not observed in SEC-MALLS and sedimentation velocity studies (chapter 4). This is understandable given that the *P(r)* function is very sensitive to small structural changes when compared with analysis by SEC-MALLS and AUC.
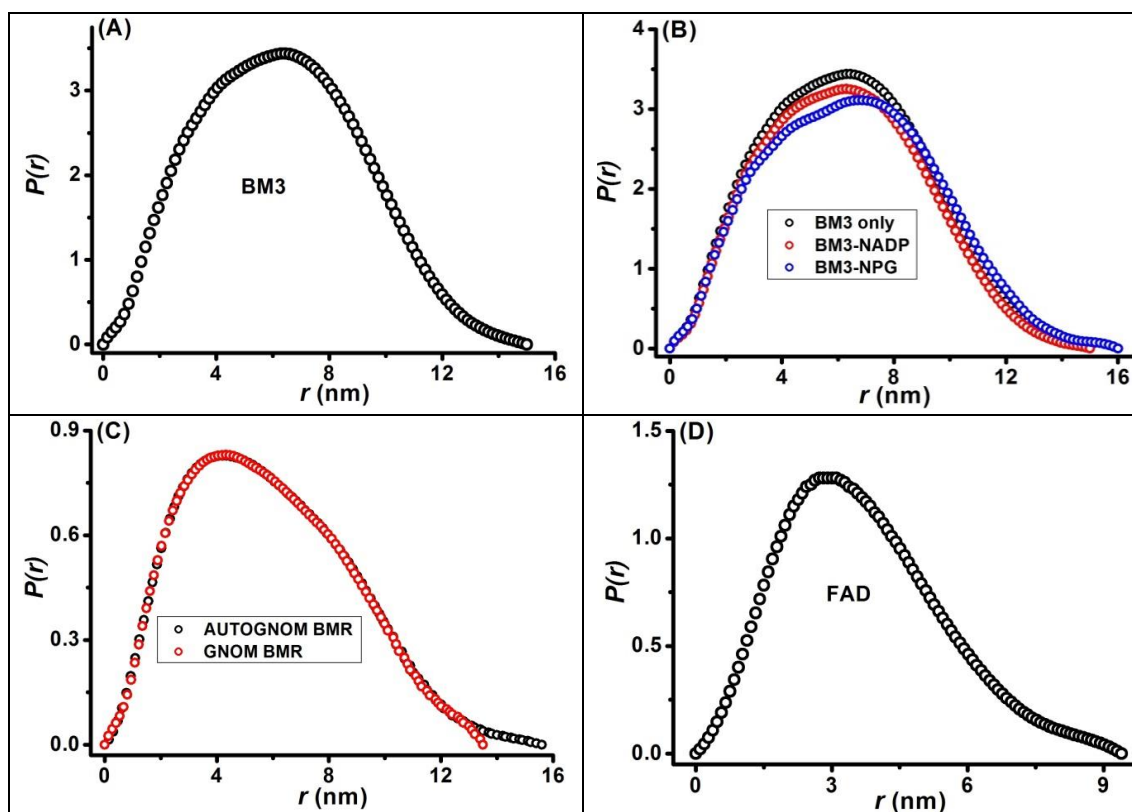
Figure 5.4: Distance distribution (GNOM) functions for BM3, BMR and the FAD domain. *(A) Plot showing pair-distance distribution function for 6 mg/mL BM3 using GNOM. (B) Plot comparing the GNOM plots for BM3 alone (black circles) with BM3 bound to NADP (red circles) and BM3 bound to NPG (blue circles). The pair distribution function for BMR is also shown (C) for initial calculations using AUTOGNOM (black circles); and re-calculated using GNOM (red circles) to give better solutions. (D) GNOM plot for 5 mg/mL FAD.*

As mentioned earlier, one of the automated reduction steps of SAXS data at the beamline is the estimation of maximum particle dimension using *AUTOGNOM* and the calculation of the accuracy of the solution obtained automatically. While the solutions (fits) obtained for free and modified BM3 using *AUTOGNOM* were excellent, those for the FAD domain and BMR were subject to improvement. Thus the data were manually re-analysed using *GNOM* and the fits were improved for BMR but no improvements were observed with the FAD domains. The *P(r)* functions obtained for BMR using both *AUTOGNOM* and *GNOM* are shown in Figure 5.4C. The *GNOM* plots in both cases are similar with a maximum at 4.1 nm and a bump at 7.5 nm. The major difference between the plots is the maximum dimension estimated at 15.6 nm for fit obtained using *AUTOGNOM*, and at 13.5 nm when using *GNOM*. As with BM3, the observed maxima in both cases are at distances less than $D_{max}/2$; however, the peaks are observed at much lower values of *r*. The observed *P(r)* plots suggest that BMR is not compact in solution

(as seen in BM3) but extended/elongated. This is further supported by the value of D_{max} obtained for BMR (~ 15.6 nm) in comparison with that of BM3 (15.0 nm) which is 54 kDa bigger (due to the P450 domain) than BMR. As also seen in BM3, the bump observed in both BMR GNOM [$P(r)$] and Kratky plots are suggestive of the presence of intra-domain subunits.

The FAD $P(r)$ plot has a perfect bell-shaped structure with an extended tail. The peak is at 2.9 nm while the D_{max} is estimated as 9.4 nm. Although the maximum in the plot occurs at a value of r less than $D_{max}/2$, the fully formed bell shape is suggestive of a compact and globular structure with an extended region. Further, the absence of a bump on both FAD domain Kratky and $P(r)$ plots supports our hypothesis that the bump is a function of an organised internal repeat (for a multi-domain enzyme).

The real-space radius of gyration obtained from *GNOM* analysis of data collected for BM3, BM3-NADP and BM3-NPG, BMR and the FAD samples are shown in Table 5.2. These values are slightly higher than those from using the Guinier approximation, but are more accurate since they take into consideration the whole scattering profile for R_g estimation. The corresponding values are similar, indicating that the data obtained are of good quality and that no aggregation is present in the samples. Further, there is little difference between the values of R_g obtained for ligand-free BM3 and NADP-bound BM3, but the R_g value for NPG-bound BM3 is higher than that for non-modified BM3. This also supports our hypothesis that while binding of NADP does not induce conformational change in BM3, binding of NPG induces a slight conformational change in the overall structure of BM3. In addition, the values of R_g and D_{max} obtained for BMR are similar to those obtained for BM3, also supporting our proposition that, while BM3 is compact and near-globular in solution, BMR has a more extended and elongated structure, like an ellipsoid.

Table 5.2: Maximum dimensions and radii of gyration for BM3, BMR and the FAD domain. *The real-space R_g values (obtained using GNOM/AUTOGNOM) are compared to the R_g values obtained from Guinier approximation.*

Enzyme	Maximum/Peak (nm)	D_{max} (nm)	Real-space R_g (nm)	Guinier R_g (nm)
BM3	6.30	15.02	4.90	4.84
BM3-NADP	6.30	15.05	4.85	4.96
BM3-NPG	6.97	16.05	5.10	4.78
AUTOGNOM BMR	4.10	15.64	4.60	4.39
GNOM BMR	4.10	13.47	4.54	4.36
FAD	2.92	9.40	2.87	3.01

In this section, SAXS has been used to determine the shapes of BM3 and its domains in solution. The data obtained were shown to be of good quality with no aggregation. BM3 is proposed to be compact and near globular in solution, while BMR is proposed to exist as a more extended structure, most likely resembling an ellipsoid. These conclusions are in agreement with deductions from frictional ratios measured using AUC sedimentation velocity (Section 4.2.1) Further, the FAD domain has been shown to be compact and globular containing an extended region. Visual inspection of the *P(r)* function is not enough in isolation to predict solution conformations of proteins. Thus *ab initio* modelling was employed to generate 3-D low-resolution structures of these enzymes, from which their molecular shapes can be deduced as discussed in the following section.

5.2 *AB INITIO* ENVELOPE DETERMINATION
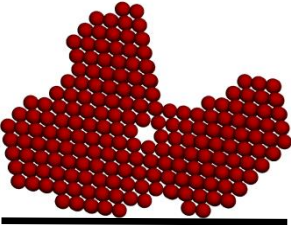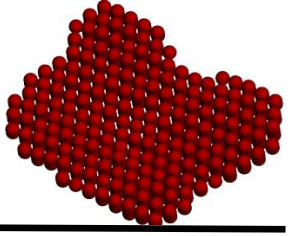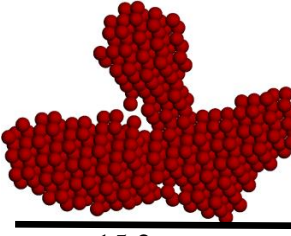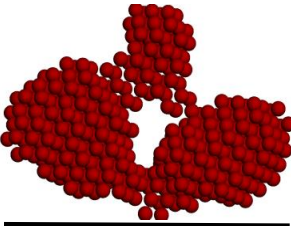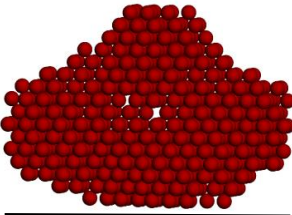
In *ab initio* modelling, low-resolution 3D models are constructed from the scattering data using automated bead modelling techniques (*316*). Using *DAMMIN* (*282*), a spherical volume of densely packed beads (with initial diameter equal to the value of D_{max} from *GNOM*) is gradually reduced to a final model that provides good fits to the raw scattering data. Subsequently, the experimental and the calculated scattering (of the resulting model) intensities are compared and the difference between the two is quantified by the value of χ^2. As a general principle, satisfactory χ^2 values are expected to be around 1 (*282*). Since the symmetry for BM3 and the domains are not known, fitting of the data using *DAMMIN* was carried out by generating structure with both P1 and P2 symmetries and the resulting best-fit models with their χ^2 values were compared. 20 models were obtained for each symmetry and aligned, averaged and filtered using

DAMAVER (*283*) with *SUPCOMB* (*317*). The results for free and modified BM3, BMR and FAD samples are presented in this section.

5.2.1 *Ab Initio* Models for Free and Modified BM3

Ab initio SAXS envelopes for BM3, BM3-NPG and BM3-NADP samples were generated using the *GNOM* output files in section 5.1.4. Twenty separate simulations were produced for each sample using both P1 and P2 symmetry. Subsequently, *DAMAVER* was used to average these simulations using three different options. The first option was averaging the models with no symmetry imposed (P1) and using *SUBCOMB 13*, which is significantly slower than the default *SUPCOMB 20* but gives more accurate results (Figure 5.5). Other options trialled for comparison purposes, were averaging the models with P1 symmetry using *SUPCOMB 20* and P2 symmetry using *SUPCOMB 20*. The full results for all three options assessed are shown in Appendix H. Figure 5.5 also shows the average χ^2 values obtained for each approach. The table also shows the average normalised spatial discrepancy (NSD). NSD describes the similarities between the individual structural fits from which the average structural model is obtained. NSD values are closer to zero for very similar structures and above 1 for sets where fit structures differ significantly from each other (*317*).

	BM3	BM3-NADP	BM3-NPG
DAMMIN **P1** **Models**	**(A)** 13.9 nm **Average NSD**: 0.91 ± 0.03 **Average** χ^2:1.13 ± 0.01	**(B)** 14.1 nm **Average NSD**: 0.82 ± 0.05 **Average** χ^2: 0.99 ± 0.01	**(C)** 15.2 nm **Average NSD**: 0.96 ± 0.03 **Average** χ^2: 099 ± 0.01
DAMMIN **P2** **Models**	**(D)** 14.5 nm **Average NSD**: 1.03 ± 0.03 **Average** χ^2: 1.13 ± 0.01	**(E)** 13.7 nm **Average NSD**: 0.94 ± 0.05 **Average** χ^2: 0.99 ± 0.01	**(F)** 15.6 nm **Average NSD**: 1.05 ± 0.05 **Average** χ^2: 1.00 ± 0.01
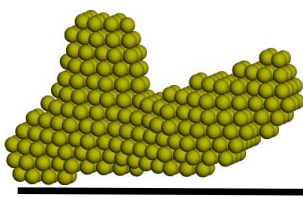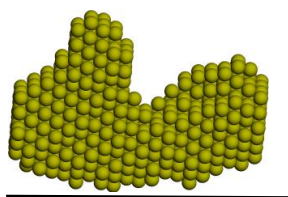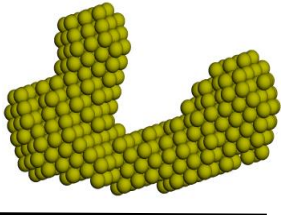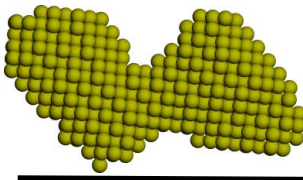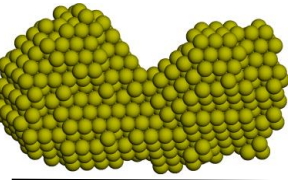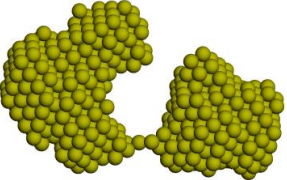
Figure 5.5: Ab initio envelopes of BM3, BM3-NADP and BM3-NPG. *Twenty different models were generated using DAMMIN with no symmetry (P1)/ SUBCOMB 13 imposed and averaged using DAMAVER for BM3 (A), BM3-NADP (B) and BM3-NPG (C). DAMAVER was also used to generate averaged models from 20 different DAMMIN models with P2 symmetry/ SUBCOMB 20 for BM3 (D), BM3-NADP (E) and BM3-NPG (F). The average chi-square (χ^2) values for these models generated from the DAMMIN runs are also shown alongside the normalised spatial discrepancy (NSD) values generated from DAMAVER, which indicates the degree of similarity between the 20 different models averaged for P1 and P2 symmetry.*

Results indicate that very similar structural models were generated for all three options trialled (Appendix H) but lowest NSD values were obtained for *DAMAVER* runs on structures with no symmetry when using *SUBCOMB 13* (Figure 5.5). Further, looking at results from P1 and P2 averaged models, a very compact and near globular structure is obtained for BM3 in the presence of NADP. This structure is marginally extended for ligand-free BM3, but is a lot more extended in the presence of NPG. This finding also agrees with *P(r)* and R_g results which indicate that, while binding of NADP might not

induce any significant conformational change, the binding of NPG does induce a quantifiable conformational change to the BM3 structure.

5.2.2 *Ab Initio* **Models for BMR**

DAMMIN was used to calculate twenty different BMR models (each for P1 and P2 symmetry) from *P(r)* functions generated using both *AUTOGNOM* and *GNOM* (Figure 5.4C). In addition, models were generated using just a low q-range (q-range equals 0-3 nm^{-1}) as well as using the full q-range (q-range equals 0-6 nm^{-1}) of the scattering curve for comparison purposes. The high q-range of the curve contains information relating to the internal structure of the particle and is usually omitted for *DAMMIN* runs since *DAMMIN* assumes that the particles are of uniform internal density. The generated models for either P1 or P2 symmetry were then superimposed and averaged using *DAMAVER* and *SUPCOMB 13* or *SUPCOMB 20*. (section 5.2.1; Appendix I). As observed for BM3, results show that very comparable models were obtained with all three options assessed. However, lower NSD values were obtained for structures with P1 symmetry using *SUPCOMB 13* option and the averaged models are shown in Figure 5.6.

	BMR *AUTOGNOM* (q = 2.2 nm^{-1})	BMR *GNOM* (q = 3 nm^{-1})	BMR *GNOM* (q =6 nm^{-1})
***DAMMIN* P1 Models**	**(A)** 14.7 nm **Average NSD:** 0.82 ± 0.03 **Average χ^2:** 0.98 ± 0.01	**(B)** 12.5 nm **Average NSD:** 0.79 ± 0.03 **Average χ^2:** 1.20 ± 0.01	**(C)** 13.1 nm **Average NSD:** 0.85 ± 0.03 **Average χ^2:** 1.119 ± 0.003
***DAMMIN* P2 Models**	**(D)** 14.5 nm **Average NSD:** 0.92 ± 0.05 **Average χ^2:** 0.99 ± 0.01	**(E)** 13.1 nm **Average NSD:** 0.88 ± 0.05 **Average χ^2:** 1.21 ± 0.01	**(F)** 13.3 nm **Average NSD:** 0.93± 0.04 **Average χ^2:** 1.13 ± 0.01
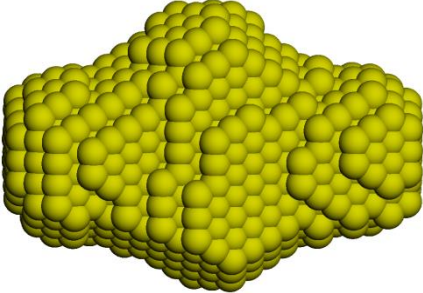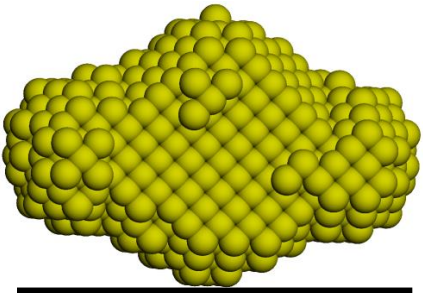
Figure 5.6: BMR Ab initio envelopes. *Twenty models were generated using DAMMIN with no symmetry (P1 models) and with P2 symmetry (P2 models) imposed, and averaged using DAMAVER. The input files for P1 and P2 DAMAVER runs include BMR AUTOGNOM scattering curve (A, D), half range of BMR GNOM scattering curve (B, E) and full range of BMR GNOM scattering curve (C, F) respectively. The average chi-square (χ^2) values for these models generated from the DAMMIN runs are also shown alongside the normalised spatial discrepancy (NSD) values obtained from DAMAVER, which indicates the degree of similarity between the 20 different models averaged.*

The BMR models shown in Figure 5.6 depict an elongated molecule with projected ends. This is in agreement with predictions from considering the *P(r)* function discussed in section 5.1.4. Further, best average χ^2 values were obtained for the P1 model generated using the *AUTOGNOM* scattering curve (Figure 5.6A). On the contrary, lowest NSD values were obtained for the P1 model generated using half of the q-range (Figure 5.6B) of the *GNOM* output file (whose solution was earlier demonstrated to be better than that generated using *AUTOGNOM*). However, these models are quite similar to each other and even to the model generated using the full q-range of the scattering

curve was used (Figure 5.6C). Moreover, the P1 and P2 models do not appear to differ significantly from each other. This suggests that the likely conformation of BMR in solution is elongated with P2 symmetry. Thus, rigid body modelling of the BMR domain was attempted using P2 symmetry as discussed in section 5.4.

5.2.3 *Ab Initio* Models for the FAD domain

Twenty *ab initio* envelopes for the FAD domain with either P1 or P2 symmetry were calculated with *DAMMIN* and averaged with *DAMAVER* using the three options previously described for BM3 and BMR. The results (shown in Appendix J) also indicate that similar models were obtained for all three options, with the highest NSD values recorded for the models with no symmetry using *SUPCOMB 13* option (Figure 5.7).

DAMMIN **P1 Models**	 9.0 nm **Average NSD:** 0.48 ± 0.02 **Average** χ^2: 1.55 ± 0.01
DAMMIN **P2 Models**	 9.4 nm **Average NSD:** 0.48 ± 0.04 **Average** χ^2: 1.55 ± 0.01

Figure 5.7: FAD ab initio envelopes. *Twenty models were generated using DAMMIN with no symmetry (P1 models) and with P2 symmetry (P2 models) imposed and averaged using DAMAVER. The average chi-square (χ^2) values for these models generated from the DAMMIN runs are also shown alongside the normalised spatial discrepancy (NSD) values obtained from DAMAVER.*

Although the χ^2 values obtained from the individual models are high, the standard deviation indicates that the models are quite similar. The low NSD values also show that the averaged models were marginally different. These low NSD values compared to the values obtained for BMR or BM3 might indicate that inter-domain flexibility contributes to the scattering profiles of BMR and BM3, while FAD is a single domain protein and only samples a single structure. In addition, the P1 and P2 averaged models are very similar, suggesting that the FAD dimer exists in solution as a very compact, near-globular structure with P2 symmetry. In the following section, the SAXS information obtained for the FAD domain is compared to the existing information on the FAD domain crystal structure recently published.

5.3 FAD: SAXS VERSUS X-RAY CRYSTALLOGRAPHY

MALLS analysis on the wild type FAD domain showed the domain to be dimeric in solution while analysis on the FAD domain double mutant (C773A/C999A) reveals a monomeric enzyme (*115*). This mutant also crystallizes as a monomer and is the only known FAD domain structure available in the literature. The FAD domain crystal structure contains two molecules in the asymmetric unit and the close proximity between Ala773 and Cys810 suggests the cysteine pair (C773/C810) occurs in the interface of the two molecules for the wild type FAD domain. A strong intramolecular disulfide linkage could be formed at this interface. This possibly explains the dimerization of the wild type enzyme (via a disulfide linkage) which is not observed in the double mutant.

In this section, the experimental SAXS data are compared to the theoretical scattering of the FAD domain crystal structure (of a single FAD domain molecule as well as for the two FAD domain molecules in the asymmetric unit) using *CRYSOL* (*284*). Further, the FAD domain crystal structure is compared to the *ab initio* models via superimposition.

5.3.1 Comparing Theoretical and Experimental Scattering Data for FAD

CRYSOL was used to generate a theoretical scattering curve for FAD using the PDB file – 4DQK- as input file. The curve was generated for both molecules in the asymmetrical unit as well as for a theoretical dimer with a structure given by the asymmetric unit in the crystal. These curves were compared to the SAXS experimental scattering curve for FAD and the discrepancy between the curves were output as the χ^2

values. As a general rule, χ^2 values of around 1 indicate good agreement between the experimental and theoretical scattering curves and the χ^2 value increases with increasing variation between the curves. The comparison plots are shown in Figure 5.8.
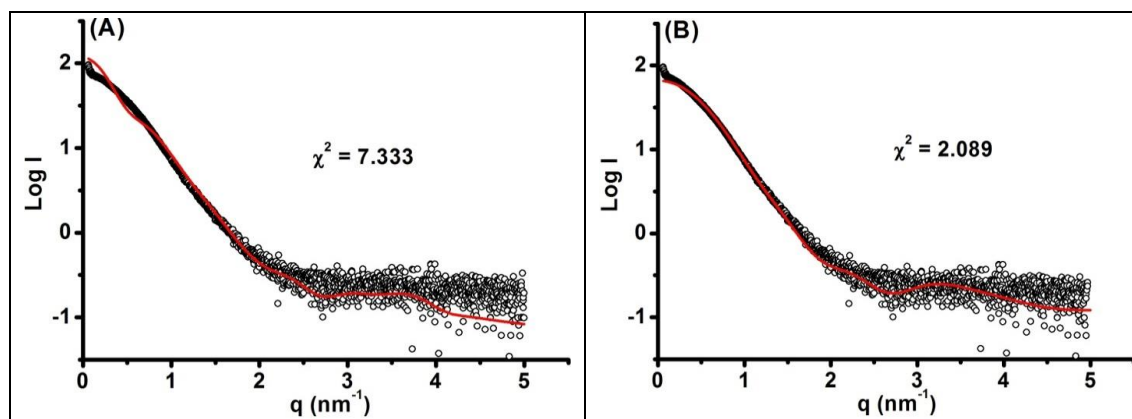
Figure 5.8: Theoretical and Experimental solution scattering curves for the FAD. Plots showing fits (red line) of the FAD domain theoretical scattering curve for two molecules in the asymmetric unit (A) and for a single molecule in the asymmetric unit (B) to the SAXS experimental curve (black circles). PDB file: 4DQK. The χ^2 values for the goodness of fit obtained are also shown on the plots.

The χ^2 value obtained for a single molecule in the asymmetric unit of 4DQK is closer to 1 and provides a good fit compared to the fit with two molecules in the asymmetric unit. From *ab initio* envelopes, it was proposed that the FAD domain exists in solution as a compact dimer with P2 symmetry. However, by comparing the crystal structure with the SAXS solution structure, this does not seem to be the case, as best fits are obtained when using the crystal structure of the monomer FAD domain although it is already established that a dimer is formed in solution. This discrepancy suggests that the dimer formed in solution does not have the same configuration as the dimer formed by the asymmetric unit. This is not surprising as the crystal contact interface formed in the asymmetric unit is much smaller than expected for a dimer interface. A further comparison was drawn between these forms by superimposition with the P1 and P2 models, as discussed in the following section.

5.3.2 Superimposition of the FAD domain *ab initio* envelope with the FAD domain crystal structure

The SAXS experimental data collected for FAD were used to generate several *ab initio* envelopes with no symmetry (P1) and with P2 symmetry as shown in Figure 5.7. These P1 and P2 models were very compact and similar to one another, suggesting that the

FAD domain is dimeric in solution and most likely has P2 symmetry. However, the existing FAD crystal structure is not a dimer (that is, there are no dimer interfaces observed between the monomers in the asymmetric unit), but two monomers in the asymmetric unit. Comparison of the theoretical scattering curve generated using this crystal structure with the SAXS experimental data has shown that the best fits were obtained with only a single molecule of the asymmetric unit. This is also in agreement with the superimposed structures (Fig 5.9), as only one molecule of the asymmetric unit could fit on the *ab initio* model, while the other molecule was "hanging" outside the envelope. This observed mismatch between the FAD crystal structure and the SAXS solution structure implies that the dimer in solution has a different structure from that given by the crystal structure. That is, the dimer formed by two similar monomers could not be the correct solution structure for FAD. In addition, the solution structure of the native form of FAD could be different from the mutant. It is also likely that the disulphide bond formation is linked to a change in the monomer structure upon dimer formation. Is it possible that the FAD domain dimer is very compact and globular while the monomer is extended, and as a result, both possess similar characteristics? This is discussed further in section 5.6.2.
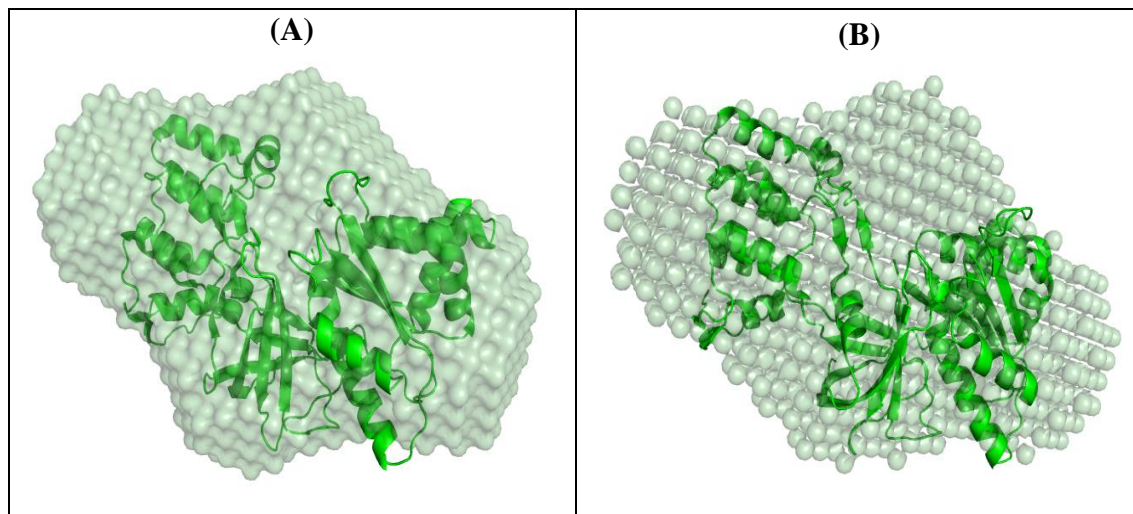
Figure 5.9: Superimposition of the FAD domain crystal structure with the ab initio model. A single molecule of the asymmetric unit from the FAD crystal structure (PDB – 4DQK) is superimposed with the ab initio models generated with P1 (A) and P2 symmetry (B) using pymol (318).

5.4 RIGID BODY REFINEMENT (BMR AND BM3)

SAXS data can be fit to determine a 3-dimensional low resolution structure of a multi-domain protein when the atomic resolution structures of the single domains are known. These rigid body models are constructed by merging the information contained in the theoretical scattering curves of the single domains (generated using CRYSOL) with the information on the experimental scattering curve for the multi-domain enzyme (*285, 319*). In this section, structural models of BMR and BM3 are generated using SASREF in which case the FMN, FAD, and heme domains are treated as rigid bodies with atomic resolution taken from the published crystal structures.

Rigid body refinement is particularly useful in understanding the orientations of the individual domains within the full-length enzyme. The modelling process becomes more challenging with increasing number of individual domains as well as oligomeric states, but the challenge can be eased with the use of restraints such as symmetry, distance restraints and other docking criteria already known from other sources. In previous studies, it has been observed that BMR and BM3 are dimers and, as a result, the rigid body models will contain 4 and 6 domains respectively. Thus, the BMR and BM3 rigid body models were constructed with and without symmetry, with half and full *q*-range of the experimental data, as well as using distance constraints to reduce the number of realistic models.

Further, although rigid body and *ab initio* models are both low-resolution models, they are constructed completely independent of each other. Thus, an agreement between both models usually indicates that the solutions are accurate. In this section, the generated BMR and BMR rigid body models are superimposed with the *ab initio* models constructed in section 5.2 for comparison purposes.

5.4.1 BMR rigid body modelling

Rigid body models of the BMR domain were constructed using crystal structures of the FMN domain from the PDB file- 1BVY (*114*) and a single molecule from the asymmetric unit of the FAD domain structure (PDB-4DQK; (*115*)).

5.4.1.1 BMR rigid body models with and without symmetry constraints

<u>BMR monomer</u>

5 rigid body models were constructed using one molecule each of the FAD and FMN domain, assuming that BMR is a monomer. No symmetry constraints were applied and the full range of experimental data was used. The resulting rigid body model and its fit to the experimental data are shown in Figure 5.10. The FAD and FMN domains of the rigid body model are far away from each other with an FMN-to-FAD distance of ~90 Å obtained. This distance can only be true if there was a much extended linker joining the component domains of BMR. Further, the theoretical scattering of the rigid body construct does not fit the experimental SAXS data and a very high χ^2 value of 4.44 was obtained (χ^2 values around 1 indicate good fits and good solutions). These results imply that BMR is definitely not monomeric in solution and agrees with earlier studies in this report which suggest that BMR is predominantly dimeric in solution. Thus, further models were constructed assuming that BMR is a dimer with no symmetry (P1) or with P2 symmetry.
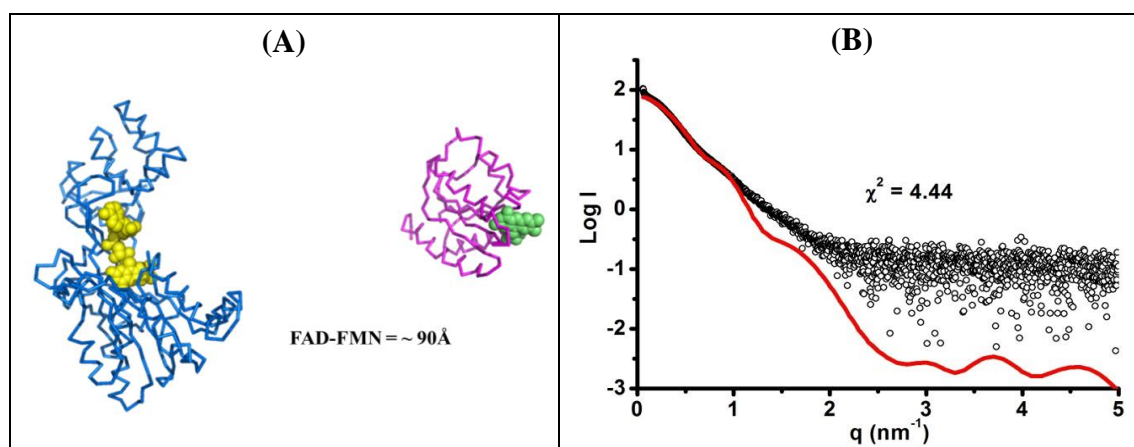
Figure 5.10: BMR monomer rigid body model and fit to experimental data. (A) BMR monomer rigid body model constructed using one molecule each of the FAD domain (blue) and the FMN domain (magenta) domains with no symmetry applied. A distance of ~90 Å was obtained between the FAD (yellow) and FMN (lime) cofactors for this model. (B) Fit of the theoretical scattering of the rigid body model (red line) to the experimental curve (black circles). The experimental χ^2 value for the fit obtained by SASREF is 4.44, indicating that the model obtained is likely not the correct orientation of the FAD and FMN domains within BMR.

BMR dimer with no symmetry

Using SASREF, 20 rigid body models were constructed using two molecules each of the FAD and FMN domains, and using both the full (q = 6 nm^{-1}; 10 models) and half q-range (q = 3 nm^{-1}; 10 models) of the experimental curve. Better fits were obtained when half the experimental curve data was used with chi square values of 1.30-1.38. The range of χ^2 values obtained with the full experimental curve data was between 1.66 and 1.89. Of the 20 BMR rigid body models generated with no symmetry (10 each from full and half experimental curve data), 3 common orientations (BMR-P1-A; BMR-P1-B; and BMR-P1-C as shown in Figure 5.11) were observed. However, superposition of the models observed for each of these 3 orientations did not generate good fits. Thus, representative models (with the lowest χ^2 values) for each of the 3 orientations, alongside the fits of the theoretical scattering of these curves to the experimental data, were selected and these are shown in Figure 5.11.
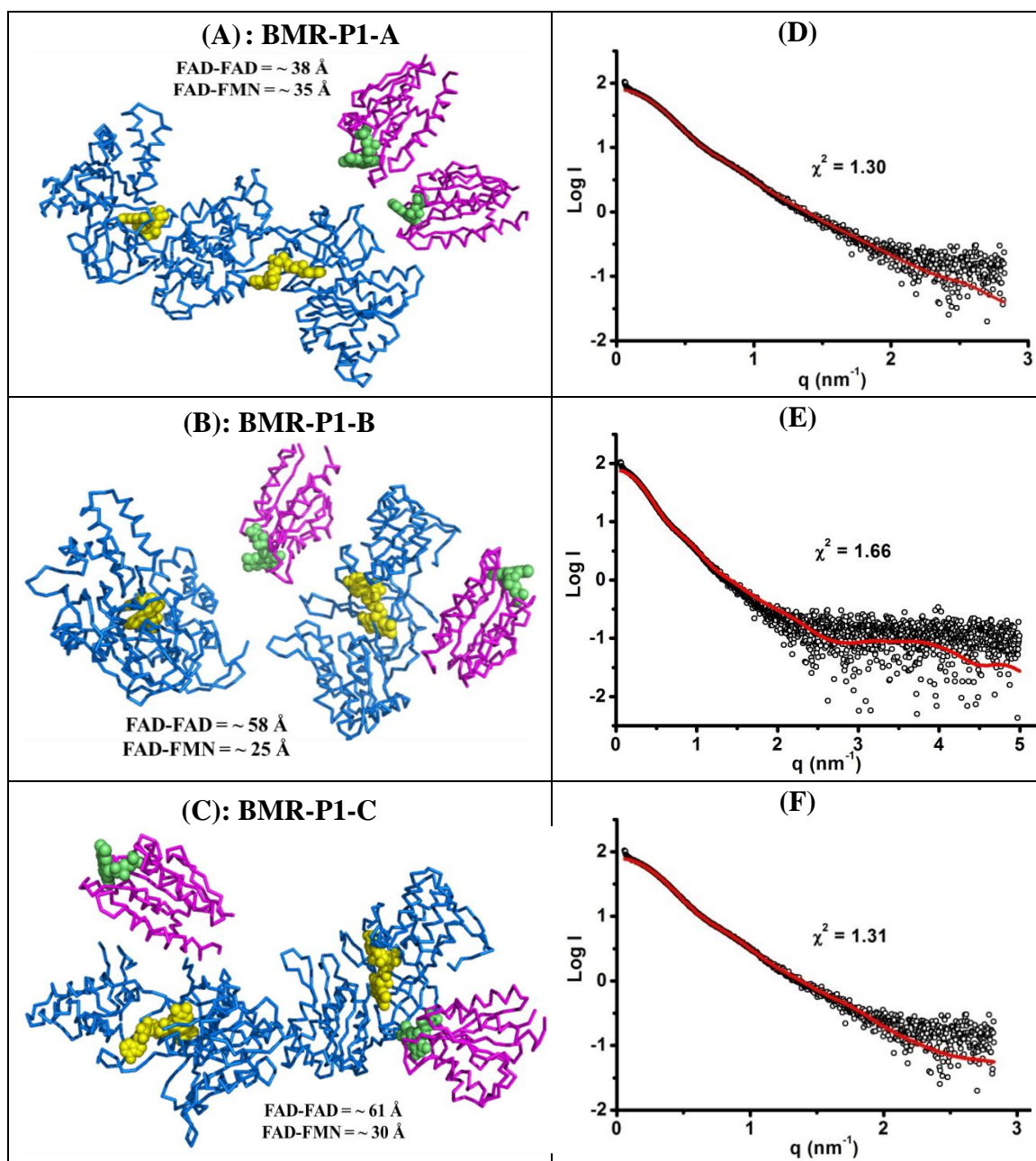
Figure 5.11: BMR dimer rigid body models with P1 symmetry and fits to experimental data. *Representatives of the three common orientations observed for 20 different BMR models generated using two molecules each of the FAD (blue) and FMN (magenta) domains are shown in A (7 out of 20), B (4 out of 20) and C (6 out of 20). The FAD-FAD distance and the lowest FMN-FAD distance within the BMR dimer are also shown within each figure. Fits of the theoretical scattering of the representative rigid body model (red line) to the experimental curve (black circles) are also shown in D-F. Structures A and C were generated using the full q-range while structure B was generated using half of the q-range of the scattering data.*

For all the 20 models generated, the BMR dimer is linked via the FAD domain which is in agreement with our deductions from previous studies. Further, it can be seen from the χ^2 values (Figure 5.11D-F) that relatively good fits of the theoretical scattering to the experimental data were obtained for each of these models, indicating that the generated orientations are plausible. However, these models are not exactly alike, even within each of the model groups (A-C), and hence cannot be superimposed for a perfect fit.

For the first model (BMR-P1-A, 7 out of 20 models), the two FMN domains are positioned close to each other and above one of the FAD domains with no contacts whatsoever with the second FAD domain. The separation of the FMN domain from the FAD domains suggests that this orientation may be unlikely. Further, most of these models were obtained using half range of the experimental curve. Cutting off the high q-range, which usually contains useful information regarding the internal organization of the molecule, might result in useful information being omitted, resulting in this orientation where contacts within the FMN and FAD domains are stretched.

For the second model (BMR-P1-B, 4 out of 20 models), the FMN domains are closer to the FAD domain, flanking one FAD cofactor, with the second FAD cofactor almost separated, but closer to one FMN domain than seen in model A. This orientation might require the movement of the second FAD cofactor closer to one FMN domain for efficient electron transfer, hence this orientation is likely.

The third model (BMR-P1-C, 6 out of 20) seems to have the most likely orientation of all three models for efficient electron transfer. In this model, one FMN domain is positioned close to one FAD domain with maximum contacts between the FAD domains. However, the positioning of the FMN domain within the BMR varies. While some models show the FMN domains positioned adjacent to each other as shown in Figure 5.11C, other models show the FMN domains positioned parallel to each other (data not shown). In all six cases, the FMN domain is usually positioned close to the FAD cofactor with a maximum FMN-to-FAD cofactor distance of 40 Å, as opposed to model groups A and B where FMN-to-FAD cofactor distances of above 70 Å were obtained.

All three orientations generated suggest that BMR will exist in solution in an open conformation. The third model seems to be the most likely conformation of BMR in solution, but this will be confirmed using bead modelling (section 5.5). Further, the

variations observed for all models generated with no symmetry implies that the use of restraints could yield better models that could be superimposed on each other to provide better fits. Thus, the BMR rigid body modelling was repeated with P2 symmetry.

BMR dimer with P2 symmetry

BMR rigid body models with P2 symmetry were generated as described in the previous section, also using the half and full range (15 each) of the experimental curve. The range of χ^2 values (1.42 – 2.00) obtained for models using the low q-range (q = 3 nm^{-1}) of the experimental curve were, on average, higher than χ^2 values (1.64-1.79) obtained using the full q-range data (q = 3 nm^{-1}), implying that the latter models had more accurate fits. Moreover, the 15 models obtained using the low q-range data were all different; the model with the lowest χ^2 value is shown in Figure 5.12 alongside the theoretical fit of the model to the experimental data. As observed with the P1 models, the BMR dimer was shown to be linked at the FAD domain, although the FAD domains of the BMR dimer were closer to each other in the P2 models than in the P1 model.
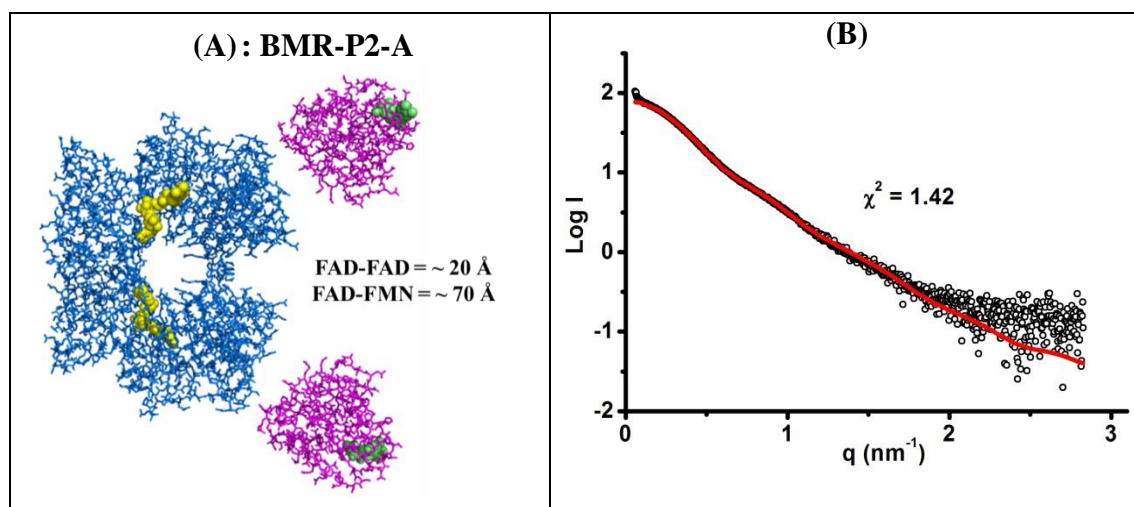
Figure 5.12: BMR dimer rigid body model with P2 symmetry and fit to experimental data (1). *(A) A representative model of the BMR dimer with P2 symmetry generated using two molecules each of FAD (blue) and FMN (magenta) domains and the low q-range of SAXS experimental data. The FAD-FAD cofactor distance and the lowest FMN-FAD cofactor distance within the BMR dimer are also shown within the figure. (B) Fit of the theoretical scattering of the representative rigid body model (red line) to the experimental curve (black circles). The experimental χ^2 value for the fit obtained by SASREF is 1.42, indicating an accurate fit to the data. For comparison purposes in subsequent analysis, this model has been named BMR-P2-A*.

On the other hand, BMR rigid body models obtained with P2 symmetry were similar to each other when using the full experimental curve data. Two common superimposable orientations (10 out of 15 models) were observed (Figure 5.13), while the other models were not very different, although could not be superimposed on each other. The most common orientation (BMR-P2-B, 7 out of 15 models) is shown in Figure 5.13A superimposed with varying colours with a representative model (5.13B- the model with the lowest chi-value of the 7 superimposed models). The position of the FAD and FMN cofactors within the BMR dimer are also shown. The FAD molecules are positioned close to each other (~ 24 Å) within the BMR dimer but the FMN molecules are a little far from the FAD molecules (~39 Å in each case), implying that domain movement will be required for electron transfer between the FMN and the FAD domains if this orientation exists. The other common orientation (BMR-P2-C, 3 out of 15 models) is shown in Figure 5.13D superimposed with varying colours. As seen in the representative model for this group with the lowest χ^2 value (Figure 5.13E), the FAD cofactors are closer to the FMN cofactors (~ 25 Å) which implies that less domain motion will be required between the FAD and FMN domains for efficient electron transfer. Further, the theoretical fits of the scattering curves of the models to the experimental data (Figures 5.12 C and F) are good, implying that the solutions obtained here represent likely orientations of BMR in solution.
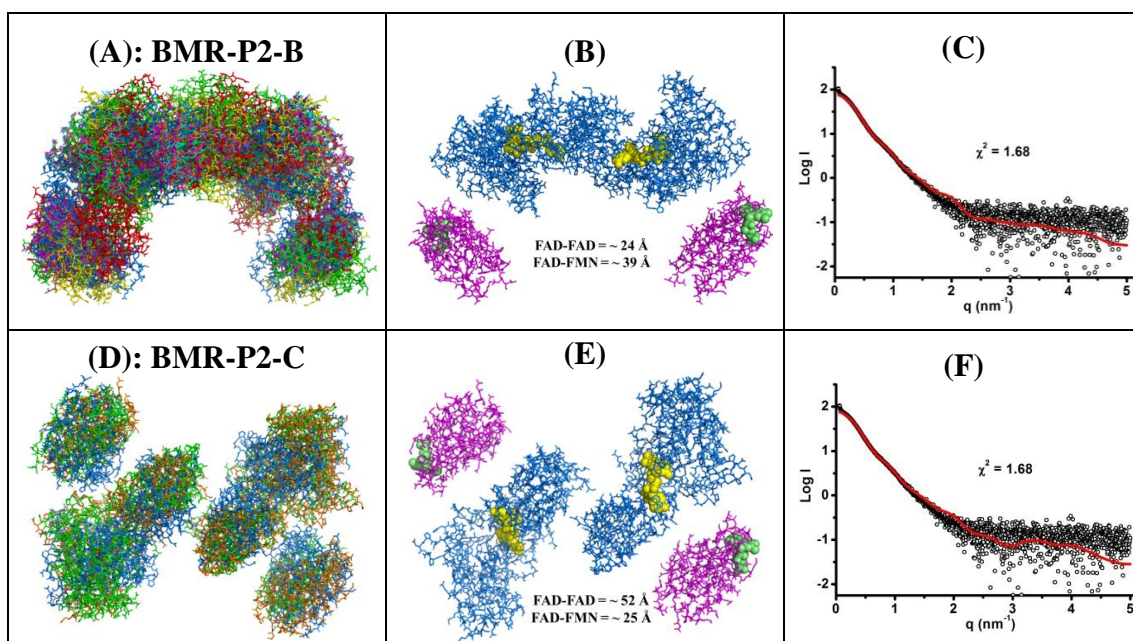
Figure 5.13: BMR dimer rigid body models with P2 symmetry and fits to experimental data (2). BMR rigid body models with P2 symmetry generated with SASREF, using two molecules each of the FAD and FMN domains and the full q-range of the experimental curve, are shown superimposed with varying colours. The two common orientations are shown in A and D alongside their representatives (in B and E) as well as the fits of the theoretical scattering of the representative rigid body model (red line) to the experimental curve (black circles) in C and F respectively. The FAD-FAD cofactor distance and the lowest FMN-FAD cofactor distance within the BMR dimer are also shown within each figure.

Applying symmetry constraints generated BMR rigid body models that were similar and superimposable with two common orientations. None of these orientations are similar to those models generated without symmetry, suggesting that BMR may not exist in solution with symmetry. However, this may not be conclusive as the models generated using P1 symmetry were different from each other. Thus, more P1 and P2 symmetry modelling was attempted using additional constraints, as discussed in the next section.

5.4.1.2 BMR rigid body models with distance constraints

In a recent study using pulsed electron-electron double resonance spectroscopy (PELDOR), a distance of 29 Å was estimated between FAD cofactors in a reduced BMR dimer with the FAD molecules mainly in the semiquinone (EPR-active) state (Dr. Adrian Dunford and Dr. Steve Rigby, University of Manchester; verbal communication). Although some of the models generated with P1 and P2 symmetry, as discussed above, had FAD-to-FAD cofactor distances of around 29 Å and below,

further rigid body modelling studies for BMR dimer was carried out using a fixed FAD-to-FAD cofactor distance of 29 Å. These modelling studies were carried out using only the full q-range of the experimental data and for P1 and P2 symmetry (15 models each) only.

Chi square values obtained for P1 symmetry with distance constraints varied from 1.64 to 1.70. This range of values indicate that applying distance restraints produced better solution(s) when compared to chi square values of 1.66 to 1.89 obtained under the same conditions, but without distance restraints. However, the resulting models were also very different from each other (with no two models looking exactly alike); imposing the distance restraints positioned the two FAD domains closer to each other when compared to P1 models without distance constraints. Similarly, there was little or no difference between P2 symmetry models with or without the distance restraints, and the χ^2 values were comparable. Hence, the most common orientation obtained here was similar to that obtained for P2 symmetry models with no distance restraints (BMR-P2-B).
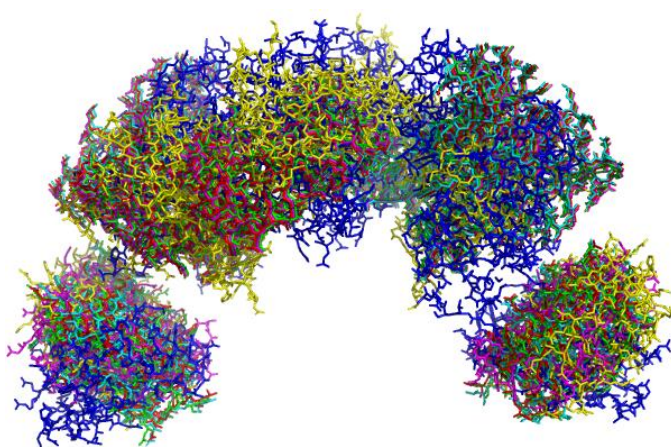
Figure 5.14: BMR dimer rigid body models with P2 symmetry and distance restraints. BMR rigid body models with P2 symmetry and FAD-to-FAD cofactor distance of 29 Å and generated with SASREF, using two molecules each of FAD and FMN domains and the full q-range of the experimental curve, are shown superimposed with varying colours. The FMN domains are the smaller spherical entities at the bottom of the image.

These results indicate that imposing distance restraints does not yield fits to BMR scattering curves with lower χ^2 values. However, from the models produced, 3 different orientations each for P1 and P2 symmetry are the likely orientations of the BMR dimer in solution. These 6 BMR rigid body models were compared to *ab initio* BMR models with P1 and P2 symmetry to further narrow down the result to one or two likely BMR dimer orientation(s) in solution. Further elimination of these models was carried out using bead modelling studies as discussed in section 5.5.

5.4.1.3 BMR rigid body versus ab initio models

Ab initio and rigid body models are constructed independently of each other. When the crystal structures of the sub-domains of a multi-domain enzyme are available, rigid body modelling is preferred over *ab initio* modelling. However, an agreement between both *ab initio* and rigid body models provides more confidence that the correct structure has been found. In this study, a common orientation for BMR between all the models generated was not obtained as expected, but 3 common orientations each (6 in total) were obtained for P1 (BMR-P1-A, B and C) and P2 (BMR-P2-A, B and C) symmetry, respectively. These 6 P1 and P2 BMR rigid body models are superimposed with the BMR *ab initio AUTOGNOM* P1 and P2 models shown in Figure 5.6 A and D respectively (Figure 5.15).
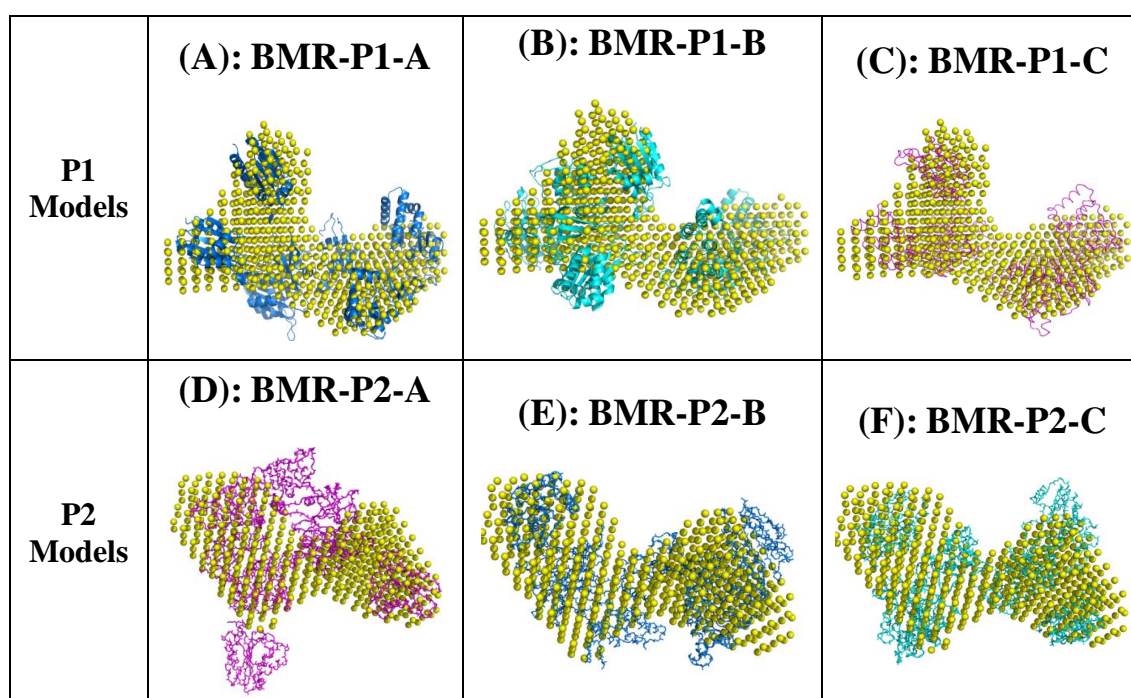
Figure 5.15: BMR rigid body models superimposed with ab initio models. The P1 models are shown as superimposed in A, B and C, corresponding to the rigid body models BMR-P1-A, B and C respectively. The P2 models are shown as superimposed in D, E and F, corresponding to BMR-P2-A, B and C respectively.

The rigid body models fit relatively well with the *ab initio* models for all six orientations, implying that the BMR rigid body models are relatively accurate, but not

perfect. However, best fits for the P1 and P2 models were obtained for BMR-P1-C (Figure 5.15C) and BMR-P2-B/C (Figure 5.15E/F), respectively. Hence, these 3 models (Figure 5.16) represent the likely orientations of BMR in solution. Further analysis using bead modelling (section 5.4.2) to match the hydrodynamic information from these models to hydrodynamic/spectroscopic information derived using other biophysical techniques will provide more confidence in this finding.

(A)	(B)	(C)
P1 model: BMR-P1-C	**P2 model: BMR-P2-B**	**P2 model: BMR-P2-C**
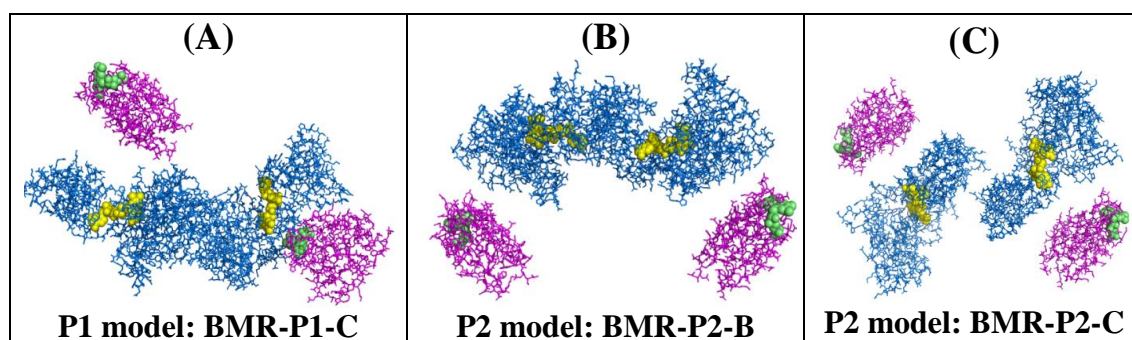
Figure 5.16: Possible orientations of BMR in solution. *The likely orientation of BMR with no symmetry based on a fit with an ab initio model is shown in A; while the likely orientations of BMR with P2 symmetry are shown in B and C. The FAD domains are shown in blue while the FMN domains are shown in magenta. The FAD and FMN cofactors are shown in spheres and coloured yellow and lime respectively.*

5.4.2 BM3 rigid body modelling

Full length BM3 enzyme consists of one molecule each of FMN, FAD and BMP domains. In the previous chapter, biophysical studies showed that BM3 exists in solution as a dimer, which is also supported by preliminary SAXS data analysis discussed earlier on in this chapter. BM3 rigid body modelling was attempted using the FMN domain from the PDB file- 1BVY (*114*), a single molecule from the asymmetric unit of the FAD domain (PDB-4DQK; (*115*)), and the P450 (heme) domain from the PDB file 2IJ2 (*137*). Initial modelling was carried out assuming BM3 was a monomer in solution using the experimental SAXS data and one unit each of the FMN, FAD and BMP domains. As observed with attempts to model BMR monomer, the domains were far from each other with high χ^2 values (3.61), implying that BM3 is not a monomer in solution (Figure 5.17).
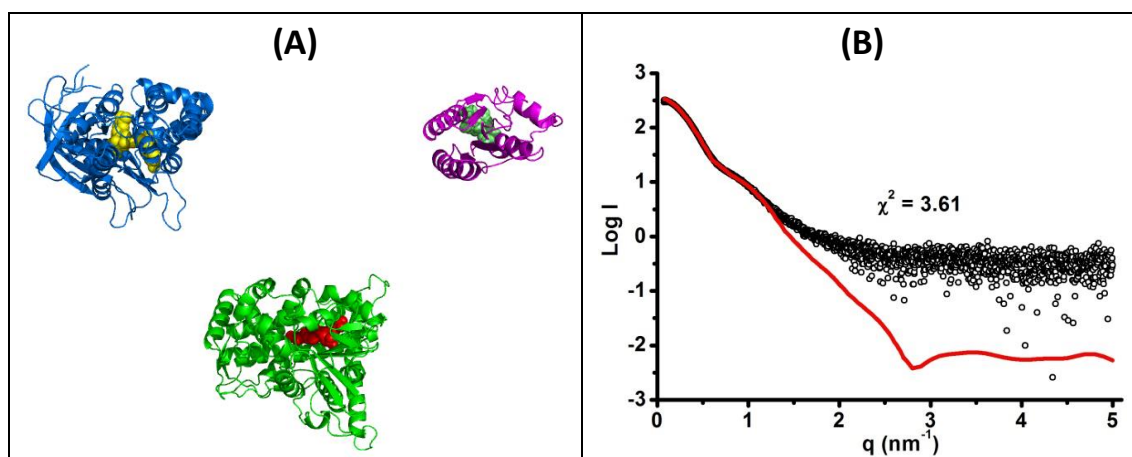
Figure 5.17: BM3 monomer rigid body model and fit to experimental data. *(A) BM3 monomer rigid body model constructed using one molecule each of BMP (green), FAD (blue) and FMN (magenta) domains with no symmetry applied. The heme (red), FAD (yellow) and FMN (lime) molecules for this model are also shown. (B) Fit of the theoretical scattering of the rigid body model (red line) to the experimental curve (black circles). The experimental χ^2 value for the fit obtained by SASREF is 3.61, indicating that the model obtained is likely not the correct orientation of the BMP, FAD and FMN domains within intact BM3.*

Modelling the BM3 dimer posed a great challenge, as 2 molecules each of FMN domain, FAD domain and BMP domain (6 domains in total) were required. Several models were initially produced without any symmetry imposed, but all the solutions were different with contacts shown between the FMN, FAD and BMP domains within the BM3 dimer. Imposing symmetry and distance constraints only improved the solutions slightly, but no common solutions or models were observed. The use of a BMR model (in place of FMN and FAD) for rigid body modelling of the BM3 dimer might be less challenging as the number of molecules required will be reduced from 6 to 4, but this was not attempted in this study as a reliable rigid body model for BMR was not obtained.

5.5 BEAD MODELLING

Hydrodynamic bead modelling is used to compare the crystal lattice structure of a molecule to the conformation of the molecule in solution. We used the algorithm *AtoB* which allows the construction of shell or bead models from atomic coordinates of the crystal structure (*320-322*). Structural parameters that can be experimentally determined are computationally synthesized from these bead/shell models. The parameters of interest to this study include radius of gyration (R_g) and maximum dimension of particle

(D_{max}) obtained from SAXS, hydrodynamic radius (r_H), sedimentation coefficient ($s_{20,w}$) and frictional ratio (f/f_o) obtained from analytical ultracentrifugation.

In this section, HYDROPRO (*286*) was used to generate shell models from the *ab initio* models while SOMO (*323*) was used to generate bead models from the rigid body models and the required structural parameters were generated from these shell and bead models. These parameters were compared to those experimentally determined in this work to check for the accuracy of the *ab initio* and rigid body models.

5.5.1 Hydrodynamic bead modelling for *ab initio* envelopes

To construct shell models from the *ab initio* envelopes, HYDROPRO requires a manual input of the enzyme molecular weight and partial specific volumes. As established in this study, BM3 and BMR are dimers in solution. Thus the full dimer molecular weights of 238 kDa and 128 kDa were used for constructing shell models for BM3 and BMR, respectively. The partial specific volumes were estimated from the amino acid sequence using SEDNTERP (*310*) and the values used were 0.736 and 0.732 mL/g for BM3 and BMR respectively. The hydrodynamic parameters for BM3 and BMR *ab initio* models are given in Tables 5.3 – 5.4. The R_g values used for comparison purposes are the real-space values obtained from the probability distribution plots.

For BM3, the R_g and r_H values calculated for both P1 and P2 *ab initio* models were lower, while the D_{max} and $s_{20,w}$ values were higher than the experimental values (Table 5.3). The difference in these values suggests that the *ab initio* models might not accurately represent the conformation of BM3 in solution. On the other hand, there was little difference between the experimental and theoretical hydrodynamic calculations for the *ab initio* models of BMR(Table 5.4). This is in agreement with earlier observations that the BMR dimer exists in solution with no symmetry and suggests that the derived models accurately represent the conformation of BMR in solution. Similarly, the R_g values for both P1 and P2 FAD domain models are very close to those determined experimentally (Table 5.5), implying accurate fits to the AUC and SAXS data.

Table 5.3: Comparison of hydrodynamic parameters of BM3 derived from ab initio envelopes to experimentally determined parameters. The P1 and P2 envelopes used for the shell models are as shown in Figure 5.5 A and D respectively. The experimental R_g and D_{max} values were obtained from SAXS (Table 5.2) while the r_H and $s_{20,w}$ values were obtained from AUC (Chapter 4).

MODELS	R_g (nm)	r_H (nm)	D_{max} (nm)	$s_{20,w}$ (x 10^{-13} s)
Experimental	4.9	5.7	15.0	9.7
BM3 P1	4.6	5.2	15.4	10.6
BM3 P2	4.6	5.1	15.7	10.9

Table 5.4: Comparison of hydrodynamic parameters of BMR derived from ab initio envelopes to experimentally determined parameters. The P1 and P2 envelopes used for the shell models are as shown in Figure 5.6 A/B and D/E respectively. The experimental R_g and D_{max} values were obtained from SAXS (Table 5.2) while the r_H and $s_{20,w}$ values were obtained from AUC (Chapter 4).

MODELS	R_g (nm)	r_H (nm)	D_{max} (nm)	$s_{20,w}$ (x 10^{-13} s)
AUTOGNOM-DERIVED MODELS				
Experimental	4.6	4.9	13.5	6.3
BMR AUTOGNOM P1	4.4	4.7	15.4	6.4
BMR AUTOGNOM P2	4.4	4.5	15.6	6.7
GNOM-DERIVED MODELS				
Experimental	4.5	4.9	15.6	6.3
BMR GNOM P1	4.6	4.8	14.0	6.3
BMR GNOM P2	4.4	4.9	14.1	6.3

5.5.2 Hydrodynamic bead modelling for rigid body models

As discussed in section 5.4.1, rigid body models were constructed for BMR and 6 common orientations (3 each for P1 and P2 symmetry) were found to fit the scattering profiles. The theoretical hydrodynamic parameters of these models were calculated from bead models using SOMO and the results are compared to experimental values as shown in Table 5.6. Of all the hydrodynamic parameters listed in Table 5.6, the radius of gyration is most important as it is estimated directly from the SAXS experimental data. Thus, an agreement between the theoretical and experimental R_g indicates a good rigid body model solution. As seen in the table, the theoretical values of all the hydrodynamic parameters are in close agreement with the experimental data indicating that all the solutions were accurate. However, it is not clear from the table which of the six BMR rigid body models give the best solution and, as a result, these six orientations remain the most likely orientations of BMR in solution.

Table 5.6: Comparison of BMR hydrodynamic parameters derived from rigid body models to experimentally determined parameters. *The experimental R_g and D_{max} values were obtained from SAXS (Table 5.2) while the r_H and $s_{20,w}$ were obtained from AUC (Chapter 4). $^a R_g$ and D_{max} were obtained using GNOM and $^b R_g$ and D_{max} were obtained using AUTOGNOM.*

MODELS	R_g (nm)	r_H (nm)	D_{max} (nm)	$s_{20,w}$ (x 10^{-13} s)	f/f_o
Experimental	$4.5^a/4.6^b$	4.9	$13.5^a/15.6^b$	6.3	1.5
BMR-P1-A	4.5	4.7	14.6	6.1	1.4
BMR-P1-B	4.4	4.6	14.6	6.3	1.4
BMR-P1-C	4.5	4.7	15.0	6.2	1.4
BMR-P2-A	4.4	4.8	13.3	6.1	1.5
BMR-P2-B	4.3	4.6	13.6	6.2	1.4
BMR-P2-C	4.3	4.6	12.7	6.3	1.5

5.6 SUMMARY AND DISCUSSION

Despite a high level of activity and pliability, the structure-function relationships of the self-sufficient flavocytochrome P450 BM3 (and its reductase domain) are not yet fully understood. In this study, small angle X-ray scattering was applied to the elucidation of solution structures and the conformation of intact BM3 and its BMR and FAD domains. Preliminary analysis of the SAXS data has shown that all three enzymes studied were folded in solution (prominent peak at low angles on Kratky plots) and no aggregation was observed on the Guinier plots. Inferences drawn from SAXS analysis of all three enzymes are discussed in the following sections.

5.6.1 Oligomerization states of BM3, BMR and the FAD domain

There are a number of factors that contribute to errors in estimating protein molecular weights (and subsequent oligomerization state) from SAXS measurements. Inaccurate concentration measurements and error in the calibration with BSA could skew the molecular weight estimates. The measured molecular weights for BM3 and BMR are all above the monomer molecular weights and slightly less than to the dimer molecular weights of these enzymes. On the other hand, the resulting FAD domain molecular weight is almost exactly twice the expected monomer molecular weight. These results are in agreement with molecular weight measurements obtained using SEC-MALLS and AUC (see chapter 4), supporting our hypothesis that, while BM3 and BMR form a reversible dimerization in solution, the FAD domain is fully dimeric in solution.

5.6.2 Solution conformation and symmetry of BM3, BMR and the FAD domain

Preliminary information on solution conformations of BM3 and BMR were acquired in the previous chapter using frictional ratios obtained from sedimentation velocity studies (see Section 4.2.1). The results suggested that BM3 exists in solution as compact and near-globular with no symmetry in the quarternary structure, and that BMR exists in solution as an ellipsoidal shaped molecule. This suggestion was confirmed using various interpretations of SAXS data in this chapter. In the Kratky plots obtained for BM3 and BMR samples, prominent peaks were observed at low angles suggesting that both enzymes were properly folded and compact in solution. An unusual second peak occurred also at low angles for both Kratky plots (albeit smaller in intensity when compared to the first peak). This second peak was more pronounced for BM3, while that of BMR continued into a tail - which was not observed with intact BM3. This implies that, while both enzymes are shown to be compact, the tail observed for Kratky plot of the BMR sample indicates an extended conformation in comparison to BM3.

Further, the probability distribution function *P(r)* obtained using *GNOM* usually gives a clear indication of conformation of molecules in solution. An asymmetric bell-shaped distribution curve was observed for BM3 while an extended curve was observed for BMR. In addition, *ab initio* models calculated for BM3 corresponded to compact and near-globular structures, while those for BMR were slightly compact, but extended. Moreover, it is expected that BM3, which is 54 kDa bigger than BMR, will give higher values of maximum dimension (D_{max}) than BMR if they were of similar conformations in solution. However, D_{max} value for BMR samples (15.64 nm) was greater than for intact BM3 (15.02 nm). Based on these observations, BM3 adopts a compact and near-globular conformation in solution, while BMR adopts a more extended conformation in solution, possibly similar to the shape of an ellipsoid.

Addition of NPG to BM3 solutions affected neither the measured molecular weight obtained using SEC-MALLS nor the sedimentation coefficient observed from AUC. The AUC finding indicated the presence of fatty acids might not induce a significant change on the solution conformation of BM3 and the MALLS result indicated the oligomerization state was not affected by NPG binding. Preliminary analysis of SAXS data indicated that addition of NADP or NPG to BM3 samples had no effect on the raw scattering profiles and the observed radius of gyration from Guinier plots. However,

these methods are not as sensitive as the probability distribution function to the conformational changes of molecules in solution. When using the $P(r)$ function to calculate properties, the values of D_{max} and R_g for BM3 in the presence of NPG were higher than those for ligand-free BM3, but no change was observed on addition of NADP. The $P(r)$ plot for BM3-NPG sample was slightly extended in comparison to those of ligand-free BM3 and BM3-NADP. These data suggest that, on binding NPG, the compact shape of BM3 becomes slightly extended. The results are consistent with the *ab initio* models which indicated BM3-NADP is more globular than BM3, while BM3-NPG is slightly extended. Thus, it can be inferred that, while binding of NADP results in a slight conformational change in BM3 towards a more globular structure, binding of NPG results in a more extended conformation.

The Kratky and GNOM plots for the FAD domain indicate the domain is folded and compact with extended ends as visualised in the *ab initio* models. The *ab initio* models were compared to the recently solved FAD domain crystal structure (4DQK, (*115*)) using CRYSOL and via superposition. The FAD domain crystallised with two molecules within the asymmetric unit but the interface region formed in the asymmetric unit was small indicating the molecules do not form a stable dimer. A better fit was observed when the SAXS experimental scattering was compared to the theoretical scattering of a single molecule, as opposed to that of a 'dimer' with a configuration given by the molecules in the asymmetric unit. Further, the 'dimer' of the asymmetric unit could not be superimposed on the *ab initio* model, but a good superposition fit was observed with a single molecule. The dimerization of FAD is driven by disulfide linkages; if the disulfide bonds are broken, then monomer FAD is formed. Further, the crystallization of the FAD domain was only possible by mutating two cysteine residues which occur in the interface formed between the monomers contained in the asymmetric unit of the crystal structure. Thus, it can be inferred that the FAD monomers are joined together by disulfide linkages into a compact dimer, and that breaking the disulfide linkages leads to dissociation of the dimers into extended monomers of similar dimensions. On the other hand, the solution structure of the FAD domain might differ significantly from the crystal structure. Further, it is possible that the conformational mobility between the FAD- and NADP-binding domains in solution might lead to reorientation which enables these sub-domains to fill the spaces in the *ab initio* envelope (Figure 5.9) better. These suggestions are subject to further studies.

The second peak observed in the Kratky plots for BM3 and BMR samples is not seen on the Kratky plot for the FAD domain. Further, the *P(r)* plots of BM3 and BMR samples are skewed near the peak, but this feature is not observed for the FAD domain. Thus, it could be inferred that these features are due to an internal organised repeat as might occur for a multi-domain enzyme with flexible linkers, or alternatively are due to the presence of a monomer-dimer equilibrium. In addition, the second peak could be as a result of inter-domain flexibility resulting in an ensemble of different configurations contributing to the scattering profile of the enzyme. Further, the *ab initio* models for BM3, BMR and the FAD domain were calculated assuming both no symmetry, P1 and P2 symmetry. The models generated with P1 and P2 symmetry were slightly different from each other for BM3 samples and for BMR samples, but similar to each other for the FAD domain. This suggests that BM3 and BMR exist in solution with no symmetry present, while the FAD domain could exist in solution with P2 symmetry. This finding however needs further studies.

5.6.3 BMR structure

Rigid body models were calculated for BMR using the SAXS data and the previously published crystal structures of the BM3 FAD and FMN domains. Three common orientations were observed in each set of structures generated with either P1 or P2 symmetry (as shown in Figure 5.15) and the hydrodynamic parameters obtained for the six models were similar to each other (Table 5.6). Further, the FMN-to-FAD cofactor distance observed for the 6 models were above 25 Å suggesting that BMR exists in solution in an open conformation.

This is the first modelling study where BMR structural information has been obtained using (i) AUC data, (ii) SAXS data, and (iii) published structural data for the FAD and FMN domains. In a recent publication, a BMR model was reconstructed based on the rat CPR structure, in which case the BM3 FAD and FMN domains were shown to superimpose on the CPR structure forming an interface region in which the FAD and FMN cofactors approach one another for direct inter-flavin electron transfer (*115*). Further, the FMN-to-FAD distance in this model was shown to be 4 Å, suggestive of a closed conformation and similar to the distance observed in the rat CPR structure. The theoretical scattering of the published BMR model was compared to the experimental SAXS data using CRYSOL and a χ^2 value of 14 was obtained. This high χ^2 value is

expected since the published BMR model is of a closed conformation and the six models generated in this study using the experimental SAXS data all correspond to an open conformation.

Further, the theoretical scattering of the four published CPR structures (2 open and 2 closed) were compared to the experimental SAXS data using CRYSOL. The two closed structures include rat (PDB code 1AMO; (*53*)) and yeast CPR (PDB code 2BF4; (*324*)) and were crystallised as two molecules within the asymmetric unit. One of the CPR structures with an open conformation is the yeast-human chimera (YH) where the FMN domain is obtained from yeast and the FAD domain is obtained from rat (PDB code 3FJO; (*325*)). The other CPR structure with an open conformation is a rat CPR mutant with a 4-amino acid deletion in the hinge region connecting the FMN domain to the FAD domain (PDB code 3ES9; (*326*)). No dimeric interfaces were observed in the crystal structures for all these CPR structures and as a result they were classed as monomers, although some of them crystallized with more than one molecule each of the FAD and FMN domains in the asymmetric unit. Table 5.7 shows the χ^2 values obtained from comparing the theoretical scattering of these CPR structures to the experimental SAXS data, alongside the FMN-to-FAD cofactor distances within these structures. The χ^2 values obtained in all the cases are very high, suggesting that the BMR structures might be different from the CPR structures. This is further supported by our findings that BMR exists as a dimer in solution while CPR (as far as is known) exists as a monomer in solution.

Table 5.7: Comparison of CPR theoretical scattering with BMR experimental scattering data. The FMN-to-FAD cofactor distances for the CPR structures are shown in the table, signifying two structures with closed conformations and two structures with open conformation. The χ^2 values obtained in all cases are very high. The FMN-to-FAD cofactor distances for the various CPR structures shown in the table are only for information purposes indicating closed conformation for 1AMO and 2BF4 and open conformations for 3FJO and 3ES9.

CPR PDB Code	FMN-to-FAD distance (Å)	χ^2 (Theoretical scattering of CPR structures versus BMR SAXS scattering)
1AMO	4	8.86
2BF4	4	5.72
3FJO	86	9.57
3ES9	29	6.16

In summary, SAXS experiments have shown that BM3 is near-completely dimeric in solution and adopts a compact and near globular conformation. BMR is also near-completely dimeric in solution, but adopts a more extended conformation, likely resembling an ellipsoid. On the other hand, the FAD domain is fully dimeric in solution and adopts a compact and globular conformation with extended sides. Six rigid body models have been developed for BMR and all models imply that BMR adopts an open conformation and might be significantly different from CPR in its conformational arrangement.

CHAPTER 6

CONCLUSIONS AND RECOMMENDATIONS FOR FUTURE WORK

CHAPTER SIX: CONCLUSIONS AND RECOMMENDATIONS FOR FUTURE WORK

6.0 INTRODUCTION

Many cellular processes depend upon weak protein-protein interactions (PPIs). Understanding these interactions is thus imperative to further developments in cell biology. Due to the difficulty in trapping transient complexes in solution, characterization of weak PPIs has lagged behind those of strong PPIs.

In this work, weak PPIs that occur in cytochrome P450s were studied using flavocytochrome P450 BM3 (BM3) as a model. BM3 is a 119 kDa self-sufficient fatty acid monooxygenase which can be truncated into a 55 kDa heme (BMP) domain and a 64 kDa reductase domain (BMR). The reductase domain can be further split into a 45 kDa FAD domain (FAD) and a 19 kDa FMN domain (FMN). Within the BM3 enzyme, electrons are transferred from the donor (usually NADPH) to the FAD domain, then to the FMN domain and finally to the P450 domain. Since discovery, BM3 has been well characterized and is known to have the highest fatty oxidase activities observed among all cytochrome P450s (*5*). Moreover, the ease of expression and purification of BM3 and its respective domains has made BM3 a model for the understanding of activities and mechanism of cytochrome P450s in general. BM3 has also found applications in various biotechnological studies including the agricultural, chemical, medical, and pharmaceutical sectors (see section 1.2.5).

Understanding weak PPIs in BM3 and the domains requires in-depth biochemical, biophysical and structural examinations; an approach undertaken in this thesis. For the first time, a collection of information describing the structure of BM3 and its domains has been reported.

6.1 BIOCHEMICAL CHARACTERIZATION OF BM3 AND ITS DOMAINS

In this section, steady-state kinetics and stopped-flow techniques were used in characterizing weak interactions between the P450 (BMP) and reductase (BMR) domains of the flavocytochrome BM3 (BM3) enzyme. Initial studies involved the use of

equilibrium optical binding and steady-state kinetics to study the ligand-binding characteristics and reductase activities of the full length enzyme, as well as those of the component domains. The interaction of the BMP and BMR domains was then studied in both the intact BM3 enzyme and for the reconstituted domains, by monitoring the rate of formation of a ferrous-CO complex in the presence of NADPH reductant and across a range of salt concentrations.

From binding titration studies, substrate binding results in blue, type I Soret spectral shifts, while binding of inhibitors result in red, type II Soret shifts. The observed shift direction and magnitude is consistent with data reported for other cytochrome P450s. Further, the catalytic efficiency (k_{cat}/K_M) of BM3 with cytochrome c is higher than that obtained for the BMR domain, suggesting that the heme domain has a role in e.g., preventing non-successful collisions of cytochrome c with the enzyme, or in promoting favourable interactions of the reductase with cytochrome c.

Results obtained for the dependence of BMP-BMR interactions in the presence of NADPH and various salt concentrations shows that rate constants for electron transfer between these domains in the reconstituted system is about a thousand fold less than the rate constant in the intact enzyme. Moreover, the observed decrease in the electron transfer rate constants as a function of salt concentration is unexpected and is inconsistent with light scattering results obtained previously (*305*) and with other data in the literature (*261*). However, this inconsistency could be explained by the fact that, while the literature data report studies that were conducted on the oxidized forms of the enzyme, the studies done in this thesis were carried out with reduced forms of the enzyme (and followed electron transfer events). Thus, for future studies, it is pertinent to conduct a more elaborate analysis on interactions between different reduced and oxidized forms of BM3 and its domains, following reactions occurring both within and between the different domains. It is also vital to investigate in more details the ability of the reconstituted system to catalyse fatty acid hydroxylation.

Direct reduction of BMP by NADPH in the absence of the reductase domain has been reported for the first time in this work, and was most noticeable when the experiment was conducted over 1000 seconds (i.e. the rate constant for this reaction is very slow). This brings to the fore the need to be cautious when interpreting results obtained from studies on the BM3 enzyme in the presence of NADPH that are conducted over extended time courses. This is of particular relevance in relation to the relatively

inefficient interactions between the dissected BMP and BMR domains. In such experiments, the inefficient direct reduction of the BMP heme iron by NADPH should be accounted for fully to ensure that true rates of inter-domain electron transfer can be determined.

Having observed the dependence of electron transfer rate constants on ionic strength for both the intact P450 BM3 enzyme and the domain-dissected forms (i.e. electron transfer between BMR and BMP) using steady-state and stopped-flow kinetic methods, the studies were extended to the assessment of the hydrodynamic and spectroscopic/structural properties of the P450 BM3 enzyme and its domains, as discussed in the following sections.

6.2 BIOPHYSICAL AND STRUCTURAL CHARACTERIZATION OF BM3 AND ITS DOMAINS

6.2.1 Oligomeric states of all P450 BM3 and its domains

A clear understanding of the oligomeric states of BM3 and its domains is currently lacking in the literature, as various inconclusive reports have been presented. From a literature search, only four groups have conducted studies in this field. Black and Martin used HPLC to show that BM3, BMR and FAD all exist as a combination of various oligomeric states (monomers, dimers, trimers etc.) in solution (*109*). Govindaraj and Poulos used FPLC and SDS-PAGE to show that BMR and FAD each exist as a combination of monomers and dimers in solution, while BM3 exists as a dimer in solution; no higher oligomers were observed for these enzymes (*107*). The Munro group showed that the BM3 dimer is the active species in fatty acid hydroxylation using enzyme assays (*9*). The Peterson group (using a combination of enzyme kinetics, cross-linking experiments and SEC) suggested that BM3 could exists as a dimer or trimer (predominantly dimeric), but that the dimeric form is the state with significant levels of fatty acid hydroxylase activity (*212*). They also proposed that the BMR and FAD domains were at least dimeric in solution. Thus, the literature data suggests that BM3, BMR and FAD all exist in more than one oligomeric form in solution, but that the intact P450 BM3 enzyme is predominantly dimeric.

In this report, more accurate and precise biophysical techniques were employed to investigate the oligomeric states of BM3, BMP, BMR, and the FAD and FMN domains in solution. The factors stabilizing the resulting oligomers as well as the dimerization constants (where possible) were also elucidated. These techniques include size exclusion chromatography coupled with multi angle laser light scattering (SEC-MALLS) for more accurate molecular weight measurements, analytical ultracentrifugation (AUC) and composite gradient multi angle laser light scattering (CG-MALLS).

BM3, BMR, the FAD and FMN domains, and BMP all eluted as single peaks on the size exclusion column (using SEC-MALLS). Based on the resulting weight average molecular weight obtained for all the peaks resolved, BM3 and BMR were shown to be "near-dimeric" (83% and 77% of the expected dimer molecular weight respectively), the FAD domain was shown to be fully dimeric (97% of the expected dimer molecular weight) and the BMP and FMN domains were shown to be monomeric. Using sedimentation velocity, the BM3 SEC-MALLS peak could be further resolved into 2% monomeric, 94% dimeric, and 4% trimeric peaks, while the BMR SEC-MALLS peak could be resolved into 24% monomeric and 74% dimeric peaks. Sedimentation coefficients of 9.7 and 5.8 were obtained for BM3 and BMR respectively, corresponding to dimeric peaks. Further BM3 dimerization as a function of salt concentration was shown to be strongest at 0.15 M KCl via sedimentation equilibrium and SEC-MALLS experiments.

BM3 molecular weight estimates obtained from all the techniques used in this research are greater than the molecular weight predicted from the amino acid sequence, indicating that BM3 cannot exist in solution as a monomer. Also, high chi-square values for BM3 and BMR (4.4 and 3.6 respectively) were obtained from monomer rigid body modeling of SAXS data, confirming that BM3 and BMR also could not exist as a monomer in solution. However, BM3 monomers were observed at very low ionic strength (5 mM KPi). At low salt, long-range repulsive forces dominate, preventing self-association of the monomers. These long-range repulsive forces are screened as the ionic strength is increased to 50 mM using potassium phosphate buffer.

SEC-MALLS studies on a BM3-formaldehyde mixture yielded 42% dimer and 58% monomer peaks. A re-run of the monomeric peak resulted in more monomers (88%) than dimers (12%). The monomer fraction was then studied by sedimentation velocity, in which case a peak occurred at the same position (with the same sedimentation coefficient) as a BMR dimer, but the hydrodynamic values obtained were similar to those obtained for BM3 monomer. These results suggest that the presence of formaldehyde could prevent the BM3 monomers from associating or might have caused the heme domain to dissociate and the BMR domains to dimerize (although this is highly unlikely unless treatment with formaldehyde can in some way result in cleavage of the peptide linker region between the BMP and BMR domains of BM3). Thus, for future studies, it is vital to identify the exact effects of formaldehyde on BM3. If BM3 monomers are actually obtained by treatment with formaldehyde, this could be useful for various studies including crystallization trials for BM3 (i.e. if formaldehyde could produce a homogeneous monomeric state – although any such monomers might also be covalently modified by formaldehyde at various positions). It will also be useful for SAXS studies as the scattering data of BM3 monomer can be used in rigid body modeling of BM3 dimer.

No higher oligomers (i.e. above the dimers) were observed with BM3, as apparent molecular weight decreased when protein concentration was increased to values above those required for dimer formation at all ionic strengths studied using CG-MALLS. Also, positive B_{dd} values indicating repulsive interactions between dimers were observed, thus providing further indication that no significant amounts of higher oligomers were present. In addition, R_g was observed to decrease with increasing BM3 concentration, again suggesting dimer-dimer repulsion and hence little possibility of higher oligomer formation.

6.2.2 Characterization of BM3, BMR, and FAD dimerization

The near-dimer molecular weight observed for BM3 and BMR implies that the dimerization is weak and suggests the presence of monomer-dimer equilibrium (reversible dimerization). On the other hand, the FAD domain dimerizes fully and addition of DTT to the FAD domain resulted in a split peak containing 76% dimer and 24% monomer. This ratio was not significantly affected when the ionic strength was increased, but the dimerization of BM3 and BMR has been shown to be highly

dependent on the ionic strength of the solution. These suggest that the interactions driving the dimerization of BM3 are the same for BMR, but not for the FAD domain. In other words, while BM3 and BMR dimerize reversibly (stabilized presumably by electrostatic interactions due to ionic strength dependence of dimerization), the FAD domain may dimerize irreversibly, possibly by forming intermolecular disulfide bonds. Moreover, disulfide linkages appear to play a negligible role in BM3 dimerization, but the effect of disulfide linkages on oligomerization of BMR was inconclusive, as the resulting molecular weight change at high salt was small compared to that at low salt, and this change might be attributed to many other factors.

Further evidence supporting the oligomeric properties of BM3 and BMR as observed in this research include:

- ❖ According to a study by Yu *et al* (*308*), reversible dimerization can be seen on chromatogram peaks as tailing, merging and fronting. These characteristics (mostly peak tailing) are observed on BM3 and BMR SEC-MALLS chromatogram peaks, providing further evidence for reversible dimerization of these enzymes

- ❖ From sedimentation velocity studies, more monomers were obtained at a low concentration of BMR in comparison to data from studies done at higher BMR concentration, again suggestive of the presence of a reversible monomer/dimer equilibrium.

- ❖ Sedimentation equilibrium studies confirm the presence of a monomer/dimer equilibrium, as this is the only model that could fit the equilibrium data collected.

- ❖ Further, the observed dissociation constants decreased with increasing ionic strength. This is in agreement with SEC-MALLS and CG-MALLS studies showing that BM3 dimerization is weakened with increasing salt concentration, and hence reversible.

- ❖ The inability to fit batch SLS data to a non-associating model suggests the presence of reversible equilibrium, possibly involving different kinds of inter-molecular interactions.

- ❖ The second peaks on Kratky and P(r) plots for BM3 and BMR suggests the presence of an ensemble of different conformations contributing to the scattering

profile. These conformations could be responsible for maintaining the monomer-dimer equilibrium observed in BM3 and BMR.

A dissociation constant for the BM3 dimer of 0.29 µM was obtained at 0.15 M KCl, indicating that BM3 dimerization is relatively strong (although perhaps transient – i.e. a rapid monomer-dimer equilibrium). Further, the characteristics of the BMR dimer are very similar to those of BM3 indicating that, although the reversible dimerization of BMR is weaker than that of BM3, it can be concluded that BMR dimerization likely drives BM3 dimerization. However, since the FAD domain dimerizes near-irreversibly (i.e. probably with the involvement of one or more disulfide bonds) and BMR dimerizes reversibly, it is unlikely that the FAD domain dimerization exclusively drives BMR dimerization, although most of the BMR *ab initio* and rigid body models (see section 6.2.4) have been shown to link at the FAD domain. Thus, for future studies, the effects of disulfide linkage on BMR dimerization should be investigated. If the disulfide linkages actually stabilize BMR dimerization, then it could be concluded that FAD dimerization drives BMR dimerization (either partially or fully). The inability to obtain a full complement of BM3 monomer at a high ionic strength of 1 M KCl indicates that factors other than electrostatics might be involved in stabilizing the dimer, such as hydrogen bonding or hydrophobic interactions, but that attractive electrostatic interactions likely play a dominant role.

6.2.3 Effects of ligand binding on BM3 dimerization

Binding of ligands (particularly substrates) to BM3 has been shown to induce changes to the spin state of the ferric heme iron, which can be observed in the UV-visible spectrum of the hemoprotein (See Figure 1.8). There is a likelihood that this spin state change could result in a conformation change in BM3, resulting from structural alteration in the environment of the heme (occurring as a consequence of the spin-state change and alterations in the position of the iron) and elsewhere in the active site (due to structural changes in the environment of the bound ligand/substrate). In this study, the influence of substrate binding on BM3 conformation/oligomerization was investigated using various techniques.

AUC and SEC-MALLS results showed no change in apparent molecular weight or sedimentation coefficient on the addition of the substrate NPG to a BM3 sample. Also, Addition of NPG or $NADP^+$ did not appear to change the BM3 scattering profiles or to

significantly alter the R_g, suggesting that addition of a substrate ligand does not affect the overall shape/oligomerization state of BM3. On the other hand, no change was observed for the P(r) curve of BM3-NADP$^+$ in comparison to the ligand-free BM3 curve, but the binding of NPG slightly extended the curve (larger D_{max}). This is apparently confirmed by the *ab initio* structural data, where the BM3 and BM3-NADP$^+$ structural models are compact, but that of BM3-NPG is extended. The P(r) curve is more sensitive to conformational changes than are other techniques used in this study. From these results, it can be inferred that binding of NADP$^+$ does not induce any considerable conformational change in BM3, but that binding of NPG does induce a conformational change on BM3 structure, albeit minimal. That is, the conformational change induced on binding of NPG to BM3 is so small that it can only be captured by only sensitive techniques.

6.2.4 FAD domain, BMR and BM3 structure

Small angle X-ray scattering (SAXS) was used to study the structure of BM3, BMR and the FAD domain, and also for comparing the solution structure of the FAD domain to that of the crystal structure. The P(r) function of the FAD domain shows that this domain is compact and globular with extended ends. This was confirmed with *ab initio* models, which also showed that the FAD domain is compact and near-globular. 20 *ab initio* models were each constructed with P1 and P2 symmetry, and the average of these models was taken. Although the average chi-square value for these models was slightly high (1.55), the NSD values for both P1 and P2 symmetry were low (~0.5) indicating that the 20 models were similar to one another. Further, the P1 and P2 averaged models were comparable, suggesting that the FAD domain dimer exists in solution with P2 symmetry. Comparing the FAD domain solution structure (using both scattering data and superimposition) with the existing FAD crystal structure did not yield good fits (probably because the dimer structure in solution is different from the dimer formed in the crystal). This implies that the FAD domain solution structure might be different from the crystal structure, or that the wild-type FAD domain structure could be different in conformation from the mutant crystal structure currently available. This conclusion is subject to further studies.

Initial studies using sedimentation equilibrium suggest that BM3 and BMR exist in solution as compact molecules, but that while BM3 is relatively globular, BMR is more

extended in shape (likely ellipsoidal). This suggestion is supported by the P(r) plots and by considering the second peaks on the Kratky plots of BM3 and BMR. The plot for BM3 has a a bell-shaped structure albeit with a double peak, while the plot of BMR has a tail indicating that BMR is more extended in structure comparison to BM3. The second peak is also observed on the P(r) plots for BM3 and BMR, but is absent on both Kratky and P(r) plots of the FAD domain. The dual peaks are thus indicative of the presence of a multi-domain enzyme with a flexible linker.

Ab initio models were determined for BMR and BM3 using the SAXS scattering data. All BMR models show an elongated molecule shape, resembling an ellipsoid, with average NSD values of around 0.8. Rigid body models were also calculated for BMR using crystal structures of the BM3 FAD and FMN domains. 6 common orientations were observed for the BMR models, including 3 P1 and 3 P2 models; applying distance constraints did not improve the solution. These BMR rigid body models were superimposed on the *ab initio* envelopes and relatively good fits were obtained. Most of the models were shown to be linked at the FAD domain, suggesting that FAD domain dimerization might play a role in BMR dimerization. Further, hydrodynamic parameters obtained from BMR *ab initio* and rigid body models were similar to those obtained using other techniques in this study, implying that these models are relatively accurate. Unlike CPR, all BMR rigid body models here have been shown to exist in an open conformation, as the minimum FAD-to-FMN domain distance observed is 25 Å.

Rigid body modeling for full length BM3 posed a great challenge as six individual domains were required for calculating a rigid body model. Imposing symmetry and distance constraints improved the solutions slightly, but no common models were observed. Further, bead modeling techniques revealed that the values of hydrodynamic parameters of BM3 *ab initio* models were significantly different to those obtained from other methods used in this research. This implies that the resulting *ab initio* models may not accurately represent the solution structure of BM3.

In summary, the averaged *ab initio* models generated for the FAD domain were marginally different (low NSD values of ~ 0.5) as opposed to BMR and BM3 (NSD values of ~0.8 and ~1.0 respectively), likely indicating that these envelopes represent the solution conformation of the FAD domain. Inter-domain flexibility within BM3 and BMR has been demonstrated via the higher NSD values obtained for the BM3 and BMR *ab initio* envelopes (in comparison to the FAD domain) and the second peak on

both Kratky and P(r) plots of BM3 and BMR (this second peak is absent in the FAD domain). Further, it is likely that BM3 and BMR exists in solution with no symmetry, while the FAD domain exists with P2 symmetry. This is because *ab initio* models with P1 and P2 models were different from each other for BM3 and BMR, but quite similar for the FAD domain.

6.2.5 C773A BMR structure

The molecular weight estimate for the C773A BMR mutant was similar to that of the wild-type BMR protein, indicating that this mutation (alone) does not influence BMR dimerization. Sedimentation velocity studies for the C773A BMR gave inconclusive results and crystallization trials produced crystals, but these did not diffract X-rays to a sufficient resolution to enable determination of a crystal structure. For future studies, an additional mutation could be introduced at C999, creating a BMR double mutant (C999A/C773A) similar to the FAD double mutant from which the existing FAD domain crystal structure was obtained. This double mutant could then be used for further biophysical studies and for crystallization trials, with the hope that a crystal structure could then be determined. Also, SAXS data for the BMR double mutant from could be compared to the SAXS data for the BMR wild type, as reported in this thesis. This information will be useful in ascertaining the effects this double mutation has on the overall structure of BMR.

REFERENCES

1. Prudencio, M., and Ubbink, M. (2004) Transient complexes of redox proteins: structural and dynamic details from NMR studies, *Journal of Molecular Recognition 17*, 524-539.

2. Sevrioukova, I. F., and Poulos, T. L. (2011) Structural biology of redox partner interactions in P450cam monooxygenase: A fresh look at an old system, *Archives of Biochemistry and Biophysics 507*, 66-74.

3. Tyson, C. A., Lipscomb, J. D., and Gunsalus, I. C. (1972) The role of putidaredoxin and P450 cam in methylene hydroxylation., *Journal of Biological Chemistry 247*, 5777-5784.

4. Narhi, L. O., and Fulco, A. J. (1986) Characterization of a Catalytically Self-Sufficient 119,000-Dalton Cytochrome-P-450 Monooxygenase Induced by Barbiturates in *Bacillus-Megaterium*, *Journal of Biological Chemistry 261*, 7160-7169.

5. Noble, M. A., Miles, C. S., Chapman, S. K., Lysek, D. A., MacKay, A. C., Reid, G. A., Hanzlik, R. P., and Munro, A. W. (1999) Roles of key active-site residues in flavocytochrome P450 BM3, *Biochemical Journal 339*, 371-379.

6. Narhi, L. O., and Fulco, A. J. (1987) Identification and characterization of two functional domains in cytochrome P-450BM-3, a catalytically self-sufficient monooxygenase induced by barbiturates in *Bacillus megaterium*, *Journal of Biological Chemistry 262*, 6683-6690.

7. Miles, J. S., Munro, A. W., Rospendowski, B. N., Smith, W. E., McKnight, J., and Thomson, A. J. (1992) Domains of the catalytically self-sufficient cytochrome P-450 BM-3. Genetic construction, overexpression, purification and spectroscopic characterization, *Biochemical Journal 288*, 503-509.

8. Girvan, H. M., Dunford, A. J., Neeli, R., Ekanem, I. S., Waltham, T. N., Joyce, M. G., Leys, D., Curtis, R. A., Williams, P., Fisher, K., Voice, M. W., and Munro, A. W. (2011) Flavocytochrome P450 BM3 mutant W1046A is a NADH-dependent fatty acid hydroxylase: Implications for the mechanism of electron transfer in the P450 BM3 dimer, *Archives of Biochemistry and Biophysics 507*, 75-85.

9. Neeli, R., Girvan, H. M., Lawrence, A., Warren, M. J., Leys, D., Scrutton, N. S., and Munro, A. W. (2005) The dimeric form of flavocytochrome P450 BM3 is catalytically functional as a fatty acid hydroxylase, *FEBS Letters 579*, 5582-5588.

10. Ozbabacan, S. E. A., Engin, H. B., Gursoy, A., and Keskin, O. (2011) Transient protein–protein interactions, *Protein Engineering Design and Selection 24*, 635-648.

11. Fuentes, M., Mateo, C., Pessela, B. C. C., Batalla, P., Fernandez-Lafuente, R., and Guisán, J. M. (2007) Solid phase proteomics: Dramatic reinforcement of very weak protein–protein interactions, *Journal of Chromatography B 849*, 243-250.

12. Nooren, I. M. A., and Thornton, J. M. (2003) Diversity of protein-protein interactions, *EMBO Journal 22*, 3486-3492.

13. Stites, W. E. (1997) Protein Interactions: Interface Structure, Binding Thermodynamics, and Mutational Analysis, *Chemical Reviews 97*, 1233-1250.

14. Schneider, S., Marles-Wright, J., Sharp, K. H., and Paoli, M. (2007) Diversity and conservation of interactions for binding heme in b-type heme proteins, *Natural Product Reports 24*, 621-630.

15. Jagow, G., and W, S. (1980) b-type cytochromes, *Annual Review of Biochemistry 49*, 281-314.

16. Omura, T. (2005) Heme–thiolate proteins, *Biochemical and Biophysical Research Communications 338*, 404-409.

17. Ullrich, R., and Hofrichter, M. (2007) Enzymatic hydroxylation of aromatic compounds, *Cellular and Molecular Life Sciences 64*, 271-293.

18. Shaw, P. D., and Hager, L. P. (1959) Biological Chlorination, *Journal of Biological Chemistry 234*, 2565-2569.

19. Morris, D. R., and Hager, L. P. (1966) Chloroperoxidase. I. Isolation and properties of the crystalline glycoprotein, *Journal of Biological Chemistry 241*, 1763-1768.

20. Anh, D. H., Ullrich, R., Benndorf, D., Svatos, A., Muck, A., and Hofrichter, M. (2007) The Coprophilous Mushroom *Coprinus radians* Secretes a Haloperoxidase that Catalyzes Aromatic Peroxygenation, *Applied and Environmental Microbiology 73*, 5477-5485.

21. Hofrichter, M., and Ullrich, R. (2006) Heme-thiolate haloperoxidases: versatile biocatalysts with biotechnological and environmental significance, *Applied Microbiology and Biotechnology 71*, 276-288.

22. Piontek, K., Ullrich, R., Liers, C., Diederichs, K., Plattner, D. A., and Hofrichter, M. (2010) Crystallization of a 45 kDa peroxygenase/peroxidase from the mushroom *Agrocybe aegerita* and structure determination by SAD utilizing only the haem iron, *Acta Crystallographica Section F Structural Biology and Crystallization Communications 66*, 693-698.

23. Santolini, J. (2011) The molecular mechanism of mammalian NO-synthases: A story of electrons and protons, *Journal of Inorganic Biochemistry 105*, 127-141.

24. Crane, B. R., Sudhamsu, J., and Patel, B. A. (2010) Bacterial Nitric Oxide Synthases, *Annual Review of Biochemistry 79*, 445-470.

25. Bruckdorfer, R. (2005) The basics about nitric oxide, *Molecular Aspects of Medicine 26*, 3-31.

26. Costa, C., Tozzi, A., Siliquini, S., Galletti, F., Cardaioli, G., Tantucci, M., Pisani, F., and Calabresi, P. (2011) A critical role of NO/cGMP/PKG dependent pathway in hippocampal post-ischemic LTP: Modulation by zonisamide, *Neurobiology of Disease 44*, 185-191.

27. Fröhlich, A., and Durner, J. (2011) The hunt for plant nitric oxide synthase (NOS): Is one really needed?, *Plant Science 181*, 401-404.

28. Wilson, I. D., Neill, S. J., and Hancock, J. T. (2008) Nitric oxide synthesis and signalling in plants, *Plant, Cell & Environment 31*, 622-631.

29. Gupta, K. J., Igamberdiev, A. U., Manjunatha, G., Segu, S., Moran, J. F., Neelawarne, B., Bauwe, H., and Kaiser, W. M. (2011) The emerging roles of nitric oxide (NO) in plant mitochondria, *Plant Science 181*, 520-526.

30. Foresi, N., Correa-Aragunde, N., Parisi, G., Caló, G., Salerno, G., and Lamattina, L. (2010) Characterization of a Nitric Oxide Synthase from the Plant Kingdom: NO Generation from the Green Alga *Ostreococcus tauri* Is Light Irradiance and Growth Phase Dependent, *The Plant Cell Online 22*, 3816-3830.

31. Gorren, A. C. F., and Mayer, B. (2007) Nitric-oxide synthase: A cytochrome P450 family foster child, *Biochimica et Biophysica Acta (BBA) - General Subjects 1770*, 432-445.

32. Daff, S. (2010) NO synthase: Structures and mechanisms, *Nitric Oxide 23*, 1-11.

33. Goodrich, L. E., Paulat, F., Praneeth, V. K. K., and Lehnert, N. (2010) Electronic Structure of Heme-Nitrosyls and Its Significance for Nitric Oxide Reactivity, Sensing, Transport, and Toxicity in Biological Systems, *Inorganic Chemistry 49*, 6293-6316.

34. Nelson, D. R. (2009) The Cytochrome P450 Homepage, *Human Genomics 4*, 59-65.

35. Omura, T., and Sato, R. (1962) A new cytochrome in liver microsomes, *Journal of Biological Chemistry 237*, 1375–1376.

36. Klingenberg, M. (1958) Pigments of rat liver microsomes, *Archives of Biochemistry and Biophysics 75*, 376-386.

37. Estabrook, R. W. (2003) A passion for P450s (remembrances of the early history of research on cytochrome P450) *Drug Metabolism and Disposition 31*, 1461-1473.

38. Pochapsky T. C, Kazanis S, and M., D. (2010) Conformational plasticity and structure/function relationships in cytochromes P450., *Antioxidants and Redox Signaling 13*, 1273-1296.

39. Luthra, A., Denisov, I. G., and Sligar, S. G. (2011) Spectroscopic features of cytochrome P450 reaction intermediates, *Archives of Biochemistry and Biophysics 507*, 26-35.

40. Wang, J. F., and Chou, K. C. (2010) Molecular modeling of cytochrome P450 and drug metabolism., *Current Drug Metabolism 11*, 342-346.

41. Singh, D., Kashyap, A., Pandey, R. V., and Saini, K. S. (2011) Novel advances in cytochrome P450 research, *Drug Discovery Today 16*, 793-799.

42. Hannemann, F., Bichet, A., Ewen, K. M., and Bernhardt, R. (2007) Cytochrome P450 systems—biological variations of electron transport chains, *Biochimica et Biophysica Acta (BBA) - General Subjects 1770*, 330-344.

43. Isin, E. M., and Guengerich, F. P. (2007) Complex reactions catalyzed by cytochrome P450 enzymes, *Biochimica et Biophysica Acta - General Subjects 1770*, 314-329.

44. Kumar, S. (2010) Engineering cytochrome P450 biocatalysts for biotechnology, medicine and bioremediation, *Expert Opinion on Drug Metabolism & Toxicology 6*, 115-131.

45. O'Reilly, E., Köhler, V., Flitsch, S. L., and Turner, N. J. (2011) Cytochromes P450 as useful biocatalysts: addressing the limitations, *Chemical Communications 47*, 2490.

46. Grogan, G. (2011) Cytochromes P450: exploiting diversity and enabling application as biocatalysts, *Current Opinion in Chemical Biology 15*, 241-248.

47. Stevenson, P. M., Ruettinger, R. T., and Fulco, A. J. (1983) Cytochrome P-450 revealed: the effect of the respiratory cytochromes on the spectrum of bacterial cytochrome P-450, *Biochemical and Biophysical Research Communications 112*, 927-934.

48. Stumpe, M., and Feussner, I. (2006) Formation of Oxylipins by CYP74 Enzymes, *Phytochemistry Reviews 5*, 347-357.

49. Modi, S., Sutcliffe, M. J., Primrose, W. U., Lian, L. Y., and Roberts, G. C. K. (1996) The catalytic mechanism of cytochrome P450 BM3 involves a 6 Å movement of the bound substrate on reduction, *Nature Structural Biology 3*, 414-417.

50. Stone, K. L., Behan, R. K., and Green, M. T. (2005) X-ray absorption spectroscopy of chloroperoxidase compound I: Insight into the reactive intermediate of P450 chemistry, *Proceedings of the National Academy of Sciences 102*, 16563-16565.

51. Rittle, J., and Green, M. T. (2010) Cytochrome P450 Compound I: Capture, Characterization, and C-H Bond Activation Kinetics, *Science 330*, 933-937.

52. Murataliev, M. B., Feyereisen, R., and Walker, F. A. (2004) Electron transfer by diflavin reductases, *Biochimica et Biophysica Acta (BBA) - Proteins & Proteomics 1698*, 1-26.

53. Wang, M., Roberts, D. L., Paschke, R., Shea, T. M., Masters, B. S. S., and Kim, J.-J. P. (1997) Three-dimensional structure of NADPH–cytochrome P450 reductase: Prototype for FMN- and FAD-containing enzymes, *Proceedings of the National Academy of Sciences 94*, 8411-8416.

54. Sevrioukova, I., and Peterson, J. A. (1995) Reduction of the Heme Domain of P450BM3, *FASEB Journal 9*, A1488-A1488.

55. Alderton, W. K., Cooper, C. E., and Knowles, R. G. (2001) Nitric Oxide Synthases : Structure, Function and Inhibition, *Biochemical Journal 357*, 593-615.

56. Ghosh, D. K., and Salerno, J. C. (2003) Nitric oxide synthases: domain structure and alignment in enzyme function and control, *Frontiers in Bioscience 8*, d193-209.

57. Li, H., Shimizu, H., Flinspach, M., Jamal, J., Yang, W., Xian, M., Cai, T., Wen, E. Z., Jia, Q., Wang, P. G., and Poulos, T. L. (2002) The Novel Binding Mode of N-Alkyl-N′-hydroxyguanidine to Neuronal Nitric Oxide Synthase Provides Mechanistic Insights into NO Biosynthesis, *Biochemistry 41*, 13868-13875.

58. Garcin, E. D., Bruns, C. M., Lloyd, S. J., Hosfield, D. J., Tiso, M., Gachhui, R., Stuehr, D. J., Tainer, J. A., and Getzoff, E. D. (2004) Structural basis for isozyme-specific regulation of electron transfer in nitric-oxide synthase, *Journal of Biological Chemistry 279*, 37918-37927.

59. Olteanu, H., and Banerjee, R. (2001) Human methionine synthase reductase, a soluble P-450 reductase-like dual flavoprotein, is sufficient for NADPH-dependent methionine synthase activation, *Journal of Biological Chemistry 276*, 35558-35563.

60. Paine, M. J. I., Garner, A. P., Powell, D., Sibbald, J., Sales, M., Pratt, N., Smith, T., Tew, D. G., and Wolf, C. R. (2000) Cloning and Characterization of a Novel Human Dual Flavin Reductase, *Journal of Biological Chemistry 275*, 1471-1478.

61. Eschenbrenner, M., Coves, J., and Fontecave, M. (1995) The Flavin Reductase Activity of the Flavoprotein Component of Sulfite Reductase from *Escherichia coli.* A New Model for the Protein Structure, *Journal of Biological Chemistry 270*, 20550-20555.

62. Ruettinger, R. T., Wen, L. P., and Fulco, A. J. (1989) Coding nucleotide, 5' regulatory, and deduced amino acid sequences of P-450BM-3, a single peptide cytochrome P-450:NADPH-P-450 reductase from *Bacillus megaterium*, *Journal of Biological Chemistry 264*, 10987-10995.

63. Roitel, O., Scrutton, N. S., and Munro, A. W. (2003) Electron transfer in flavocytochrome P450 BM3: kinetics of flavin reduction and oxidation, the role of cysteine 999, and relationships with mammalian cytochrome P450 reductase, *Biochemistry 42*, 10809-10821.

64. Mandai, T., Fujiwara, S., and Imaoka, S. (2009) Construction and engineering of a thermostable self-sufficient cytochrome P450, *Biochemical and Biophysical Research Communications 384*, 61-65.

65. Hlavica, P. (2009) Assembly of non-natural electron transfer conduits in the cytochrome P450 system: A critical assessment and update of artificial redox constructs amenable to exploitation in biotechnological areas, *Biotechnology Advances 27*, 103-121.

66. Karplus, P. A., and Bruns, C. M. (1994) Structure-Function Relations for Ferredoxin Reductase, *Journal of Bioenergetics and Biomembranes 26*, 89-99.

67. Whitehouse, C. J. C., Bell, S. G., and Wong, L.-L. (2012) P450BM3 (CYP102A1): connecting the dots, *Chemical Society Reviews 41*, 1218-1260.

68. Kunst, F., Ogasawara, N., Moszer, I., Albertini, A. M., Alloni, G., Azevedo, V., Bertero, M. G., Bessieres, P., Bolotin, A., Borchert, S., Borriss, R., Boursier, L., Brans, A., Braun, M., Brignell, S. C., Bron, S., Brouillet, S., Bruschi, C. V., Caldwell, B., Capuano, V., Carter, N. M., Choi, S. K., Codani, J. J., Connerton, I. F., Cummings, N. J., Daniel, R. A., Denizot, F., Devine, K. M., Dusterhoft, A., Ehrlich, S. D., Emmerson, P. T., Entian, K. D., Errington, J., Fabret, C., Ferrari, E., Foulger, D., Fritz, C., Fujita, M., Fujita, Y., Fuma, S., Galizzi, A., Galleron, N., Ghim, S. Y., Glaser, P., Goffeau, A., Golightly, E. J., Grandi, G., Guiseppi, G., Guy, B. J., Haga, K., Haiech, J., Harwood, C. R., Henaut, A., Hilbert, H., Holsappel, S., Hosono, S., Hullo, M. F., Itaya, M., Jones, L., Joris, B., Karamata, D., Kasahara, Y., Klaerr-Blanchard, M., Klein, C., Kobayashi, Y., Koetter, P., Koningstein, G., Krogh, S., Kumano, M., Kurita, K., Lapidus, A., Lardinois, S., Lauber, J., Lazarevic, V., Lee, S. M., Levine, A., Liu, H., Masuda, S., Mauel, C., Medigue, C., Medina, N., Mellado, R. P., Mizuno, M., Moestl, D., Nakai, S., Noback, M., Noone, D., O'Reilly, M., Ogawa, K., Ogiwara, A., Oudega, B., Park, S. H., Parro, V., Pohl, T. M., Portetelle, D., Porwollik, S., Prescott, A. M., Presecan, E., Pujic, P., Purnelle, B., Rapoport, G., Rey, M., Reynolds, S., Rieger, M., Rivolta, C., Rocha, E., Roche, B., Rose, M., Sadaie, Y., Sato, T., Scanlan, E., Schleich, S., Schroeter, R., Scoffone, F., Sekiguchi, J., Sekowska, A., Seror, S. J., Serror, P., Shin, B. S., Soldo, B., Sorokin, A., Tacconi, E., Takagi, T., Takahashi, H., Takemaru, K., Takeuchi, M., Tamakoshi, A., Tanaka, T., Terpstra, P., Tognoni, A., Tosato, V., Uchiyama, S., Vandenbol, M., Vannier, F., Vassarotti, A., Viari, A., Wambutt, R., Wedler, E., Wedler, H., Weitzenegger, T., Winters, P., Wipat, A., Yamamoto, H., Yamane, K., Yasumoto, K., Yata, K., Yoshida, K., Yoshikawa, H. F., Zumstein, E., Yoshikawa, H., and Danchin, A. (1997) The complete genome sequence of the Gram-positive bacterium *Bacillus subtilis*, *Nature 390*, 249-256.

69. Budde, M., Maurer, S. C., Schmid, R. D., and Urlacher, V. B. (2004) Cloning, expression and characterisation of CYP102A2, a self-sufficient P450 monooxygenase from *Bacillus subtilis*, *Applied Microbiology and Biotechnology 66*, 180-186.

70.   Lentz, O., Urlacher, V., and Schmid, R. D. (2004) Substrate specificity of native and mutated cytochrome P450 (CYP102A3) from *Bacillus subtilis*, *Journal of Biotechnology 108*, 41-49.

71.   Budde, M., Morr, M., Schmid, R. D., and Urlacher, V. B. (2006) Selective hydroxylation of highly branched fatty acids and their derivatives by CYP102A1 from *Bacillus megaterium*, *ChemBioChem 7*, 789-794.

72.   Chowdhary, P. K., Alemseghed, M., and Haines, D. C. (2007) Cloning, Expression and Characterization of a Fast Self-Sufficient P450: CYP102A5 from *Bacillus cereus*, *Archives of Biochemistry and Biophysics 468*, 32-43.

73.   Gustafsson, M. C. U., Roitel, O., Marshall, K. R., Noble, M. A., Chapman, S. K., Pessegueiro, A., Fulco, A. J., Cheesman, M. R., von Wachenfeldt, C., and Munro, A. W. (2004) Expression, Purification, and Characterization of *Bacillus subtilis* Cytochromes P450 CYP102A2 and CYP102A3: Flavocytochrome Homologues of P450 BM3 from *Bacillus megaterium*, *Biochemistry 43*, 5474-5487.

74.   Lentz, O., Feenstra, A., Habicher, T., Hauer, B., Schmid, R. D., and Urlacher, V. B. (2006) Altering the regioselectivity of cytochrome P450 CYP102A3 of *Bacillus subtilis* by using a new versatile assay system, *ChemBioChem 7*, 345-350.

75.   Dietrich, M., Eiben, S., Asta, C., Do, T. A., Pleiss, J., and Urlacher, V. B. (2008) Cloning, expression and characterisation of CYP102A7, a self-sufficient P450 monooxygenase from *Bacillus licheniformis*, *Applied Microbiology and Biotechnology 79*, 931-940.

76.   Nakayama, N., Takemae, A., and Shoun, H. (1996) Cytochrome P450foxy, a Catalytically Self-Sufficient Fatty Acid Hydroxylase of the Fungus *Fusarium oxysporum*, *Journal of Biochemistry 119*, 435-440.

77.   Kitazume, T. (2000) *Fusarium oxysporum* Fatty-acid Subterminal Hydroxylase (CYP505) Is a Membrane-bound Eukaryotic Counterpart of *Bacillus megaterium* Cytochrome P450BM3, *Journal of Biological Chemistry 275*, 39734-39740.

78.   Kitazume, T., Tanaka, A., Takaya, N., Nakamura, A., Matsuyama, S., Suzuki, T., and Shoun, H. (2002) Kinetic analysis of hydroxylation of saturated fatty acids by recombinant P450foxy produced by an *Escherichia coli* expression system, *European Journal of Biochemistry 269*, 2075-2082.

79.   Seo, J.-A., Proctor, R. H., and Plattner, R. D. (2001) Characterization of Four Clustered and Coregulated Genes Associated with Fumonisin Biosynthesis in *Fusarium verticillioides*, *Fungal Genetics and Biology 34*, 155-165.

80.   Mason, J. R., and Cammack, R. (1992) The Electron-Transport Proteins of Hydroxylating Bacterial Dioxygenases, *Annual Review of Microbiology 46*, 277-305.

81.   De Mot, R., and Parret, A. H. A. (2002) A novel class of self-sufficient cytochrome P450 monooxygenases in prokaryotes, *Trends in Microbiology 10*, 502-508.

82.   Nagy, I., Schoofs, G., Compernolle, F., Proost, P., Vanderleyden, J., and de Mot, R. (1995) Degradation of the thiocarbamate herbicide EPTC (S-ethyl dipropylcarbamothioate) and biosafening by *Rhodococcus sp.* strain NI86/21 involve an inducible cytochrome P-450 system and aldehyde dehydrogenase, *Journal of Bacteriology 177*, 676-687.

83.   Nagy, I., Compernolle, F., Ghijs, K., Vanderleyden, J., and De Mot, R. (1995) A Single Cytochrome P-450 System is Involved in Degradation of the Herbicides EPTC (S-Ethyl Dipropylthiocarbamate) and Atrazine by *Rhodococcus sp.* Strain NI86/21, *Applied and Environmental Microbiology 61*, 2056–2060.

84.   Roberts, G. A., Grogan, G., Greter, A., Flitsch, S. L., and Turner, N. J. (2002) Identification of a New Class of Cytochrome P450 from a *Rhodococcus sp.*, *Journal of Bacteriology 184*, 3898-3908.

85.   Roberts, G. A. (2003) A Self-sufficient Cytochrome P450 with a Primary Structural Organization that Includes a Flavin Domain and a [2Fe-2S] Redox Center, *Journal of Biological Chemistry 278*, 48914-48920.

86.   Celik, A., Roberts, G. A., White, J. H., Chapman, S. K., Turner, N. J., and Flitsch, S. L. (2006) Probing the substrate specificity of the catalytically self-sufficient cytochrome P450 RhF from a *Rhodococcus sp*, *Chemical Communications 43*, 4492-4494.

87.   Hunter, D., Roberts, G., Ost, T., White, J., Muller, S., Turner, N., Flitsch, S., and Chapman, S. (2005) Analysis of the domain properties of the novel cytochrome P450 RhF, *FEBS Letters 579*, 2215-2220.

88.   Munro, A. W., Girvan, H. M., and McLean, K. J. (2007) Cytochrome P450–redox partner fusion enzymes, *Biochimica et Biophysica Acta - General Subjects 1770*, 345-359.

89.   Liu, L., Schmid, R. D., and Urlacher, V. B. (2006) Cloning, expression, and characterization of a self-sufficient cytochrome P450 monooxygenase from *Rhodococcus ruber* DSM 44319, *Applied Microbiology and Biotechnology 72*, 876-882.

90.   Jackson, C. J. (2002) A Novel Sterol 14 alpha -Demethylase/Ferredoxin Fusion Protein (MCCYP51FX) from *Methylococcus capsulatus* Represents a New Class of the Cytochrome P450 Superfamily, *Journal of Biological Chemistry 277*, 46959-46965.

91.   Rylott, E. L., Jackson, R. G., Edwards, J., Womack, G. L., Seth-Smith, H. M. B., Rathbone, D. A., Strand, S. E., and Bruce, N. C. (2006) An explosive-degrading cytochrome P450 activity and its targeted application for the phytoremediation of RDX, *Nature Biotechnology 24*, 216-219.

92.   Kim, B. S., Kim, S. Y., Park, J., Park, W., Hwang, K. Y., Yoon, Y. J., Oh, W. K., Kim, B. Y., and Ahn, J. S. (2007) Sequence-based screening for self-sufficient P450 monooxygenase from a metagenome library, *Journal of Applied Microbiology 102*, 1392-1400.

93.   Brodhun, F., Gobel, C., Hornung, E., and Feussner, I. (2009) Identification of PpoA from *Aspergillus nidulans* as a Fusion Protein of a Fatty Acid Heme Dioxygenase/Peroxidase and a Cytochrome P450, *Journal of Biological Chemistry 284*, 11792-11805.

94.   Kizawa, H., Tomura, D., Oda, M., Fukamizu, A., Hoshino, T., Gotoh, O., Yasui, T., and Shoun, H. (1991) Nucleotide sequence of the unique nitrate/nitrite-inducible cytochrome P-450 cDNA from *Fusarium oxysporum*, *Journal of Biological Chemistry 266*, 10632-10637.

95.   Nakahara, K., Tanimoto, T., Hatano, K., Usuda, K., and Shoun, H. (1993) Cytochrome P-450 55A1 (P-450dNIR) acts as nitric oxide reductase employing NADH as the direct electron donor, *Journal of Biological Chemistry 268*, 8350-8355.

96.   Park, S.-Y., Shimizu, H., Adachi, S.-i., Yoshitsugu, S., Iizuka, T., Nakagawa, A., Tanaka, I., Shoun, H., and Hori, H. (1997) Crystallization, preliminary diffraction and electron paramagnetic resonance studies of a single crystal of cytochrome P450nor, *FEBS Letters 412*, 346-350.

97.   Shimizu, H., Park, S.-Y., Shiro, Y., and Adachi, S.-i. (2002) X-ray structure of nitric oxide reductase (cytochrome P450nor) at atomic resolution, *Acta Crystallographica Section D 58*, 81-89.

98.   Miura, Y., and Fulco, A. J. (1974) (Omega -2) hydroxylation of fatty acids by a soluble system from *Bacillus megaterium*, *Journal of Biological Chemistry 249*, 1880-1888.

99.   Matson, R. S., Hare, R. S., and Fulco, A. J. (1977) Characteristics of a cytochrome P-450-dependent fatty acid omega-2 hydroxylase from *Bacillus megaterium*, *Biochim Biophys Acta - Lipids and Lipid Metabolism 487*, 487-494.

100. Miura, Y., and Fulco, A. J. (1975) Omega-1, Omega-2 and Omega-3 hydroxylation of long-chain fatty acids, amides and alcohols by a soluble enzyme system from *Bacillus megaterium*, *Biochim Biophys Acta 388*, 305-317.

101. Matson, R. S., Stein, R. A., and Fulco, A. J. (1980) Hydroxylation of 9-hydroxystearate by a soluble cytochrome P-450 dependent fatty acid hydroxylase from *Bacillus megaterium*, *Biochemical and Biophysical Research Communications 97*, 955-961.

102. Ruettinger, R. T., and Fulco, A. J. (1981) Epoxidation of Unsaturated Fatty-Acids by a Soluble Cytochrome-P-450-Dependent System from *Bacillus-Megaterium*, *Journal of Biological Chemistry 256*, 5728-5734.

103. Hare, R. S., and Fulco, A. J. (1975) Carbon monoxide and hydroxymercuribenzoate sensitivity of a fatty acid (omega-2) hydroxylase from *Bacillus megaterium*, *Biochemical and Biophysical Research Communications 65*, 665-672.

104. Munro, A. W., Girvan, H. M., and McLean, K. J. (2007) Variations on a (t)heme—novel mechanisms, redox partners and catalytic functions in the cytochrome P450 superfamily, *Natural Product Reports 24*, 585-609.

105. Ost, T. W. B., Miles, C. S., Munro, A. W., Murdoch, J., Reid, G. A., and Chapman, S. K. (2001) Phenylalanine 393 Exerts Thermodynamic Control over the Heme of Flavocytochrome P450 BM3, *Biochemistry 40*, 13421-13429.

106. Boddupalli, S. S., Oster, T., Estabrook, R. W., and Peterson, J. A. (1992) Reconstitution of the fatty acid hydroxylation function of cytochrome P-450BM-3 utilizing its individual recombinant hemo- and flavoprotein domains, *Journal of Biological Chemistry 267*, 10375-10380.

107. Govindaraj, S., and Poulos, T. L. (1997) The Domain Architecture of Cytochrome P450BM-3, *Journal of Biological Chemistry 272*, 7915-7921.

108. Govindaraj, S., and Poulos, T. L. (1996) Probing the structure of the linker connecting the reductase and heme domains of cytochrome P450BM-3 using site-directed mutagenesis., *Protein Science 5*, 1389–1393.

109. Black, S. D., and Martin, S. T. (1994) Evidence for conformational dynamics and molecular aggregation in cytochrome P450 102 (BM-3), *Biochemistry 33*, 12056-12062.

110. Sevrioukova, I., Truan, G., and Peterson, J. A. (1996) The flavoprotein domain of P450BM-3: expression, purification, and properties of the flavin adenine dinucleotide- and flavin mononucleotide-binding subdomains, *Biochemistry 35*, 7528-7535.

111. Ravichandran, K. G., Boddupalli, S. S., Hasemann, C. A., Peterson, J. A., and Deisenhofer, J. (1993) Crystal structure of hemoprotein domain of P450BM-3, a prototype for microsomal P450's, *Science 261*, 731-736.

112. Li, H. Y., and Poulos, T. L. (1997) The structure of the cytochrome P450BM-3 haem domain complexed with the fatty acid substrate, palmitoleic acid, *Nature Structural Biology 4*, 140-146.

113. Haines, D. C., Tomchick, D. R., Machius, M., and Peterson, J. A. (2001) Pivotal role of water in the mechanism of P450BM-3, *Biochemistry 40*, 13456-13465.

114. Sevrioukova, I. F., Li, H., Zhang, H., Peterson, J. A., and Poulos, T. L. (1999) Structure of a cytochrome P450–redox partner electron-transfer complex, *Proceedings of the National Academy of Sciences 96*, 1863-1868.

115. Joyce. M. G., Ekanem, I. S., Roitel, O., Dunford, A. J., Neeli, R., Girvan, H. M., Baker, G. J., Curtis, R. A., Munro, A. W., and Leys, D. (2012) The crystal structure of the FAD/NADPH binding domain of flavocytochrome P450 BM3, *FEBS Journal 279*, 1694-1706.

116. Munro, A. W., Daff, S., Coggins, J. R., Lindsay, J. G., and Chapman, S. K. (1996) Probing electron transfer in flavocytochrome P-450 BM3 and its component domains, *European Journal of Biochemistry 239*, 403-409.

117. Deng, T.-j., Proniewicz, L. M., Kincaid, J. R., Yeom, H., Macdonald, I. D. G., and Sligar, S. G. (1999) Resonance Raman Studies of Cytochrome P450BM3 and Its Complexes with Exogenous Ligands, *Biochemistry 38*, 13699-13706.

118. Boddupalli, S. S., Pramanik, B. C., Slaughter, C. A., Estabrook, R. W., and Peterson, J. A. (1992) Fatty acid monooxygenation by P450BM-3: product identification and proposed mechanisms for the sequential hydroxylation reactions, *Archives of Biochemistry and Biophysics 292*, 20-28.

119.   Ost, T. W. B., Miles, C. S., Murdoch, J., Cheung, Y. F., Reid, G. A., Chapman, S. K., and Munro, A. W. (2000) Rational re-design of the substrate binding site of flavocytochrome P450 BM3, *FEBS Letters 486*, 173-177.

120.   Hegde, A., Haines, D. C., Bondlela, M., Chen, B., Schaffer, N., Tomchick, D. R., Machius, M., Nguyen, H., Chowdhary, P. K., Stewart, L., Lopez, C., and Peterson, J. A. (2007) Interactions of Substrates at the Surface of P450s Can Greatly Enhance Substrate Potency, *Biochemistry 46*, 14010-14017.

121.   Gudiminchi, R. K., and Smit, M. S. (2011) Identification and characterization of 4-hexylbenzoic acid and 4-nonyloxybenzoic acid as substrates of CYP102A1, *Applied Microbiology and Biotechnology 90*, 117-126.

122.   Capdevila, J. H., Wei, S., Helvig, C., Falck, J. R., Belosludtsev, Y., Truan, G., Graham-Lorence, S. E., and Peterson, J. A. (1996) The Highly Stereoselective Oxidation of Polyunsaturated Fatty Acids by Cytochrome P450BM-3, *Journal of Biological Chemistry 271*, 22663-22671.

123.   Oliver, C. F., Modi, S., Sutcliffe, M. J., Primrose, W. U., Lian, L.-Y., and Roberts, G. C. K. (1997) A Single Mutation in Cytochrome P450 BM3 Changes Substrate Orientation in a Catalytic Intermediate and the Regiospecificity of Hydroxylation, *Biochemistry 36*, 1567-1572.

124.   Li, H., and Poulos, T. (1999) Fatty acid metabolism, conformational change, and electron transfer in cytochrome P-450BM-3, *Biochimica et Biophysica Acta - Molecular and Cell Biology of Lipids 1441*, 141-149.

125.   Dietrich, M., Do, T. A., Schmid, R. D., Pleiss, J., and Urlacher, V. B. (2009) Altering the regioselectivity of the subterminal fatty acid hydroxylase P450 BM-3 towards γ- and δ-positions, *Journal of Biotechnology 139*, 115-117.

126.   Appel, D., Lutz-Wahl, S., Fischer, P., Schwaneberg, U., and Schmid, R. D. (2001) A P450 BM-3 Mutant Hydroxylates Alkanes, Cycloalkanes, Arenes and Heteroarenes, *Journal of Biotechnology 88*, 167-171.

127.   Li, Q.-S., Schwaneberg, U., Fischer, P., and Schmid, R. D. (2000) Directed Evolution of the Fatty-Acid Hydroxylase P450 BM-3 into an Indole-Hydroxylating Catalyst, *Chemistry 6*, 1531-1536.

128.   Brenner, S., Hay, S., Girvan, H. M., Munro, A. W., and Scrutton, N. S. (2007) Conformational dynamics of the cytochrome P450 BM3/N-palmitoylglycine complex: the proposed "proximal-distal" transition probed by temperature-jump spectroscopy, *Journal of Physical Chemistry B 111*, 7879-7886.

129.   Modi, S., Primrose, W. U., Boyle, J. M. B., Gibson, C. F., Lian, L. Y. and Roberts, G. C. K. (1995) NMR studies of substrate binding to cytochrome P(450 BM3): Comparisons to cytochrome P(450 cam). *Biochemistry 34*, 8982-8988.

130.   Truan, G., and Peterson, J. A. (1998) Thr268 in substrate binding and catalysis in P450BM-3, *Archives of Biochemistry and Biophysics 349*, 53-64.

131.   Daff, S. N., Chapman, S. K., Turner, K. L., Holt, R. A., Govindaraj, S., Poulos, T. L., and Munro, A. W. (1997) Redox control of the catalytic cycle of flavocytochrome P-450 BM3, *Biochemistry 36*, 13816-13823.

132.   Yeom, H., Sligar, S. G., Li, H. Y., Poulos, T. L., and Fulco, A. J. (1995) The Role of Thr268 in Oxygen Activation of Cytochrome P450(BM-3), *Biochemistry 34*, 14733-14740.

133.   Clark, J. P., Miles, C. S., Mowat, C. G., Walkinshaw, M. D., Reid, G. A., Daff, S. N., and Chapman, S. K. (2006) The role of Thr268 and Phe393 in cytochrome P450 BM3, *Journal of Inorganic Biochemistry 100*, 1075-1090.

134.   Cryle, M. J., and De Voss, J. J. (2008) The role of the conserved threonine in P450 BM3 oxygen activation: substrate-determined hydroxylation activity of the Thr268Ala mutant, *ChemBioChem 9*, 261-266.

135.   Joyce, M. G., Girvan, H. M., Munro, A. W., and Leys, D. (2004) A single mutation in cytochrome P450 BM3 induces the conformational rearrangement seen upon

substrate binding in the wild-type enzyme, *Journal of Biological Chemistry 279*, 23287-23293.

136. Girvan, H. M., Marshall, K. R., Lawson, R. J., Leys, D., Joyce, M. G., Clarkson, J., Smith, W. E., Cheesman, M. R., and Munro, A. W. (2004) Flavocytochrome P450 BM3 mutant A264E undergoes substrate-dependent formation of a novel heme iron ligand set, *Journal of Biological Chemistry 279*, 23274-23286.

137. Girvan, H. M., Seward, H. E., Toogood, H. S., Cheesman, M. R., Leys, D., and Munro, A. W. (2007) Structural and spectroscopic characterization of P450 BM3 mutants with unprecedented P450 heme iron ligand sets. New heme ligation states influence conformational equilibria in P450 BM3., *Journal of Biological Chemistry 282*, 564-572.

138. Girvan, H. M., Toogood, H. S., Littleford, R. E., Seward, H. E., Smith, W. E., Ekanem, I. S., Leys, D., Cheesman, M. R., and Munro, A. W. (2009) Novel haem co-ordination variants of flavocytochrome P450 BM3, *Biochemical Journal 417*, 65-76.

139. Graham-Lorence, S., Truan, G., Peterson, J. A., Falck, J. R., Wei, S., Helvig, C., and Capdevila, J. H. (1997) An Active Site Substitution, F87V, Converts Cytochrome P450 BM-3 into a Regio- and Stereoselective (14S,15R)-Arachidonic Acid Epoxygenase, *Journal of Biological Chemistry 272*, 1127-1135.

140. Oliver, C. F., Modi, S., Primrose, W. U., Lian, L. Y. and Roberts, G. C. K. . (1997) Engineering the substrate specificity of *Bacillus megaterium* cytochrome P-450 BM3: Hydroxylation of alkyl trimethylammonium compounds, *Biochemical Journal 327*, 537-544.

141. Cowart, L. A., Falck, J. R., and Capdevila, J. H. (2001) Structural determinants of active site binding affinity and metabolism by cytochrome P450 BM-3, *Archives of Biochemistry and Biophysics 387*, 117-124.

142. Schwaneberg, U., Schmidt-Dannert, C., Schmitt, J., and Schmid, R. D. (1999) A continuous spectrophotometric assay for P450 BM-3, a fatty acid hydroxylating enzyme, and its mutant F87A, *Analytical Biochemistry 269*, 359-366.

143. Raner, G. M., Hatchell, A. J., Morton, P. E., Ballou, D. P., and Coon, M. J. (2000) Stopped-flow spectrophotometric analysis of intermediates in the peroxo-dependent inactivation of cytochrome P450 by aldehydes, *Journal of Inorganic Biochemistry 81*, 153-160.

144. Rock, D. A., Boitano, A. E., Wahlstrom, J. L., Rock, D. A., and Jones, J. P. (2002) Use of kinetic isotope effects to delineate the role of phenylalanine 87 in P450(BM-3), *Bioorganic Chemistry 30*, 107-118.

145. Branco, R. J. F., Seifert, A., Budde, M., Urlacher, V. B., Ramos, M. J., and Pleiss, J. (2008) Anchoring effects in a wide binding pocket: The molecular basis of regioselectivity in engineered cytochrome P450 monooxygenase from *B. megaterium*, *Proteins: Structure, Function and Genetics 73*, 597-607.

146. Ost, T. W. B., Munro, A. W., Mowat, C. G., Taylor, P. R., Pesseguiero, A., Fulco, A. J., Cho, A. K., Cheesman, M. A., Walkinshaw, M. D., and Chapman, S. K. (2001) Structural and Spectroscopic Analysis of the F393H Mutant of Flavocytochrome P450 BM3, *Biochemistry 40*, 13430-13438.

147. Chen, Z., Ost, T. W. B., and Schelvis, J. P. M. (2004) Phe393 Mutants of Cytochrome P450 BM3 with Modified Heme Redox Potentials Have Altered Heme Vinyl and Propionate Conformations, *Biochemistry 43*, 1798-1808.

148. Hudecek, J., Anzenbacherova, E., Anzenbacher, P., Munro, A. W., and Hildebrandt, P. (2000) Structural similarities and differences of the heme pockets of various P450 isoforms as revealed by resonance Raman spectroscopy, *Archives of Biochemistry and Biophysics 383*, 70-78.

149. Macdonald, I. D. G., Munro, A. W., and Smith, W. E. (1998) Fatty Acid-Induced Alteration of the Porphyrin Macrocycle of Cytochrome P450 BM3, *Biophysical journal 74*, 3241-3249.

150. Jovanovic, T., Farid, R., Friesner, R. A., and McDermott, A. E. (2005) Thermal equilibrium of high- and low-spin forms of cytochrome P450 BM-3: repositioning of the substrate?, *Journal of the American Chemical Society 127*, 13548-13552.

151. Macdonald, I. D. G., Smith, W. E., and Munro, A. W. (1996) Inhibitor/fatty acid interactions with cytochrome P-450 BM3, *FEBS Letters 396*, 196-200.

152. Noble, M. A., Quaroni, L., Chumanov, G. D., Turner, K. L., Chapman, S. K., Hanzlik, R. P., and Munro, A. W. (1998) Imidazolyl carboxylic acids as mechanistic probes of flavocytochrome P-450 BM3, *Biochemistry 37*, 15799-15807.

153. Smith, S. J., Munro, A. W., and Smith, W. E. (2003) Resonance Raman scattering of cytochrome P450 BM3 and effect of imidazole inhibitors, *Biopolymers 70*, 620-627.

154. Haines, D. C., Chen, B., Tomchick, D. R., Bondlela, M., Hegde, A., Machius, M., and Peterson, J. A. (2008) Crystal structure of inhibitor-bound P450BM-3 reveals open conformation of substrate access channel, *Biochemistry 47*, 3662-3670.

155. Klein, M. L., and Fulco, A. J. (1993) Critical Residues Involved in FMN Binding and Catalytic Activity in Cytochrome-P450(BM-3), *Journal of Biological Chemistry 268*, 7553-7561.

156. Macdonald, I. D. G., Smith, W. E., and Munro, A. W. (1999) Analysis of the structure of the flavin-binding sites of flavocytochrome P450 BM3 using surface enhanced resonance Raman scattering, *European Biophysics Journal 28*, 437-445.

157. Neeli, R., Roitel, O., Scrutton, N. S., and Munro, A. W. (2005) Switching pyridine nucleotide specificity in P450 BM3: mechanistic analysis of the W1046H and W1046A enzymes, *Journal of Biological Chemistry 280*, 17634-17644.

158. Dunford, A. J., Girvan, H. M., Scrutton, N. S., and Munro, A. W. (2009) Probing the molecular determinants of coenzyme selectivity in the P450 BM3 FAD/NADPH domain, *Biochimica et Biophysica Acta - Proteins and Proteomics 1794*, 1181-1189.

159. Quaroni, L. G., Seward, H. E., McLean, K. J., Girvan, H. M., Ost, T. W. B., Noble, M. A., Kelly, S. M., Price, N. C., Cheesman, M. R., Smith, W. E., and Munro, A. W. (2004) Interaction of Nitric Oxide with Cytochrome P450 BM3, *Biochemistry 43*, 16416-16431.

160. McLean, M. A., Yeom, H., and Sligar, S. G. (1996) Carbon monoxide binding to cytochrome P450BM-3: evidence for a substrate-dependent conformational change, *Biochimie 78*, 700-705.

161. Bec, N., Anzenbacher, P., Anzenbacherova, E., Gorren, A. C. F., Munro, A. W., and Lange, R. (1999) Spectral properties of the oxyferrous complex of the heme domain of cytochrome P450BM-3 (CYP102), *Biochemical and Biophysical Research Communications 266*, 187-189.

162. Marchal, S., Girvan, H. M., Gorren, A. C. F., Mayer, B., Munro, A. W., Balny, C., and Lange, R. (2003) Formation of transient oxygen complexes of cytochrome P450BM3 and nitric oxide synthase under high pressure, *Biophysical Journal 85*, 3303-3309.

163. Murataliev, M. B., Klein, M., Fulco, A., and Feyereisen, R. (1997) Functional interactions in cytochrome P450BM3: flavin semiquinone intermediates, role of NADP(H), and mechanism of electron transfer by the flavoprotein domain, *Biochemistry 36*, 8401-8412.

164. Sevrioukova, I., Shaffer, C., Ballou, D. P., and Peterson, J. A. (1996) Equilibrium and transient state spectrophotometric studies of the mechanism of reduction of the flavoprotein domain of P450BM-3, *Biochemistry 35*, 7058-7068.

165. Hanley, S. C., Ost, T. W. B., and Daff, S. (2004) The unusual redox properties of flavocytochrome P450 BM3 flavodoxin domain, *Biochemical and Biophysical Research Communications 325*, 1418-1423.

166. Chen, H.-C., and Swenson, R. P. (2008) Effect of the Insertion of a Glycine Residue into the Loop Spanning Residues 536–541 on the Semiquinone State and Redox Properties of the Flavin Mononucleotide-Binding Domain of Flavocytochrome P450BM-3 from *Bacillus megaterium*, *Biochemistry 47*, 13788-13799.

167.   Murataliev, M. B., and Feyereisen, R. (2000) Functional interactions in cytochrome P450BM3. Evidence that NADP(H) binding controls redox potentials of the flavin cofactors, *Biochemistry 39*, 12699-12707.

168.   Munro, A. W., Lindsay, J. G., Coggins, J. R., Kelly, S. M., and Price, N. C. (1995) NADPH Oxidase Activity of Cytochrome-P-450 BM3 and its Constituent Reductase Domain, *Biochimica Et Biophysica Acta-Bioenergetics 1231*, 255-264.

169.   Murataliev, M. B., and Feyereisen, R. (1996) Functional interactions in cytochrome P450BM3. Fatty acid substrate binding alters electron-transfer properties of the flavoprotein domain, *Biochemistry 35*, 15029-15037.

170.   Daff, S. (2004) An Appraisal of Multiple NADPH Binding-Site Models Proposed for Cytochrome P450 Reductase, NO Synthase, and Related Diflavin Reductase Systems, *Biochemistry 43*, 3929-3932.

171.   Nazor, J., Dannenmann, S., Adjei, R. O., Fordjour, Y. B., Ghampson, I. T., Blanusa, M., Roccatano, D., and Schwaneberg, U. (2008) Laboratory evolution of P450 BM3 for mediated electron transfer yielding an activity-improved and reductase-independent variant, *Protein Engineering, Design and Selection 21*, 29-35.

172.   Zhao, L., Güven, G., Li, Y., and Schwaneberg, U. (2011) First steps towards a Zn/Co(III)sep-driven P450 BM3 reactor, *Applied Microbiology and Biotechnology 91*, 989-999.

173.   Holtmann, D., Mangold, K. M., and Schrader, J. (2009) Entrapment of cytochrome P450 BM-3 in polypyrrole for electrochemically- driven biocatalysis, *Biotechnology Letters 31*, 765-770.

174.   Zilly, F. E., Taglieber, A., Schulz, F., Hollmann, F., and Reetz, M. T. (2009) Deazaflavins as mediators in light-driven cytochrome P450 catalyzed hydroxylations, *Chemical Communications 46*, 7152-7154.

175.   Mouri, T., Shimizu, T., Kamiya, N., Goto, M., and Ichinose, H. (2009) Design of a cytochrome P450BM3 reaction system linked by two-step cofactor regeneration catalyzed by a soluble transhydrogenase and glycerol dehydrogenase, *Biotechnology Progress 25*, 1372-1378.

176.   Sevrioukova, I., and Peterson, J. A. (1996) Domain-domain interaction in cytochrome P450BM-3, *Biochimie 78*, 744-751.

177.   Lange, R., Bec, N., Anzenbacher, P., Munro, A. W., Gorren, A. C. F., and Mayer, B. (2001) Use of high pressure to study elementary steps in P450 and nitric oxide synthase, *Journal of Inorganic Biochemistry 87*, 191-195.

178.   Munro, A. W., Lindsay, J. G., Coggins, J. R., Kelly, S. M., and Price, N. C. (1994) Structural and enzymological analysis of the interaction of isolated domains of cytochrome P-450 BM3, *FEBS Letters 343*, 70-74.

179.   Ost, T. W. B., Clark, J., Mowat, C. G., Miles, C. S., Walkinshaw, M. D., Reid, G. A., Chapman, S. K., and Daff, S. (2003) Oxygen Activation and Electron Transfer in Flavocytochrome P450 BM3, *Journal of the American Chemical Society 125*, 15010-15020.

180.   Klein, M. L., and Fulco, A. J. (1994) The interaction of cytochrome *c* and the heme domain of cytochrome P-450(BM-3) with the reductase domain of cytochrome P-450(BM-3), *Biochimica et Biophysica Acta - General Subjects 1201*, 245-250.

181.   Hazzard, J. T., Govindaraj, S., Poulos, T. L., and Tolling, G. (1997) Electron transfer between the FMN and heme domains of cytochrome P450BM- 3: Effects of substrate and CO, *Journal of Biological Chemistry 272*, 7922-7926.

182.   van Vugt-Lussenburg, B. M. A., Damsten, M. C., Maasdijk, D. M., Vermeulen, N. P. E., and Commandeur, J. N. M. (2006) Heterotropic and homotropic cooperativity by a drug-metabolising mutant of cytochrome P450 BM3, *Biochemical and Biophysical Research Communications 346*, 810-818.

183. Van Vugt-Lussenburg, B. M. A., Stjernschantz, E., Lastdrager, J., Oostenbrink, C., Vermeulen, N. P. E., and Commandeur, J. N. M. (2007) Identification of critical residues in novel drug metabolizing mutants of cytochrome P450 BM3 using random mutagenesis, *Journal of Medicinal Chemistry 50*, 455-461.

184. Stjernschantz, E., Van Vugt-Lussenburg, B. M. A., Bonifacio, A., De Beer, S. B. A., Van Der Zwan, G., Gooijer, C., Commandeur, J. N. M., Vermeulen, N. P. E., and Oostenbrink, C. (2008) Structural rationalization of novel drug metabolizing mutants of cytochrome P450 BM3, *Proteins: Structure, Function and Genetics 71*, 336-352.

185. Damsten, M. C., van Vugt-Lussenburg, B. M. A., Zeldenthuis, T., de Vlieger, J. S. B., Commandeur, J. N. M., and Vermeulen, N. P. E. (2008) Application of drug metabolising mutants of cytochrome P450 BM3 (CYP102A1) as biocatalysts for the generation of reactive metabolites, *Chemico-Biological Interactions 171*, 96-107.

186. Di Nardo, G., Fantuzzi, A., Sideri, A., Panicco, P., Sassone, C., Giunta, C., and Gilardi, G. (2007) Wild-type CYP102A1 as a Biocatalyst: Turnover of Drugs Usually Metabolised by Human Liver Enzymes, *Journal of Biological Inorganic Chemistry 12*, 313-323.

187. Kim, D. H., Kim, K. H., Liu, K. H., Jung, H. C., Pan, J. G., and Yun, C. H. (2008) Generation of human metabolites of 7-ethoxycoumarin by bacterial cytochrome P450 BM3, *Drug Metabolism and Disposition 36*, 2166-2170.

188. Kim, D. H., Ahn, T., Jung, H. C., Pan, J. G., and Yun, C. H. (2009) Short communication: Generation of the human metabolite piceatannol from the anticancer-Preventive agent resveratrol by bacterial cytochrome P450 BM3, *Drug Metabolism and Disposition 37*, 932-936.

189. Kim, D. H., Kim, K. H., Kim, D., Jung, H. C., Pan, J. G., Chi, Y. T., Ahn, T., and Yun, C. H. (2010) Oxidation of human cytochrome P450 1A2 substrates by *Bacillus megaterium* cytochrome P450 BM3, *Journal of Molecular Catalysis B: Enzymatic 63*, 179-187.

190. Kim, K. H., Kang, J. Y., Kim, D. H., Park, S. H., Kim, D., Park, K. D., Lee, Y. J., Jung, H. C., Pan, J. G., Ahn, T., and Yun, C. H. (2011) Generation of human chiral metabolites of simvastatin and lovastatin by bacterial CYP102A1 mutants, *Drug Metabolism and Disposition 39*, 140-150.

191. Meinhold, P., Peters, M. W., Hartwick, A., Hernandez, A. R., and Arnold, F. H. (2006) Engineering Cytochrome P450 BM3 for Terminal Alkane Hydroxylation, *Advanced Synthesis & Catalysis 348*, 763-772.

192. Meinhold, P., Peters, M. W., Chen, M. M. Y., Takahashi, K., and Arnold, F. H. (2005) Direct Conversion of Ethane to Ethanol by Engineered Cytochrome P450 BM3, *ChemBioChem 6*, 1765-1768.

193. Kawakami, N., Shoji, O., and Watanabe, Y. (2011) Use of perfluorocarboxylic acids to trick cytochrome P450BM3 into initiating the hydroxylation of gaseous alkanes, *Angewandte Chemie - International Edition 50*, 5315-5318.

194. Chowdhary, P. K., Stewart, L., Lopez, C., and Haines, D. C. (2008) A single mutation in P450BM-3 enhances acyl homoserine lactone: Acyl homoserine substrate binding selectivity nearly 250-fold, *Journal of Biotechnology 135*, 374-376.

195. Fasan, R., Meharenna, Y. T., Snow, C. D., Poulos, T. L., and Arnold, F. H. (2008) Evolutionary History of a Specialized P450 Propane Monooxygenase, *Journal of Molecular Biology 383*, 1069-1080.

196. Lewis, J. C., and Arnold, F. H. (2009) Catalysts on Demand: Selective Oxidations by Laboratory-Evolved Cytochrome P450 BM3, *CHIMIA International Journal for Chemistry 63*, 309-312.

197. Weber, E., Seifert, A., Antonovici, M., Geinitz, C., Pleiss, J., and Urlacher, V. B. (2011) Screening of a minimal enriched P450 BM3 mutant library for hydroxylation of cyclic and acyclic alkanes, *Chemical Communications 47*, 944-946.

198.   Huang, W. C., Cullis, P. M., Raven, E. L., and Roberts, G. C. K. (2011) Control of the stereo-selectivity of styrene epoxidation by cytochrome P450 BM3 using structure-based mutagenesis, *Metallomics 3*, 410-416.

199.   Whitehouse, C. J. C., Bell, S. G., and Wong, L.-L. (2008) Desaturation of Alkylbenzenes by Cytochrome P450BM3(CYP102A1), *Chemistry - A European Journal 14*, 10905-10908.

200.   Li, H. M., Mei, L. H., Urlacher, V. B., and Schmid, R. D. (2008) Cytochrome P450 BM-3 evolved by random and saturation mutagenesis as an effective indole-hydroxylating catalyst, *Applied Biochemistry and Biotechnology 144*, 27-36.

201.   Hu, S., Huang, J., Mei, L., Yu, Q., Yao, S., and Jin, Z. (2010) Altering the regioselectivity of cytochrome P450 BM-3 by saturation mutagenesis for the biosynthesis of indirubin, *Journal of Molecular Catalysis B: Enzymatic 67*, 29-35.

202.   Whitehouse, C. J. C., Bell, S. G., Tufton, H. G., Kenny, R. J. P., Ogilvie, L. C. I., and Wong, L. L. (2008) Evolved CYP102A1 (P450BM3) variants oxidise a range of non-natural substrates and offer new selectivity options, *Chemical Communications 8*, 966-968.

203.   Park, S. H., Kim, D. H., Kim, D., Jung, H. C., Pan, J. G., Ahn, T., and Yun, C. H. (2010) Engineering Bacterial Cytochrome P450 (P450) BM3 into a Prototype with Human P450 Enzyme Activity Using Indigo Formation, *Drug Metabolism and Disposition 38*, 732-739.

204.   Eiben, S., Bartelmäs, H., and Urlacher, V. B. (2007) Construction of a thermostable cytochrome P450 chimera derived from self-sufficient mesophilic parents, *Applied Microbiology and Biotechnology 75*, 1055-1061.

205.   Fuziwara, S., Sagami, I., Rozhkova, E., Craig, D., Noble, M. A., Munro, A. W., Chapman, S. K., and Shimizu, T. (2002) Catalytically functional flavocytochrome chimeras of P450 BM3 and nitric oxide synthase, *Journal of Inorganic Biochemistry 91*, 515-526.

206.   Degregorio, D., Sadeghi, S. J., Di Nardo, G., Gilardi, G., and Solinas, S. P. (2011) Understanding uncoupling in the multiredox centre P450 3A4-BMR model system, *Journal of Biological Inorganic Chemistry 16*, 109-116.

207.   Helvig, C., and Capdevila, J. H. (2000) Biochemical characterization of rat P450 2C11 fused to rat or bacterial NADPH-P450 reductase domains, *Biochemistry 39*, 5196-5205.

208.   Murataliev, M. B., Trinh, L. N., Moser, L. V., Bates, R. B., Feyereisen, R., and Walker, F. A. (2004) Chimeragenesis of the fatty acid binding site of cytochrome P450BM3. Replacement of residues 73-84 with the homologous residues from the insect cytochrome P450 CYP4C7, *Biochemistry 43*, 1771-1780.

209.   Chen, C.-K. J., Shokhireva, T. K., Berry, R. E., Zhang, H., and Walker, F. A. (2008) The effect of mutation of F87 on the properties of CYP102A1-CYP4C7 chimeras: altered regiospecificity and substrate selectivity, *Journal of Biological Inorganic Chemistry 13*, 813-824.

210.   Chen, C. K. J., Berry, R. E., Shokhireva, T. K., Murataliev, M. B., Zhang, H., and Walker, F. A. (2010) Scanning chimeragenesis: The approach used to change the substrate selectivity of fatty acid monooxygenase CYP102A1 to that of terpene ω-hydroxylase CYP4C7, *Journal of Biological Inorganic Chemistry 15*, 159-174.

211.   Gotoh, O. (1992) Substrate recognition sites in cytochrome P450 family 2 (CYP2) proteins inferred from comparative analyses of amino acid and coding nucleotide sequences, *Journal of Biological Chemistry 267*, 83-90.

212.   Kitazume, T., Haines, D. C., Estabrook, R. W., Chen, B., and Peterson, J. A. (2007) Obligatory intermolecular electron-transfer from FAD to FMN in dimeric P450BM-3, *Biochemistry 46*, 11892-11901.

213.   Siddhanta, U., Presta, A., Fan, B., Wolan, D., Rousseau, D. L., and Stuehr, D. J. (1998) Domain Swapping in Inducible Nitric-oxide Synthase: ELECTRON TRANSFER OCCURS BETWEEN FLAVIN AND HEME GROUPS LOCATED ON ADJACENT SUBUNITS IN THE DIMER, *Journal of Biological Chemistry 273*, 18950-18958.

214. Cunha, C. A., Romao, M. J., Sadeghi, S. J., Valetti, F., Gilardi, G., and Soares, C. M. (1999) Effects of protein-protein interactions on electron transfer: docking and electron transfer calculations for complexes between flavodoxin and c-type cytochromes, *Journal of Biological Inorganic Chemistry 4*, 360-374.

215. Gómez-Moreno, C., Martínez-Júlvez, M., Medina, M., Hurley, J. K., and Tollin, G. (1998) Protein-protein interaction in electron transfer reactions: The ferrodoxin/flavodoxin/ferredoxin:NADP+ reductase system from *Anabaena*, *Biochimie 80*, 837-846.

216. Pawson, T., and Nash, P. (2000) Protein-protein interactions define specificity in signal transduction, *Genes & Development 14*, 1027-1047.

217. Randolph, T. W., and Carpenter, J. F. (2007) Engineering challenges of protein formulations, *AIChE Journal 53*, 1902-1907.

218. Tsai, C. J., Xu, D., and Nussinov, R. (1997) Structural motifs at protein-protein interfaces: protein cores versus two-state and three-state model complexes, *Protein Science 6*, 1793-1805.

219. Perkins, J. R., Diboun, I., Dessailly, B. H., Lees, J. G., and Orengo, C. (2010) Transient Protein-Protein Interactions: Structural, Functional, and Network Properties, *Structure 18*, 1233-1243.

220. Rowe, A. J. (2011) Ultra-weak reversible protein–protein interactions, *Methods 54*, 157-166.

221. Martínez-Fábregas, J., Rubio, S., Díaz-Quintana, A., Díaz-Moreno, I., and De la Rosa, M. Á. (2011) Proteomic tools for the analysis of transient interactions between metalloproteins, *FEBS Journal 278*, 1401-1410.

222. Bonvin, A. M. J. J., Boelens, R., and Kaptein, R. (2005) NMR analysis of protein interactions, *Current Opinion in Chemical Biology 9*, 501-508.

223. Qin, J., Vinogradova, O., and Gronenborn, A. M. (2001) Protein-protein interactions probed by nuclear magnetic resonance spectroscopy, In *Methods in Enzymology* (Thomas L. James, V. D., and Uli, S., Eds.), pp 377-389, Academic Press.

224. Zuiderweg, E. R. P. (2001) Mapping Protein–Protein Interactions in Solution by NMR Spectroscopy, *Biochemistry 41*, 1-7.

225. Jensen, M., Ortega-Roldan, J.-L., Salmon, L., van Nuland, N., and Blackledge, M. (2011) Characterizing weak protein–protein complexes by NMR residual dipolar couplings, *European Biophysics Journal 40*, 1371-1381.

226. Salmon, L., Ortega Roldan, J.-L., Lescop, E., Licinio, A., van Nuland, N., Jensen, M. R., and Blackledge, M. (2011) Structure, Dynamics, and Kinetics of Weak Protein–Protein Complexes from NMR Spin Relaxation Measurements of Titrated Solutions, *Angewandte Chemie International Edition 50*, 3755-3759.

227. Wang, Q., Zhuravleva, A., and Gierasch, L. M. (2011) Exploring Weak, Transient Protein–Protein Interactions in Crowded *in vivo* Environments by In-Cell Nuclear Magnetic Resonance Spectroscopy, *Biochemistry 50*, 9225-9236.

228. Seegar, T., and Barton, W. (2010) Imaging Protein-Protein Interactions *in vivo*, *Journal of Visualized Experiments 44*, e2149.

229. Benítez, J. J., Keller, A. M., and Chen, P. (2010) Nanovesicle Trapping for Studying Weak Protein Interactions by Single-Molecule FRET, *Methods in Enzymology 472*, 41-60.

230. Banham, J. E., Timmel, C. R., Abbott, R. J. M., Lea, S. M., and Jeschke, G. (2006) The Characterization of Weak Protein–Protein Interactions: Evidence from DEER for the Trimerization of a von Willebrand Factor A Domain in Solution, *Angewandte Chemie International Edition 45*, 1058-1061.

231. Truong, K., and Ikura, M. (2001) The use of FRET imaging microscopy to detect protein-protein interactions and protein conformational changes *in vivo*, *Current Opinion in Structural Biology 11*, 573-578.

232. Tessier, P. M., Jinkoji, J., Cheng, Y.-C., Prentice, J. L., and Lenhoff, A. M. (2008) Self-Interaction Nanoparticle Spectroscopy: A Nanoparticle-Based Protein Interaction Assay, *Journal of the American Chemical Society 130*, 3106-3112.

233. Bengali, A. N., and Tessier, P. M. (2009) Biospecific protein immobilization for rapid analysis of weak protein interactions using self-interaction nanoparticle spectroscopy, *Biotechnology and Bioengineering 104*, 240-250.

234. Barone, G., Sayers, Z., Svergun, D., and Koch, M. H. J. (1999) A synchrotron radiation X-ray scattering study of aqueous solutions of native DNA, *Journal of Synchrotron Radiation 6*, 1031-1034.

235. Zhang, F., Roosen-Runge, F., Skoda, M. W. A., Jacobs, R. M. J., Wolf, M., Callow, P., Frielinghaus, H., Pipich, V., Prevost, S., and Schreiber, F. (2012) Hydration and interactions in protein solutions containing concentrated electrolytes studied by small-angle scattering, *Physical Chemistry Chemical Physics 14*, 2483-2493.

236. Attri, A. K., and Minton, A. P. (2005) New methods for measuring macromolecular interactions in solution via static light scattering: basic methodology and application to nonassociating and self-associating proteins, *Analytical Biochemistry 337*, 103-110.

237. Some, D., Hitchner, E., and Ferullo, J. (2009) Characterizing Protein—Protein Interactions via Static Light Scattering: Nonspecific Interactions, *American Biotechnology Laboratory 27* 16-20.

238. Tessier, P. M., Vandrey, S. D., Berger, B. W., Pazhianur, R., Sandler, S. I. and Lenhoff, A. M. (2002) Self-interaction chromatography: a novel screening method for rational protein crystallization., *Acta Crystallographica Section D-Biological Crystallography 58*, 1531-1535.

239. Bloustine, J., Berejnov, V., and Fraden, S. (2003) Measurements of protein-protein interactions by size exclusion chromatography, *Biophysical Journal 85*, 2619-2623.

240. Wen, J., Arakawa, T., and Philo, J. S. (1996) Size-exclusion chromatography with on-line light-scattering, absorbance, and refractive index detectors for studying proteins and their interactions, *Analytical Biochemistry 240*, 155-166.

241. Bajaj, H., Sharma, V. K., and Kalonia, D. S. (2004) Determination of second virial coefficient of proteins using a dual-detector cell for simultaneous measurement of scattered light intensity and concentration in SEC-HPLC, *Biophysical Journal 87*, 4048-4055.

242. Winzor, D. J., and Wills, P. R. (2007) Characterization of weak protein dimerization by direct analysis of sedimentation equilibrium distributions: The INVEQ approach, *Analytical Biochemistry 368*, 168-177.

243. Tang, C., Iwahara, J., and Clore, G. M. (2006) Visualization of transient encounter complexes in protein-protein association, *Nature 444*, 383-386.

244. Tang, C., Ghirlando, R., and Clore, G. M. (2008) Visualization of Transient Ultra-Weak Protein Self-Association in Solution Using Paramagnetic Relaxation Enhancement, *Journal of the American Chemical Society 130*, 4048-4056.

245. Morell, M., Espargaró, A., Avilés, F. X., and Ventura, S. (2007) Detection of transient protein–protein interactions by bimolecular fluorescence complementation: The Abl-SH3 case, *Proteomics 7*, 1023-1036.

246. Zhang, H., Tang, X., Munske, G. R., Tolic, N., Anderson, G. A., and Bruce, J. E. (2009) Identification of Protein-Protein Interactions and Topologies in Living Cells with Chemical Cross-linking and Mass Spectrometry, *Molecular & Cellular Proteomics 8*, 409-420.

247. Sato, Y., Kameya, M., Arai, H., Ishii, M., and Igarashi, Y. (2011) Detecting weak protein–protein interactions by modified far-western blotting, *Journal of Bioscience and Bioengineering 112*, 304-307.

248. Dey, S., Pal, A., Chakrabarti, P., and Janin, J. (2010) The Subunit Interfaces of Weakly Associated Homodimeric Proteins, *Journal of Molecular Biology 398*, 146-160.

249. Veselovsky, A. V., Ivanov, Y. D., Ivanov, A. S., Archakov, A. I., Lewi, P., and Janssen, P. (2002) Protein-protein interactions: mechanisms and modification by drugs, *Journal of Molecular Recognition 15*, 405-422.

250. Nelson, D. L., and Cox, M. M. (2005) *Lehninger Principles of Biochemistry*, 4th ed., W.H. Freeman and Company, New York.

251. Fexby, S., and Bulow, L. (2004) Hydrophobic peptide tags as tools in bioseparation, *Trends in Biotechnology 22*, 511-516.

252. Murray, K. Y., Granner, D. K., Rodwell, V. W. (2006) *Harper's illustrated biochemistry*, 27th ed., McGraw Hill companies, Inc, New York.

253. Leckband, D. (2000) Measuring the forces that control protein interactions, *Annual Review of Biophysics and Biomolecular Structure 29*, 1-26.

254. Kumar, S., and Nussinov, R. (2002) Close-Range Electrostatic Interactions in Proteins, *ChemBioChem 3*, 604-617.

255. Jones, S., and Thornton, J. M. (1996) Principles of protein-protein interactions, *Proceedings of the National Academy of Sciences USA 93*, 13-20.

256. Melander, W., and Horvath, C. (1977) Salt effect on hydrophobic interactions in precipitation and chromatography of proteins: an interpretation of the lyotropic series, *Archives of Biochemistry and Biophysics 183*, 200-215.

257. Paliwal, A., Asthagiri, D., Abras, D., Lenhoff, A. M., and Paulaitis, M. E. (2005) Light-scattering studies of protein solutions: role of hydration in weak protein-protein interactions, *Biophysical Journal 89*, 1564-1573.

258. Teske, C. A., Blanch, H. W., and Prausnitz, J. M. (2004) Chromatographic measurement of interactions between unlike proteins, *Fluid Phase Equilibria 219*, 139-148.

259. Velev, O. D., Kaler, E. W., and Lenhoff, A. M. (1998) Protein interactions in solution characterized by light and neutron scattering: comparison of lysozyme and chymotrypsinogen, *Biophysical Journal 75*, 2682-2697.

260. Elcock, A. H., and McCammon, J. A. (2001) Calculation of weak protein-protein interactions: the pH dependence of the second virial coefficient, *Biophysical Journal 80*, 613-625.

261. Davydov, D. R., Kariakin, A. A., Petushkova, N. A., and Peterson, J. A. (2000) Association of cytochromes P450 with their reductases: opposite sign of the electrostatic interactions in P450BM-3 as compared with the microsomal 2B4 system, *Biochemistry 39*, 6489-6497.

262. Nisimoto, Y., and Edmondson, D. E. (1992) Effect of KCl on the interactions between NADPH:cytochrome P-450 reductase and either cytochrome *c*, cytochrome b_5 or cytochrome P-450 in octyl glucoside micelles, *European Journal of Biochemistry 204*, 1075-1082.

263. Voznesensky, A. I., and Schenkman, J. B. (1994) Quantitative analyses of electrostatic interactions between NADPH-cytochrome P450 reductase and cytochrome P450 enzymes, *Journal of Biological Chemistry 269*, 15724-15731.

264. Gao, Q., Doneanu, C. E., Shaffer, S. A., Adman, E. T., Goodlett, D. R., and Nelson, S. D. (2006) Identification of the Interactions between Cytochrome P450 2E1 and Cytochrome b_5 by Mass Spectrometry and Site-directed Mutagenesis, *Journal of Biological Chemistry 281*, 20404-20417.

265. Davydov, D. R. (2011) Microsomal monooxygenase as a multienzyme system: the role of P450-P450 interactions, *Expert Opinion on Drug Metabolism &Toxicology 7*, 543-558.

266. Dürr, U. H. N., Waskell, L., and Ramamoorthy, A. (2007) The cytochromes P450 and b5 and their reductases—Promising targets for structural studies by advanced solid-state NMR spectroscopy, *Biochimica et Biophysica Acta - Biomembranes 1768*, 3235-3259.

267. Fantuzzi, A., Meharenna, Y. T., Briscoe, P. B., Guerlesquin, F., Sadeghi, S. J., and Gilardi, G. (2009) Characterisation of the electron transfer and complex formation between

Flavodoxin from *D. vulgaris* and the haem domain of Cytochrome P450 BM3 from *B. megaterium, Biochimica et Biophysica Acta - Bioenergetics 1787*, 234-241.

268. Ellis, J., Gutierrez, A., Barsukov, I. L., Huang, W.-C., Grossmann, J. G., and Roberts, G. C. K. (2009) Domain Motion in Cytochrome P450 Reductase: Conformational equilibria revealed by NMR and small angle X-ray scattering, *Journal of Biological Chemistry 284*, 36628-36637.

269. Ivanov, A., Kopylov, A., Zgoda, V., Toropygin, I., Khryapova, E., and Ivanov, Y. (2009) Mass spectrometry identification of cytochrome P450 2B4 interaction sites for NADPH: Cytochrome P450 reductase, *Biochemistry (Moscow) Supplemental Series B: Biomedical Chemistry 3*, 361-371.

270. Bumpus, N. N., and Hollenberg, P. F. (2010) Cross-linking of human cytochrome P450 2B6 to NADPH-cytochrome P450 reductase: Identification of a potential site of interaction, *Journal of Inorganic Biochemistry 104*, 485-488.

271. Hu, G., Johnson, E. F., and Kemper, B. (2010) CYP2C8 Exists as a Dimer in Natural Membranes, *Drug Metabolism and Disposition 38*, 1976-1983.

272. Szczesna-Skorupa, E., Mallah, B., and Kemper, B. (2003) Fluorescence Resonance Energy Transfer Analysis of Cytochromes P450 2C2 and 2E1 Molecular Interactions in Living Cells, *Journal of Biological Chemistry 278*, 31269-31276.

273. Ozalp, C., Szczesna-Skorupa, E., and Kemper, B. (2005) Bimolecular Fluorescence Complementation Analysis of Cytochrome P450, 2C2, 2E1, and NADPH-Cytochrome P450 Reductase Molecular Interactions in Living Cells, *Drug Metabolism and Disposition 33*, 1382-1390.

274. Praporski, S., Ng, S. M., Nguyen, A. D., Corbin, C. J., Mechler, A., Zheng, J., Conley, A. J., and Martin, L. L. (2009) Organization of Cytochrome P450 Enzymes Involved in Sex Steroid Synthesis, *Journal of Biological Chemistry 284*, 33224-33232.

275. Hannemann, F., Rottmann, M., Schiffler, B., Zapp, J., and Bernhardt, R. (2001) The Loop Region Covering the Iron-Sulfur Cluster in Bovine Adrenodoxin Comprises a New Interaction Site for Redox Partners, *Journal of Biological Chemistry 276*, 1369-1375.

276. Omura, T., and Sato, R. (1964) The Carbon Monoxide-Binding Pigment of Liver Microsomes. II. Solubilization, Purification, and Properties, *Journal of Biological Chemistry 239*, 2379-2385.

277. Demeler, B. UltraScan version 9.9. A Comprehensive Data Analysis Software Package for Analytical Ultracentrifugation Experiments. The University of Texas Health Science Center at San Antonio, Department of Biochemistry. http:/www.ultrascan.uthscsa.edu.

278. Cao, W., and Demeler, B. (2005) Modeling analytical ultracentrifugation experiments with an adaptive space-time finite element solution of the Lamm equation, *Biophysical journal 89*, 1589-1602.

279. Vistica, J., Dam, J., Balbo, A., Yikilmaz, E., Mariuzza, R. A., Rouault, T. A., and Schuck, P. (2004) Sedimentation equilibrium analysis of protein interactions with global implicit mass conservation constraints and systematic noise decomposition, *Analytical Biochemistry 326*, 234-256.

280. Petoukhov, M. V., Konarev, P. V., Kikhney, A. G., and Svergun, D. I. (2007) ATSAS 2.1 – towards automated and web-supported small-angle scattering data analysis, *Journal of Applied Crystallography 40*, s223–s228.

281. Svergun, D. I. (1992) Determination of the regularization parameter in indirect-transform methods using perceptual criteria., *Journal of Applied Crystallography 25*, 495-503.

282. Svergun, D. I. (1999) Restoring low resolution structure of biological macromolecules from solution scattering using simulated annealing., *Biophysical Journal 76*, 2879-2886.

283. Volkov, V. V., and Svergun, D. I. (2003) Uniqueness of ab-initio shape determination in small-angle scattering., *Journal of Applied Crystallography 36*, 860-864.

284. Svergun, D. I., Barberato, C., and Koch, M. H. J. (1995) CRYSOL - a Program to Evaluate X-ray Solution Scattering of Biological Macromolecules from Atomic Coordinates., *Journal of Applied Crystallography 28*, 768-773.

285. Petoukhov, M. V., and Svergun, D. I. (2005) Global rigid body modelling of macromolecular complexes against small-angle scattering data., *Biophysical Journal 89*, 1237-1250.

286. Ortega, A., Amoros, D., and de laTorre, G. (2011) Prediction of hydrodynamic and other solution properties of rigid proteins from atomic- and residue-level models, *Biophysical Journal 101*, 892-898

287. Peterson, J. A., Ullrich, V., and Hildebra.Ag. (1971) Metyrapone Interaction with *Pseudomonas putida* Cytochrome P-450, *Archives of Biochemistry and Biophysics 145*, 531-542.

288. Zhao, J., Das, A., Schatz, G. C., Sligar, S. G., and Van Duyne, R. P. (2008) Resonance localized surface plasmon spectroscopy: Sensing substrate and inhibitor binding to cytochrome P450, *Journal of Physical Chemistry C 112*, 13084-13088.

289. Adak, S., Santolini, J., Tikunova, S., Wang, Q., Johnson, J. D., and Stuehr, D. J. (2001) Neuronal Nitric-oxide Synthase Mutant (Ser-1412 → Asp) Demonstrates Surprising Connections between Heme Reduction, NO Complex Formation, and Catalysis, *Journal of Biological Chemistry 276*, 1244-1252.

290. Aigrain, L., Fatemi, F., Frances, O., Lescop, E., and Truan, G. (2012) Dynamic Control of Electron Transfers in Diflavin Reductases, *International Journal of Molecular Sciences 13(11)*, 15012-15041.

291. Govindaraj, S., and Poulos, T. (1995) Role of the linker region connecting the reductase and heme domains in cytochrome P450BM-3., *Biochemistry. 34* 11221-11226.

292. Girvan, H. M., Heyes, D. J., Scrutton, N. S., and Munro, A. W. (2007) Laser photoexcitation of NAD(P)H induces reduction of P450 BM3 heme domain on the microsecond time scale, *Journal of the American Chemical Society 129*, 6647-6653.

293. TgK-Scientific. (2012) Stopped-Flow Technique; http://www.hi-techsci.com/techniques/stoppedflow, Bradford-on-Avon.

294. Noble, M. A., Turner, K. L., Chapman, S. K., and Munro, A. W. (1998) Mechanistic probes of flavocytochrome P-450 BM3, *Biochemical Society Transactions 26*.

295. Li, H. Y., Darwish, K., and Poulos, T. L. (1991) Characterization of Recombinant *Bacillus-megaterium* Cytochrome-P450BM-3 and its 2 Functional Domains, *Journal of Biological Chemistry 266*, 11909-11914.

296. Oster, T., Boddupalli, S. S., and Peterson, J. A. (1991) Expression, Purification, and Properties of the Flavoprotein Domain of Cytochrome-P-450BM-3 - Evidence for the Importance of the Amino-Terminal Region for FMN Binding, *Journal of Biological Chemistry 266*, 22718-22725.

297. Kelley, R. W., Reed, J. R., and Backes, W. L. (2005) Effects of ionic strength on the functional interactions between CYP2134 and CYP1A2, *Biochemistry 44*, 2632-2641.

298. Shen, S. J., and Strobel, H. W. (1992) The Role of Cytochrome-P450 Lysine Residues in the Interaction between Cytochrome-P450IA1 and NADPH-Cytochrome-P450 Reductase *Archives of Biochemistry and Biophysics 294*, 83-90.

299. Nadler, S. G., and Strobel, H. W. (1988) Role of electrostatic interactions in the reaction of NADPH-cytochrome P-450 reductase with cytochromes P-450, *Archives of Biochemistry and Biophysics 261*, 418-429.

300. Brewer, C. B., and Peterson, J. A. (1988) Single turnover kinetics of the reaction between oxycytochrome-P-450cam and reduced putidaredoxin, *Journal of Biological Chemistry 263*, 791-798.

301. Hintz, M. J., and Peterson, J. A. (1981) The Kinetics of Reduction of Cytochrome P-450cam by Reduced Putidaredoxin, *Journal of Biological Chemistry 256*, 6721-6728.

302.   Kimmich, N., Das, A., Sevrioukova, I., Meharenna, Y., Sligar, S. G., and Poulos, T. L. (2007) Electron Transfer between Cytochrome P450cin and Its FMN-containing Redox Partner, Cindoxin, *Journal of Biological Chemistry 282*, 27006-27011.

303.   Putnam, C. (2006) Protein Calculator v 3.3 (http://www.scripps.edu/~cdputnam/protcalc.html).

304.   Page, C. C., Moser, C. C., Chen, X. X., and Dutton, P. L. (1999) Natural engineering principles of electron tunnelling in biological oxidation-reduction, *Nature 402*, 47-52.

305.   Ekanem, I. S. (2007) Measurement of weak Protein-Protein Interactions, In *School of Chemical Engineering and Analytical Sciences*, University of Manchester, Manchester.

306.   Fulco, A. J. (1991) P450 BM-3 and other inducible bacterial P450 cytochromes: Biochemistry and Regulation, *Annual Review of Pharmacology and Toxicology 31*, 177-203.

307.   Jovanovic, T., and McDermott, A. E. (2005) Observation of Ligand Binding to Cytochrome P450 BM-3 by Means of Solid-State NMR Spectroscopy, *Journal of the American Chemical Society 127*, 13816-13821.

308.   Yu, C.-M., Mun, S., and Wang, N.-H. L. (2006) Theoretical analysis of the effects of reversible dimerization in size exclusion chromatography, *Journal of Chromatography A 1132*, 99–108.

309.   Schuck, P. (2000) Size distribution analysis of macromolecules by sedimentation velocity ultracentrifugation and Lamm equation modeling. , *Biophysical Journal 78*, 1606-1619.

310.   Hayes, D., Laue, T., and Philo, J. (1995) *Program Sednterp: Sedimentation Interpretation Program* Alliance Protein Laboratories, Thousand Oaks, CA.

311.   Some, D., and Kenrick, S. (2010) *Characterization of Protein-Protein Interactions via Static and Dynamic Light Scattering, Protein Interactions, Jianfeng Cai and Rongsheng E. Wang (Ed.), ISBN: 978-953-51-0244-1, InTech, Available from: http://www.intechopen.com/books/protein-interactions/characterization-of-protein-protein-interactions-via-static-and-dynamic-light-scattering*.

312.   Schaink, H. M., and Smit, J. A. M. (2000) Determination of the osmotic second virial coefficient and the dimerization of β-lactoglobulin in aqueous solutions with added salt at the isoelectric point, *Physical Chemistry Chemical Physics 2*, 1537-1541.

313.   Neal, B. L., and Lenhoff, A. M. (1995) Excluded Volume Contribution to the Osmotic Second Virial Coefficient for Proteins, *AIChE Journal 41*, 1010-1014.

314.   Le Brun, V., Friess, W., Bassarab, S., Mühlau, D., and Garidel, P. (2010) A critical evaluation of self-interaction chromatography as a predictive tool for the assessment of protein–protein interactions in protein formulation development: A case study of a therapeutic monoclonal antibody, *European Journal of Pharmaceutics and Biopharmaceutics 75*, 16-25.

315.   Svergun, D. I., and Koch, M. H. J. (2003) Small-angle scattering studies of biological macromolecules in solution, *Reports on Progress in Physics 66* 1735–1782.

316.   Mertens, H. D. T., and Svergun, D. I. (2010) Structural characterization of proteins and complexes using small-angle X-ray solution scattering, *Journal of Structural Biology 172*, 128–141.

317.   Kozin, M., and Svergun, D. I. (2001) Automated matching of high- and low-resolution structural models, *Journal of Applied Crystallography 34*, 33-41.

318.   Schrödinger, L. L. C. The PyMOL Molecular Graphics System, Version 1.5.0.4

319.   Putnam, C. D., Hammel, M., Hura, G. L., and Tainer, J. A. (2007) X-ray solution scattering (SAXS) combined with crystallography and computation: defining accuratemacromolecular structures, conformations and assemblies in solution, *Quarterly Reviews of Biophysics 40*, 191-285.

320. Byron, O. (1997) Construction of Hydrodynamic Bead Models from High-Resolution X-Ray Crystallographic or Nuclear Magnetic Resonance Data, *Biophysical Journal 72*, 408-415.

321. García de la Torre, J., Huertas, M. L., and Carrasco, B. (2000) Calculation of Hydrodynamic Properties of Globular Proteins from Their Atomic-Level Structure, *Biophysical journal 78*, 719-730.

322. Carrasco, B., and García de la Torre, J. (1999) Hydrodynamic Properties of Rigid Particles: Comparison of Different Modeling and Computational Procedures, *Biophysical journal 76*, 3044-3057.

323. Brookes, E., Demeler, B., Rosana, C., and Rocco, M. (2010) The implementation of SOMO (SOlution MOdeller) in the UltraScan analytical ultracentrifugation data analysis suite: enhanced capabilities allow the reliable hydrodynamic modeling of virtually any kind of biomacromolecule, *European Biophysics Journal 39*, 423-435.

324. Lamb, D. C., Kim, Y., Yermalitskaya, L. V., Yermalitsky, V. N., Lepesheva, G. I., Kelly, S. L., Waterman, M. R., and Podust, L. M. (2006) A Second FMN Binding Site in Yeast NADPH-Cytochrome P450 Reductase Suggests a Mechanism of Electron Transfer by Diflavin Reductases, *Structure 14*, 51-61.

325. Aigrain, L., Pompon, D., More´ra, S., and Truan, G. (2009) Structure of the open conformation of a functional chimeric NADPH cytochrome P450 reductase, *EMBO reports 10(7)*, 742-747.

326. Hamdane, D., Xia, C., Im, S.-C., Zhang, H., Kim, J.-J. P., and Waskell, L. (2009) Structure and Function of an NADPH-Cytochrome P450 Oxidoreductase in an Open Conformation Capable of Reducing Cytochrome P450, *Journal of Biological Chemistry 284*, 11374-11384.

327. Ouano, A. C., and Kaye, W. (1974) Gel-permeation chromatography: X. Molecular weight detection by low-angle laser light scattering, *Journal of Polymer Science: Polymer Chemistry Edition 12*, 1151-1162.

328. Ralston, G. (1993) *Introduction to Analytical Ultracentrifugation*, Beckman Instruments, Fullerton, CA.

329. Howlett, G., Minton, A., and Rivas, G. (2006) Analytical ultracentrifugation for the study of protein association and assembly, *Current Opinion in Chemical Biology 10*, 430-436.

330. Stockmayer, W. H. (1950) Light Scattering in multicomponent systems, *Journal of Chemical Physics 18*, 58-61.

331. Migneault, I., Dartiguenave, C., Bertrand, M. J., and Waldron, K., C. (2004) Glutaraldehyde: behavior in aqueous solution, reaction with proteins, and application to enzyme crosslinking, *BioTechniques 37*, 790-802.

332. Sinz, A. (2003) Chemical cross-linking and mass spectrometry for mapping three-dimensional structures of proteins and protein complexes, *Journal of Mass Spectrometry 38*, 1225-1237.

333. Allan, D. A., Villarda, F., and Marsh, M. (2007) An automated microseed matrix-screening method for protein crystallization, *Acta Crystallographica Section D D63*, 550-554.

334. Lipfert, J., and Doniach, S. (2007) Small-Angle X-Ray Scattering from RNA, Proteins, and Protein Complexes, *Annual Review of Biophysics and Biomolecular Structure 36*, 307-327.

335. Konarev, P. V., Kikhney, A. G., Franke, D., Petoukhov, M. V., and Svergun, D. I. (2007) Automated SAXS Data Processing on the X33 Beamline, *HASY LAB Annual Report Part II*, 339–340.

336. Bernado, P. (2010) Effect of interdomain dynamics on the structure determination of modular proteins by small-angle scattering, *European Biophysics Journal 39*, 769-780.

337.   Fischer, H., Neto, M. d. O., Napolitano, H. B., Polikarpov, I., and Craievich, A. F. (2010) Determination of the molecular weight of proteins in solution from a single small-angle X-ray scattering measurement on a relative scale, *Journal of Applied Crystallography 43*, 101-109.

338.   Konarev, P. V., Volkov, V. V., Sokolova, A. V., Koch, M. H. J., and Svergun, D. I. (2003) PRIMUS - a Windows-PC based system for small-angle scattering data analysis, *Journal of Applied Crystallography 36*, 1277-1282.

APPENDICES

APPENDIX A: THEORIES AND PRINCIPLES OF SEC-MALLS

Size exclusion chromatography (SEC) is one of the most reliable techniques for macromolecular molecular weight determination. The approach is used to separate molecules on the basis of their hydrodynamic volume (or size), which, in turn, depends on the chemical composition of the molecule and the interaction with the solvent. In earlier measurements, a calibration curve (containing retention times of molecules with known molecular weights) was constructed on the assumption that samples with the same hydrodynamic volume will have the same elution volume. This implies that the molecular weight measurement is proportional to the hydrodynamic volume; as the calibration curve reflects the molecular size and not the molecular weight, it is pertinent to know that polymers with the same hydrodynamic volume do not necessarily have the same molecular weight. Thus, the molecular weights obtained from this technique are only an approximation.

With technological advancements, the combination of SEC with light scattering has replaced the use of calibration curves, providing rapid and accurate molecular weight determinations (*327*). In recent developments, the system has been expanded to include the use of SEC with on-line multi-angle laser light scattering (MALLS) and quasi-elastic light scattering (QELS) which not only provides information on the molecular weight distribution (polydispersity index; PDI) of the molecule but also its size and shape (hydrodynamic radius; r_H). PDI is a measure of the molecular weight distribution in a given sample solution, which is given as the ratio of the weight average molecular weight (M_w) to the number average molecular weight (M_n).

$$PDI = \frac{M_W}{M_n}$$

Equation A1

MALLS is a form of static light scattering (see appendix C) where the intensities of light scattered at different angles are used in conjunction with the refractive index of the solvent and the refractive index increments of the macromolecule (both measured using a differential refractometer) to estimate the weight average molecular weight of the biopolymer. On the other hand, QELS is used to study the hydrodynamic properties of the macromolecule in real time. QELS is used to measure the particle diffusion coefficient, which provides a measure of the hydrodynamic size. The diffusion coefficient is a measure of intra-particle interactions and is dependent on particle size, shape and flexibility.

The diffusion coefficient (D) is inversely proportional to the hydrodynamic radius (R_H) according to the Stokes-Einstein equation.

$$D = \frac{\kappa_B T}{f} = \frac{\kappa_B T}{6\pi\eta R_H}$$

Equation A2

where k_B is the Boltzmann constant, T is the temperature, η is the viscosity of the solvent and f is the frictional coefficient given by

$$f = 6\pi\eta R_H$$

Equation A3

R_H is the radius of a hypothetical hard sphere with the same diffusion rate to the protein under study. However, most proteins are non-spherical, dynamic and hydrated by water molecules in solution. As a result, the measurement corresponds to the hydrodynamic size of the protein, but not necessarily the true physical size of the protein,.

APPENDIX B: THEORIES AND PRINCIPLES OF AUC

Having been around for over eight decades now, it is no surprise that there is a vast amount of available reviews and publications on both practical and theoretical aspects of analytical ultracentrifugation (AUC). AUC is a classical method for the characterization of macromolecules and their interactions in solutions. Interpretation of data obtained from AUC does not require the use of any standards, references or assumptions, and is hence one of the most accurate and absolute means of determining biophysical properties of proteins in solution, such as the size and the molecular weight. AUC is governed by the principles of equilibrium (ie. sedimentation equilibrium mode) and non-equilibrium (sedimentation velocity mode) thermodynamics, where all the required parameters can be determined experimentally. AUC is also versatile in the sense that a lot of information can be obtained from a single run at very low protein concentration. The downside is that long run times are required. Here, the principles and applications of AUC are highlighted, but detailed information can be obtained from excellent reviews available in the literature (*328, 329*).

AUC is used to separate macromolecules in solution by sedimentation at a relatively high rotor speed. There is a large wealth of detailed structural information available by AUC. Some of these include
   ❖ Verification of sample heterogeneity in solution by a single experiment
   ❖ Accurate determination of molecular weight over a wide range (from hundreds to millions of mass units)
   ❖ Elucidation of the oligomeric states of macromolecules in solution
   ❖ The stoichiometry of single or multiple protein-protein or protein-ligand complexes
   ❖ Hydrodynamic size and shape of molecules in solution
   ❖ Detailed analysis of associating systems, including association states and equilibrium rates for reversibly interacting systems
   ❖ Hydrodynamic size distributions and their dependence on various solvent and binding conditions
   ❖ Detection of solution non-ideality and protein conformational changes

Depending on the solution behaviour and nature of the macromolecular association, two methods are available for characterizing macromolecular behaviour using AUC. In both cases, an initially uniform sample is centrifuged at a high angular velocity, causing gradual sedimentation of the solute to the bottom of the cell. AUC experiments are used to measure the concentration distribution formed in this process, which can be detected using a suitable optical system such as absorbance, refractive index, interference, or fluorescence. Sedimentation Velocity (SV) is used to determine static associations, which are slowly reversible or irreversible during the course of the experiment, and provides information on solution heterogeneity in terms of hydrodynamic size and shape. On the other hand, rapidly reversible interactions can be characterized using Sedimentation Equilibrium (SE). SE is used to determine macromolecular oligomeric states and binding stoichiometries as well as dissociation constants.

In the SV method, a high centrifugal force is applied to an initially uniform solution placed in a cell by spinning at a high angular velocity with rotor speeds of 40,000 to 60,000 rpm. The applied field causes rapid depletion of macromolecules at the meniscus forming a concentration boundary as the solute moves away from the centre of the rotor towards the bottom of the cell as a function of time. The rate at which this boundary

moves is obtained by measuring the concentration of the sample at various positions in the cell (radial distributions) and at different intervals during the course of the experiment. , The sedimentation and diffusion coefficients can be obtained from the motion and shape of the boundary.

The sedimentation coefficient, *s,* is directly proportional to the effective or buoyant mass (M_b) and inversely proportional to the frictional coefficient (*f*) of the particle (equation A4).

$$s = \frac{v}{\omega^2 r} = \frac{M_b}{f}$$

Equation A4

where *v* is the particle velocity, ω is the rotor speed and *r* is the distance of particle from the centre of the rotor. The frictional coefficient of a molecule (defined by Equation A3) is a function of the particle size and shape as described by the Stokes relationship (equation A2) and is larger for aspherical versus spherical shapes of the same molecular weight (*328*).

The translational frictional ratio (*f/f₀*) provides information on the shape of a macromolecule. This term is defined as the ratio of the measured frictional coefficient (*f*) of the macromolecule to that of a rigid sphere (*f₀*) of the same molecular weight and specific volume. This ratio is usually about 1.2 for globular particles and increases with asymmetry and expansion to about 3.1 for rod-like particles (*328*). Consider a slightly unfolded protein (A) or an elongated protein of the same molecular weight with a perfectly globular protein (B). Protein A will experience a greater hydrodynamic friction than B and hence will have a higher value of *f*. This implies that Protein A will have a higher sedimentation coefficient and a smaller translational frictional ratio than B.

In SE experiments, the sample is spun at lower rotor speeds compared to that needed for SV experiments. The lower centrifugal field creates a concentration gradient as the solute sediments away from the centre of the rotor towards the bottom of the cell. The sedimentation velocity is opposed by solute diffusion back up the cell in the direction of decreasing concentration. At equilibrium, there is a balance between sedimentation and diffusion so that the concentration distribution is invariant with time. The equilibrium solute concentration is measured as a function of radial position using a suitable optical technique. If the sample obeys the Beer-Lambert law across the full range of concentration, then optical absorbance is the preferred detection technique.

In SE equilibrium, concentration distribution is independent of the size and shape, but entirely dependent on the buoyant molecular mass of the molecule (M_b), the angular velocity (ω) and temperature. Thus, SE is a good technique for determining protein molecular weight. Furthermore, SE can be used for the analysis of weak protein-protein interactions, which is the focus of this study.

Sedimentation Velocity Data Analysis

Three different forces act on a molecule suspended in a particular solvent within a gravitational field. The force on the particle due to the gravitational field (F_g) is opposed by the buoyancy force generated from replacing the solvent as the molecule sediments (F_b) and the frictional force resulting from the movement of the molecule through the solvent (F_f). The equations describing the forces are:

$$F_g = M_p \omega^2 r$$
Equation A5

$$F_b = -M_s \omega^2 r$$
Equation A6

$$F_f = -fv$$
Equation A7

where M_p is the mass of the particle, M_s is the mass of the solvent displaced by the particle, ω is the rotor speed in radians per unit time, r is the particle distance from the rotational axis, f is the frictional coefficient and v is the particle velocity.

Because a terminal velocity is reached almost instantaneously, there is no net force on the particle

$$F_g + F_b + F_f = 0$$
Equation A8

Substituting into Equations A5 to A7 gives

$$M_p \omega^2 r - M_s \omega^2 r - fv = 0$$
Equation A9

$$(M_p - M_s)\omega^2 r - fv = 0$$
Equation A10

The term $\left(M_p - M_s\right)$ represents the buoyant mass of the particle, M_b.

But the mass of the displaced solvent can also be defined as a product of the mass of the particle (M_p), the partial specific volume of particle ($\bar{v}$ in volume/mass) and the mass density (ρ) of the solvent.

$$M_s = M_p \bar{v} \rho$$
Equation A11

Thus the effective mass of particle M_b can be reduced to

$$M_b = M_p - M_s = M_p - M_p \bar{v} \rho = M_p (1 - \bar{v} \rho)$$
Equation A12

Substituting Equation A12 into Equation A10 gives

$$M_b \omega^2 r - fv = M_p \omega^2 r(1 - \bar{v}\rho) - fv = 0$$
Equation A13

Rearranging the equation produces a relationship that defines the sedimentation coefficient *s* by:

$$s = \frac{v}{w^2 r} = \frac{M_b}{f}$$
Equation A14

where *s* is usually reported in Svedberg units (S), where S is equal to 10^{-13} seconds.

The frictional coefficient is, however calculated using equation A3

Most compact proteins can be approximated as spheres in which case R_H can be related to the protein volume and molecular weight by:

$$R = \left(\frac{3M_p \bar{v}}{4\pi N_a} \right)^{\frac{1}{3}}$$
Equation A15

Equations A12, A14, A3 and A15 can be combined to give

$$s = \frac{M_p (1 - \bar{v}\rho)}{6\pi\eta \left(\dfrac{3M_p \bar{v}}{4\pi N_a} \right)^{\frac{1}{3}}}$$
Equation A16

This equation shows how first principle sedimentation coefficient, and hence molecular masses, can be obtained from sedimentation velocity runs. The viscosity and density of the solution can easily be calculated, while the partial specific volume and mass of the particle (an enzyme and its domains for studies in this thesis) can be estimated from the amino acid sequence of the protein.

The Lamm equation (A17) is often used to fit the radial concentration profile by solving the differential mole balance equation given by

$$\frac{\partial c}{\partial t} = D\left[\frac{\partial^2 c}{\partial r^2} + \frac{1}{r}\frac{\partial c}{\partial r} \right] - s\omega^2 \left[r\frac{\partial c}{\partial r} + 2c \right]$$
Equation A17

where *c* is the concentration of macromolecular species and *t* is the time. Two different programs have been developed for rapid modelling and interpretation of such data. In this study, SEDFIT was used to fit the measured concentration distributions to the Lamm equations in order to extract the values for *D* and *s*. Further modelling to determine other required parameters (such as frictional ratio) was done using the

SEDNTERP software. It is important to note that a correction for the experimentally determined *s*-value to the standard state of water at 20°C ($s_{20,\text{w}}$) is required for comparison purposes. This can easily be performed using the SEDNTERP software.

Sedimentation Equilibrium Data Analysis

While analysis of SV data involves the use of hydrodynamics, SE requires thermodynamic knowledge and applications. In most cases, the optical detection system used for measuring the concentration distribution during the SE experiment is the absorbance. Here, the measured absorbance as a function of radial position for a solution containing a mixture of ideal non-interacting species (*n*) is given as

$$a(r) = \sum_n c_{n,0}\varepsilon_n l \ \exp\left[\frac{M_n(1-\bar{v}_n\rho)\omega^2}{2RT}(r^2 - r_0^2)\right] + \delta$$

Equation A18

where $c_{n,0}$ is the concentration of species *n* at an arbitrary reference position r_0, ε_n is the extinction coefficient and M_n is the molar mass of species *n*, *l* is the path length, $\bar{v}$ is the partial specific volume, ω is the rotor speed in radians per second, ρ is the solvent density, *r* is the particle distance from the rotational axis, *R* is the universal gas constant, *T* is the absolute temperature, and δ is the baseline offset.

For a single ideal non-interacting system, the above equation can be reduced to an equilibrium radial concentration gradient *c(r)* as follows

$$c(r) = c_0 \exp\left[\frac{M(1-\bar{v}\rho)\omega^2}{RT}\left(\frac{r^2 - r_0^2}{2}\right)\right] = c_0 \exp\left[\frac{M_b\omega^2}{RT}\left(\frac{r^2 - r_0^2}{2}\right)\right]$$

Equation A19

To estimate the molecular weight of the species, the above equation can be converted to a linear form where the concentration of every species [*c(r)*] varies exponentially with r^2 as a function of the reduced molecular weight of the species (σ), which is the slope of the graph as shown:

$$\frac{\ln(c_r)}{r^2} = \sigma = \frac{M_b\omega^2}{2RT}$$

Equation A20

This is a traditional way of estimating the molecular weight of a single species in solution. More recently, however, a couple of non-linear least squares fitting programs have been developed which enable direct fitting of multiple experimental data sets for molar mass determinations (global fitting). As the process is highly dependent on the concentration of the solute, accurate determination of concentration is required.

Self-Association

Least square methods are also used to get best estimates of association parameters by directly fitting the primary experimental data to proposed models that describe the association. The simplest model with the best residual fit is always selected.

Equation A18 can be expanded to obtain a model equation that describes the monomer-n-mer equilibrium for a self-association system as follows:

$$c(r) = c_{monomer,0}\, \exp\left[\frac{M_b\omega^2}{RT}\left(\frac{r^2 - r_0^2}{2}\right)\right] + c_{n-mer,0}\, \exp n\left[\frac{M_b\omega^2}{RT}\left(\frac{r^2 - r_0^2}{2}\right)\right]$$

Equation A21

The integer n describes the stoichiometry for the various species.

For ease of derivation, equation A21 can be reduced to

$$c(r) = c_{1,0}\, \exp\{X\} + c_{n-mer,0}\, \exp\{nX\}$$

Equation A22

where $c_{1,0}$ equals monomer concentration at position r_0 and $X = \left[\frac{M_b\omega^2}{RT}\left(\frac{r^2 - r_0^2}{2}\right)\right]$

The association constant for a monomer-n-mer equilibrium reaction is given as

$$K_a = \frac{c_{n-mer}}{(c_1)^n}$$

Equation A23

Substituting equation A23 in A21 gives a model to solve directly for K_a and eliminating the $c_{n\text{-mer}}$ term:

$$c(r) = c_{1,0}\, \exp\{X\} + K_a(c_{1,0})^n\, \exp\{nX\}$$

Equation A24

Rearranging the equation constrains the $c_{1,0}$ and K_a terms to positive numbers:

$$c(r) = \exp\left(\ln\{c_{1,0}\} + \{X\}\right) + \exp\left(n\left[\ln\{c_{1,0}\}\right] + \ln\{k_a\} + \{nX\}\right)$$

Equation A25

Models can be derived that describe the equilibrium distribution of up to four interacting species:

$$c(r) = \begin{array}{l} c_{1,0}\, \exp\{X\} \\[4pt] + (c_{1,0})^{n_2} K_{a,2}\, \exp\{n_2 X\} \\[4pt] + (c_{1,0})^{n_3} K_{a,3}\, \exp\{n_3 X\} \\[4pt] + (c_{1,0})^{n_4} K_{a,4}\, \exp\{n_4 X\} + \delta \end{array}$$

Equation A26

where n_2, n_3, and n_4 are stoichiometries of species 2, 3 and 4; $K_{a,2}$, $K_{a,3}$, and $K_{a,4}$ are association constants for the monomer-n-mer equilibrium of species 2, 3 and 4; δ is the baseline offset.

Non-Ideality

Non-ideality basically describes deviations arising from various conditions such as charge or macromolecular crowding. This factor can be accounted for in models describing interacting systems by the addition of the second virial coefficient term, B_{22}:

$$c(r) = \begin{aligned} &c_{1,0} \exp\{X - B_{22}M(c_r - c_0)\} \\ &+ (c_{1,0})^{n_2} K_{a,2} \exp\{n_2 X - B_{22}M(c_r - c_0)\} \\ &+ (c_{1,0})^{n_3} K_{a,3} \exp\{n_3 X - B_{22}M(c_r - c_0)\} \\ &+ (c_{1,0})^{n_4} K_{a,4} \exp\{n_4 X - B_{22}M(c_r - c_0)\} + \delta \end{aligned}$$

Equation A27

The goal of the fitting process is to find the simplest model that describes the data: each set of data was initially fitted using a single ideal species model followed by fitting using equations describing increasingly complex reversible association schemes.

APPENDIX C: THEORIES AND PRINCIPLES OF SLS

Light Scattering is a biophysical technique that has proven to be one of the most powerful techniques for understanding structure and dynamics of biomacromolecules, and has now been in use for many decades. Using lasers over conventional light sources has led to increased development of high-throughput light scattering techniques not only for understanding macromolecules, but also for assessing their interactions. Light scattering can be applied in chromatography mode (See appendix A) or in batch mode, as discussed here and in the following section.

In classical (also known as static) light scattering, the dependence of the intensity of average scattered light on the scattering angle and protein concentration provides information on the mass, shape, composition, structure, aggregation, and interparticle interactions of biopolymers. On the other hand, dynamic light scattering [commonly known as photon correlation spectroscopy (PCS) or quasi-elastic light scattering (QELS)] measures the temporal correlations of the scattered light to produce spectral information from which the rate of diffusion of the protein particles can be estimated. The use of static light scattering to assess weak PPIs is discussed in this section.

When incident light hits a solution containing macromolecules, the light is scattered in all directions. The intensity of the scattered light is dependent on the solute molecular weight as well as the size. Thus, static light scattering is used to measure the root mean square radius (from the angular dependence of the scattered light), molecular weight, and osmotic second virial coefficient of the macromolecules.

Static light scattering theory was proposed by Lord Rayleigh and further developed by Stockmayer (*330*) as described by the equation

$$\frac{K°c}{\overline{R_\theta}} = \frac{1}{M} + 2B_{22}c$$
Equation A28

where c represents the protein concentration, M is the average molecular weight of the protein, B_{22} is the osmotic second virial coefficient, $\overline{R_\theta}$ is the excess Rayleigh ratio given as ($R_{\theta,sample}$ - $R_{\theta,solvent}$) and $K°$ is an optical constant. The above equation only applies when the particle size is less than $1/20^{th}$ the wavelength of the incident light in which case the angular dependence of the scattered light is negligible (note in this case the root mean square radius cannot be estimated from light scattering).

The osmotic second virial coefficient (B_{22}) is an average measure of the protein-protein interaction, and reflects the deviation of an aqueous solution from ideality. B22 is referred to as the protein pair potential of mean force (*W*), a sum of all the non-covalent forces that govern the weak protein-protein interaction. Equation A29 relates B_{22} to *W* averaged over the relative positions and the orientations of the protein molecules.

$$B_{22} = -2\pi \int_0^\infty (e^{-W(r)/\kappa_B T} - 1)r^2 dr$$

Equation A29

where *W(r)* describes the *pmf*, which is the work required to bring a pair of protein molecules from infinite separation to a fixed configuration in the solution, and *r* defines the protein centre-centre separation distance.

The Rayleigh ratio is normalized using the intensity of scattered light as a function of angle, and is given as:

$$R_\theta = \frac{I_\theta r^2}{I_\theta V}$$

Equation A30

where I_θ is the scattered intensity, I_0 is the incident intensity, V is the volume of the scattering medium, and r is the distance between the scattering volume and the detector.

R_θ is calculated using a calibration factor (A_{CSCC}) that represents proportionality between R_θ and I_θ, and proportionality between the detector voltages and the light intensity at 90°, according to equation A30.

$$R_{90} = A_{CSCC}\left(\frac{V_{90} - V_{90,dark}}{V_{laser} - V_{laser,dark}}\right)$$

Equation A31

where V_{laser} and V_{90} are the laser monitor signal and the detector signal voltage at 90°, respectively, and $V_{laser,dark}$ and $V_{90,dark}$ represent the laser monitor signal and the detector signal voltage at 90° when the laser is turned off. A_{CSCC} is a single configuration specific calibration constant that is dependent on the refractive indices of solvent (n_s) and cell (n_g) type (Equation A32).

$$A_{CSCC} = A_{inst}\left(\frac{n_s n_g}{F}\right)$$

Equation A32

where A_{inst} is the instrument constant and F is known as the Fresnel factor given by the equation

$$F = \left[1 - \left(\frac{n_g - n_s}{n_g + n_s}\right)^2\right]^2\left[1 - \left(\frac{n_g - 1}{n_g + 1}\right)^2\right]$$

Equation A33

The excess Rayleigh ratio equation is

$$\overline{R_\theta} = R_{\theta,sample} - R_{\theta,solvent}$$

Equation A34

Equation A31 can be substituted into equation A34 to give an expression for the Rayleigh ratio at a detector angle of 90° (equation A35).

$$\overline{R_\theta} = A_{CSCC} \left(\frac{V_{90,sample} - V_{90,solvent}}{V_{laser} - V_{laser,dark}} \right)$$

Equation A35

When working with coloured solutions, it is important to account for the intensity drop (since the coloured solutions will absorb a certain amount of light). This intensity drop is reflected in the forward monitor signal and, using Beer's Absorption Law, the drop can be calculated (equation A36)

$$I_{(x)} = I_0 e^{(-aL)}$$

Equation A36

where, $I_{(x)}$ is the intensity after passing through the sample, I_0 is the incident intensity, L is the path length and a is the molar absorptivity. Thus, the intensity drop at the end and centre of the flow cell are

$$\frac{I_{(end)}}{I_0} = \frac{I_L}{I_0} = e^{(-aL)}$$

Equation A37

and

$$\frac{I_{center}}{I_0} = \frac{I_{(L/2)}}{I_0} = e^{(-a\frac{L}{2})} = \sqrt{e^{-aL}}$$

Equation A38

As shown in equation A31, a proportionality is found between the detector voltages and light intensities, since these intensities cannot be measured directly from the experiment (equation A41)

$$\frac{V_1}{V_0} = \frac{I_{end}}{I_0} = e^{(-aL)}$$

Equation A39

where V_0 is the forward monitor voltage at the baseline of the buffer used, and V_1 is the forward monitor voltage of the samples.

Combining equations A38 and A39, the intensity drop at the centre of the flow cell is equal to

$$\frac{I_{centre}}{I_0} = \sqrt{\frac{V_1}{V_0}}$$

Equation A40

APPENDIX D: THEORIES AND PRINCIPLES OF CG-MALLS

In the previous section, light scattering was discussed with reference to measurement of root mean square radius, weight average molecular weights, and second osmotic virial coefficient. With recent advances in technology, light scattering has been introduced to the study of reversible associations in macromolecules (i.e. specific protein-protein interactions) (*236*). The composition multi-angle laser light scattering (CG-MALLS) technique can be used to fit light scattering and concentration data to various association models by means of non-linear least-squares fitting programmes (*311*). These programmes can be used to fit data to dissociation constants to quantify reversible protein association and to virial coefficients which reflect non-specific protein-protein interactions as discussed in the previous section (*311*).

In this thesis, various association models have been employed to describe the behaviour for the BM3 systems, and a dimerization model can be used to describe the data which is also consistent with the findings from SE. Thus, the discussion below is limited to fitting light scattering data to a dimerization model. The light scattering equation is given by

$$\frac{Kc_t}{R_\theta} = \frac{1}{M_w} + 2B_{avg}c_t$$
Equation A41

where K is the light scattering constant, M_w is the weight average molecular weight defined by

$$M_w = \Sigma_i w_i M_i = \Sigma_i w_{i,irrev} + w_m M_m + w_d M_d$$
Equation A42

where the sum is over all different sized aggregates (monomers, dimers, and higher oligomers), w_i is the mass fraction of the ith sized aggregate with molecular weight given by M_i. Here, the sum includes the presence of a small fraction of higher molecular weight aggregates, which have been assumed to be formed irreversibly. As such, they occur at a constant mass fraction independent of total protein concentration, and a constant fitting parameter $I = \Sigma_i w_{i,irrev} M_{i,irrev}$ is defined. In addition, the light scattering depends on an osmotic virial coefficient which is averaged over all types of interactions involving monomers and dimers:

$$B_{avg} = \frac{1}{M_w^2}\Sigma_i\Sigma_j M_i M_j w_i w_j B_{ij} = \frac{M_d^2}{M_w^2}w_d^2 B_{dd} + \frac{M_m M_d}{M_w^2}w_d^2 B_{md}$$
Equation A43

Here, the contribution to the average from the monomer-monomer non-specific interactions as characterized in terms of B_{mm} has been assumed to be negligible, in which case we are assuming that the interactions that lead to the dimerization are much stronger than the non-specific interactions between the monomers. In this case, the contribution to the light scattering from the B_{mm} term is very small relative to how quickly the molecular weight changes due to the monomer-dimer equilibrium. In

addition, the interactions between the high molecular weight irreversibly formed aggregates have been neglected because they occur at a much smaller mass fraction than the dimers. As a first approximation, the interactions that occur between a monomer and a dimer have also been neglected and the value of B_{md} has been set to zero. If the data are not fitted well by this model, then the first change will be to include B_{md} in the fitting procedure.

The dissociation constant K_d is defined by the monomer-monomer equilibrium to form the dimer. As mentioned above, the parameters K_d, B_{dd} and I will be fitted to the experimental data measured as a function of protein concentration c_t. Thus the light scattering equation (A41) will be re-written as a function of only the protein concentration (c_t), the fitting parameters (K_d, B_{dd} and I), and the constants M_m and M_d, according to equation A44:

$$\frac{Kc_t}{R_\theta} = \frac{1}{M_w(c_t, K_d, I)} + \frac{M_d^2}{M_w^2(c_t, K_d, I)} w_d^2(c_t, K_d) B_{dd} c_t$$

Equation A44

where $M_w(c_t, K_d, I) = I + w_m(c_t, K_d)M_m + w_d(c_t, K_d)M_d$
Equation A45

The monomer-dimer equilibrium can be used to express the mass fractions w_m and w_d in terms of c_t and the dissociation constant, K_d,

$$K_d = \frac{\rho_m^2}{\rho_d} = \frac{(^{c_m}/_{M_m})^2}{^{c_d}/_{M_d}} \frac{c_t^2}{c_t^2} = \frac{w_m^2 M_d}{w_d M_m^2} c_t$$

Equation A46

where ρ_m and ρ_d are the molar concentrations of monomer and dimer, respectively. Conservation of mass also implies that $1 = w_d + w_m$ (assuming that the mass fraction of irreversibly formed aggregates is small). Substituting $w_m = 1 - w_d$ into equation A48 and solving for w_d gives the desired expression

$$w_d = 1 + \frac{K_d M_m^2}{2c_t M_d} - \sqrt{\frac{K_d M_m^2}{c_t M_d}\left(1 + \frac{K_d M_m^2}{4c_t M_d}\right)}$$

Equation A47

Equation A47 was substituted into equation A44 to provide a relation between the measured light scattering data Kc_t / R_θ and the fitting parameters, K_d, B_{dd} and I, and protein concentration, c_t.

APPENDIX E: MECHANISM OF ACTIONS OF CROSS-LINKERS USED IN THIS STUDY

Formaldehyde: Formaldehyde is a homobifunctional cross-linker that targets the amine groups of proteins. A methylene bridge is usually formed at the end of the reaction as shown in the scheme below:

$$HCHO + NH_2\text{-}Protein^A \xleftrightarrow{\quad H_2O \quad} Protein^A\text{-}N\text{-}CH_2 + NH_2\text{-}Protein^B \longleftrightarrow \begin{matrix} Protein^A\text{-}NH \\ Protein^B\text{-}NH \end{matrix} \Big\rangle CH_2$$

Formaldehyde   **Cross-linked Product**
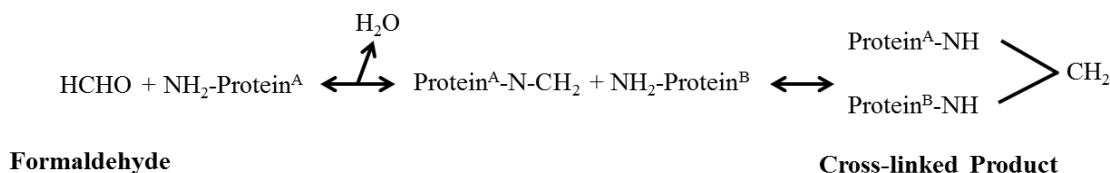
Glutaraldehyde: The mechanism of glutaraldehyde cross linking is similar to that of formaldehyde, but the cross-linking process is not as simple as that of formaldehyde considering that glutaraldehyde has two aldehyde groups as opposed to a single aldehyde group on formaldehyde. Glutaraldehyde is also a homobifunctional cross-linker, but has been shown to target other side groups on proteins besides amines (such as thiols and phenols; (*331*)). The simplest reaction mechanism is as shown in the scheme below:

$$OHC\text{-}(CH_2)_3\text{-}CHO + \begin{matrix} NH_2\text{-}Protein \ ^A \\ NH_2\text{-}Protein^B \end{matrix} \quad \longleftrightarrow \quad \begin{matrix} Protein^A\text{-}NH \\ Protein^B\text{-}NH \end{matrix} \Big\rangle (CH_2)_3$$

Glutaraldehyde   **Cross-linked Product**
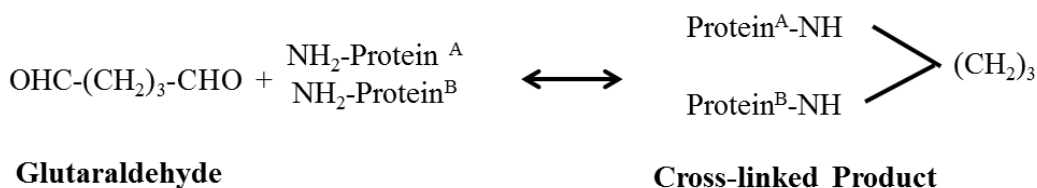
1-Ethyl-3-[3-dimethylaminopropyl]Carbodiimide Hydrochloride (EDC): EDC is a heterobifunctional cross-linker grouped under carbodiimides. Carbodiimides are zero-length cross-linkers that catalyse the formation of amide bonds between the carboxylic group of protein A and the amine group of protein B as shown in the scheme below.

$$CH_3CH_2\text{-}N\text{=}C\text{=}N\text{-}(CH_2)_3.N.(CH_3)_2 \quad + \quad \begin{matrix} COOH\text{-}Protein \ ^A \\ NH_2\text{-}Protein^B \end{matrix}$$

EDC

$$\updownarrow$$

$$Protein^A\text{-}CO\text{-}NH\text{-}Protein^B \quad + \quad CH_3CH_2\text{-}NH\text{-}\underset{O}{\overset{}{C}}\text{-}NH\text{-}(CH_2)_3.N.(CH_3)_2$$

Cross-linked Product
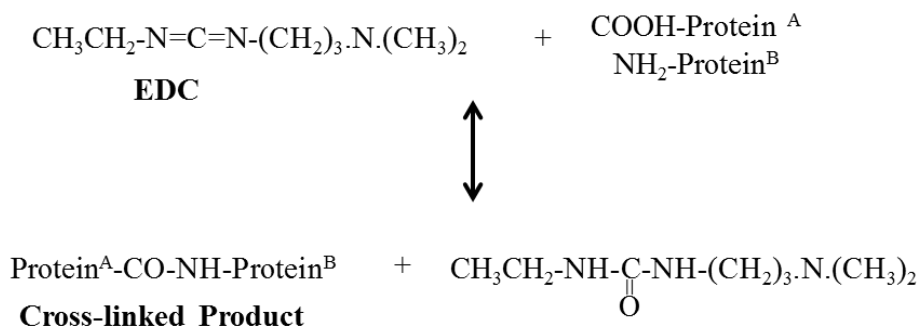
1,5-Difluoro-2,4-dinitrobenzene (DFDNB): DFDNB is a homobifunctional aryl halide cross-linker. The amine groups of proteins displace its two reactive fluorine atoms and a stable arylamine is formed in the process.

O_2N ... F

$+$ NH_2-Protein A
NH_2-Protein B

O_2N ... F

DFDNB

O_2N ... NH-Protein A

O_2N ... NH-Protein B

$+$ 2HF

Cross-linked Product
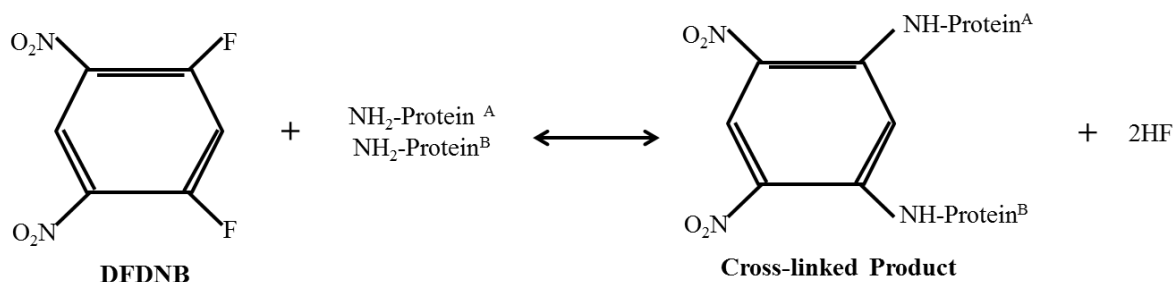
Bis(sulfosuccinimidyl) suberate (BS³): BS3 is an Amine-to-Amine homobifunctional cross-linker grouped under NHS esters (*332*), carrying the *N*-hydroxysulfosuccinimide ester leaving group at each end of the spacer arm. After cross-linking, the NHS groups leave the cross-linked product as shown in the scheme below:

NaO_3S ... N -O-C-$(CH_2)_6$-C-O-N ... SO_3Na

$+$ NH_2-Protein A
NH_2-Protein B

BS³

Protein^A-NH-C-$(CH_2)_6$-C-NH-Protein^B

Cross-linked Product

$+$ 2 $\left[NaO_3S \text{ ... } N\text{—OH} \right]$
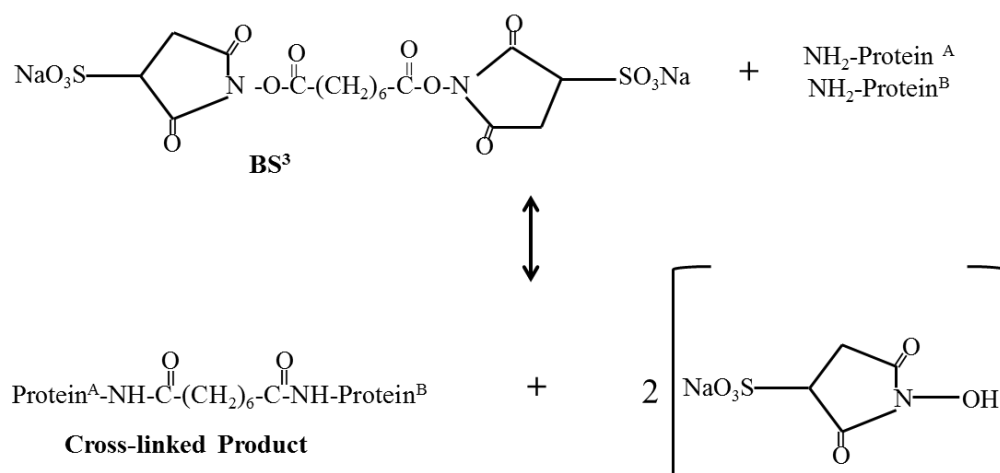
Dimethyl pimelimidate dihydrochlride (DMP): DMP is a homobifunctional cross-linker that contains the imidoester functional group (at each end of the spacer arm) which reacts with the amine groups of proteins to form stable imidoamides as shown in the scheme below:

$NH_2^+Cl^-$ $NH_2^+Cl^-$
CH_3-O-C-$(CH_2)_5$-C-O-CH_3

$+$ NH_2-Protein A
NH_2-Protein B

$NH_2^+Cl^-$ $NH_2^+Cl^-$
Protein^A-NH-C-$(CH_2)_5$-C-NH-Protein^B $+$ $2[CH_3OH]$

DMP

Cross-linked Product
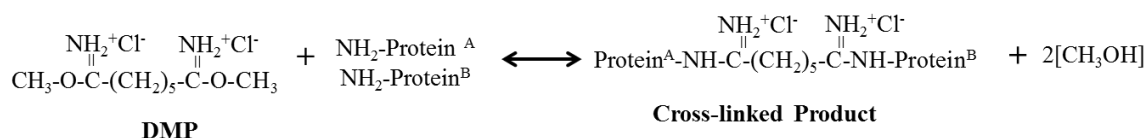
APPENDIX F: SEEDING PROTOCOL

The seeding protocol (as described by (*333*)) used for improving the quality of C773A mutant reductase crystals obtained in this study was as follows. The contents of the well containing crystals from initial screens were collected and suspended in 0.5 mL of their respective mother liquor in an Eppendorf tube. The mixture was vortexed for 3 minutes and a homogenous seed stock solution was obtained. This seed stock was then diluted 5-fold in 18 mg/mL C773A. The screens were then prepared by mixing 200 nL of the diluted mixture with 200 nL of the respective mother liquor and incubating at 4ºC for crystallization.

APPENDIX G: THEORIES AND PRINCIPLES OF SAXS

The principles of small angle X-ray scattering (SAXS) are similar to those of light scattering (discussed in Appendix C) where the main difference is the wavelength of the incident light. When incident X-ray beam hits a solution containing macromolecules, the light is scattered in all directions and at different angles. Analysing the scattering intensity (recorded by a detector) as a function of the scattering angle provides information on the structure and spatial correlation of the sample studied. Here, the basic theory of SAXS will be summarized, but in-depth information can be obtained from other reviews (*282-284, 316, 317, 334-338*). The information in this section will be cited from these reviews without further reference.

Automated SAXS data processing at the beamline

The scattering intensity data are initially processed at the beamline using automated methods. First, the data are radially averaged and normalised (to check for radiation damage) using the *AUTOMAR/AUTOPILATUS* program. Second, the *AUTOSUB* program is used to subtract the scattering intensity of the background (buffer) from the sample measurements. Finally, the required parameters, M_w, R_g and distance distribution functions are estimated using the *AUTORG* and *AUTOGNOM* programs, respectively. Also, *DAMMIF/DAMMIN* is used for 3D low resolution determination of *ab initio* shapes. These programs are discussed further in the following sub-sections.

AUTORG uses the Guinier formula (equation A48) to estimate the R_g of the molecule.

$$I(q) = I(0)e^{\left(\frac{-q^2 R_g^2}{3}\right)}$$
Equation A48

where *I(q)* represents scattering intensity as a function of the modulus of momentum transfer or scattering vector *q, I(0)* represents scattering intensity at zero angle (or zero scattering vector), R_g is the radius of gyration. *q* is given by

$q = 4\pi \sin(\theta)/\lambda$
Equation A49

where *2θ* is the angle between the incident and the scattered beam and *λ* is the wavelength of the X-ray beam. The values for R_g and *I(0)* can be obtained from the slope and intercept of a plot of the logarithm of the scattering intensity as a function of the square of the scattering vector (q^2) according to the equation:

$$\ln[I(q)] = \ln[I(0)] - \frac{q^2 R_g^2}{3}$$
Equation A50

where

$$R_g = \sqrt{-3 * slope}$$
Equation A51

The molecular weight (M_w) can then be estimated from the estimated value for $I(0)$ using the following relation:

$$I(0) = \kappa c (\Delta\rho)^2 (M_w)^2$$
Equation A52

where κ represents a proportionality constant obtained from measurements of known molecular weight standards, c is the protein concentration in the sample, and $\Delta\rho$ is the average electron density contrast of the macromolecule.

AUTOGNOM is an automated version of the program *GNOM* and both programs are used to calculate the distance distribution function [*P(r)*]. The programs use numerical methods to calculate P(r) from the indirect Fourier transformation of the scattering intensity

$$P(r) = \frac{r^2}{2\pi^2} \int_0^\infty q^2 I(q) \frac{\sin qr}{qr} dq$$
Equation A53

The numerical solutions depend on the choice of the maximum particle dimension (D_{max}), which corresponds to the value of r where P(r) goes to 0. As a result, D_{max} is user-defined in the *GNOM* program and needs to be found iteratively through successive solutions of Equation A53. In the *AUTOGNOM* program, multiple *GNOM* runs are carried out to find the optimum D_{max} and hence *P(r)* functions. Once P(r) is determined; R_g can be obtained according to the following equation

$$R_g^2 = \left. \int_0^{D_{max}} r^2 P(r) dr \middle/ \int_0^{D_{max}} P(r) dr \right.$$

Equation A54

DAMMIF is used for automated on-line *ab initio* shape determination. *DAMMIF* is the new version of *DAMMIN* and is about 25-40 times faster than its predecessor, but follows the general algorithm of *DAMMIN*. The algorithm depicts a particle as a collection of M ($>>1$) densely packed small spheres or beads (dummy atoms) inside a constrained search volume (no constraints in *DAMMIF*) with a maximum diameter defined by D_{max}. The configuration defined by the number and locations of beads is globally minimised via a simulated annealing algorithm. The algorithm calculates the scattering intensity for the configuration using spherical harmonics

$$I(q) = 2\pi^2 \sum_{1=0}^{\infty} \sum_{m=-1}^{1} |A_{1m}(q)|^2$$
Equation A55

where A_{1m} are the partial scattering amplitudes

A penalty term (equation A56) is introduced which ensures that the beads must be connected and the models are compact.

$$f(X) = \chi^2 + \alpha P(X)$$
Equation A56

where $\alpha > 0$ and equals the weight of looseness penalty.

The scattering intensity of the resulting model is compared to the experimental scattering intensity and the discrepancy is defined by the χ^2 term, according to equation A57. χ^2 is expected to be around 1 for a correct solution (where a perfect match is obtained between the experimental and theoretical scattering intensities).

$$\chi^2 = \frac{1}{N-1} \sum_{j=1}^{N} \left[\frac{I_{exp}(q_j) - CI_{calc}(q_j)}{\sigma(q_j)} \right]$$
Equation A57

where N equals the number of points in the scattering curve, while I_{exp} and I_{calc} represent the scattering intensity for the experimental and calculated curves, respectively, C equals a scaling factor and σ represents experimental errors.

3-D reconstruction of *ab initio* models using *DAMMIN* provides many solutions. As a result, it is advised to run the program multiple times and compare (and average) the resulting models as an indicator for the stability of the solution. The program *SUPCOMB* performs rapid superposition of structural models obtained from DAMMIN, and calculates the degree of structural similarity between these models. The measure of dissimilarity is known as the NSD (calculated from equation A58) and NSD values above 1 indicate unstable solutions. Subsequently, *DAMAVER* is used to average the superimposed models based on the NSD and outputs a smoothed model containing the most recurring features.

$$NSD = \left\{ \frac{1}{2} \left(\frac{1}{N_1 d_2^2} \sum_{i=1}^{N_1} \rho^2(S_{1i}, S_2) + \frac{1}{N_2 d_1^2} \sum_{i=1}^{N_2} \rho^2(S_{2i}, S_1) \right) \right\}^{1/2}$$
Equation A58

Equation A58 describes the NSD between two structure sets S_1 and S_2 with coordinates of points, N_i represents the number of points in S_i, d_i represents the average distance between the neighbouring points in S_i. At every point, $S_1 = (S_{1i}, i=1,...., N_1)$ and $S_2 = (S_{2i}, i=1, ..., N_2)$. $\rho(S_1, S_2)$ describes the minimum value among the distances between S_{1i} and all the points in the set S_2.

Other programs used for analysing SAXS scattering intensity data

A host of other programs are used for analysis of SAXS scattering data, but only the ones used in this study are described here. These include *CRYSOL*, *PRIMUS* and *SASREF*. *CRYSOL* is an efficient program for the calculation of scattering intensity of macromolecules from known atomic structures (and homology models). *CRYSOL* can also be used to fit the solution scattering curve to the experimental curve using the

average displaced solvent volume per atomic group and the contrast of the hydration layer. The program is based on spherical harmonics using multipole expansion and takes into account the inhomogeneous filling of the excluded volume and the hydration shell surrounding the macromolecules in solution. The scattering intensity is calculated from the atomic models as follows:

$$I(q) = \sum_{l=0}^{L} \sum_{m=-l}^{l} |A_{lm}(q) - \rho_0 C_{lm}(q) + \partial \rho B_{lm}(q)|^2$$
Equation A59

where A_{lm} equals the partial scattering amplitudes (i.e. atomic scattering in vacuum), L is the truncation value which defines the resolution of the representation of the particle, $\rho 0$ is the scattering density of the solvent, $\delta \rho$ represents unitary density given as $\rho_0 - \rho_b$ (ρ_b is the density of hydration shell), and C_{lm} and B_{lm} represent scattering from the excluded volume and the hydration shell, respectively.

As discussed earlier in this section, SAXS data can be automatically processed at the beamline and the functions include data averaging and subtraction as well as measurement of size and shape parameters (R_g and D_{max}). These functions can also be carried out manually using the program suite *PRIMUS*. *PRIMUS* can also be used for merging SAXS data, extrapolation to zero concentration, and curve fittings. The parameters that can be measured include radius of gyration and forward scattering intensity by the Guinier approach, the Porod invariant and Porod volume using the Porod approach, and characteristics of a partially ordered system computed from the maxima in the scattering profiles. In this study, the Guinier approach was used as described previously (see equation A48).

SASREF is a comprehensive automated rigid body modelling program used for quaternary structure modelling of multi-subunit complexes formed by rigid subunits with known atomic structure. In a similar way to *ab initio* modelling, *SASREF* conducts a series of random rigid body movements and rotations of the rigid subunits, and uses a simulated annealing algorithm to search for a best fit of the resulting complex scattering data to the experimental data. Thus, the *DAMMIN* equations A54 and A56 describing the scattering intensity algorithm and the discrepancy between the complex and experimental scattering intensities, respectively, are also employed by *SASREF*. However, the penalty equation is modified to incorporate additional information such as symmetry, orientational constraints, inter-residue contacts and inter-subunit distances.
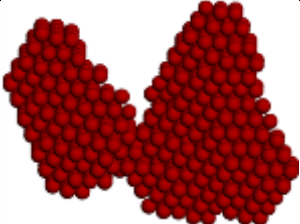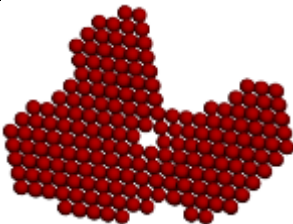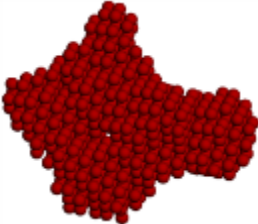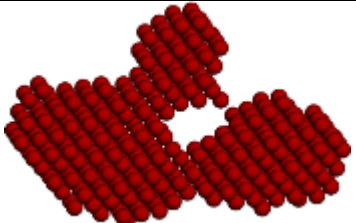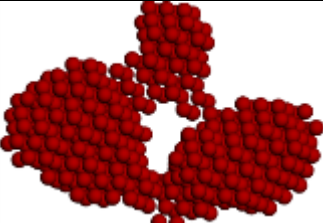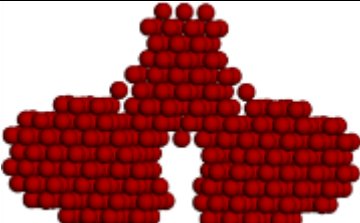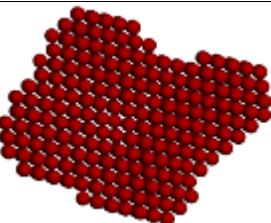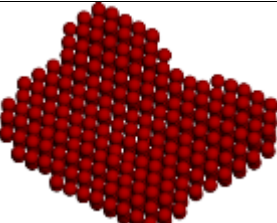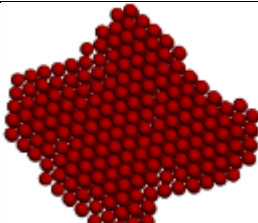
$$f(X) = \chi^2 + \sum \alpha_i P_i(X)$$
A60
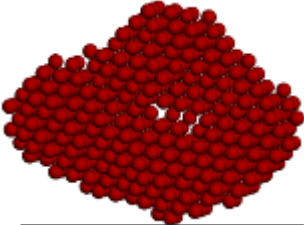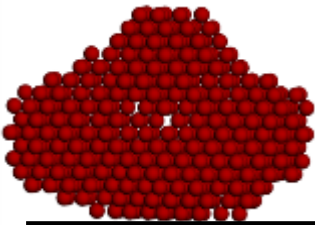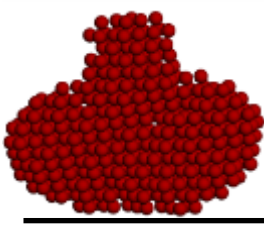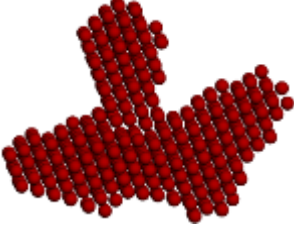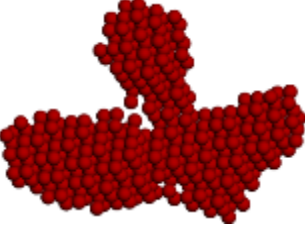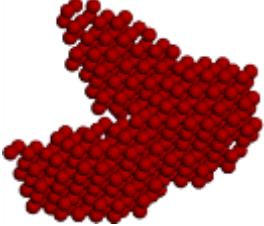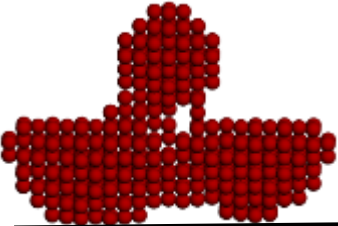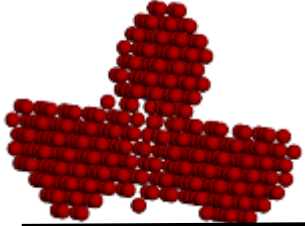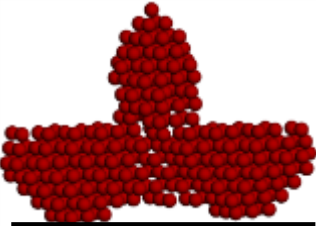
where the penalty term ($\alpha_i Pi$) accounts for the requirement of interconnectivity and absence of overlap, as well as incorporation of additional information from other methods as described above.

APPENDIX H: *AB INITIO* MODELS FOR FREE AND MODIFIED INTACT P450 BM3

Models presented here refer to data discussed in section 5.2.1
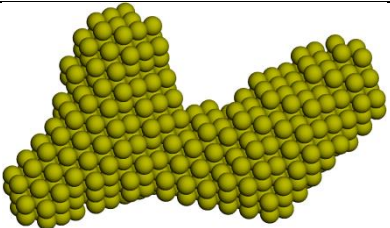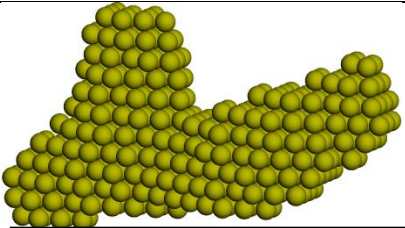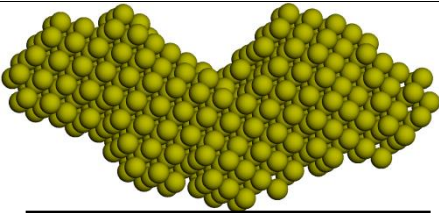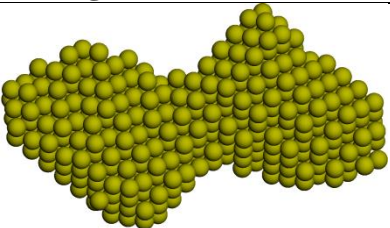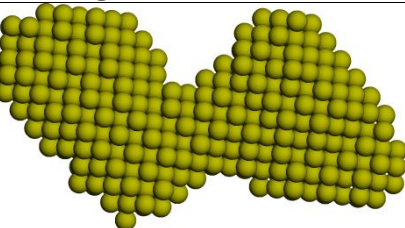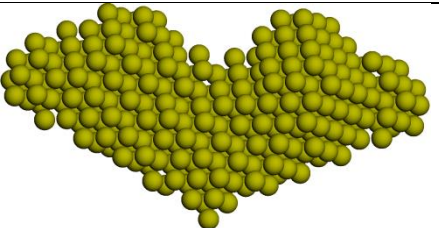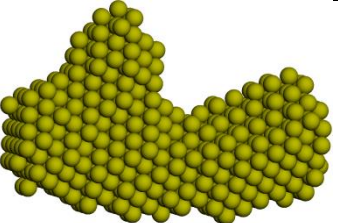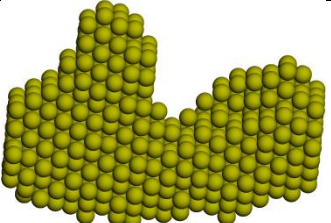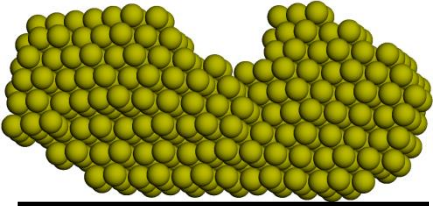
	P1/SUPCOMB 20	P1/SUPCOMB 13	P2/SUPCOMB 20
BM3 P1 MODELS Average χ^2:1.132 ± 0.006	14.2 nm **Average NSD:** 0.916 ± 0.028	13.9 nm **Average NSD:** 0.913 ± 0.029	14.0 nm **Average NSD:** 1.326 ± 0.070
BM3 P2 MODELS Average χ^2: 1.128 ± 0.011	14.7 nm **Average NSD:** 1.033 ± 0.032	14.5 nm **Average NSD:** 1.032 ± 0.033	14.5 nm **Average NSD:** 1.308 ± 0.151
BM3-NADP P1 MODELS Average χ^2: 0.985 ± 0.004	14.4 nm **Average NSD:** 0.825 ± 0.049	14.1 nm **Average NSD:** 0.819 ± 0.049	13.3 nm **Average NSD:** 1.175 ± 0.093
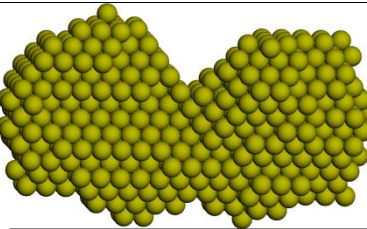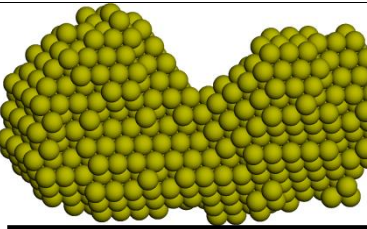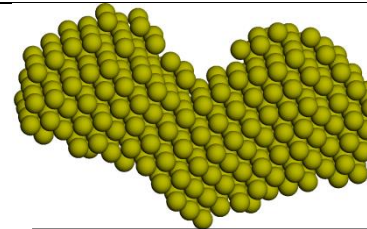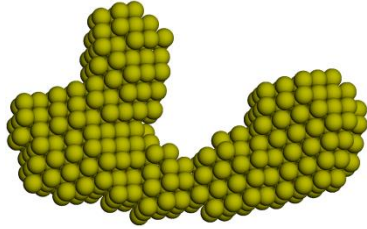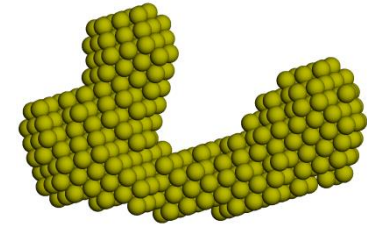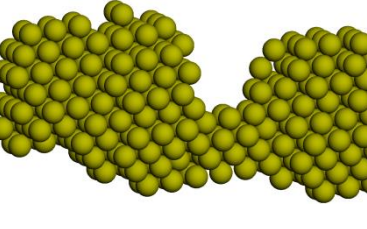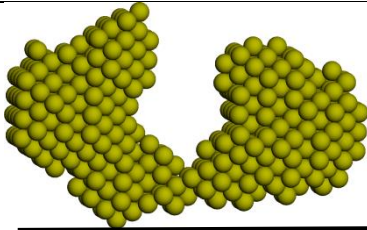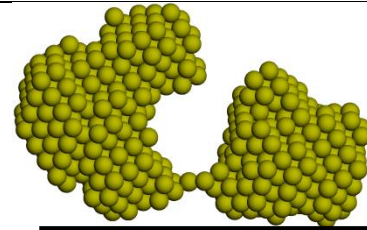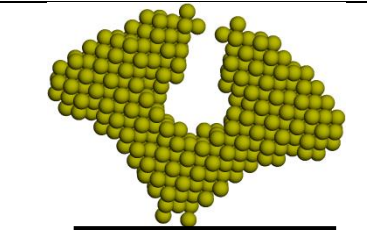
BM3-NADP P2 MODELS **Average χ^2**: 0.988 ± 0.008	 14.6 nm **Average NSD:** 0.950 ± 0.047	 13.7 nm **Average NSD:** 0.944 ± 0.048	 13.5 nm **Average NSD:** 1.243 ± 0.152
BM3-NPG P1 MODELS **Average χ^2**: 0987 ± 0.006	 15.7 nm **Average NSD:** 0.961 ± 0.032	 15.2 nm **Average NSD:** 0.960 ± 0.032	 14.2 nm **Average NSD:** 1.349 ± 0.072
BM3-NPG P2 MODELS **Average χ^2**: 1.000 ± 0.005	 15.6 nm **Average NSD:** 1.051 ± 0.056	 15.6 nm **Average NSD:** 1.052 ± 0.053	 15.7 nm **Average NSD:** 1.216 ± 0.135

APPENDIX I: *AB INITIO* MODELS FOR THE P450 BM3 BMR DOMAIN

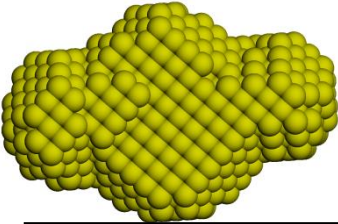## Models presented here refer to data discussed in section 5.2.2
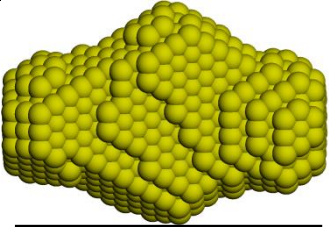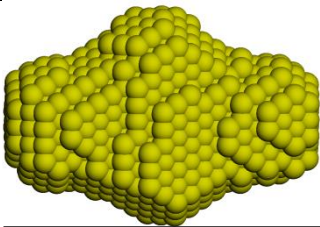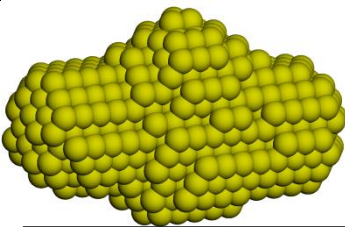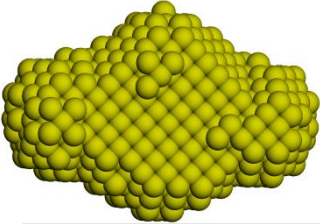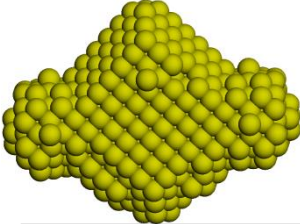
	P1/SUPCOMB 20	P1/SUPCOMB 13	P2/SUPCOMB 20
BMR *AUTOGNOM* P1 MODELS Average χ^2: 0.980 ± 0.003	14.6 nm **Average NSD:** 0.815 ± 0.027	14.7 nm **Average NSD:** 0.815 ± 0.028	15.2 nm **Average NSD:** 1.354 ± 0.092
BMR *AUTOGNOM* P2 MODELS Average χ^2: 0.987 ± 0.005	14.4 nm **Average NSD:** 0.919 ± 0.046	14.5 nm **Average NSD:** 0.918 ± 0.046	14.9 nm **Average NSD:** 1.346 ± 0.205
BMR *GNOM* P1 MODELS (q = 3 nm^{-1}) Average χ^2: 1.201 ± 0.002	13.3 nm **Average NSD:** 0.798 ± 0.026	12.5 nm **Average NSD:** 0.794 ± 0.025	13.0 nm **Average NSD:** 1.410 ± 0.091

BMR *GNOM* P2 MODELS **(q = 3 nm^{-1})** **Average χ^2:** 1.209 ± 0.005	 13.5 nm **Average NSD:** 0.872 ± 0.043	 13.1 nm **Average NSD:** 0.873 ± 0.045	 12.8 nm **Average NSD:** 1.560 ± 0.321
BMR *GNOM* P1 MODELS **(q = 6 nm^{-1})** **Average χ^2:** 1.119 ± 0.003	 13.1 nm **Average NSD:** 0.853 ± 0.026	 13.1 nm **Average NSD:** 0.851 ± 0.026	 13.0 nm **Average NSD:** 1.299 ± 0.094
BMR *GNOM* P2 MODELS **(q = 6 nm^{-1})** **Average χ^2:** 1.125 ± 0.003	 13.3 nm **Average NSD:** 0.927 ± 0.037	 13.3 nm **Average NSD:** 0.925 ± 0.037	 13.3 nm **Average NSD:** 1.484 ± 0.112

APPENDIX J: *AB INITIO* MODELS FOR THE P450 BM3 FAD DOMAIN

Models presented here refer to data discussed in section 5.2.3

	P1/SUPCOMB 20	P1/SUPCOMB 13	P2/SUPCOMB 20
FAD P1 MODELS **Average χ^2**: 1.546 ± 0.009	 9.3 nm **Average NSD:** 0.485 ± 0.024	 9.0 nm **Average NSD:** 0.481 ± 0.023	 9.1 nm **Average NSD:** 0.925 ± 0.092
FAD P2 MODELS **Average χ^2**: 1.546 ± 0.008	 9.3 nm **Average NSD:** 0.527 ± 0.106	 9.4 nm **Average NSD:** 0.479 ± 0.042	 9.4 nm **Average NSD:** 1.099 ± 0.257